Geochronology and structural geology of the Kjerringøy Peninsula, Nordland, Norway

by

Jonathan Michael Prouty

A thesis submitted to the Graduate Faculty of
Auburn University
in partial fulfillment of the
requirements for the Degree of
Master of Science

Auburn, Alabama
August 2, 2014

Keywords: structural geology, geochronology, tectonics, Scandinavian Caledonides

Approved by

Mark G. Steltenpohl, Chair, Department Chair and Alumni Professor of Geology
Ashraf Uddin, Professor of Geology
Haibo Zou, Associate Professor of Geology

ABSTRACT

Field mapping, structural and petrographic analysis, ID-TIMS U-Pb geochronology, $^{40}Ar/^{39}Ar$ thermochronology, and chemical dating of minerals were employed to decipher the geologic history of the Salten area of north-central Norway. The “Heggmovatn Dome” was examined where it is overlain by rocks of the Bodø Nappe. Geologic mapping indicates that the Landegode, Bratten, and Tårnvika megacrystic granites are one structurally continuous unit, likely a composite batholith comprising numerous plutons. An ID-TIMS U-Pb age determination of ~950 Ma for the Tårnvika pluton and ~428 Ma for the Fjærhesten granite is evidence that the “Heggmovatn Dome” is not a Baltic basement gneiss dome but rather is a Scandian thrust nappe that evolved during the Neoproterozoic Valhalla orogeny. This juxtaposition of Tonian and Ordovician-Silurian plutons gives a distinctive fingerprint unique to the Laurentian Caledonides of the North Atlantic, clearly linking the Heggmo Nappe to Laurentia. Geologic findings point to a pre-Scandian kyanite-grade metamorphic event with U-Pb ages of zircon (~460 Ma) and rutile (~460-470 Ma) and a chemical monazite age (~445-475 Ma) supporting Taconian/Grampian deformation, likely along the Laurentian margin. Apart from regional folding and tonalitic and pegmatitic intrusions, evidence for Silurian-Devonian Scandian orogenesis is not abundant in the Heggmo

Nappe. The greenschist-facies, tops-down-to-the-west Fjær-Osvika\Steigtinden shear zone (FOSZ) down-dropped rocks of the Bodø Nappe upon rocks of the Heggmo Nappe. Devonian extension along the FOSZ helps to clarify the geometry and distribution of the extensional detachment system in its northernmost extent in Norway. Brittle Mesozoic to Tertiary normal faults trend northeast/southwest throughout the study area and record rifting that eventually led to continental separation in the Eocene.

ACKNOWLEDGEMENTS

Dr. Mark Steltenpohl is thanked for his guidance and engagement during the completion of my thesis. I will be forever grateful for his influence on my development as a geologist.

Professor Arild Andresen (University of Oslo) also deserves more thanks than I can give him. His financial and logistical support while I was in the field in Kjerringøy and working in laboratories of the University of Oslo were critical to the success of this project. His friendship and wise counsel is greatly appreciated.

I am equally indebted to Professor Fernando Corfu (University of Oslo) for contributing his expertise and energies to this study and for his patient and extraordinary mentorship. I would also like to thank Gunborg Bye Fjeld (University of Oslo) for her clear instructions and continual assistance while I learned how to prepare samples for analysis using ID-TIMS.

Dr. Willis Hames played a crucial role in the completion of this project. He mentored me through producing the ^{40}Ar/^{39}Ar analysis and helped greatly with my interpretation of the metamorphic conditions of some of the rocks found in the study area. Dr. Hames also introduced me to Dr. Bob Tracy (Virginia Polytechnic Institute and State University) to whom I owe a great many thanks. Dr. Tracy donated a great deal of electron microprobe instrument time and enthusiastically discussed the results. Dr. Haibo Zou was also extremely helpful in teaching me some of the intricacies of monazite chemical dating.

I learned much through my many discussions with Dr. Lars Augland (Université du Québec à Montréal), both in the field and in the lab. I am happy to have benefited from his expertise and his friendship.

John Hawkins' companionship and assistance in the field is also much appreciated. I especially thank John for generously sharing his field notes and photos for the Tårnvika area.

I am very grateful to Dr. Mark Cooper (Sherwood Geoconsulting) and Dr. Michael Styles (British Geological Survey) for their unselfish assistance and discussion regarding the regional geology of the study area.

Many thanks are due to fellow grad students Bart Davis, Chris Howard (University of Tennessee), and Chris Hanratty (Colorado State University) for many lively discussions and much encouragement. I also thank Julia Spencer for her patience and support while I drafted this report.

Finally, I thank my family for their continual support in all things, not only in their prodding me to finish this thesis.

TABLE OF CONTENTS

LIST OF TABLES

LIST OF FIGURES

INTRODUCTION

The Salten area of Norway, one-hundred kilometers north of the Arctic Circle, is a glacially-scoured region of deep fjords and steep mountains. Stretching from Skjerstadfjorden (Fig. 1) in the south to Sagfjorden 130 km to the north, the Salten interior is dominated by an antiformal structure long known to geologists as the Heggmovatn Dome (Fig. 2). Early workers (Rutland and Nicholson, 1965; Nicholson and Rutland, 1969; Nicholson, 1970; Wilson and Nicholson, 1973; Cooper, 1978; Wilson, 1981; Cooper and Bradshaw, 1980; Cooper 1985) focused on establishing regional lithologic correlations and characterizing the major structures and fabrics. These works resulted in a regional tectonic synthesis with the Heggmovatn Dome as an exposed portion of the Baltic basement (Fig. 2A) (Rutland and Nicholson, 1965). There has been little modern geological research since this early work was completed, despite being adjacent to the relatively well-studied areas of Ofoten and Lofoten to the north and central Norway to the south (Fig. 1). This hiatus in research has left a gap in our understanding of the evolution of this portion of the Norwegian Caledonides.

Early workers in the area suggested that the Heggmovatn Dome and other structures nearby were originally diapirs of buoyant material that fractionated from a Rapakivi-like crust during the 1800-1700 Ma Svecokarelian orogeny, one of the phases of the formation of Baltica (Cooper, 1978; Bogdanova et al., 2008). It was thought that during the Scandian orogeny these diapirs rose to what are now the highest structural levels still extant, rising through the denser material thrust above them (Cooper, 1985).

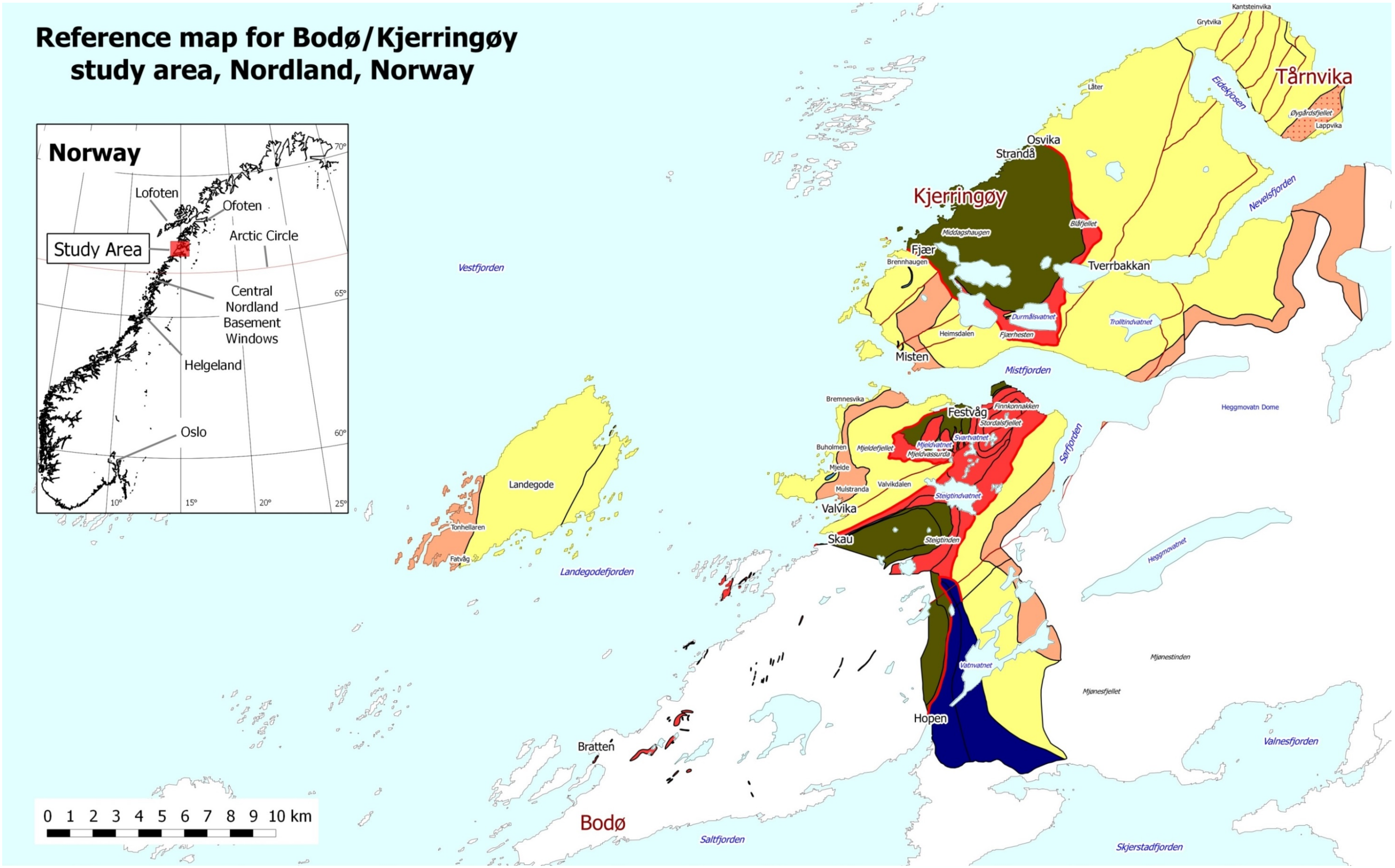

Figure 1 - Reference map for the present study area, contains all place names referenced in this report. The map is centered on the Bodø Kommune, Nordland, Norway.

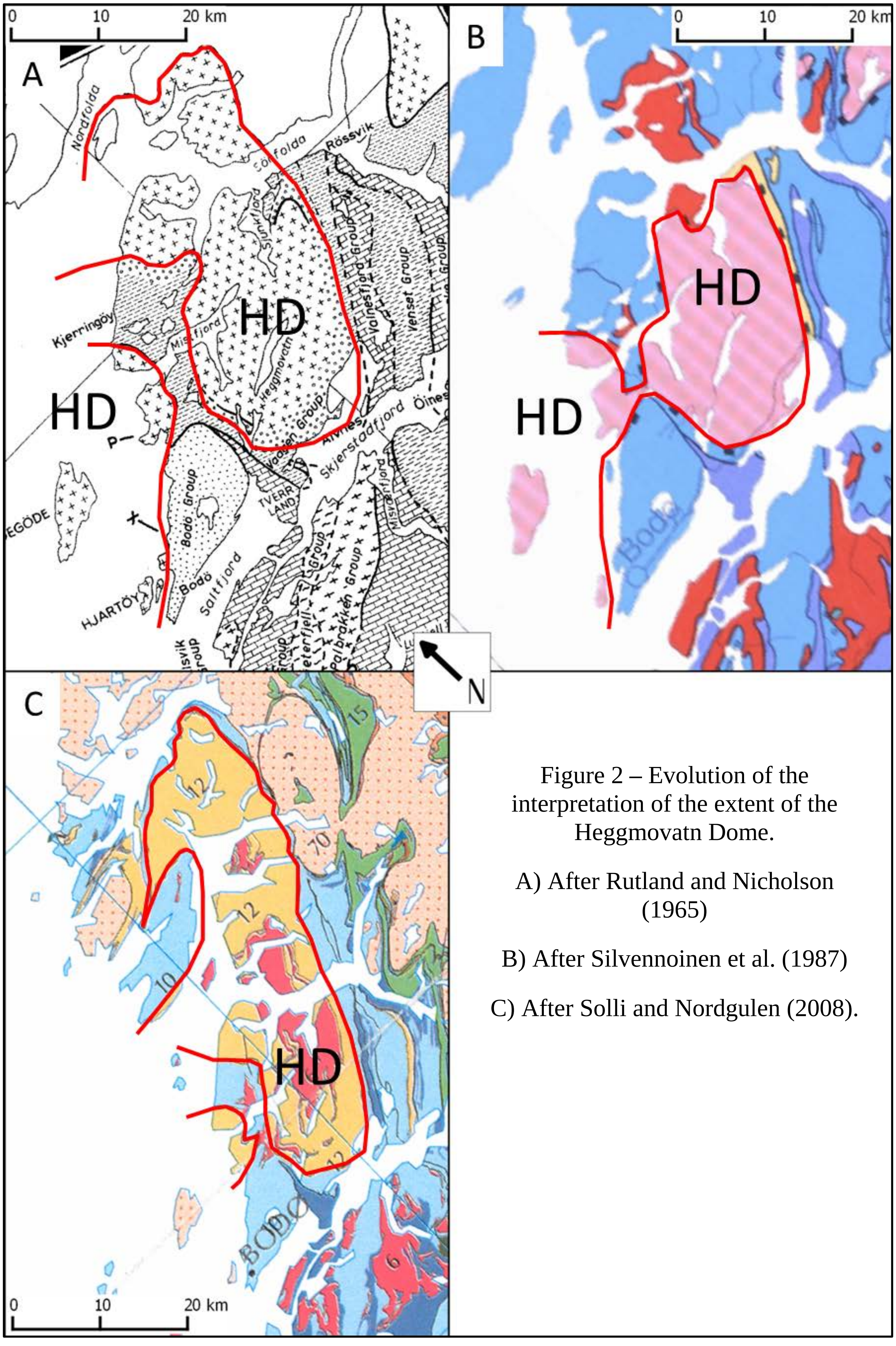

Figure 2 – Evolution of the interpretation of the extent of the Heggmovatn Dome.

A) After Rutland and Nicholson (1965)

B) After Silvennoinen et al. (1987)

C) After Solli and Nordgulen (2008).

This model of Baltican basement sourced diapirs was incorporated into the official Norsk geologisk undersøkelse (NGU, Geological Survey of Norway; Fig. 2B) Bodø and Sulitjelma map sheets (Gustavson, 1991; Gustavson and Blystad, 1995; Gustavson, 1996). Later work in the area focused on structures and began to incorporate modern geochronological analysis (Carter, 2000; Zeltner, 2001; Steltenpohl et al., 2009; Agyei-Dwarko, 2010; Andresen et al., 2011; Augland et al., 2013). These new geochronological datasets have demonstrated that the long-held “Baltican basement” model for the gneisses in the Bodø region is untenable. In the 2008 NGU bedrock map of Norway (Fig. 2C) (Solli and Nordgulen, 2008) the rocks of the Heggmo area were considered to be exotic to Baltica, which the work of Agyei-Dwarko (2010), Andresen et al. (2011), and Augland et al. (2013) confirmed. The history of how the exotic Heggmovatn rocks came to be in northern Norway is as yet unknown.

In order to pull these disparate sets of structural and geochronological data into a coherent picture, the current author developed several objectives to guide the research presented in the current study. Objective 1: Targeted field mapping to help unify the structural work of Zeltner (2001) with the recent geochronological findings of Agyei-Dwarko (2010). Objective 2: Further laboratory geochronological work to expand the pool of data that exists for the Salten region so that a more coherent regional interpretation can be attempted. To these aims, Electron Microprobe Analysis (EMPA) is used to characterize mineral compositions and to compute the pressure and temperature history of a kyanite, biotite, muscovite paragneiss. A monazite chemical age is determined for this lithology based on the data obtained via EMPA. Muscovite from this lithology is dated using $^{40}Ar/^{39}Ar$ isotopic dating methods to explore its mineral cooling history. Isotope Dilution-Thermal Ionization Mass Spectrometry (ID-TIMS) provides high resolution ages from three separate lithologies in the study area: a paragneiss, an orthogneiss, and a granite. Petrographic and structural analysis on rocks in select areas establishes the structural and spatial relationships between the lithologies examined.

Geologic Setting

The Appalachian-Caledonian mountain system is classically known for having amalgamated the supercontinent Pangaea through a series of middle-to-late Paleozoic collisions. In the northern parts of the orogen, the culminating Silurian continent-continent collision is recorded on both the Laurentian (Acadian phase) and Baltican (Scandian phase) sides (Stephens and Gee, 1985).

In the Middle Ordovician the closure of the Iapetus Ocean was completed via westward-subduction beneath Laurentia (Stephens and Gee, 1985). As Baltica came into contact with Laurentia, Baltica’s leading edge was thrust imbricated, resulting in pieces of Baltic basement and the immediately overlying sedimentary cover rocks becoming tectonized and weakly foliated, creating the Parautochthon (Roberts and Gee, 1985). As the collision continued, parts of Baltica’s passive margin were thrust on top of the Parautochton, creating a still extant group of thrust sheets collectively known as the Lower Allochthon (Fig. 3) (Roberts and Gee, 1985). The Middle Allochthon is similarly composed of rocks of Baltic affinity; however, the Middle Allochthon contains greenschist-facies and amphibolite-facies units (Fig. 3) (Roberts and Gee, 1985).

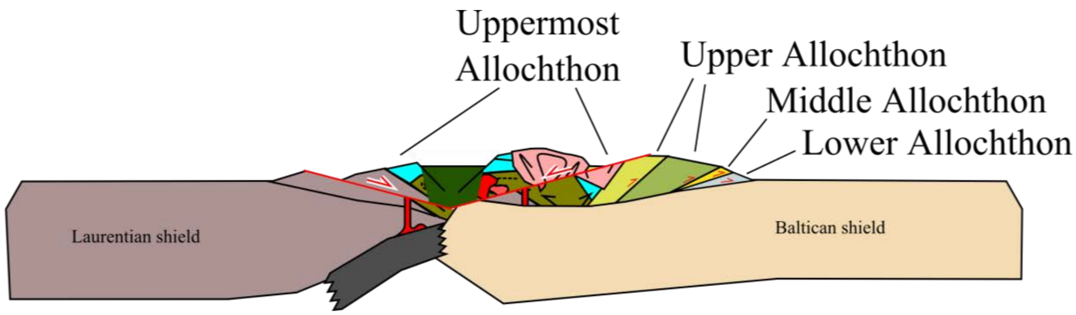

Figure 3 – Schematic cross section showing the major tectonostratigraphic units in the Scandinavian Caledonides at the end of the Scandian orogeny.

Structurally above the Middle Allochthon is the Upper Allochthon (Fig. 3), containing rocks and structures recording the subduction and destruction of Iapetan oceanic crust. The Upper Allochthon is composed of ophiolitic and arc material and associated sediments (Roberts, 2003). Final closure of Iapetus occurred and true continental collision commenced when the last portions of oceanic crust subducted, dragging down with it portions of Baltica's passive margin, initiating A-type subduction (Hodges et al., 1982a). During this presumably short-lived period, Laurentian continental crust overrode the subducting Baltican slab. The buoyant subducting Baltican crust eventually detached from the lithospheric mantle below, causing the continental lithosphere to rebound upwards (Hodges, 1982a; Andersen et al., 1991). Large swaths of Laurentian crust separated from Laurentia-proper at this time, faulted away on top of the ascending Baltican crust. This Laurentian-derived portion of the Norwegian Caledonides is known as the Uppermost Allochthon (Fig. 3) (Roberts and Gee, 1985; Roberts et al., 2007). The Uppermost Allochthon is the structurally highest unit in the Scandinavian Caledonides, composed of schists, psammites, conglomerates, dolomite, marbles, and various meta-mafic rocks, almost universally metamorphosed to amphibolite facies (Stephens and Gee, 1985). Unique to the Uppermost Allochthon are extensive

Caledonian-aged plutons and several faults interpreted as tops-up-to-northwest thrusts, suggested to be of Laurentian (Taconian/Grampian) origin (Barnes et al., 2007; Roberts et al., 2007). Emplacement of the Uppermost Allochthon represents the climactic contractional phase of the Caledonian orogeny in Scandinavia.

Shortly after the peak of Caledonian orogenesis the newly formed mountain chain began to rapidly uplift and collapse, driven by the gravitational instability created by the ascent of the Baltican crust (Andersen et al. 1991). Mass-wasting on an orogenic scale was accomplished through the development of a system of normal detachment faults, from southern Norway to the Narvik area (Fossen, 1992, 2010). Extension in the Heggmovatn area reportedly has occurred in two pulses; an orogen-parallel phase in the early Devonian and an orogen-orthogonal phase in the late Devonian and early Carboniferous (Steltenpohl et al., 2009). This timing is broadly coeval with extension in southern Norway (Andersen and Jamtveit, 1990; Walsh et al., 2007). Sediment shed during the collapse of the southern Norwegian Caledonides is preserved in Devonian basins in southwestern Norway and the British Isles, the famous Old Red Sandstone (Stephens and Gee, 1985; Fossen, 1992). No Devonian sediments are recognized farther to the north.

The present study area lies within the hinterland of the Scandian orogen, an area traditionally interpreted to consist of rocks of the Uppermost Allochthon thrust directly onto parautochthonous Baltican basement rock (Gee et al., 1985). The mountainous area to the east of the study area has historically been interpreted to consist of gneiss diapirs derived from the Baltic basement, exposed in a large tectonic window through the Uppermost Allochthon (Figs. 2, 4) (Rutland and Nicholson, 1965; Nicholson and

Rutland; 1969; Bennet, 1970; Wilson and Nicholson, 1973; Cooper, 1978; Cooper and Bradshaw, 1980; Thelander et al., 1980; Cooper, 1985; Gustavson and Blystad, 1995; Gustavson, 1996; Steltenpohl et al., 2009).

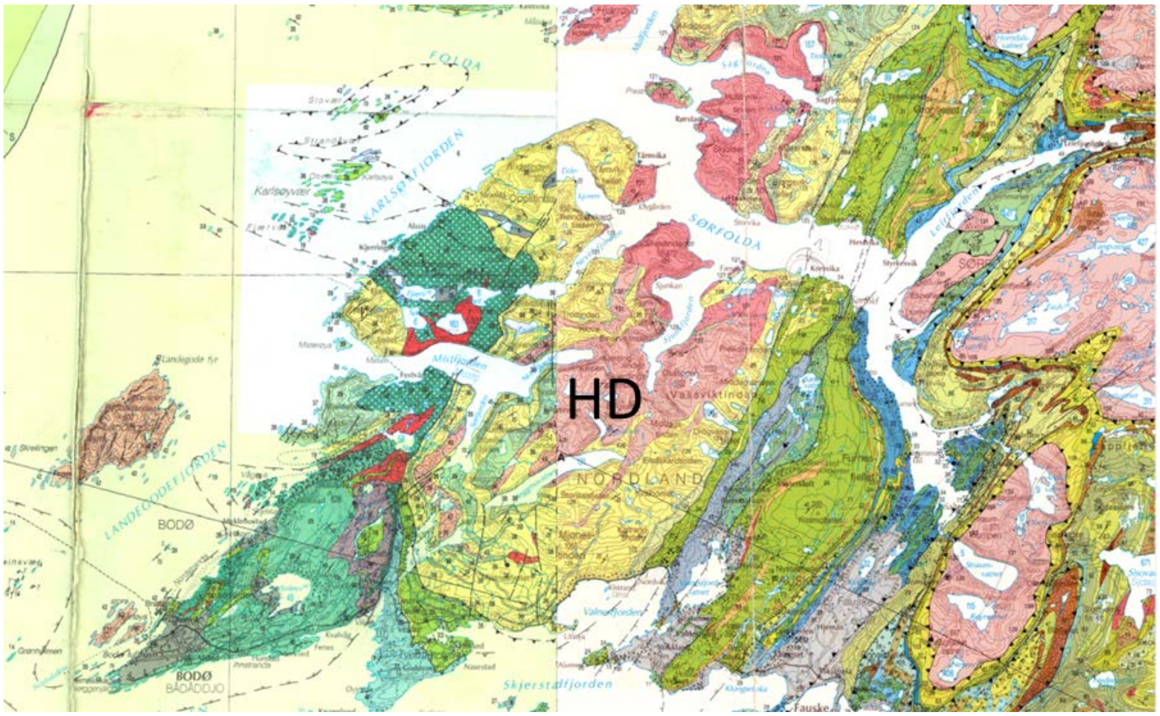

Figure 4 - The "Heggmovatn Dome" (HD) as depicted in the NGU Bodø and Sulijelma map sheets. Pink shades are Baltic basement orthogneisses and yellow shades are paragneisses interpeted to represent primary sedimentary cover to the basement. (from Gustavson and Blystad, 1995; Gustavson, 1996).

The Uppermost Allochthon in this region comprises several nappes that have been variably interpreted (Table 1): the Bodø, the Beiarn (not found in the study area), and the Rödingsfjället Nappes (Gustavson, 1996; Zeltner, 2001; Agyei-Dwarko, 2010). The Bodø Nappe is a lithologically heterogeneous and weakly studied unit consisting of mica, kyanite- and staurolite-bearing schists, calcsilicate schists, amphibole-biotite-antigorite schist, and calcite marble (Gustavson, 1996). Zeltner (2001) divided the Bodø Nappe into three units: the structurally lowest calcsilicate schists; the amphibolite-bearing Hopsfjell

Table 1 – Correlation chart for tectonostratigraphic divisions for the study area provided by previous workers. All lithologies are contained within the Uppermost Allochthon.

<table>
<tr><th>Nicholson and Rutland (1969)</th><th>Gustavson and Blystad (1995)</th><th>Zeltner (2001)</th><th>Agyei-Dwarko (2010)</th><th colspan="2">This Study</th></tr>
<tr><td></td><td>Caledonian granite</td><td>granitic pluton and dikes</td><td>NOT OBSERVED</td><td>Fjærehesten Granite</td><td rowspan="7">Bodø Nappe</td></tr>
<tr><td rowspan="6">Bodø Schist Group</td><td rowspan="3">mica schist and garnet mica schist, locally with staurolite</td><td rowspan="4">Hopsfjell schist</td><td>Dark-mica schist</td><td rowspan="4">Hopsfjell schist</td></tr>
<tr><td>garnetiferous schist</td></tr>
<tr><td>mica schist</td></tr>
<tr><td>Amphibole, biotite, antigorite schist</td><td>amphibole-biotite schist</td></tr>
<tr><td>Calcite marble</td><td>Ørntuva marble</td><td>NOT OBSERVED</td><td rowspan="2">NOT OBSERVED</td></tr>
<tr><td>Calcsilicate-bearing schist and mica schist, undifferentiated</td><td>calc-silicate schist</td><td>calcsilicate schist</td></tr>
<tr><td>Saura Group</td><td>Calcite marble with interlayered dolomite marble</td><td>Beiard Group</td><td rowspan="2">NOT OBSERVED</td><td rowspan="2">NOT OBSERVED</td><td rowspan="2">Rödingsfjället Nappe</td></tr>
<tr><td>Upper Vågen Schist Group</td><td>Mica schist</td><td>Skjøvne Group</td></tr>
<tr><td>Lower Vågen 'Sparagmite' Group</td><td>Meta arkose with layers of quartzite, feldspathic mica gneiss and calcite marble, locally migmatitic</td><td>Paragneiss</td><td>Paragneiss</td><td>Kjerringøy paragneiss</td><td rowspan="3">Heggmo Nappe</td></tr>
<tr><td rowspan="2">Heggmovatn Gneiss Group</td><td rowspan="2">Orthogneiss with layers of meta arkose and mica schist</td><td rowspan="2">Orthogneiss</td><td>Basement megacrystic Orthogneiss</td><td>Rørstad granite</td></tr>
<tr><td>Deformed orthogneiss</td><td>Kjerringøy orthogneiss</td></tr>
</table>

Schist; and the Ørntuva marble (Table 1). Rutland and Nicholson (1965) considered the Vegdal Group to the south to be correlative to the Bodø Nappe. Gustavson and Gjelle (1991) describe the Vegdal Group as consisting of fine- to medium-grained banded mica schists with occasional staurolite and sillimanite. Cooper (1978) also interpreted the Vegdal Group as having been thrust above the Beiarn Nappe, based on Styles' (1974) report of the Vegdal being a much lower grade of metamorphism than the rest of the Beiarn Nappe. Tørudbakken and Brattli (1985) identified a major discontinuity in the middle of the Vegdal Group and decided to reclassify it as the Kovdistind unit, thrust above the Habreså unit. Most recently, Augland et al. (2011) obtained an age of 434.06 ± 0.54 Ma for the Høgtind granite, which is found in both the Kovdistind and the Habreså units.

The Rödingsfjället Nappe (Table 1) is found east of Bodø in the study area and is composed of the Skjøvne Group muscovite, quartz, biotite garnet schists and the overlying Beiard Group calcite marbles (Zeltner, 2001; Table 1). Rutland and Nicholson (1965) referred to these as the Saura Marble, which in the Valnesfjord area Cooper (1978) subdivided into the Saura Nappe and the Næverhaugen Marble Group, part of the Beiarn Nappe.

The Beiarn Nappe is interpreted to have been emplaced early in the sequence of events that ultimately formed the Norwegian Caledonides in the Salten region (Rutland and Nicholson, 1965). Cooper (1978) found the Beiarn Nappe in the Valnesfjord region to be a refolded fold nappe intruded by abundant granites that are nearly absent in adjacent rocks.

LITHOLOGIES

This section details the lithological characteristics of the different rocks found in the study area. Units are described from structurally-lowest to structurally-highest. The order of observations within each unit description is from macro to micro, that is, regional descriptions followed by field characteristics followed by petrographic observations. Established formation names were used when known, and all mineral name abbreviations comply with the recommendations made by Siivola and Schmid (2007).

There are two major tectonostratigraphic units in the study area, the Heggmo Nappe and the Bodø Nappe (Plate 1). The structurally-lowest of the two is the Heggmo Nappe, which comprises three subunits: the Kjerringøy paragneiss, the Kjerringøy orthogneiss, and the Rørstad granite. Table 2 contains modal mineral abundances from select samples that are based on manual point counting and visual estimation. The Heggmo Nappe is separated from the overlying Bodø Nappe (Table 1) by the ductile tops-down-to-the-west Steigtinden/Fjær-Osvika shear zone. The Bodø Nappe is itself composed of two subunits: the Bodø schist and the Fjærehesten granite. All rocks in the study area are preserved in the Steigtinden synform. Zeltner (2001) reports the presence of the Rödingsfjället Nappe to the south, between the rocks of the Heggmo and Bodø Nappes, but no evidence was found indicating its presence in the study area.

Table 2 - Petrographic modal analysis of samples selected for geochronological analysis and for pressure-temperature analysis

Protolith	**Lithology**	**Sample**	**Analysis Type**	**Quartz**	**Muscovite**	**Plagioclase Feldspar**	**Biotite**	**Garnet**	**Potassium Feldspar**	**Kyanite**	**Apatite**	**Hornblende**	**Sericite**	**Tourmaline**	**Zircon**	**Opaque**	**Accessory**	**Points counted**	**Easting**	**Northing**
Sedimentary	Kjerringøy Paragneiss	KJR-036	EMPA $^{40}Ar/^{39}Ar$	40	30		10	15			2			1	1	1		Visual estimate	486443	7485926
	Kjerringøy Paragneiss	KJR-243	ID-TIMS	20.8		62.7	16.2	0.2					0.1				Zrn Ttn	1021	487057	7482762
	Kjerringøy Paragneiss	KJR-093	ID-TIMS	54.8	14.5	0.8		5.7	7.6	16.7							Mnz Zrn Ilm Rt	409	484326	7479327
Intrusive	Kjerringøy Orthogneiss	LND-000	ID-TIMS	33.8	8.7	28	26.3			2.1		0.1				1		492	467941	7474429
	Rørstad Granite	LEA-10-1	ID-TIMS	12.2	2.9	53.2	7		24.4						0.1	0.1		1210	505849	7493461
	Fjærehesten Granite	LEA-10-2	ID-TIMS	15.1	6.7	68.4	5.2		4.6									812	491908	7483866

Heggmo Nappe

Kjerringøy Paragneiss

The Kjerringøy paragneiss (Plate 1) is the most regionally extensive unit found in the study area and has been mapped as far as 50 km north-northeast to Sagfjorden and 10 km east by east-southeast (Gustavson, 1996). This unit has previously been considered as equivalent to the Lower Vågen Group found in the Glomfjord area to the south in Rana (Nicholson and Rutland, 1969; Gustavson and Gjelle, 1991; Table 1). The Kjerringøy paragneiss is found in the study area on the island of Landegode, both the southern and northern shores of Mistfjorden, and also from Strandå north to Sørfolda.

Throughout the study area the Kjerringøy paragneiss is predominantly quartzofeldspathic but it does contain subordinate layers of amphibolite, marble, and kyanite garnet mica schists (Gustavson, 1991, 1996; Gustavson and Blystad, 1995). The diameter of garnet porphyroblasts tends to be uniform within individual layers of the subordinate garnetiferous schist, but diameters vary widely from layer to layer, ranging from sub-millimeter to several centimeters. Amphibolite and quartzite layers are commonly isoclinally folded or stretched into boudins defining horizons that approximate original bedding. Quartzofeldspathic layers are generally white in fresh surfaces but may be a rusty-brown color where stained. Pervasive limonite and goethite occur along late brittle faults.

The most accessible exposure of the paragneiss crops out between the ferry station at Misten and its contact with the overlying Bodø schist at Fjær (Fig. 1, Plate 1).

The portion of this traverse which parallels Mistfjorden is nearly perpendicular to the regional foliation and exposes nearly two kilometers of true tectonostratigraphic thickness, which is to say that if the foliation were horizontal the outcrop would be two kilometers high. The extent of structural repetition of layers within this unit is unknown but is probably widespread given the abundance of mesoscopic isoclinal folds. The structural level exposed at Misten is migmatitic and heavily intruded by pegmatites associated with the Fjærehesten granite a few hundred meters structurally above. Unique to this tectonostratigraphic level are ultramafic bodies not observed at other levels in the Heggmo Nappe.

Gray to light tan coarse-grained marble is found in layers of up to a meter thick and is characterized by a rillenkarren texture commonly found in karst areas. The marble is invariably found associated with < 0.1 m layers of amphibolite (Fig. 5). The most accessible exposure of marble is along the beach at Mjelde and along a hill called Futskardet directly southeast of the beach, just uphill from the highpoint of the beach access road. The unit also appears along the beach approximately 1.6 km northwest of the ferry station at Misten (Fig. 1). It is again exposed roughly 1 km to the southwest of the village of Fjær where it appears as a prominent white layer in the hill to the east of the road. This marble/amphibolite package was the only distinctive marker horizon observed within the Kjerringøy paragneiss.

Amphibolite (Fig. 5) observed within the Kjerringøy paragneiss is concentrated in the Tårnvika area (Plate 1), studied in detail by John Hawkins (personal communication, 2010). The amphibolite occurs as <0.5 m thick layers parallel to the regional foliation. Amphibolite layers in the southern portion of the study area along Mistfjorden are similar

Figure 5 – Kjerringøy paragneiss exposed near Fjær. Marble layer is highlighted between red dotted lines. Well-defined dark layer highlighted between dotted-dashed lines in image is one of the distinctive amphibolite layers that are invariably found near the marble. Orange notebook is ~20 cm long.

to those found farther to the north, but were not observed in as high a concentration as they occur to the north. The Kjerringøy paragneiss is well exposed in the northern part of the study area with nearly continuous roadcut exposures from Osvika to Tårnvika (Fig. 1, Plate 1). This area was not studied in detail by the present author but John Hawkins kindly supplied the author with data he collected (personal communication, 2010). These amphibolites are likely equivalent to the Tonian "pre-Caledonian intrusives" described by Agyei-Dwarko (2010; Table 1).

The southeastern portion of the study area on the western shore of Sørfjorden is characterized by a garnet, quartz, plagioclase, biotite migmatitic paragneiss. In places, the leucosomes are nearly equal in abundance to the melanosomes. This gneiss bears a striking resemblance to the gneisses at Misten and those found on the northern shore of Kjerringøy. This gneiss is cut by two generations of pegmatites. A quartz-rich family is characteristically isoclinally-folded with axial planes parallel to the regional foliation. Plagioclase-rich pegmatite veins are found throughout all lithologies observed in the study area, including the Kjerringøy paragneiss.

Kjerringøy gneiss exposed south of the study area near Heggmovatn has been described as consisting of a gray, medium-grained, locally migmatitic and kyanite-bearing, garnetiferous biotite quartzofeldspathic schist (Zeltner, 2001). In the Vatnvatnet area the unit interfingers with quartzite and quartzofeldspathic schist (Zeltner, 2001). This interlayered character is also observed on the western side of the Steigtinden synform in the Valvikdalen area. The northeast/southwest trending ridges in this area are composed of quartzite and the streams have formed in the schistose units. Units in the Valvikdalen area are structurally above the marbles exposed at Mjelde.

Sample LND-001 (Fig. 6, Table 2) shows subgrain rotation, bulging recrystallization, and some deformation lamellae. The dominant deformation mechanism having operated in quartz is grain boundary migration. Mermekite is present. Kyanite, muscovite, biotite all show length preferred orientation, with tabular muscovite and blade-like kyanite defining the foliation in the rock. Mica minerals and quartz/feldspar are segregated into distinct layers defining gneissosity. Biotite and muscovite both contain radiation haloes around zircon.

Sample KJR-036 is a garnet biotite muscovite schist (Fig. 7, Table 2) belonging to the Bodø Group, collected in Kjerringoy. The hand sample from which the thin section was cut contained numerous euhedral garnet porphyroblasts, with some as large as ~1 cm in diameter. In thin section, the most conspicuous feature in sample KJR-036 is a large euhedral to subhedral garnet porphyroblast with abundant quartz inclusions. The quartz inclusions trace out a pronounced sigmoidal shape, as determined by the orientation of the long axes of the quartz grains. The sigmoidal inclusion trails show a sinistral sense of rotation in the plane of the thin section (sample is not oriented) of approximately 40°. The radius of curvature of the rotated inclusion trails and the cross-sectional area and aspect ratio of the inclusions themselves are both more or less constant, suggesting that the garnet itself grew in a stable stress field where the rate of rotation did not vary appreciably.

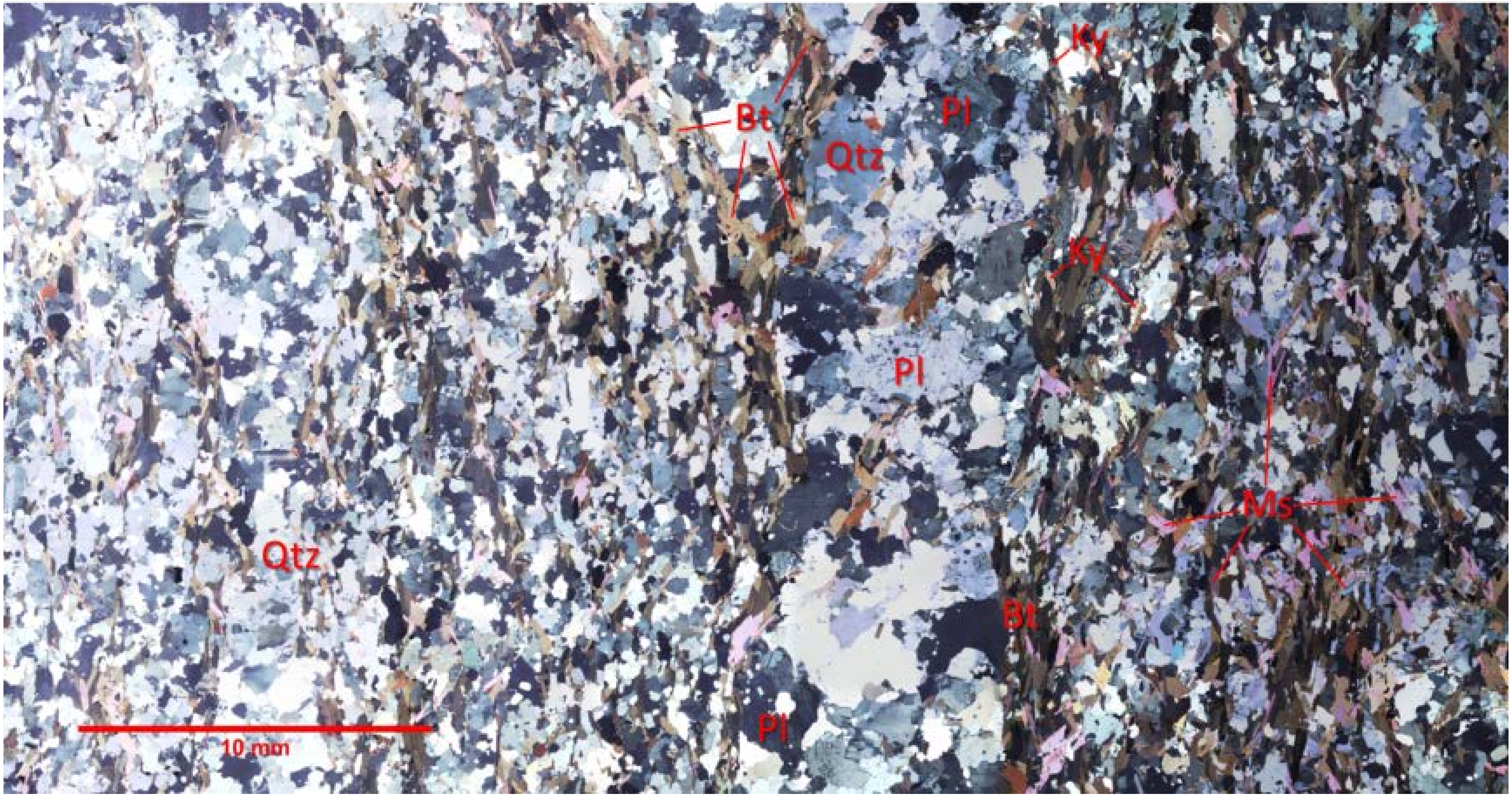

Figure 6 – Photomicrograph (XPL) of Kjerringøy paragneiss sample LND-001. See text for description, Table 2 for modal analysis. Qtz = quartz, Bt = biotite, Pl = plagioclase, Ky = kyanite, Ms = muscovite.

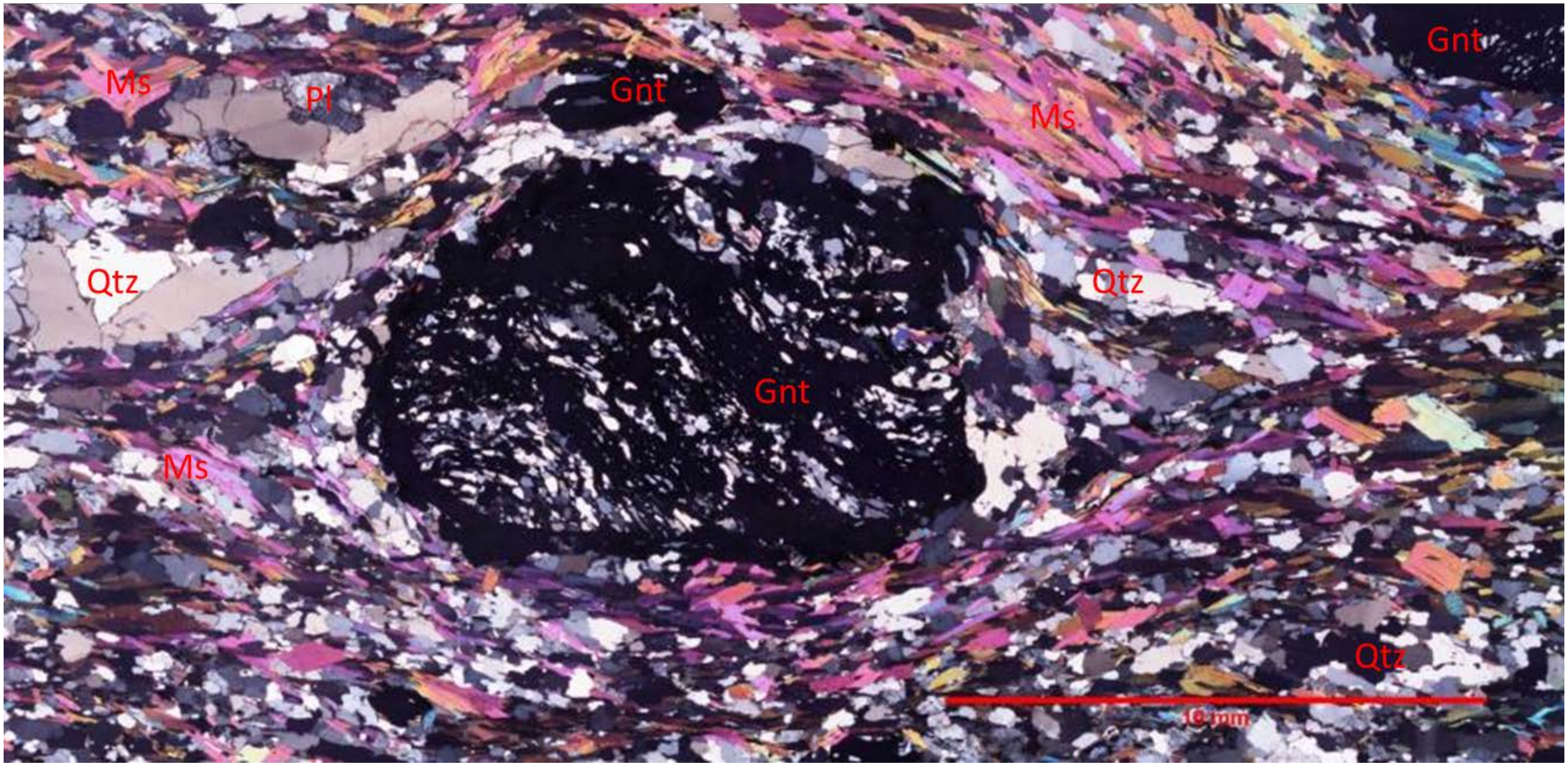

Figure 7 - Photomicrograph (XPL) of garnet biotite muscovite schist, oriented sample KJR-036. See text for description and Table 2 for modal analysis. Ms = muscovite, Pl = plagioclase, Gnt = garnet, Qtz = quartz.

A nearly inclusion-free rim surrounding the prominent garnet porphyroblast in KJR-036 (Fig. 7) suggests that the last stage of garnet growth was significantly slower. The presence of abundant quartz in symmetrical pressure shadows suggests that there was enough time for excess silica to diffuse out of the growing garnet. The pressure shadows being symmetrical about the foliation plane further suggests that the stress field had changed from simple sinistral shear to one consisting of pure shear where flattening dominated. This is further supported by the symmetrical deflection of the muscovite/biotite defined foliation around the garnet.

Bulging recrystallization and grain boundary migration is abundant at contacts between quartz grains in sample KJR-036 (Fig. 7), as are triple-point contacts between grains. Undulose extinction is found throughout the sample but is never strongly expressed, likely as a result of dynamic recrystallization and subsequent realignment of the optical axes of the quartz grains. The majority of quartz grains do not show a length-preferred orientation and have an aspect ratio of approximately 1:1. Individual quartz grains provide further support for a late stage of subgrain rotation (SGR) accommodated recovery as they are grouped in linear arrays of grains parallel to the muscovite/biotite foliation.

Euhedral zircon inclusions within the matrix quartz in sample KJR-036 (Fig. 7) demonstrate a clear length-preferred orientation. The long axes are parallel to foliation away from the previously described garnet porphyroblast, but at 90° to foliation within the strain shadows bounding it. This suggests the zircons were actively growing during the period of flattening that accompanied the last, slower period of garnet growth.

Sample KJR-036 (Fig. 7) contains record of early conditions of rapid garnet growth in simple shear conditions dominated by sinistral rotation, followed by a period of slower garnet growth in pure shear, dominated by flattening. This is all overprinted by a significant amount of static recovery, but little if any retrogression.

Kjerringøy Orthogneiss

Occurring within the paragneiss throughout the study area is an orthogneiss that is commonly difficult to differentiate from the paragneiss itself. This unit extends approximately 30 km outside of the study to the northeast (Gustavson, 1996). Nicholson and Rutland (1969) included this orthogneiss in the Lower Vågen Group (Table 1). Gustavson and Blystad (1995) describe it as a granitic gneiss, coarse to medium grained, and locally porphyritic. The porphyritic portions of this unit are referred to as the Rørstad granite in this study (Table 1).

The orthogneiss crops out extensively on the western side of the island of Landegode (Fig. 1, Plate 1). The intrusive relationship of the orthogneiss relative to the paragneiss is well displayed in a quarry that is less than a quarter of a kilometer due south of the ferry dock on Landegode. The quarry highwall is primarily orthogneiss with paragneiss country rock exposed in several areas. Augland et al. (2013) determined an age of 946 ± 5 Ma for the orthogneiss in Landegode based on U-Pb dating of zircons.

The orthogneiss holds up the mountain of Øygårdsfjellet (Fig. 1), directly to the south of the small fishing village of Tårnvika (Hawkins, personal communication, 2010). Intrusive margins of the orthogneiss are concordant with the regional foliation of the paragneiss. Locally, in the cores of plutons, large randomly oriented feldspar porphyroblasts (up to 5 cm long) preserve primary igneous textures, indicating that Caledonian strains are weak or perhaps absent.

Kjerringøy orthogneiss sample KJR-243 (Figs. 8 and 9) has a bimodal distribution in grain size with anorthoclase (0.8 x 1 cm) and biotite (3 x 3 cm) phenocrysts set in a fine-grained matrix of biotite and plagioclase. Anorthoclase phenocrysts show "tweed" twinning, with two sets of pericline twins intersecting at approximately 36° in the plane of the thin section slice. The biotite crystals in the smaller population of crystals commonly contain halos of radiation damage surrounding rutile and zircon crystals. The haloes generally are confined to single biotite crystals, not extending across crystal boundaries. This may suggest that there has been crystallographic control on radiation damage, or perhaps it is a result of the crystals having being juxtaposed next to each other after the radiation damage occurred.

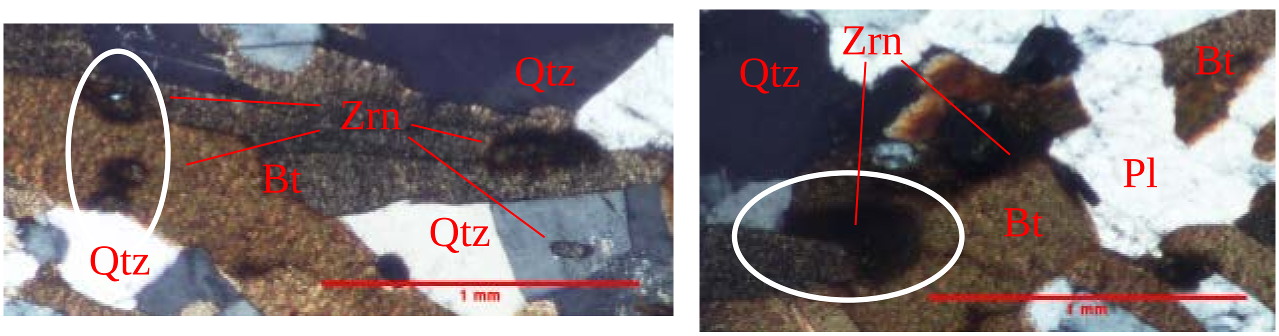

Figure 8 – Photomicrograph (XPL) of radiation damage stopping at grain boundaries in Kjerringøy paragneiss, sample KJR-243. Qtz = quartz, Bt = biotite, Zrn = zircon, Pl = plagioclase.

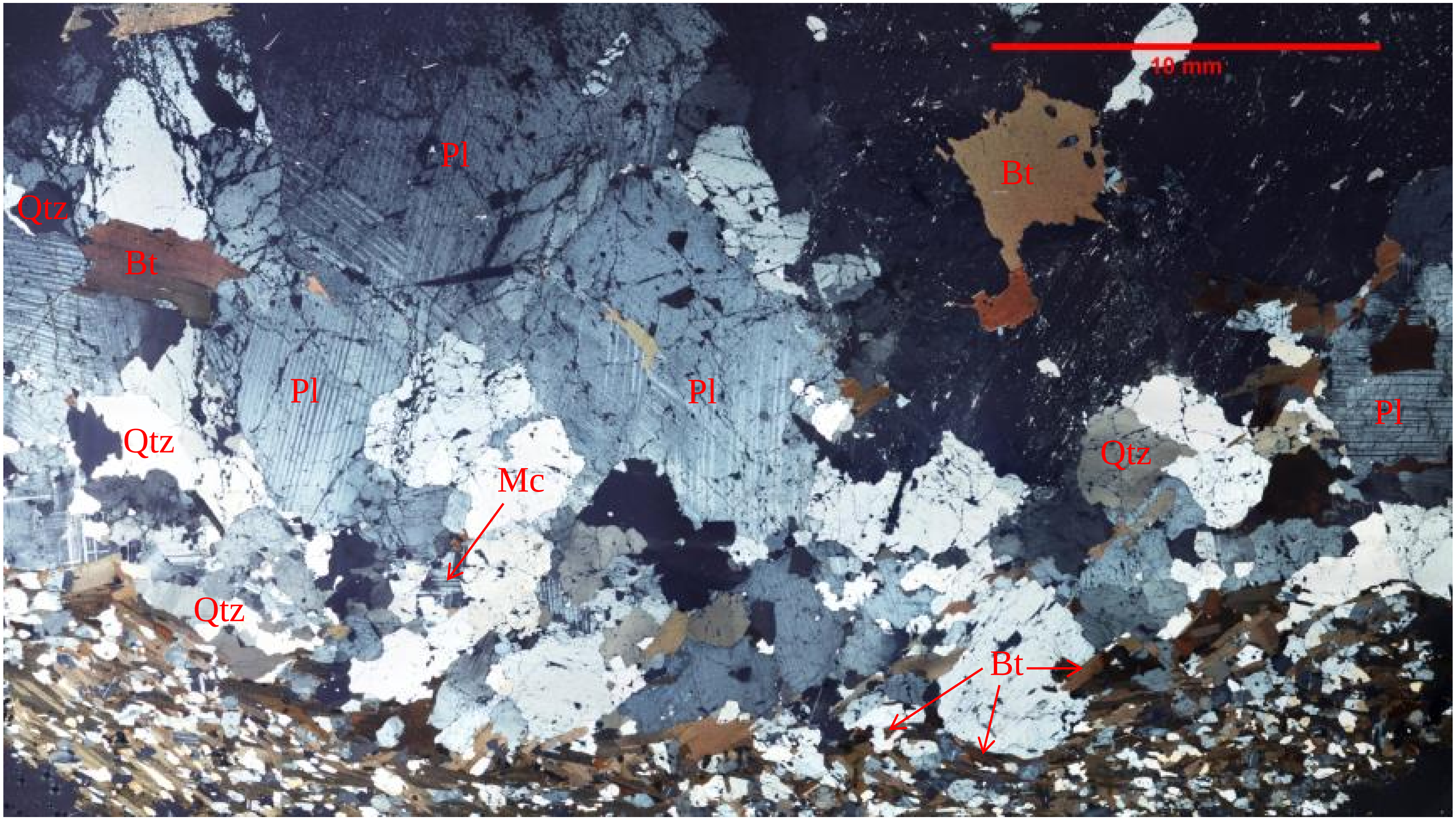

Figure 9 – Photomicrograph (XPL) of Kjerringøy orthogneiss sample KJR-243. See text for description, Table 2 for modal analysis. Qtz = quartz, Bt = biotite, Pl = plagioclase, Mc = microcline.

Rørstad Granite

The Rørstad granite (Cooper, 1980) underlies nearly 200 km^2 of the area directly to the east and north of the present study area and was earlier mapped as a late Proterozoic porphyritic granite (Gustavson and Blystad, 1995; Gustavson, 1996). The granite has been little studied due to its remoteness but it appears to be more structurally complex to the north than it is to the south. The granite is reported to be overlain by thrusted equivalents to the Kjerringøy paragneiss where it is exposed north of Sørfolda (Gustavson, 1996). South of Sørfolda, Cooper (1978) reports no signs of tectonism along this contact a few kilometers east of Tårnvika, near Korsvika. Gustavson's map (1996) has the Rørstad intrusively truncating the Kjerringøy paragneiss about 5 km to the south of Tårnvika, across Nevelsfjorden. The current author interprets that the Rørstad granite is a little deformed and porphyritic equivalent to the Kjerringøy orthogneiss.

The Rørstad Granite is texturally heterogeneous, with two distinct textures developed in different areas: zones with megacrystic plagioclase feldspar and zones without. Lath-shaped plagioclase feldspar megacrysts within the unit are concentrated in bands tens of meters thick that parallel the regional foliation. Foliation in and out of these bands is parallel to the regional foliation, except in the very centers of the megacrystic bands where crystals are randomly oriented. The textures do not appear to be mineralogically controlled, as the mineralogy and modal abundance was nowhere observed to vary significantly from that observed in hand-sample (see Table 2). It is plausible that the megacrystic zones were formed as the result of localized strain or fluid partitioning.

Sample LEA-10-1 (Fig. 10, Table 2) was collected in the center of a megacrystic band on the northern flank of Øygårdsfjellet (Fig. 1). In thin section, this sample contains quartz inclusions within the plagioclase megacrysts, in some areas as part of a mermykitic texture. Biotite and muscovite inclusions are also common. Small quartz subgrains less than 0.5 mm in diameter rim the phenocrysts along with small crystals of alkali feldspar. Biotite commonly contains radiation haloes surrounding zircon.

The microstructures found within sample LEA-10-1 are primarily plastic. The plagioclase megacrysts commonly contain Carlsbad twins that have undergone twin boundary migration, suggesting high-temperature shearing (Passchier and Trouw, 2005). Plagioclase megacrysts are commonly mantled by a corona of smaller plagioclase and quartz crystals. Subgrain rotation, grain boundary migration, and bulging recrystallization are common in quartz and also suggest high-temperature shearing. A pervasive S-C fracture plane array cuts across the entire thin section. Individual fractures are not contained within individual crystals. The S-C fractures have been recemented with quartz. The movement recorded by the S-C is unknown as sample LEA-10-1 is not oriented.

Diorite dikes (Figs. 11, 12, and 13) are seen to cut the Rørstad granite at Landegode, Bratten, and Tårnvika (Fig. 1). The diorite dikes have not been reported in the Kjerringøy paragneiss and orthogneiss in the study area, but Zeltner (2001) reports them occurring to the south. It is likely that the high degree of transposition has obscured original intrusive contacts. In all areas, the diorites are cut by deformed pegmatites containing megacrystic plagioclase (Figs. 11 and 13).

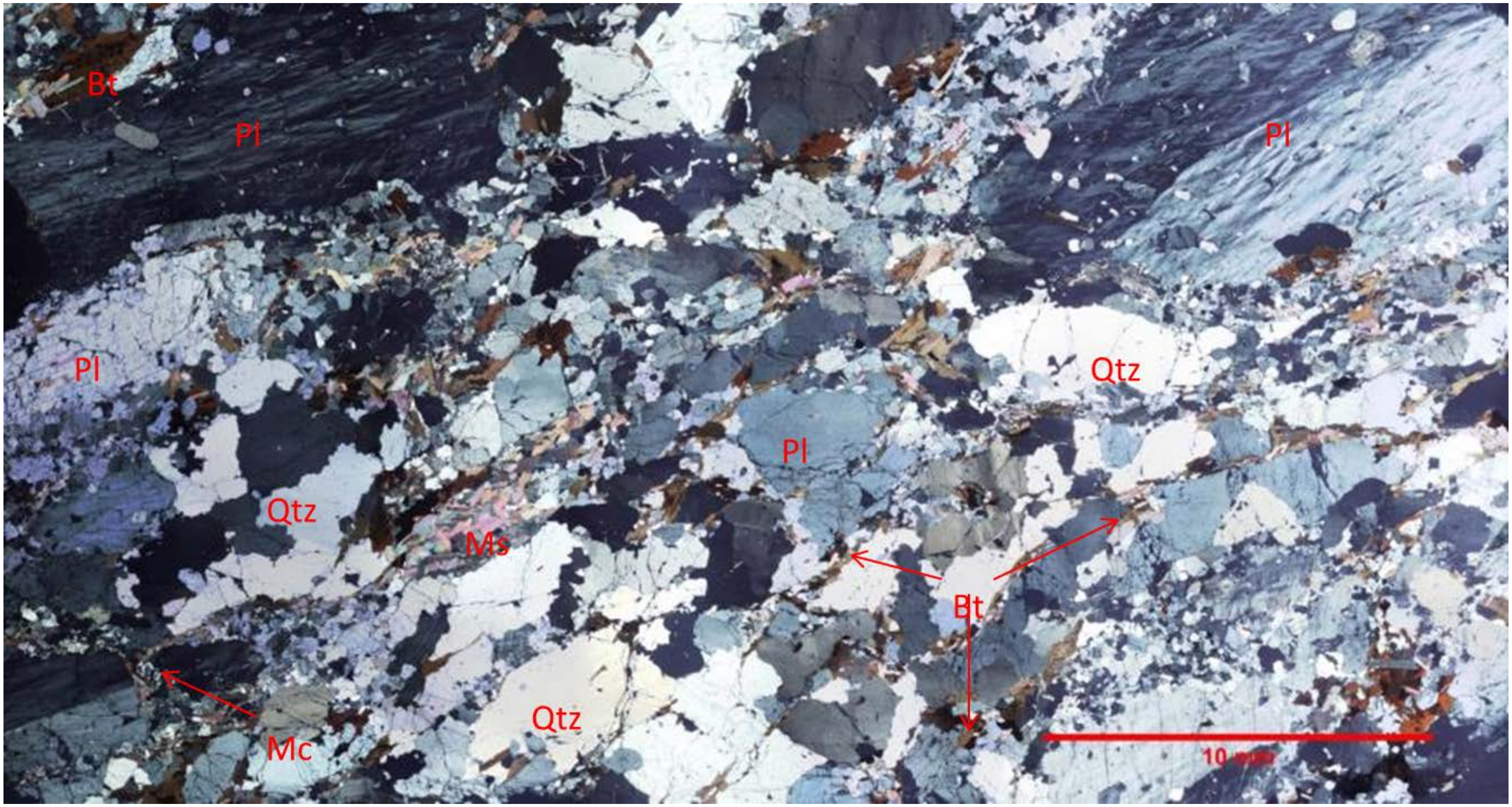

Figure 10 - Photomicrograph of mylonitic Rørstad granite sample LEA-10-1 showing abundant bulging grain boundaries and plagioclase porphyroblasts mantled by quartz. See body for description and Table 2 for modal analysis (XPL). Bt = biotite, Pl = plagioclase, Qtz = quartz, Ms = muscovite, Mc = microcline.

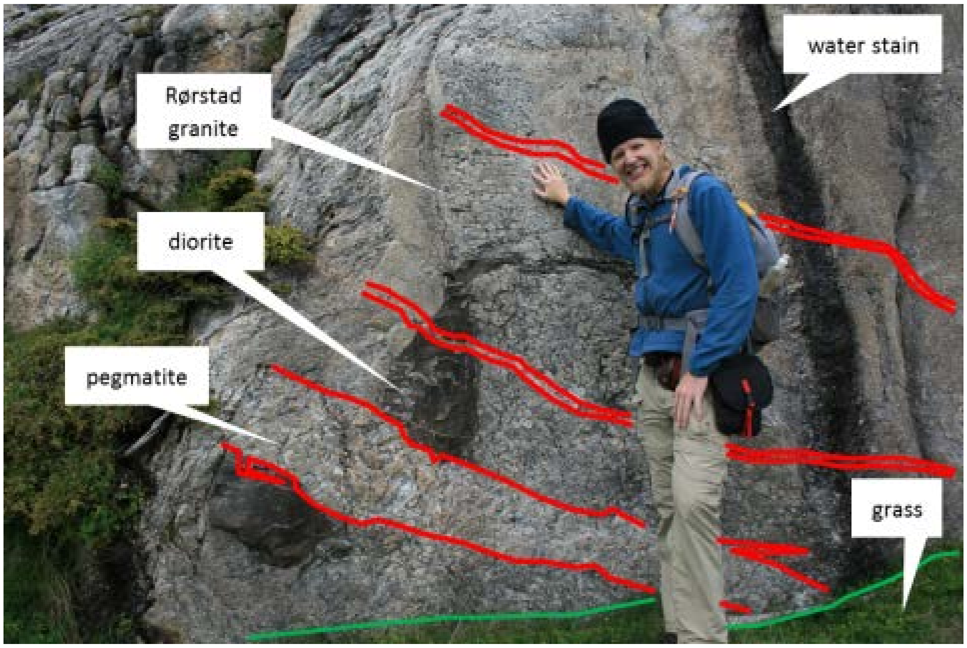

Figure 11 - Rørstad granite on Landegode intruded by diorite, all of which are intruded by pegmatites. Matrix is Rørstad granite, red solid lines outline pegmatites. Facing west at Fatvåg, Landegode, the author for scale.

Figure 12 - Looking north at a diorite dike that has acted as a slip horizon within the Rørstad granite. Sense of shear indicates tops-up-to-southeast movment. Red lines show late pegmatites, black arrows indicate sense of shear. The Rørstad granite is undeformed and unfoliated. The dike is exposed in a valley east of Tonhellaren, Landegode.

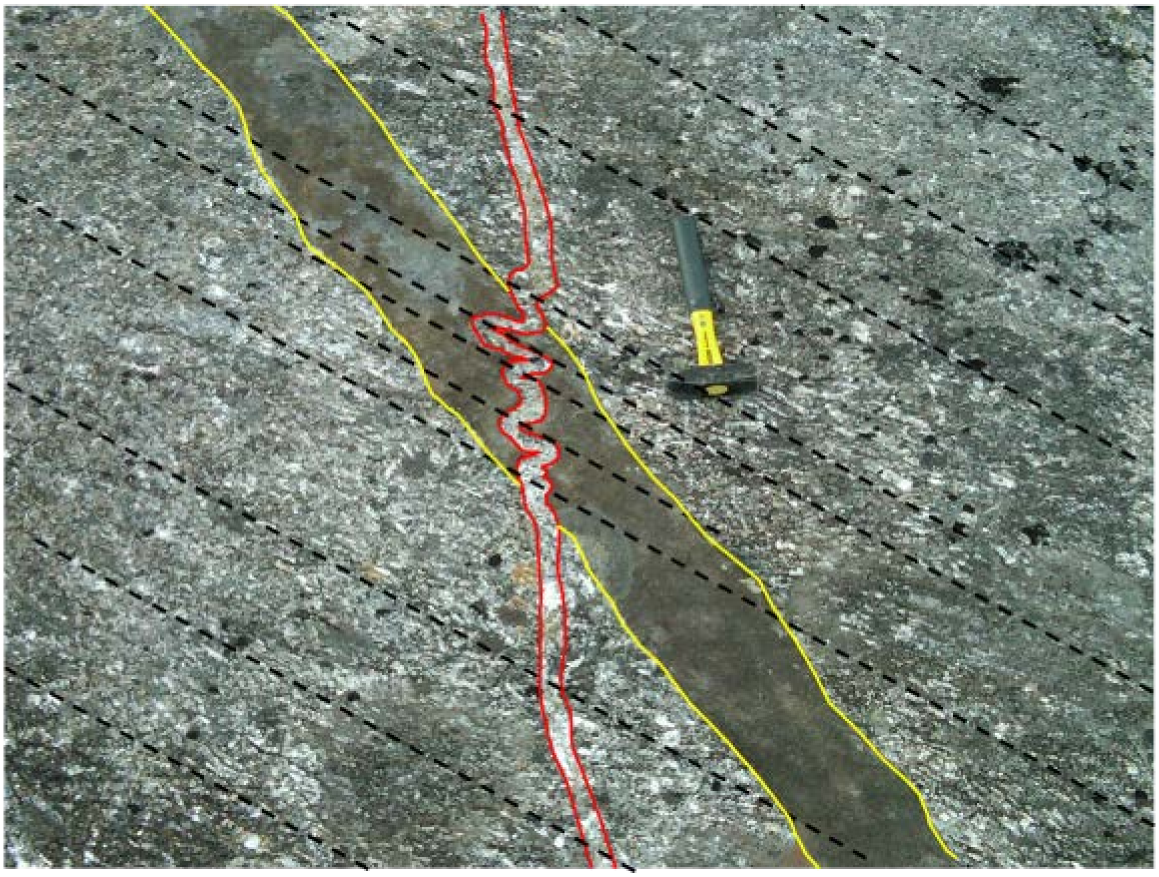

Figure 13 – Rørstad granite near Tårnvika intruded by diorite (outlined in yellow), both of which are cut by a younger pegmatite (outlined in red). Axial planes of folded pegmatites are parallel to S_1 gneissosity (blacked dashed lines). This reflects late stage D_1 flattening. Diorite was likely hot and semi-viscous when pegmatites intruded.

Bodø Nappe

Hopsfjell Schist

Nicholson and Rutland (1969) described the Bodø Group as occupying the core of the large northeast/southwest trending Steigtinden synform (Plate 2), between Bodø and Hopen (Fig. 1). The lithologies found around the town of Kjerringøy were correlated by Nicholson and Rutland (1969) with those that occur near Bodø. A tentative correlation with rocks found on South Arnøy and Sørvær was also put forth (Nicholson and Rutland, 1969).

Nicholson and Rutland (1969) described this unit as a garnetiferous quartzofeldspathic schist that grades into an impure marble. Zeltner (2001) dubbed the schist the Hopsfjell schist and the interlayered marble the Ørntuva marble (Table 1). Transposed bedding is characterized by thin greenish calcsilicate-rich layers interspersed within a pale blue-gray schist that is silver in fresh exposures. The unit weathers dark brown to black and is commonly stained with rust. The lithology that outcrops in the study area is most similar to an antigorite schist that outcrops between Vikan and Hopen (Gustavson and Blystad, 1995; Zeltner, 2001). Amphibole minerals are common, with hornblende and tremolite both occurring (Zeltner, 2001). Muscovite, biotite, antigorite, talc, quartz, plagioclase, calcite, and accessory amounts of epidote and sphene are found in this unit (Rutland and Nicholson, 1969; Zeltner, 2001).

Characteristic of the base of this of Hopsfjell schist is a hornblende garbenschiefer, with a particularly good exposure at the ferry at Festvåg. Gustavson and

Blystad (1995) and Zeltner (2001) both report a garbenscheifer in the hanging wall directly above the Steigtinden shear zone. Amphiboles are randomly oriented within the foliation plane. Epidote is found throughout the outcrop. Steffen et al. (2001) suggest that such fabrics develop in conditions of 525-575 °C at 30-40 km depth. This unit is heavily intruded by a two-mica granite that is found at Durmålsvatnet and in the area between Steigtindvatnet and Festvåg. This granite also forms the large hills Finnkonnakken and Stordalsfjellet, farther to the east of Festvåg.

The Hopsfjell schist is generally homogeneous at the outcrop scale but varies notably throughout the study area. In the core of the Kjerringøy synform (Plate 2), in the village of Kjerringøy, the calcsilicate is cut by meter-thick bands of highly altered rock. The altered zones are structurally-controlled, invariably associated with sheath folds with cores rich in quartz rimmed by a corona of epidote and amphibole (Fig. 14). The sheathfolds are a distinctive structure unique to the Bodø Nappe and are found throughout the Hopsfjell Schist. The sheathfolds are almost all highly strained, being particularly appressed and planar in the core of the Kjerringøy synform. There are also numerous quartz-rich, garnet-bearing intrusions found within the Hopsfjell schist near the core of the synform. These are seen to cut the schist in several areas and are foliated, suggesting that they either pre-date the regional metamorphism or intruded synchronously. The present author interprets the sheathfolds and the altered bands near the center of the synform are the result of syntectonic fluid flow. This alteration appears to have been restricted to the calc-silicates.

Figure 14 – Looking north at sheath folds occurring near Fjær. See text for discussion.

Fjærehesten Granite

Unfoliated intrusive rocks are found throughout the southern half of the study area, concentrated in the rocks that bound Mistfjorden. A two-mica granite found at the highest structural levels in the trough of the Steigtinden synform is particularly well-exposed at Durmålsvatnet north of Mistfjorden and at Steigtinden and Mjeldvassurda south of Mistfjorden (Cooper, 1980). It is also reported to appear on the ridge between Mjønesfjellet and Mjønestinden (Gustavson and Blystad, 1995).

The Fjærhesten granite outcrops as low rolling hills marked by white pavement outcrops where there is no vegetation. Outcrops are commonly intruded by late pegmatites. The granite is almost universally white in hand sample, but is also stained a rusty color where iron has leached out of the Kjerringøy paragneiss along the margins of the exposure at Durmålsvatnet. The white color is due to the abundance of plagioclase and quartz, with biotite, muscovite, and potassium feldspar making up a small portion of the rock by volume (see Table 2).

Quartz subgrains in sample LEA-10-2 (Fig. 15) show a slight length-preferred orientation and define a weak foliation that is not visible in hand sample. Feldspars, biotite, and muscovite are randomly oriented and do not show this length-preferred orientation. Biotite and muscovite are most commonly subhedral, of a similar size, and occur in similar concentrations. Quartz and plagioclase grains both contain inclusions and are anhedral, appearing to have been the last to crystalize from the initial melt. Sample LEA-10-2 does not show any fractured and offset grains.

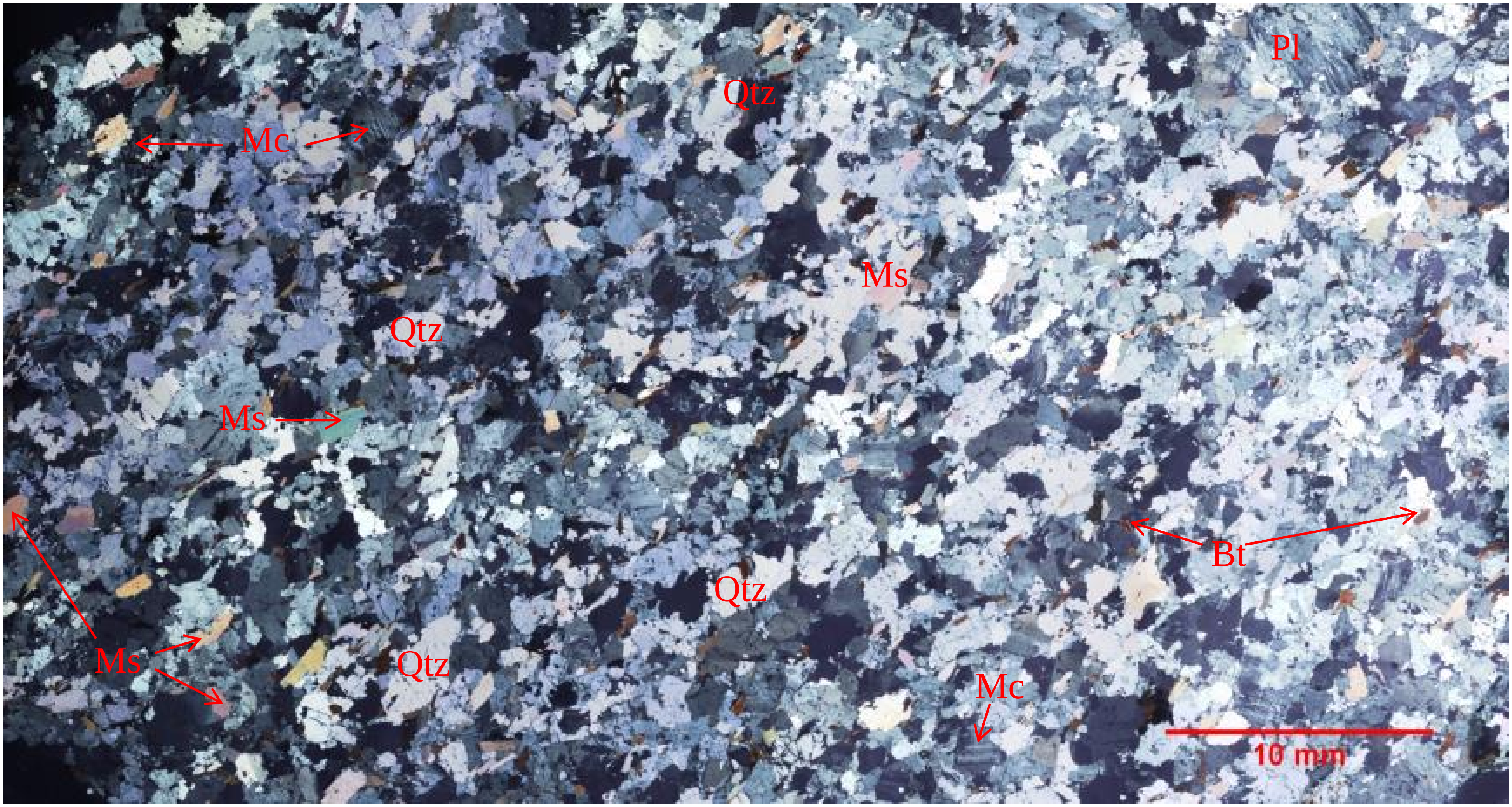

Figure 15 – Photomicrograph (XPL) of Fjærhesten granite sample LEA-10-2. Weak foliation inclined from bottom left to top right. See body for description, Table 2 for modal analysis. Mc = microcline, Qtz = quartz, Pl = plagioclase, Ms = muscovite, Mc = microcline, Bt = biotite.

STRUCTURE AND METAMORPHISM

The notation used in this chapter is that each distinct deformational phase is assigned a number, with the first phase being assigned the number 1 and later events being assigned higher numbers. Each deformational event is referred to as D_n, where the subscript n is the number denoting the deformational event. Specific types of structures associated with a given event will be similarly numbered but will have a separate letter denoting the structure: S_n = planar structures; L_n = linear structures; F_n = folds; and M_n = metamorphic events.

The tectonostratigraphy of the Bodø/Kjerringøy area (Fig. 1, Plate 1) is defined by three nappes. The structurally highest unit is the Bodø Nappe, followed by the intermediate Rödingsfjället Nappe, both of which lie above of the Heggmo Nappe. The Bodø Nappe is in contact with the Rödingsfjället Nappe in the area to the northeast of Bodø, separated from it by the tops-down-to-west Steigtinden shear zone (Zeltner, 2001). The Rödingsfjället Nappe has not been recognized in the present study area, the Bodø Nappe is instead found in direct contact with the Heggmo Nappe. The boundary between the Bodø Nappe and the Heggmo Nappe in the Kjerringøy area is the tops-down-to-west Fjær-Osvika shear zone (FOSZ) (Plate 2, Fig. 16). The Steigtinden shear zone and the FOSZ are erosionally separated by Mistfjorden (Fig. 1), but are interpreted by the present author to be the same structure.

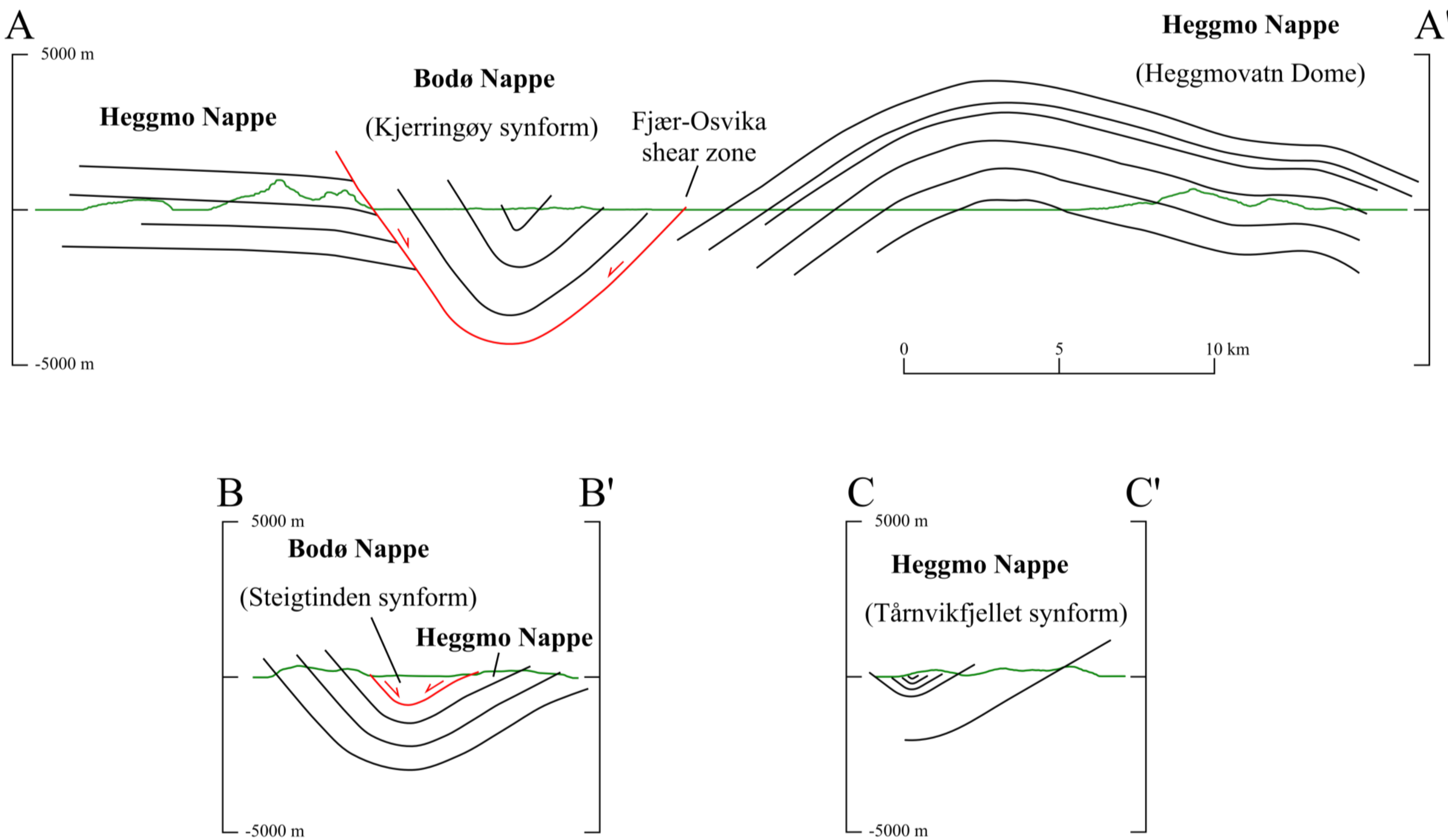

Figure 16 – Structural cross-sections showing major structures in the study area. See Plate 2 for plan view of section lines.

The Rödingsfjället Nappe is separated from the Heggmo Nappe by the tops-up-to-east Vågfjellet fault, which is itself cut by the Steigtinden shear zone about 2 km south of Steigtindvatnet (Plate 2) (Zeltner, 2001). Cooper (1978) describes the eastern boundary of the “Heggmovatn Basement Gneiss Dome” as being overturned to the east, overlying the the Beiarn Nappe. It is not known precisely what becomes of the Heggmo Nappe south of Saltfjorden, as it is overlain by the Rödingsfjället and Beiarn Nappes. West of Landegode much of the structure is hidden beneath the sea.

Structural analysis using field mapping (Plate 1), construction of cross-sections (Fig. 16) and stereonets, analysis of satellite imagery, and analysis of a structural formline map (Fig. 17) clearly demonstrate the presence of four megascopic folds in the study area: the large Steigtinden synform, its antiformal conjugate the Heggmo antiform (Heggmovatn Dome), a large synform developed in the Bodø Nappe referred to as the Kjerringøy synform in this report, and a large synform near Tårnvika referred to as the Tårnvikfjellet synform in this report (Plates 1 and 2). The Heggmo antiform and the Steigtinden synform share a northwest-dipping limb that underlies a string of lakes and fjords (Vatnvatnet, Sørfjorden, Trolltindvatnet, and Nævelsfjorden; see Plate 1) and have a wavelength of roughly 7.5 km and an axial trend of roughly southwest/northeast. The Heggmo antiform corresponds to the Heggmovatn “Dome” of Rutland and Nicholson (1965) and lies east of the Steigtinden synform. The southwestern portion of the Steigtinden synform lies beneath Landegodefjorden and separates the gneisses on the island of Landegode from their equivalents on the mainland.

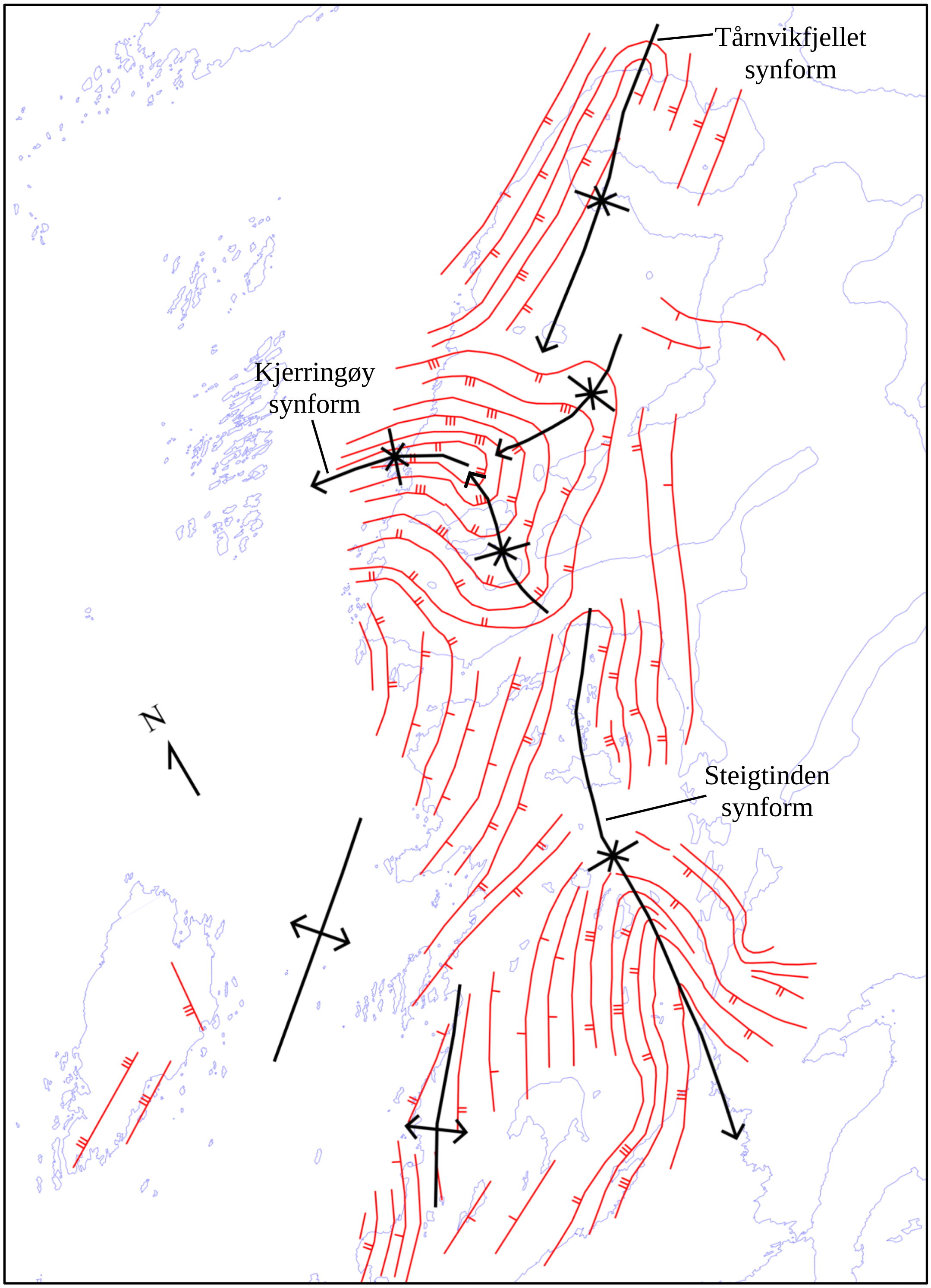

Figure 17 – Structural formline map of foliation in the Kjerringøy/Bodø area. Single tick marks indicate foliation in area dips between 0 and 30 degrees, double tick marks indicate foliations dipping from 30 to 60 degrees, triple tick marks indicates foliations dipping from 60 to 90 degrees. The lower third of the figure incorporates data from Zeltner (2001).

D_0

D_{0S} refers to the depositional event that resulted in the metasedimentary protoliths in the study area; S_{0S} refers to bedding in these units. The presence of marble, amphibolite, metapsammite, and schist as subordinate lithologies within the Kjerringøy paragneiss (Plate 1) is consistent with deposition of the protolith in a dynamic shallow marine environment. Agyei-Dwarko (2010) conducted U-Pb isotopic analysis on detrital zircons from a sample of metapsammite from the Kjerringøy paragneiss and obtained a multimodal spectrum with peaks at ~1000 Ma, ~1450 Ma, and ~1650 Ma. Agyei-Dwarko (2010) interpreted the complete absence of Archean zircons as evidence for a non-Baltican source for the sediment and determined that the most likely source area was the Laurentian basement of East Greenland.

The lithological variability of the protolith, with abundant felsic and mafic minerals, is indicative of a dynamic sediment source. Cawood et al. (2010) have suggested the existence of a Proterozoic basin between Laurentia and Baltica, underlain by thinned continental crust and newly formed oceanic crust. This basin, which Cawood et al. (2010) have named the Asgård Sea, received detritus from the Grenville-Sveconorwegian-Sunsas orogen in two identifiable pulses. The first period of sedimentation lasted from 1030 to 980 Ma and was terminated by the Renlandian event (Cawood et al., 2010), named for the Rendalen area in Andrée Land in northeast Greenland. The Renlandian event is more widely referred to as the Valhalla orogeny outside of northeast Greenland (Cawood et al., 2010).

Evidence for Valhallan orogenesis, $D_{0V,}$ is present in the Kjerringøy paragneiss and orthogneiss of the study area. Early isoclinal folds, F_{0V}, are truncated by the

Valhallan Rørstad granite (Fig. 18). F_{0V} isoclinal folds are overturned to the west and are commonly refolded by later generations of folds. The structural style D_{0V} is similar to that of the Krummedal sequence in the Hagar Bjerg thrust sheet in Andrée Land where it has been isoclinally folded, migmatized and intruded by both Tonian (950-920 Ma) and Siluro-Devonian (435-425 Ma) plutons (Kalsbeek et al., 2008; Leslie and Higgins, 2008). It is likely that the sediment of the Kjerringøy paragneiss was deposited in the Asgård Sea and then later involved in Valhallan deformation along the Laurentian margin of Rodinia.

Figure 18 – Isoclinal F_{0R} fold in the Kjerringøy paragneiss that is truncated by the Valhallan Rørstad granite. Pencil for scale.

D_1

Schistosity and compositional banding defined by length-preferred micas, quartz, amphibole, and feldspar are found in both the Bodø and Heggmo Nappes (Plate 1) and are interpreted to have developed during the Taconian orogeny and referred to as D_1 in this report. Axial planes to both large- and small-scale isoclinal folds, with amplitudes ranging from several centimeters to tens of meters, are found throughout the study area and are parallel to schistosity and compositional banding, S_1. A sample of Kjerringøy paragneiss collected near Mjelde contains M_1 kyanite crystals that were partially consumed during the growth of later M_2 garnet. M_1 biotite and kyanite in the Kjerringøy paragneiss are also both overgrown by later garnet rims (Fig. 19). Biotite, quartz inclusions, and accessory minerals preserved within garnet cores are all considered M_1 on the basis of similar mineralogy, grain size, and internal inclusion trails (S_i) relative to exterior foliation (S_e/S_2). Biotite and kyanite growth during D_1 deformation occurred under amphibolite-facies D_1 pressures and temperatures. Agyei-Dwarko (2010) attributed formation of the schistosity and gneissosity in the Bratten area to D_1.

Folds that formed in the D_1 event are tight isoclines that are overturned to the west. Such F_1 folds are most commonly found preserved in the Kjerringøy Paragneiss and have been heavily modified by later deformation, most commonly refolded and boudinaged (Fig. 20). L_1 lineations were well preserved in the study area in the form of long-axes of plagioclase feldspar megacrysts in the Rørstad granite.

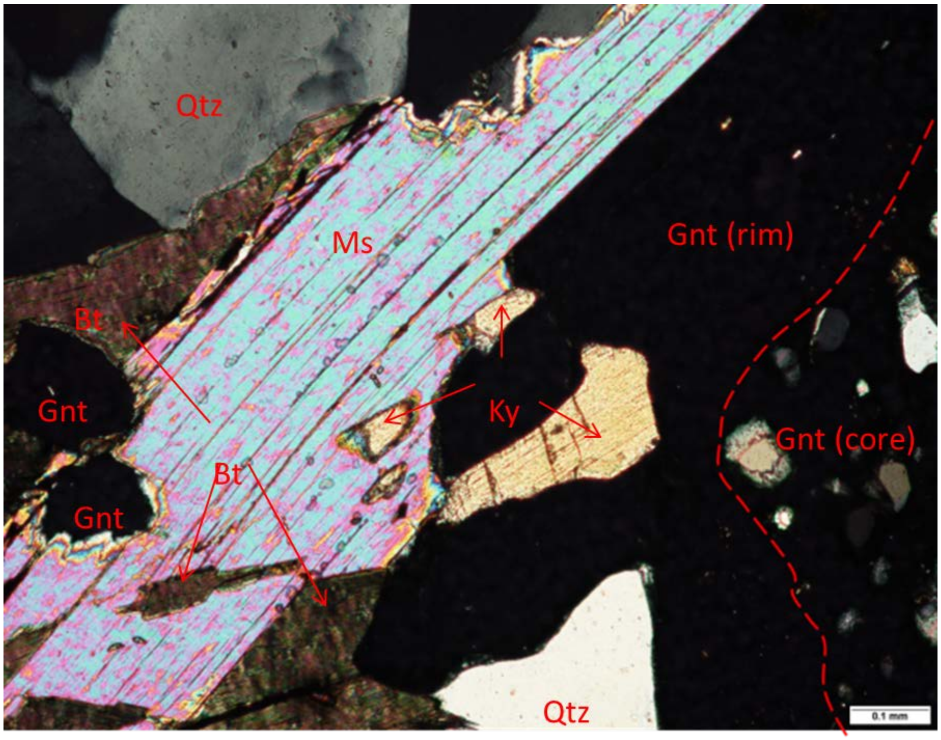

Figure 19 - Photomicrograph (XPL) of sample KJR-093. Qtz = quartz, Ms = muscovite, Gnt = garnet, Ky = kyanite, Bt = biotite. See text for discussion.

Figure 20 - Isoclinal F_1 M-fold overturned to the west in Kjerringøy paragneiss near Låter (Fig. 1). Note extended and boudinaged amphibolite layer. GPS unit circled in red is ~10 cm long. Photo provided by John Hawkins

Measurements of L_1 were not conscientously collected, regrettably. Other elongate minerals such as muscovite and biotite were affected by later D_2 deformation.

The Vågfjellet fault separating the Rödingsfjället Nappe from the underlying Heggmo Nappe (Zelter, 2001) parallels S_1 foliation and appears to have been emplaced during or prior to D_1 (Fig. 21). The orientation of the Vågfjellet fault plane was determined via three point problem solutions at 35 locations at 255 m intervals along the trace of the fault (Gustavson and Blystad, 1995), with elevation data obtained from an elevation model of the area (de Ferranti, 2013).

S_1 S-planes are preserved in S-C fabrics found in the Kjerringøy paragneiss in several locations in the Valvikdalen area. The fabrics are preserved as fracture arrays in quartz and in the phacoidal shape of strained feldspar porphyroblasts. Motion along these S-C fabrics could not be quantified as they have been deformed by later D_2 deformation and are therefore presumed to be of latest D_1 age (Figs. 21 and 22).

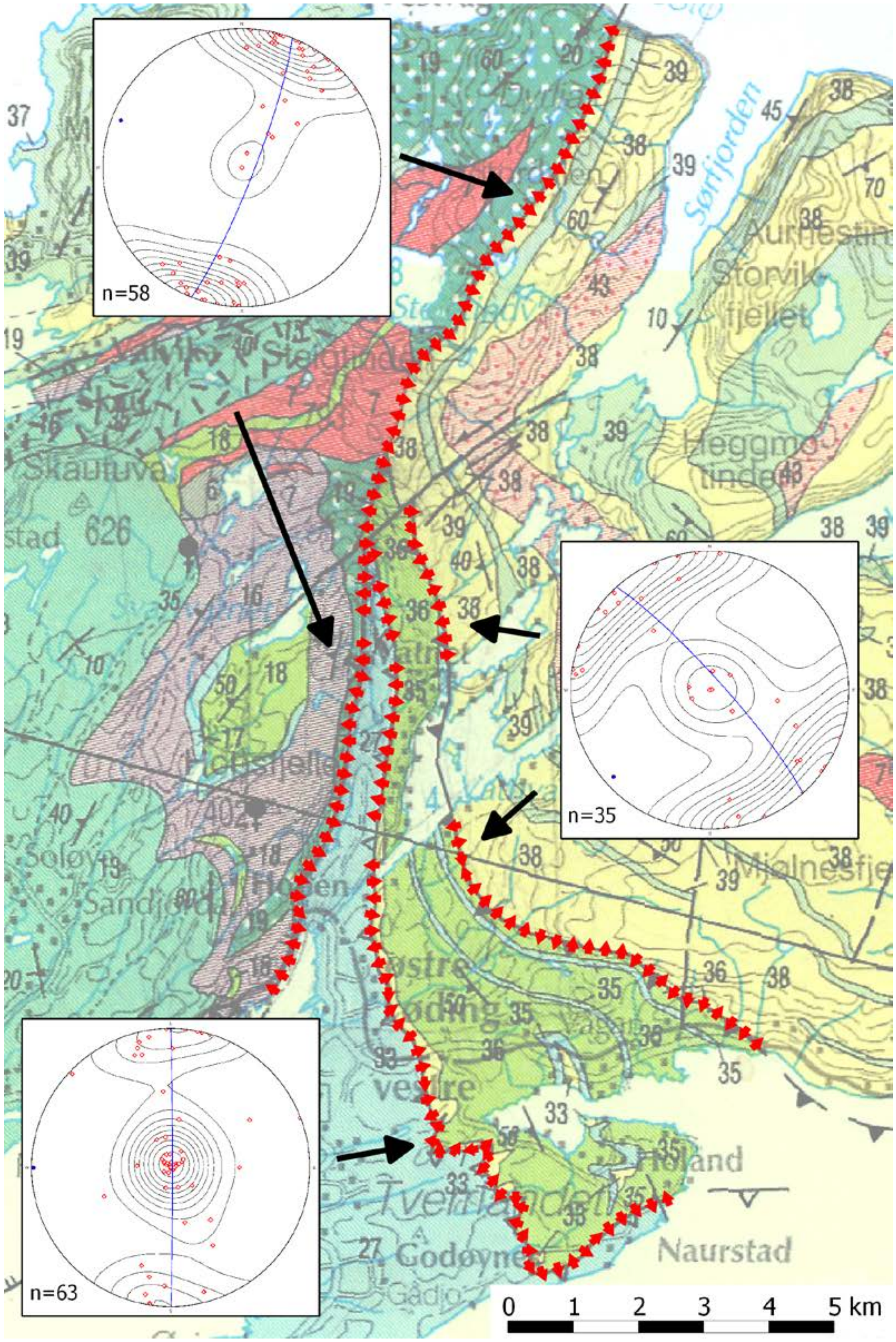

Figure 21 – Lower hemisphere equal area projection stereograms of fault orientation data. Red arrows on basemap point towards dip direction. Basemap from Gustavson and Blystad (1995).

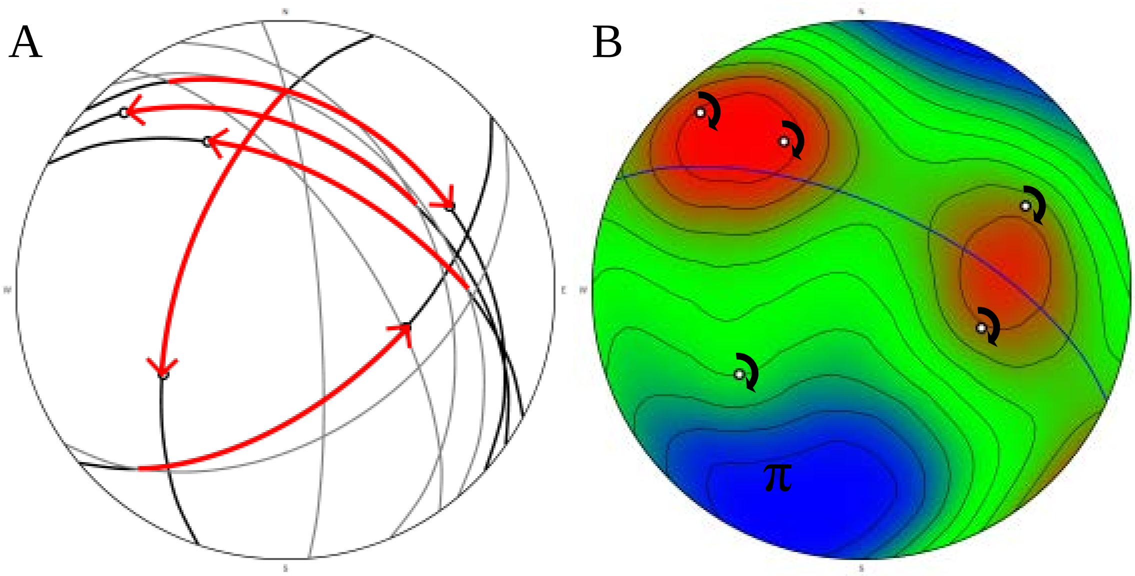

Figure 22 – A) S_1 S-C plane pairs (n=10) measured in the Heggmo and Bodø Nappes. Black lines are C-planes, grey lines are S_1 S-planes. Red arrows indicate 90 degree rotation in the C-plane from the S-C intersection line. Resulting arrow tip (circle) is the slip lineation of that S-C plane. B) Contoured version of A with great circles omitted. Circles along the blue great circle are slip lineations (n=5) in the Heggmo Nappe, as determined in A. The circle in the SW quadrant is a slip lineation in the Bodø Nappe. Arrows around symbols indicate sense of rotation. Contours represent modified Kamb contours with a contour interval of 1 standard deviation. Trend of the π-axis is 204° and plunge is 26°.

D_2

The macroscopic, regional structure in the area is the result of Scandian deformation and is referred to as D_2 in this report. D_2 deformation folded S_1 foliation into a large synform/antiform pair that can be traced along strike for more than 40 km. Analysis of equal area, lower hemisphere stereoplots of poles to compositional banding from the orthogneisses and paragneisses found at Landegode, Bratten, Tårnvika, Mjelde, Valvikdalen, and Sørfjorden (Figs. 23, 24, and 25) show gently plunging, northeast-southwest- and east-west trending, open cylindrical map-scale folds. The style and geometry of a mesoscopic F_2 fold (Fig. 26) exposed near Svartvatnet (Fig. 1) likely reflects that of the megascopic folds documented in the map and cross sections of the area (Plate 2, Fig. 16). The fold pair in Figure 26 has a wavelength of ~1.5 m and amplitude or ~1.5 m. The style is tight, with relatively sharp hinges and it is overturned to the west indicating tops-up-to-the-northwest movement. Abundant exposures of outcrop scale F_2 folds can be seen on the northern end of the Kjerringøy Peninsula along roadcuts near the village of Tårnvika (Hawkins, personal communication, 2010); the regional F_2 Tårnvikfjellet synform is found in the same area (Plate 2). Throughout the study area F_2 fold axes plunge moderately-to-steeply to either the northeast or southwest and the sense of vergence is generally tops-up-to-the-northwest.

Analysis of a lower hemisphere equal-area stereogram (Fig. 22) of the derived attitude data from S-C fabrics in the Valvikdalen area shows that the S_1 S-planes are

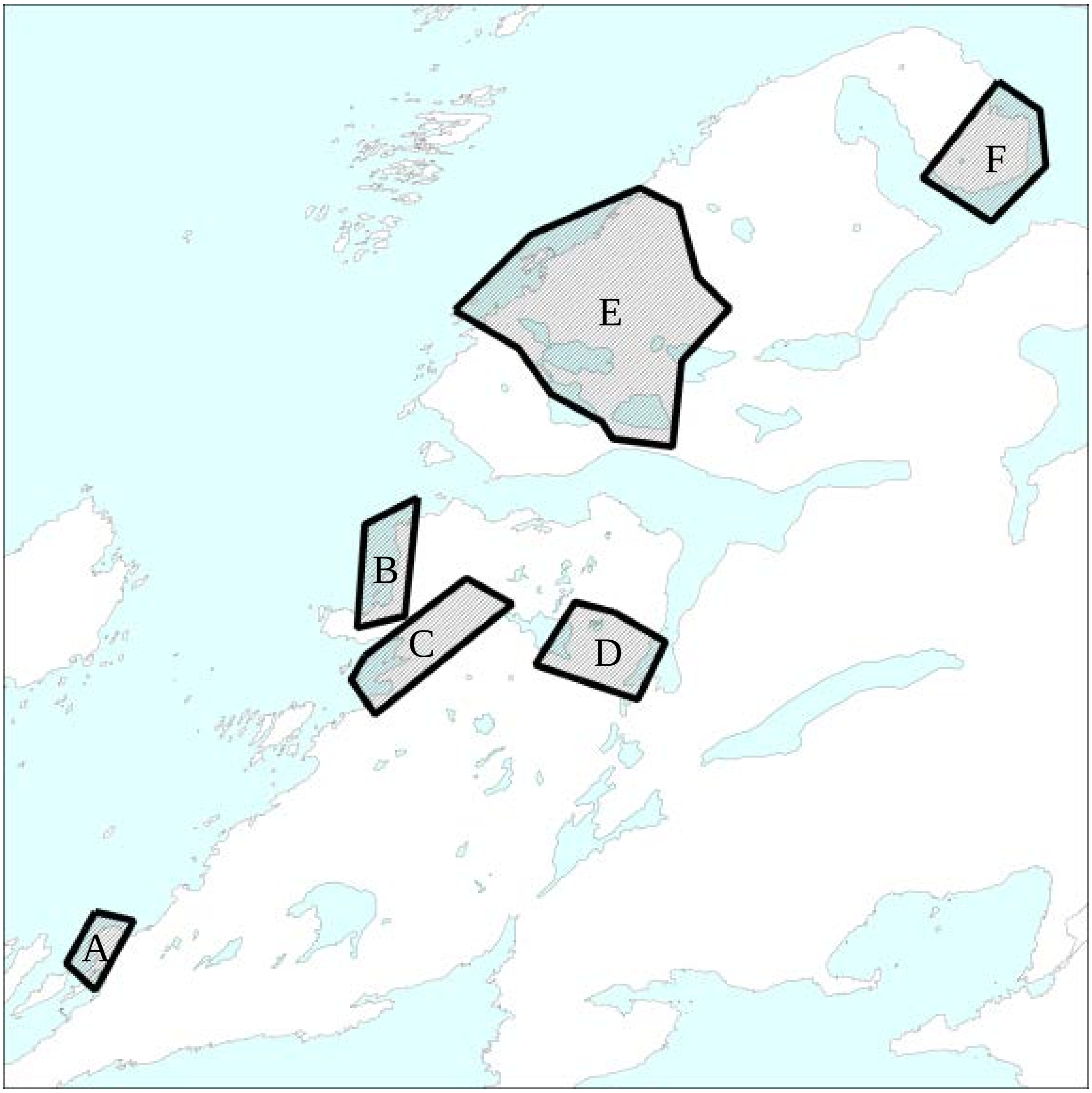

Figure 23 – Structural subareas for which stereonets have been created (See Figure 1 for reference). A) Bratten, B) Mjelde, C) Valvikdalen, D) Sørfjorden, E) Fjær/Osvika shear zone hanging wall, and F) Tårnvika.

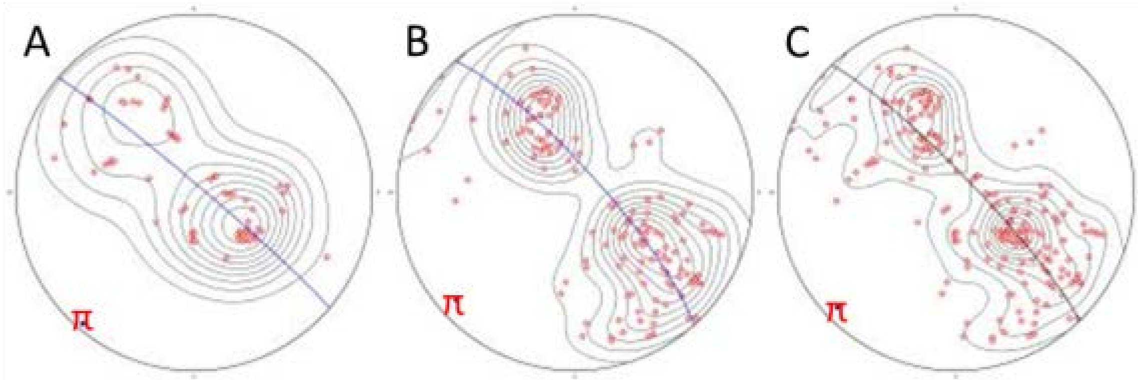

Figure 24 - Equal area, lower hemisphere stereographic plot of poles to S_1 gneissosity in the A) Bratten (n=69) and B) Tårnvika (n=143) areas, and a combined plot C) of both Bratten and Tårnvika (n=212). F_2 β-axis trend is 226°and plunge is 8°. Data is from Agyei-Dwarko (2010) and the current study.

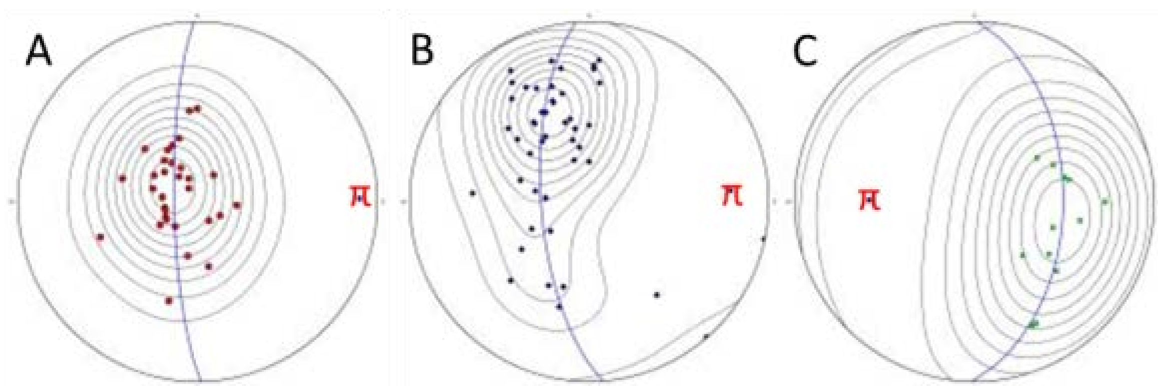

Figure 25 - Equal-area lower-hemisphere plot of poles to S_1 gneissosity in A) Mjelde, B) Valkvikdalen, and C) Sørfjorden. Mjelde and Valkvikdalen plots indicate cylindrical folds plunging shallowly to the east. The Sørfjorden area shares a similar fold style but plunges to the west. Valvikdalen (n=29), Sørfjorden (n=12), Mjelde (n=26).

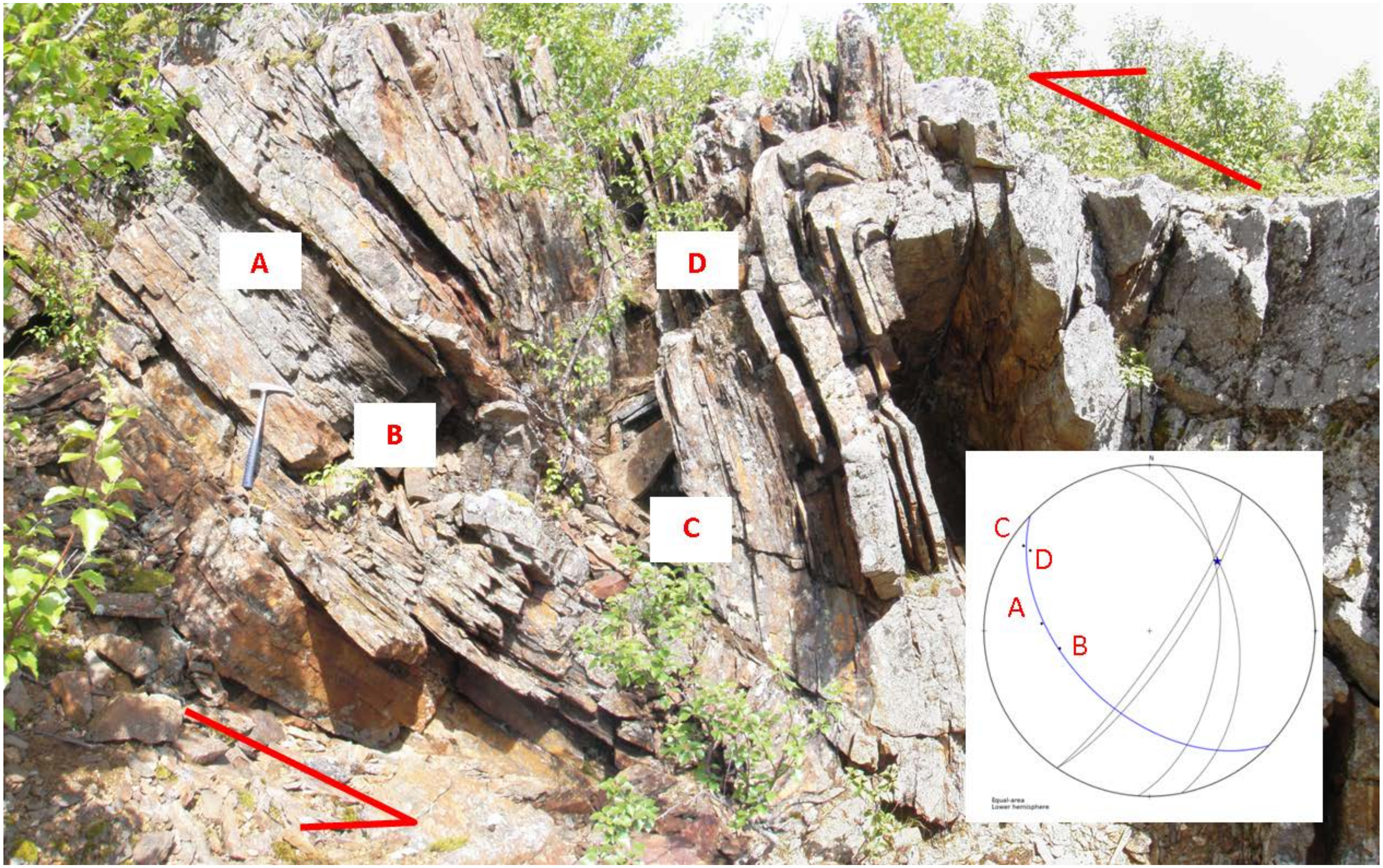

Figure 26 - Large F_2 fold in western limb of Steigtinden synform, west of Svartvatnet, showing sinistral tops-up-to-northwest motion. Labeled points in equal-area, lower-hemisphere stereonet correspond with poles to surfaces labeled with red letters in photograph (n=4). Blue star is beta axis. Facing NE, hammer (near B) for scale.

folded around a gently southwest-plunging axis, coaxial with F_2 folds seen throughout the study area (Figs. 23 and 24). A single S-C fabric measured in the Bodø Nappe shows a slip-line solution that is similarly oriented to F_2 folds, suggesting that in the Kjerringøy area the direction of transport within the Bodø Nappe was parallel to fold axes.

M_2 quartz, muscovite, and biotite are found throughout the rocks in the study area. Orientation of M_2 micas is strongly length-preferred, defining a pervasive L_2 lineation coaxial with F_2 fold axes (Fig. 27).

The tops-west directed tectonic transport recorded by F_2 folds (e.g. Fig. 26) is opposite the tops-east thrusting expected along Caledonian thrusts (Gee, 1975; Hodges et al., 1982). Three possible explanations are that they are (1) rigidly transported and orphaned Taconic structures (Barnes et al., 2007; Roberts et al., 2007), (2) collapse-related structures that formed during Devonian extension (Rykkelid and Fossen, 1992; Klein et al., 1999; Steltenpohl et al., 2004, 2010; Fossen, 2010), or (3) they are simply parasitic folds that formed on overturned limbs of the regional Steigtinden synform. Following Occam's razor, the present author interprets the folds as being parasitic to the Steigtinden synform, which is the simplest explanation based on his observations.

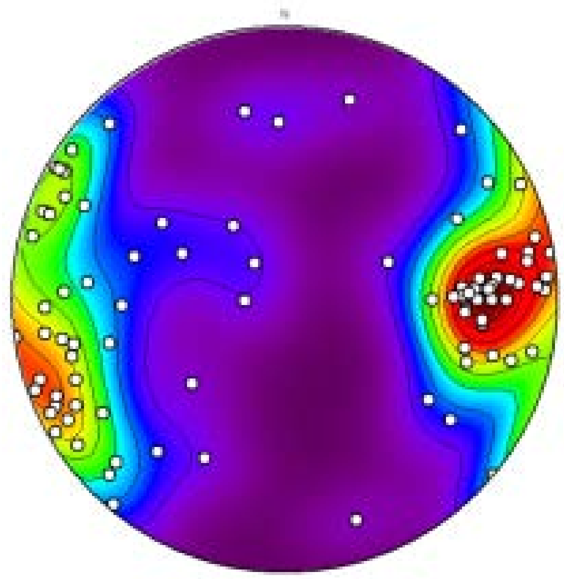

Figure 27 – Lower hemisphere stereographic plot of L_2 mineral lineations in the Heggmo Nappe, most commonly defined by elongate micas. Contours represent modified Kamb contours with a contour interval of one standard deviation (n=86).

D_3

Late-to-post-Scandian extension in the study area is referred to as D_3 in this report and is most strongly expressed by the Fjær-Osvika shear zone (FOSZ) (Plate 2). The FOSZ is a retrograde sinistral tops-down-to-the-west normal-slip mylonitic shear zone roughly 150 m thick that juxtaposes the rocks of the Bodø Nappe against the rocks of the underlying Heggmo Nappe (Plate 1). The FOSZ outcrops only sparingly along its 20 km trace on the Kjerringøy peninsula but is nonetheless easily recognized in the field. The FOSZ is invariably found where the low-lying and swampy Bodø Nappe meets the mountain-forming Kjerringøy paragneiss.

Fabrics associated with the FOSZ (Figs. 28, 29, and 30) are most strongly developed in the quartzofeldspathic gneiss of the Kjerringøy paragneiss. The best exposure of the FOSZ is just to the south of Fjær along the the coast (Fig. 1). This area contains abundant kinematic indicators, most commonly sigmoidal quartz and feldspar, showing sinistral tops-down-to-west movement (Fig. 29). Zeltner determined that the FOSZ was active under greenschist-facies conditions (Zeltner, 2001).

Shear sense indicators associated with movement along the FOSZ are present throughout the Bodø Nappe (Fig. 29). The most common kinematic features are found in the Hopsfjell Schist and are mesoscopic F_3 plastic flow folds (Fig. 30). These folds universally show tops-down-to-west motion and commonly have an S_3 axial planar crenulation cleavage that dips towards the center of the Kjerringøy synform. These folds are broadly similar in style and orientation to the large west-plunging F_3 Kjerringøy synform (Plate 2).

Figure 28 – Outcrop of mylonitic gneiss of the D_3 Fjær-Osvika shear zone. Light-colored layers and porphyroclasts are dominated by plagioclase and quartz, and darker layers have concentrations of muscovite, biotite, and garnet. Photo taken at KJR-094, near the antenna between Fjær and Brennhaugen, looking northeast.

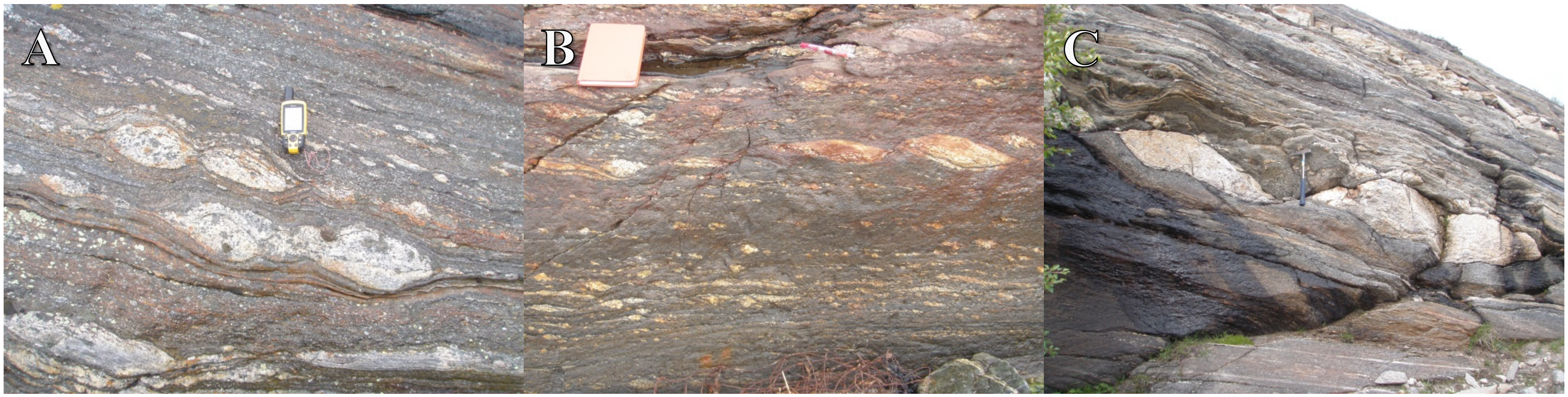

Figure 29 – Three outcrops south of Fjær showing tops-down-to-west (left in photos) sinistral motion in the Kjerringøy paragneiss. A) Normal slip shear extending composite lenses. GPS unit for scale B) Sigmoidal porphyroclasts. Field book for scale. C) Normal slip shear zone extending felsic layer. Hammer for scale.

Figure 30 - Looking towards the south at a west-vergent D_3 fold near the FOSZ, exposed on the shore west of Osvika, within the Hopsfjell Schist in the Bodø Nappe. Note axial planar foliation and Brunton for scale.

Kinematic indicators showing motion along the FOSZ are also evident in the Kjerringøy paragneiss near Fjær and Osvika. These are most commonly normal-slip extensional shears of compositional banding that show sinistral tops-down-to-west motion (Figs. 29A, 29B, and 30). Sheared boudins are also present, showing the same sense of shear (Fig 29 C).

The orientation of S_3 mylonitic foliation (Fig. 28) in the FOSZ and hanging wall of the Bodø Nappe defines a tight synform referred to as the F_3 Kjerringøy synform. This synform plunges moderately to the northwest (33° @ 319°) and shows tops-down-to-the-northwest normal-slip movement. Analysis of the regional formline map (Fig. 17) shows that S_1 foliation in the Heggmo Nappe is deflected into parallelism as one approaches the FOSZ (Fig. 31). This D_3 transposition of D_1 fabrics occurs throughout the Bodø Nappe and locally in the Heggmo Nappe where it is within one kilometer of the FOSZ. Outcrop scale D_3 structures (e.g. Figure 29) are most strongly expressed along the FOSZ and in the core of the F_3 Kjerringøy synform near the village of Kjerringøy. F_3 sheath folds that plunge obliquely relative to the Kjerringøy synform are particularly distinctive and only found within the Bodø Nappe. Elongation lineations observed as stretched muscovite show that muscovite outside of the Bodø Nappe does not share the same orientation as that found within the nappe. The long-axes of muscovite within the Bodø Nappe therefore define an L_3 lineation.

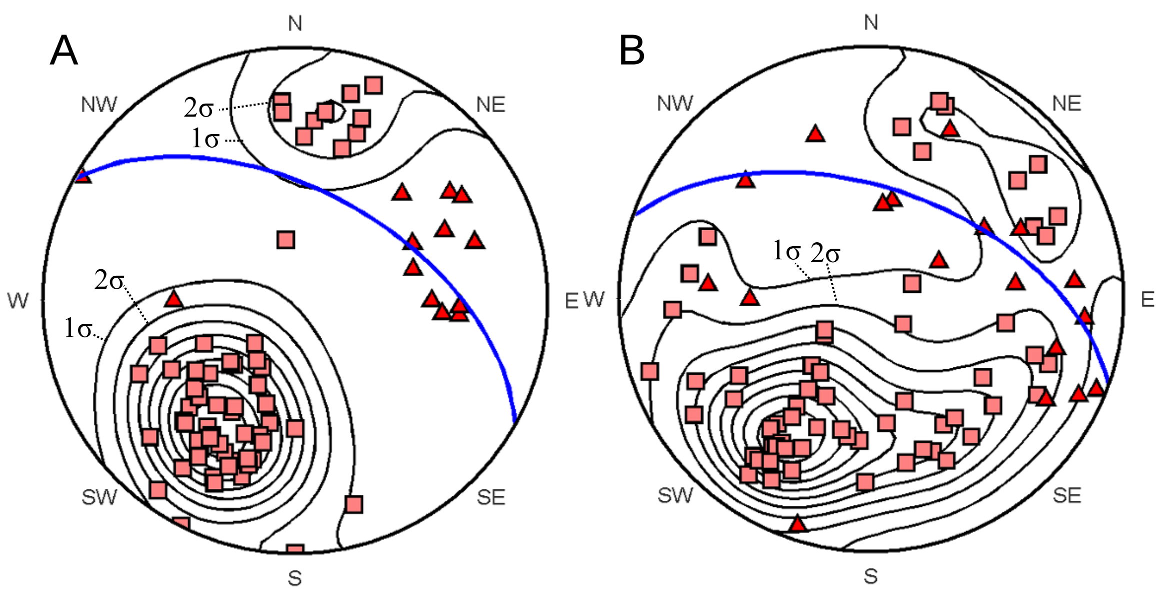

Figure 31 - Equal-area lower-hemisphere plot of foliations and lineations measured on the Kjerringøy peninsula, emphasizing the transposition of older fabrics into S_3 folia near the FOSZ. Pink squares are poles to foliations (n_A=59, n_B=60), red triangles are elongation lineations (n_A=13, n_B=18), and the blue great circle is the approximate axial surface of the F_3 Kjerringøy synform. Foliation in A and B is contoured using a modified Kamb technique with a contour interval of one standard deviation A) All measurements found within one kilometer of the FOSZ, measured in both the Bodø and Kjerringøy Nappes, i.e. the hanging wall and the footwall. B) All measurements from within the Kjerringøy Nappe, farther than one kilometer from the FOSZ. Transposition related to the D_3 FOSZ is much less evident in rocks greater than one kilometer from the FOSZ.

D_3 deformation may extend farther to the east where Rutland and Nicholson (1965) describe a synform overturned to the north that extends across Nevelsfjorden and Skjunkford (Fig. 1, Plate 2). The current authors' correlation of the Kjerringøy synform with the Stiegtinden synform becomes difficult to support if Rutland and Nicholsons' (1965) Sjunkfjord structure is indeed the true continuation of the Kjerringøy synform. The Sjunkfjord synform east of Nevelsfjorden is not well-represented on the structural formline map of the area (Fig. 17). The Kjerringøy synform does lack a clearly defined nose, which may be the result of interference between the north-south trending Steigtinden synform and the east-west trending Skunkfjorden synform. Neither of these areas was studied by the current author, so the exact nature of the relationship between the Sjunkfjord and Steigtinden synforms is unknown.

Zeltner (2001) used $^{40}Ar/^{39}Ar$ stepwise-heating analyses on a variety of phases to attempt constraining the timing of movement along the FOSZ in the Steigtinden area. Near Steigtinden, the FOSZ is a greenchist-facies shear zone that cuts across Scandian fabrics. Movement appears to have stopped by ~394 Ma, at which point undeformed muscovite in the FOSZ cooled through its closure temperature. The present author's $^{40}Ar/^{39}Ar$ muscovite cooling age of 392.0 ± 1.9 Ma from a sample (KJR-093, see below) collected from a pegmatite near Mjelde supports Zeltner's (2001) observation. Steltenpohl et al. (2011) reported that this timing is broadly similar to that determined for extensional deformation that was pervasive throughout the North Atlantic Caledonides.

D_4

D_4 brittle normal faults in the study area were most readily recognized using satellite imagery and were then confirmed by spot checking on the ground (Plates 1 and 2). These faults are tens of kilometers long and mostly parallel the Vestfjord. Outcrop-scale normal faults are particularly prevalent at the northern end of the study area near Tårnvika (Fig. 1). Relatively deep and linear valleys appear to be normal fault canyons. Normal faults in Sørfjorden trend northward into Trolltindvatnet and on to Nevelsfjorden (Fig. 1, Plate 2). Exposures of the normal faults reveal they are marked by iron-oxide staining and sulfide mineralization. Calcite is often concentrated near faults, similar to the nearby Svartvass fault, described by Zeltner (2001) as a late brittle fault associated with the opening of the Vestfjord basin.

Displacement along normal faults in the study area has nowhere been observed to be greater than a few tens of meters. Zeltner (2001) reports ~17 m displacement along the Svartvass fault. Analysis of high-resolution 3D models of the Misten area (Fig. 32) show normal displacement of nearly a kilometer distributed across several steeply dipping D_4 normal faults that are separated from each other by less than a kilometer on average.

All tectonostratigraphic units in the study area are cut by the steeply dipping D_4 brittle normal faults. These faults parallel a family of Mesozoic to Tertiary normal faults observed in Vestfjord, Lofoten, and further west in the Norwegian Sea associated with the opening of the Atlantic Ocean (Steltenpohl et al., 2004, 2011; Eig and Bergh, 2010).

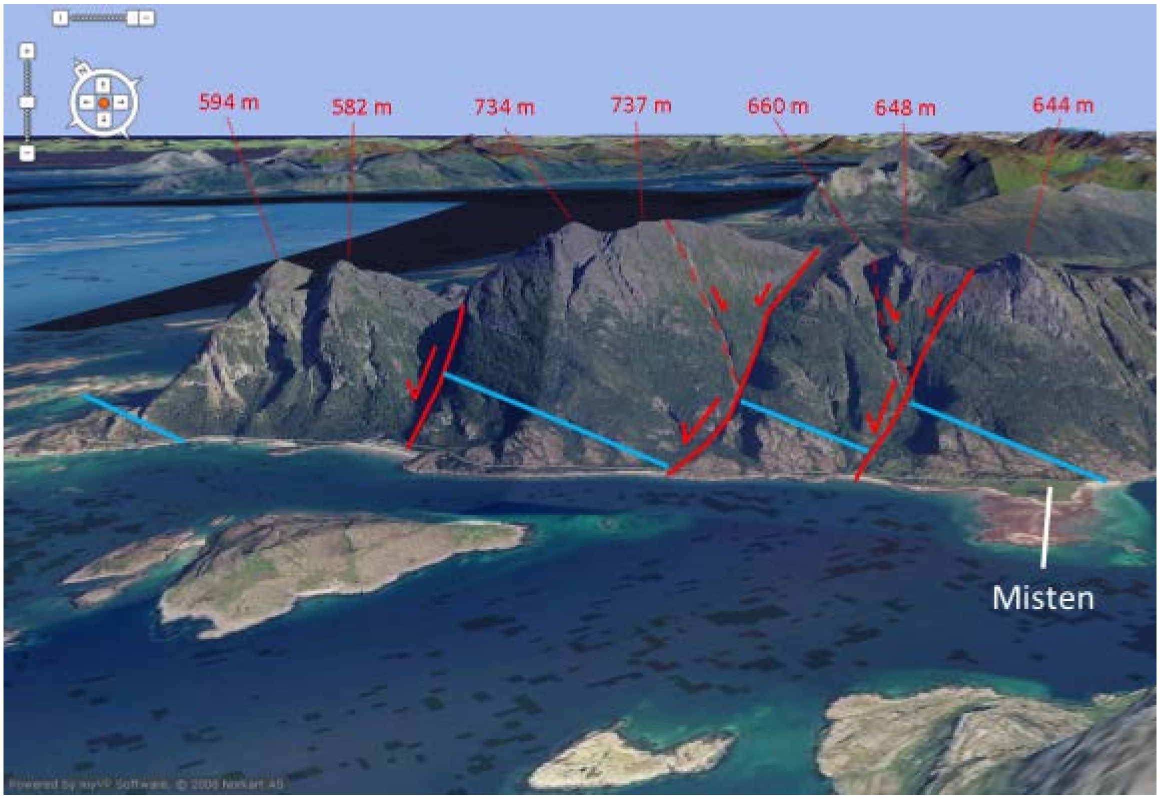

Figure 32 – Normal faults visible in the mountains that form the southwest shore of the Kjerringøy peninsula, shown with solid red lines. Faults dip steeply to the northwest. Blue horizon is a distinctive marble layer offset by the normal faults. Faults are marked by hydrothermal alteration along fault plane. Elevations are indicated with thin red lines (3D model from http://kart.finn.no).

Pressure/Temperature Conditions

Pressure-temperature estimates were determined from a garnet-muscovite-kyanite schist (sample KJR-093) collected near Buholmen (Fig. 1), north of Bodø, from within Kjerringøy paragneiss. The unit had previously been interpreted as being part of the cover sequence to the Baltic basement (Gustavson and Blystad, 1995).

Methodology

A commercially-prepared polished thin section created from sample KJR-093 was analyzed using a CAMECA SX50 electron microprobe (EMPA). All analyses were obtained by Dr. Robert Tracy, Director of the Electron Beam Laboratories in the Geosciences Department at Virginia Tech. The areal variation in the concentration of Ca, Fe, Mg, Mn, Al, Ce, K, and Ti was qualitatively determined using an energy-dispersive spectrometer. More precise compositions of SiO_2, TiO_2, Al_2O_3, FeO, MnO, MgO, CaO, Na_2O, and K_2O along four separate traverses were determined using a wavelength-dispersive spectrometer. Analytical results are presented in Appendix 2.

The microprobe chemical analyses were used to obtain average mineral formulas for the minerals present in the polished section. Formulas were obtained using the method outlined in Appendix 1 of Deer et al. (1996). The cation proportions thus obtained then served as the basis for quantitatively determining the pressure and temperature conditions under which the minerals could have formed.

The concentration of elements within a given mineral phase is often sensitive to the pressure and temperature regime within which that mineral crystallizes. For well-studied mineral systems, determining the concentration (cations per mineral unit) of certain cations allows one to then solve for the possible pressures and temperatures that the mineral system could have equilibrated under. Certain coexisting mineral systems are well-known as geothermometers or geobarometers (Spear, 1993). It is customary to use specific systems to solve for either pressure or temperature. A geothermometer would be a system that indicates equilibrium over a narrow range of temperatures while the pressure may vary greatly, while a geobarometer would indicate a system at equilibrium over a narrow range of pressures but a wide range of temperatures. At least one geobarometer and one geothermometer must therefore be used simultaneously to reasonably constrain both temperature and pressure.

In this study the garnet-biotite (GARB) geothermometer was used (Waters, 2004). This geothermometer relies on the temperature-sensitive exchange of Fe and Mg between garnet and biotite. The overall Fe-Mg exchange reaction is as follows: $KMg_3(AlSi_3)O_{10}(OH)_2$ (phlogopite) + $Fe_3Al_2(SiO_4)_3$ (almandine) = $KFe_3(AlSi_3)O_{10}(OH)_2$ (annite) + $Mg_3Al_2Si_3O_{12}$ (pyrope) (Ferry and Spear, 1978). The Fe-Mg exchange relationship has been experimentally determined and related to pressure and temperature by the following equation: $6266 - 2.35T + 0.029(P-1) + 3T\ln K_D = 0$ (Waters, 2004), where T is the temperature in degrees Kelvin, P is the pressure in bars, and $K_D = \frac{Fe_{bio}/Mg_{bio}}{Fe_{gnt}/Mg_{gnt}}$ is the thermodynamic distribution coefficient for the reaction with Fe_{bio}, Mg_{bio}, Fe_{gnt}, and Mg_{gnt} all in formula moles (Spear, 1993). In general, K_D will be larger for higher grades of metamorphism.

The geobarometer used in this study is known as the GRAIL geobarometer (**G**arnet + **R**utile = **A**l$_2$SiO$_5$+**IL**menite + Quartz) and is rooted in the following reaction: $Fe_3Al_2Si_3O_{12}$ (almandine) + $3TiO_2$ (rutile) = $3FeTiO_3$ (ilmenite) + Al_2SiO_5 + $2SiO_2$ (Bohlen et al., 1983). To use the GRAIL geobarometer, one must first determine the equilibrium constant, $K = \frac{a_{Il}^3 a_{Ky} a_{Qtz}^2}{a_{Alm} a_{Ru}^3}$, where a_{Ilm}^3 is the percent ilmenite, a_{Ky} is the percent kyanite, a_{Qtz}^2 is the percent quartz, a_{Alm} is the percent almandine, and a_{Ru}^3 is the percent rutile (all percents determined using formula mole concentration) (Bohlen et al., 1983). The value K is then used in the expression $\Delta P \cong \frac{-RTlnK}{2.303\Delta V}$ to determine pressure and temperature conditions. Analysis of this relationship has shown that the GRAIL system is particularly insensitive to variations in temperature, making it an excellent geobarometer (Bohlen et al., 1983). It is customary with the GRAIL system to plot the measured K on a graph showing pressure, temperature, and various isopleths of $\log_{10}K$ (Bohlen et al., 1983; Essene, 1989). Such graphs are calculated from solving for K using data obtained from various internally consistent thermodynamic datasets (see references in Bohlen, et al., 1983). If it is desirable, the amounts of kyanite and quartz can be left out and K can be approximated as $K = \frac{a_{Il}^3}{a_{Alm}}$ (Essene, 1989). Throughout this study, Essene's simplification is used.

Interpretation of P-T Results

The first garnet EMPA traverse consisted mostly of a single crystal with inclusions of quartz, calcium-rich inclusions that are likely apatite (phosphate composition was not measured), and ilmenite. The garnet was in contact with two large crystals: a biotite crystal and a quartz crystal. The average composition of the biotite was $[K_{0.804}Na_{0.042}][Fe_{1.209}Mg_{1.222}Al_{0.405}Ti_{0.113}Mn_{0.001}][Al_{2.1244}Si_{2.722}]O_{10}$ and the average composition of the garnet was $[Fe_{2.136}Mg_{0.503}Ca_{0.161}Mn_{0.075}K_{0.004}Na_{0.003}][Al_{2.100}Si_{2.984}]O_{12}$. Garnet composition is summarized in Figures 33 and 34.

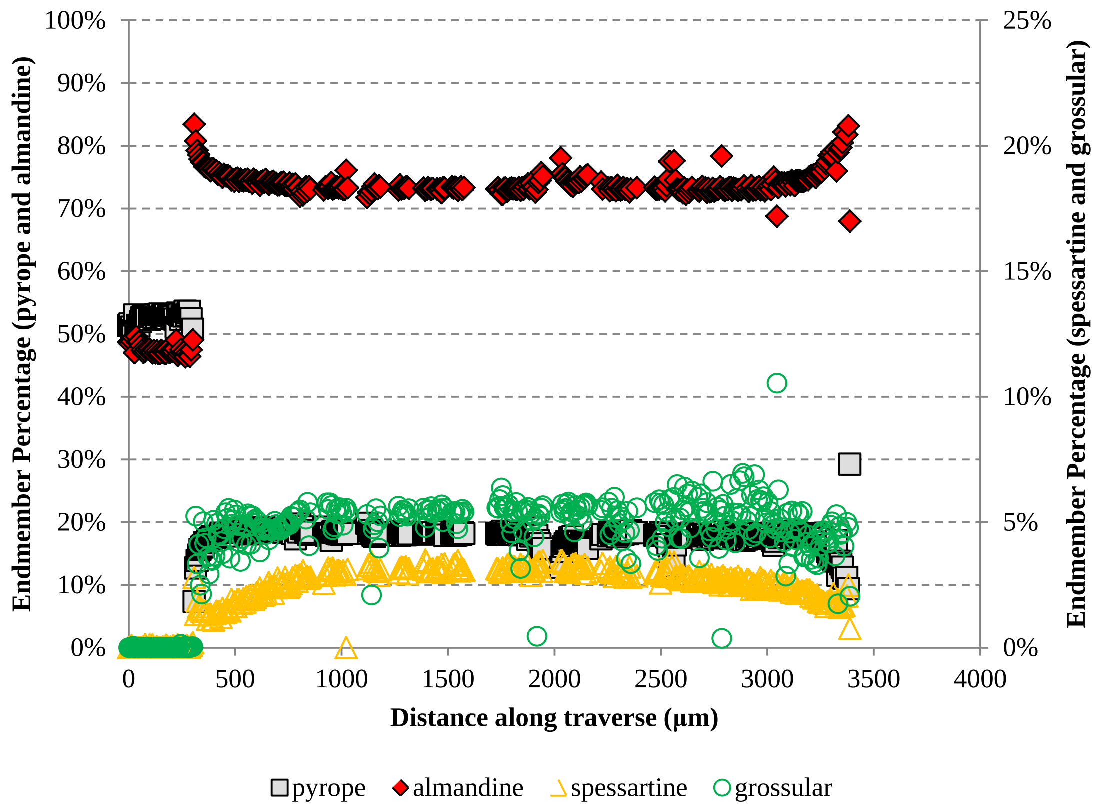

Figure 33 - Garnet end-member composition determined from Sample KJR-093. Pyrope (solid square) and almandine (solid diamond) are shown on the left y-axis, spessartine (outlined triangle) and grossular (outlined circle) are shown on the right y-axis, x axis is distance along traverse in microns.

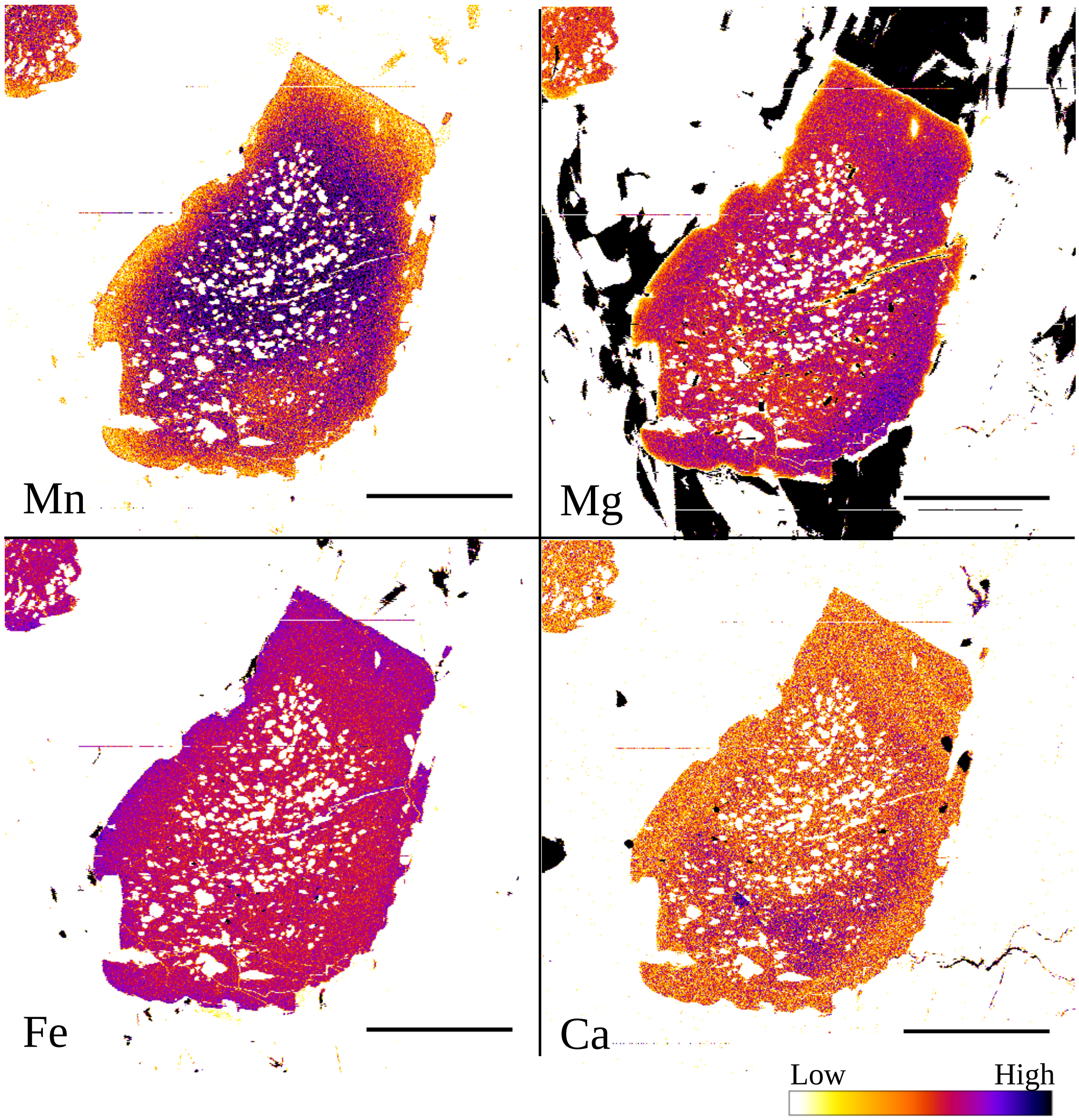

Figure 34 - Relative intensity map of Mn, Mg, Fe, and Ca in garnet analyzed from sample KJR-093. Darker colors represent higher concentrations of the element displayed in the image. Width of scale bar in lower right of each subset image is 150 microns.

From within this traverse a thermodynamic distribution coefficient $K_D = 0.215$ for the GARB geothermometer was determined using the mean formula molar concentration of Fe and Mg from biotite and garnet. Using the median values yielded a $K_D = 0.217$. The first traverse also included a small ilmenite inclusion, possibly usable in the GRAIL geobarometer. This inclusion yielded a mean K = 0.125 and a median K = 0.126.

The second traverse was conducted on a separate biotite/garnet pair, the average compositions of which are $[K_{1.216}Na_{0.057}][Mg_{2.764}Fe^{2+}_{1.440}Mn_{0.004}][Fe^{3+}_{1.084}Al_{0.783}Ti_{0.132}][Si_{5.256}Al_{2.744}]O_{10}$ and $[Fe_{2.310}Mg_{0.515}Ca_{0.152}Mn_{0.048}Na_{0.001}][Al_{2.000}Ti_{0.005}Si_{2.981}]O_{12}$, respectively. GARB K_D values for mean and median Fe and Mg in this traverse were $K_D = 0.205$ and $K_D = 0.209$, respectively.

The third traverse consisted almost entirely of muscovite $[K_{1.489}Na_{0.261}][Al_{3.639}Fe_{0.184}Mg_{0.180}Mn_{0.001}][Si_{6.482}Al_{1.818}]O_{20}$ with a minor amount of quartz.

The fourth traverse analyzed a single rutile crystal, $[Ti_{0.989}Fe_{0.040}]O_2$, flanked on either side by ilmenite, $[Fe_{1.019}Mg_{0.007}Mn_{0.004}]Ti_{0.983}O_3$. Mean and median equilibrium constants of K = 0.125 and K = 0.127 were obtained, respectively.

The appropriate use of geothermometers and geobarometers is dependent on the equilibrium of the mineral systems in question. If the phases involved in the GRAIL or GARB reactions are not at equilibrium, the P-T data obtained using the system is useless. One must carefully evaluate petrographically whether equilibrium is a reasonable assumption to make about the assemblage in question. In the case of sample KJR-093, several criteria were used to determine whether equilibrium was a reasonable assumption:

1. Large, euhedral crystals are evident in thin section and in microprobe x-ray maps.

2. Grain boundaries are sharp. There is some pitting and retrograde modification and development of a minor amount of chlorite.

3. The almandine portion of the garnet in the first traverse is largest along the boundary with biotite. The biotite is enriched in phlogopite along this same boundary. This suggests that Fe was leaving the biotite and entering the garnet while Mg was leaving the garnet and entering the biotite. While this does not necessarily imply perfect equilibrium, it does suggest that there has not been much retrogressive requilibration recorded along the traverse.

4. Ti has remained concentrated in abundant ilmenite and rutile both as inclusions in the garnet and as crystals in the matrix (Fig. 35). One would expect the titanium to diffuse back into other phases such as biotite or garnet under extensive cooling and retrogression.

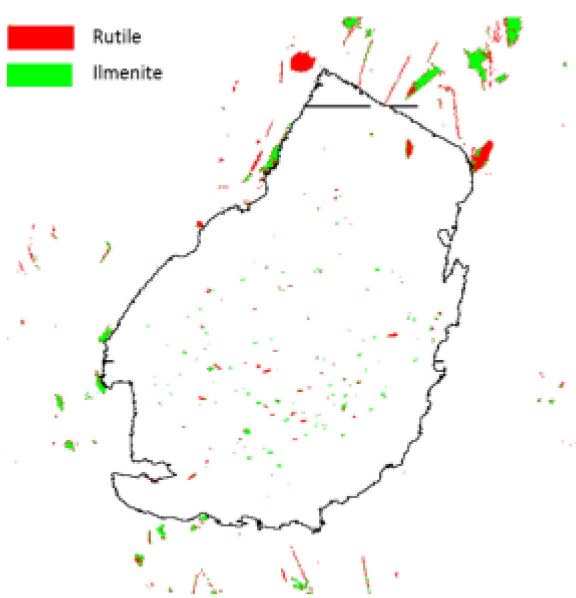

Figure 35 - Derived image showing presence of ilmenite and rutile. Red indicates areas with abundant Ti and little Fe. Green indicates areas that are abundant in both Ti and Fe. The garnet traversed in the first traverse is outlined in black.

5. There is slight Fe enrichment around an ilmenite inclusion within the garnet in the first traverse (Figs. 33 and 35, Appendix 2). This could indicate that the ilmenite grew and took in Fe from its environs. This would not be expected during retrogression or in equilibrium.

Overall, there appears to be plenty of evidence suggesting that equilibrium is not an unreasonable assumption. There is also evidence to suggest that the assemblage may represent prograde metamorphism. The temperature and pressure fields suggested by GARB and GRAIL, respectively, can be seen in Figure 36. The minimum and maximum temperatures suggested are 649 °C and 672 °C, respectively. No attempt was made to quantify error, which may have been introduced from imperfections in the thermobarometers used, from uncertainty in the chemical analyses, or from uncertainty in composition-activity relationships. The range of possible pressure and temperatures reflects derivation using all possible K_D values.

The minimum and maximum pressures suggested are 9.5 kbar and 10.1 kbar, respectively. The range in pressures reflects the graphical imprecision involved in plotting the GRAIL K value on the diagram. A small amount of interpolation was involved in picking the correct line where K was constant. The range plotted is almost certain to contain the correct constant K line, however. It is evident in this analysis that the Kjerringøy paragneiss underwent upper amphibolite facies, kyanite-zone metamorphism, with a pressure of 9.5-10.1 kbar and a temperature of 648°-672° C.

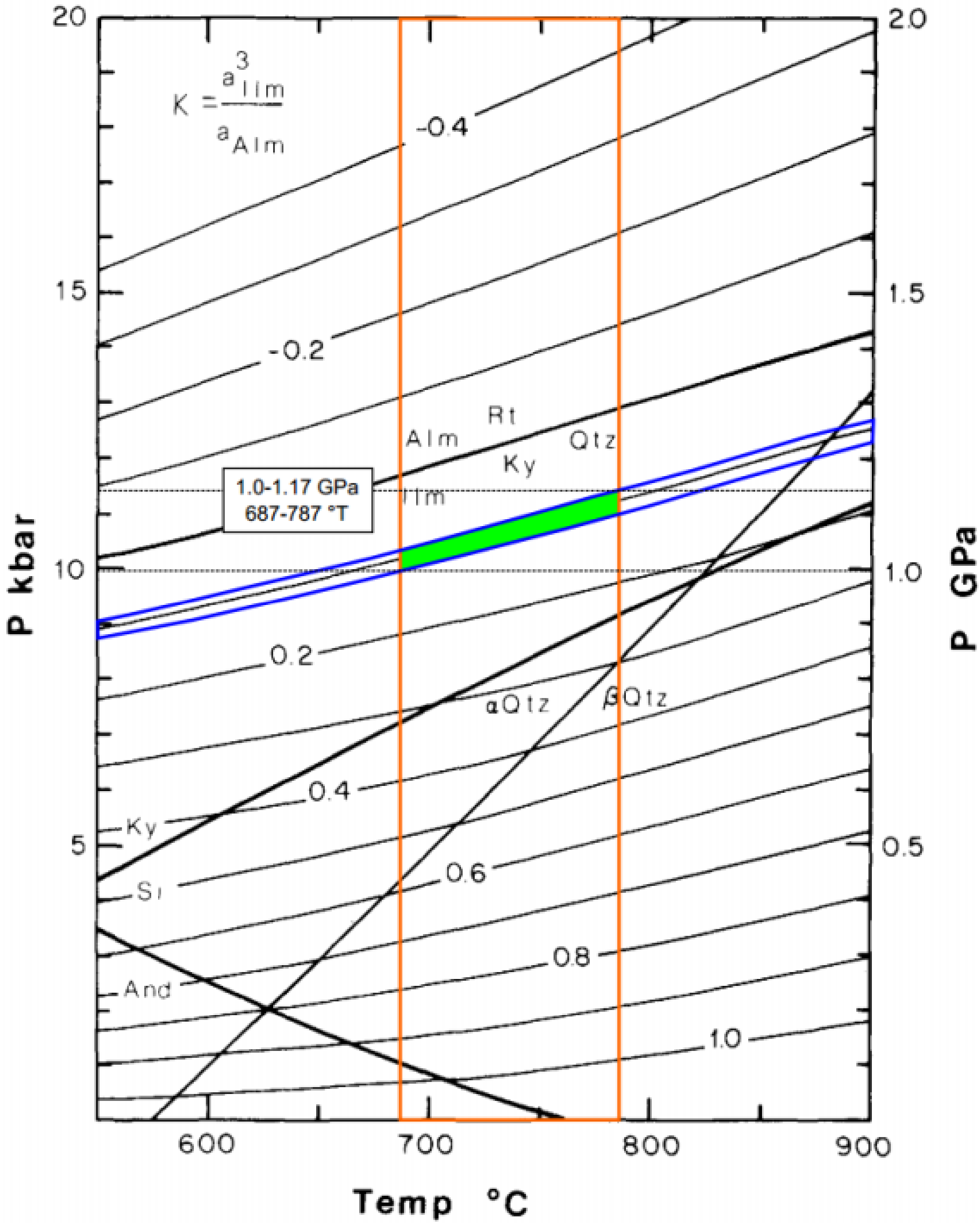

Figure 36 - P-T diagram showing temperature and pressure fields solved for using data obtained from sample KJR-09 (after Essene, 1989).

GEOCHRONOLOGY

Three samples collected from the Kjerringøy Peninsula, LEA-10-1, LEA-10-2, and KJR-243 (Fig. 37, Table 3), were analyzed using the Isotope Dilution-Thermal Ionization Mass Spectrometry (ID-TIMS) technique. The samples were prepared and analyzed in the ID-TIMS U-Pb laboratory at the University of Oslo under the guidance of Professor Fernando Corfu.

A fourth sample collected from near Mjelde, KJR-093 (Fig. 37, Table 3), was analyzed for U-Pb non-isotopic chemical age dating using an electron microprobe at the Electron Beam Laboratories in the Geosciences Department at Virginia Tech. This analysis was kindly arranged by Dr. Willis Hames, Auburn University, and Dr. Robert Tracy, Director of the Electron Beam Laboratories at Virginia Tech. In addition to the electron microprobe analysis, a single muscovite grain from sample KJR-093 was analyzed for $^{40}Ar/^{39}Ar$ by Dr. Willis Hames at the Auburn Noble Isotope Mass Analysis Laboratory.

Decay constants used are those given in Steiger and Jäger (1977) and radiogenic ages and graphical analysis of geochronological data was done using Isoplot/Ex (Ludwig, 2009). Sample collection, preparation, analysis, and interpretation are detailed in the following text.

Table 3 - Representative lithological unit, sample number, and easting and northing (UTM Zone 33N, WGS84) for samples on which geochronological analyses were performed.

Lithological Unit	Sample	Easting	Northing
Rørstad Granite	LEA-10-1	505849	7493460
Fjærehesten Granite	LEA-10-2	491908	7483866
Kjerringøy Paragneiss	KJR-243	487130	7482772
Kjerringøy Paragneiss	KJR-093	484326	7479326

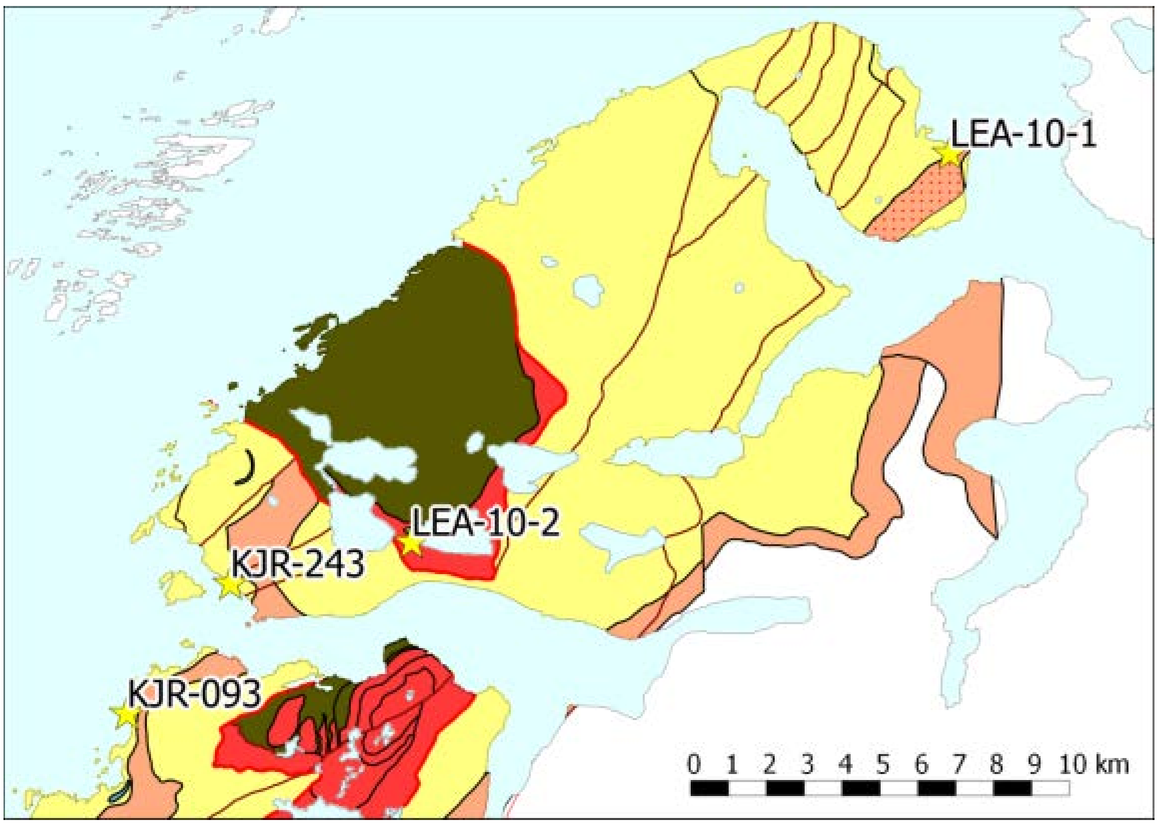

Figure 37 - Reference map showing geochronology sample locations in the study area: KJR-093, KJR-243, LEA-10-1, LEA-10-2. UTM coordinates are in Table 3.

Chemical Dating

Chemical dating of monazite was performed on the same sample of garnet kyanite muscovite schist from the Kjerringøy Paragneiss that was used for geothermobarometry, sample KJR-093. A commercially-prepared polished thin section created from the hand sample was analyzed using a CAMECA SX50 electron microprobe. Preliminary full-section x-ray intensity maps of twelve elements were generated (Mg, Ca, Mn, Fe, Na, Al, K, Ti, Si, P, K, Ce), with the map of Ce being used to identify and locate monazite crystals (bottom of Appendix 2).

Two monazite crystals were selected for quantitative analysis. X-ray intensity maps of the two crystals analyzed have distinct compositional domains (Figs. 38 and 39). Two types of domains are evident: a zone defined by high Th and low U, Pb, and Y, and a zone defined by low Th and high U, Pb, and Y. Three high-magnification traverses were run across one crystal and two across the other, with the traverses designed to characterize the two domains (Fig. 40). During the traverses Th, U, Pb, and Y were simultaneously measured on the instrument's four wavelength-dispersive spectrometers. Analysis was performed as prescribed by Montel et al. (1996) and Williams et al. (1999). Overestimation of Pb due to Y Lγ peak interference with the Pb Mα peak was corrected for (Williams et al., 2007). Data and full-section x-ray intesnsity maps are reported in Appendix 2.

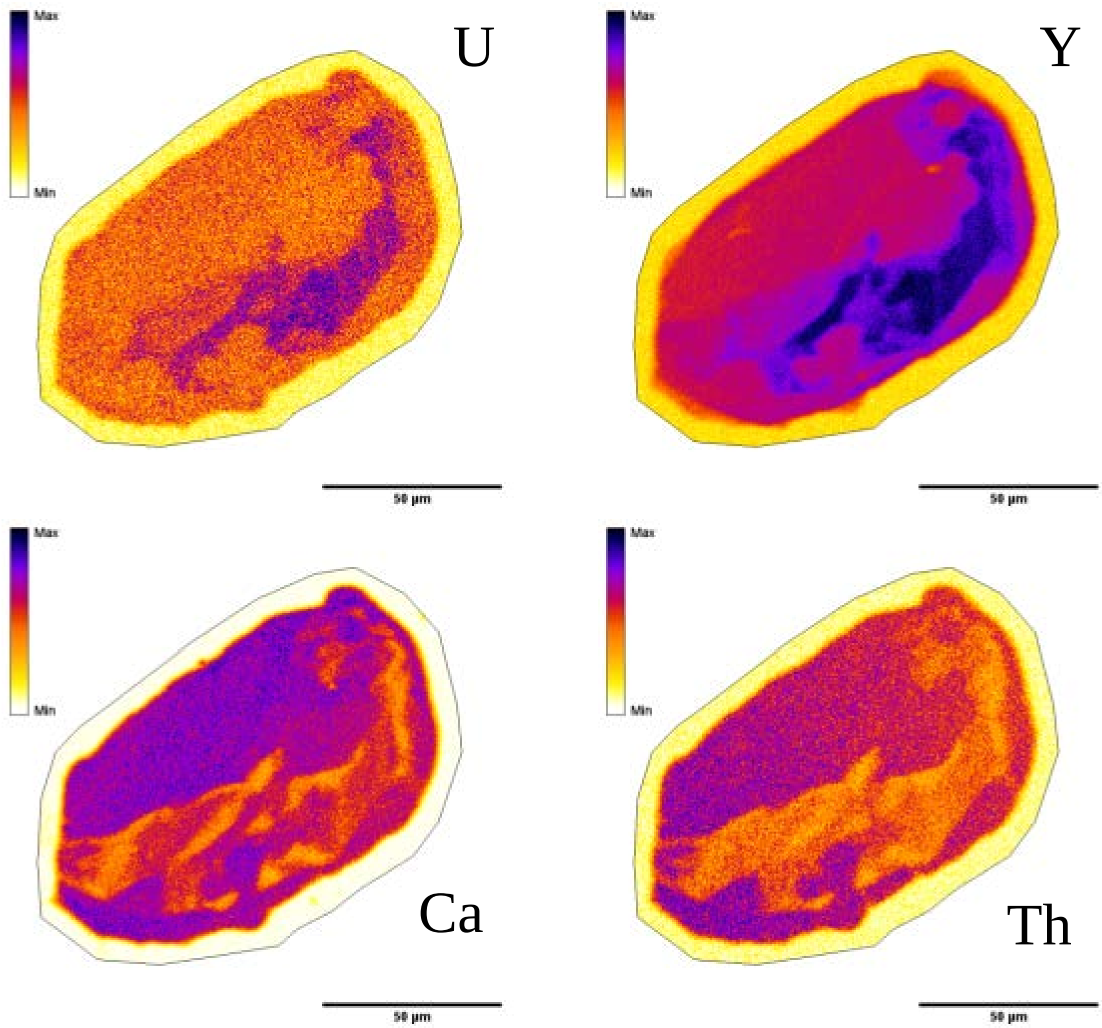

Figure 38 - Relative intensity maps of uranium, yttrium, calcium, and thorium in monazite #1 analyzed from sample KJR-093. Darker colors represent higher concentrations of the element displayed in the image. Width of scale bar in lower right of each subset image is 50 microns.

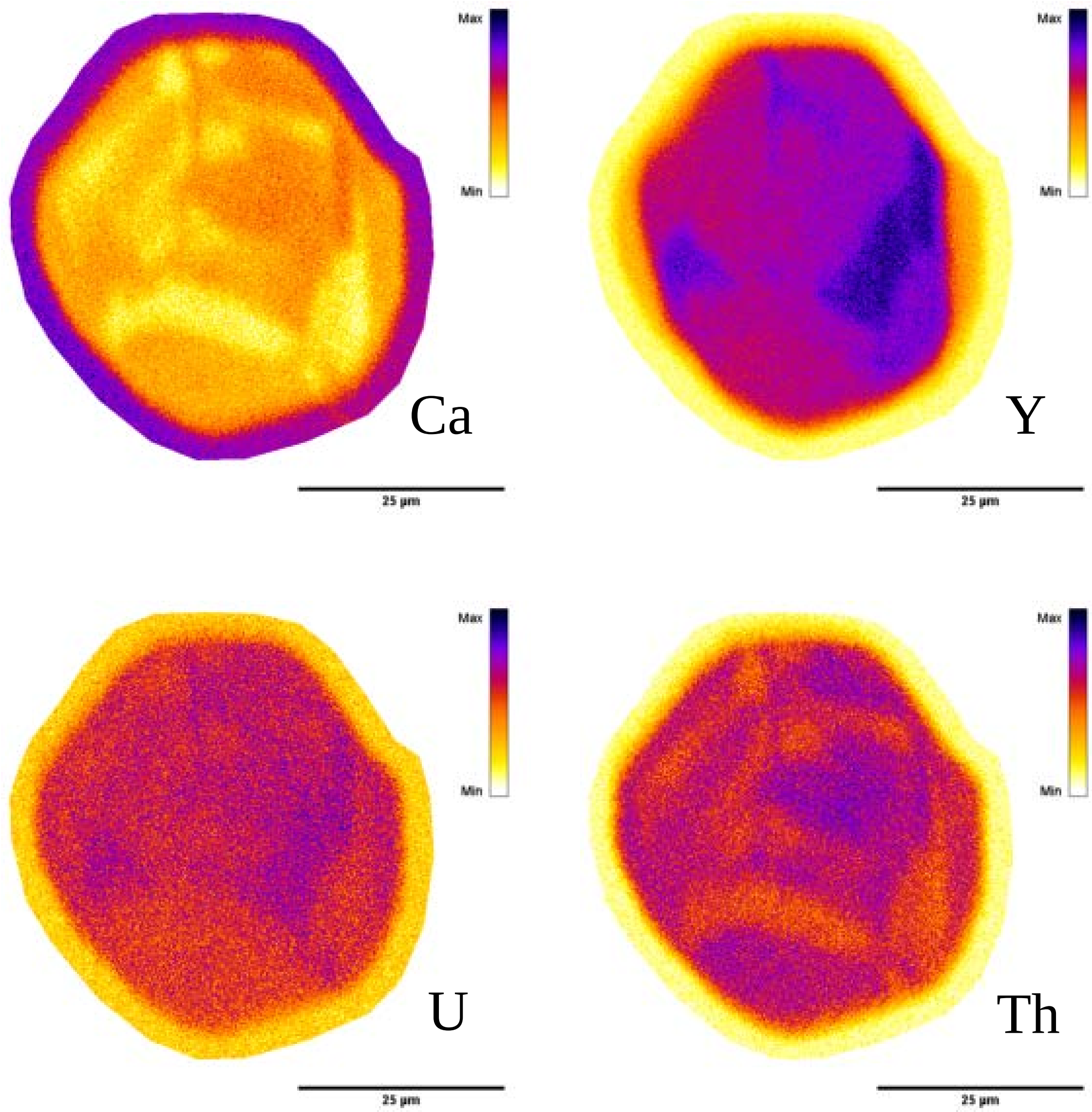

Figure 39 - Relative intensity maps of calcium, yttrium, uranium, and thorium in monazite #2 analyzed from KJR-093. Darker colors represent higher concentrations of the element displayed in the image. Width of scale bar in lower right of each subset image is 25 microns.

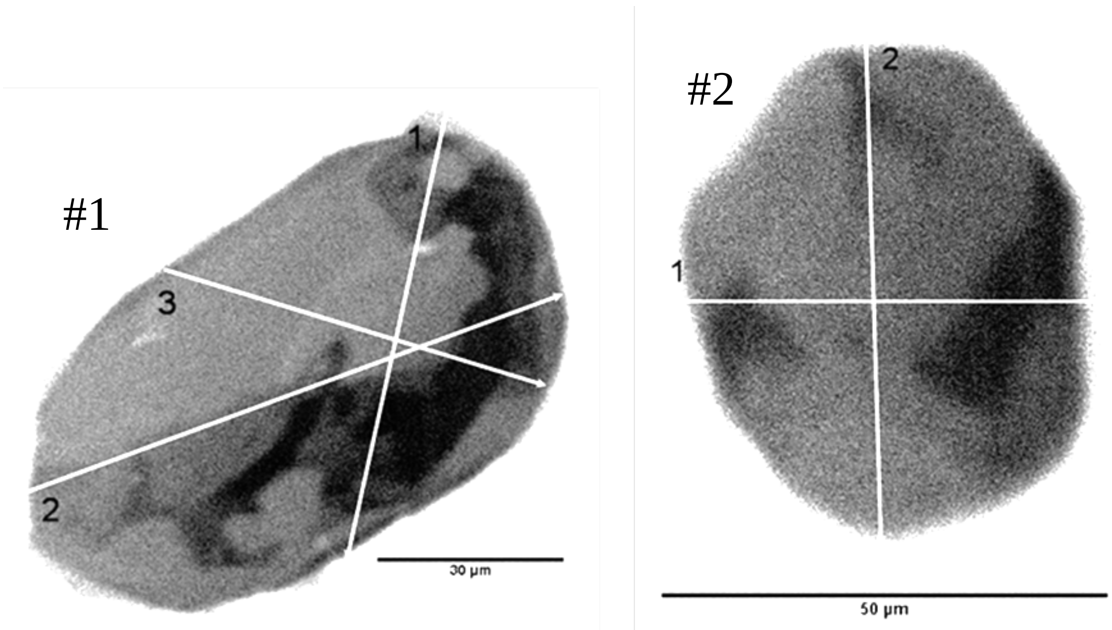

Figure 40 – Location of EMPA traverses on monazite crystals. Shown on Y x-ray intensity maps. Data reported in Appendix 2.

As only U, Pb, and Th concentrations were quantitatively determined, the amount of ^{238}U, ^{235}U, ^{206}Pb, and ^{207}Pb was determined by solving for age in the following equation at all measured points (Pb, Th, U = elemental concentration; λ^{232}, λ^{235}, λ^{238} = decay constants of ^{232}Th, ^{235}U, and ^{238}U; τ = age of the measured parent/daughter pair in years):

$$Pb = \frac{Th}{232}\left(e^{\lambda^{232}\tau} - 1\right)208 + \frac{U}{238.04}(0.9928)\left(e^{\lambda^{238}\tau} - 1\right)206 + \frac{U}{238.04}(0.0072)\left(e^{\lambda^{235}\tau} - 1\right)207$$

(from Montel et al., 1996). IsoplotEx (Ludwig, 2009) was used to perform Gaussian deconvolution on the array of determined ages, yielding “unmixed” ages for the population. IsoplotEx yielded three peaks, a peak at 426.7 ± 3.8 Ma, a peak at 469.2 ± 2.3 Ma, and a peak 511.1 ± 3.6 Ma (2σ errors, relative misfit=0.504). These ages are similar to others reported here (see below) and are interpreted to be geologically significant.

The results of the Gaussian deconvolution were confirmed by using a simple isochron analysis using the basic method described by Nicolaysen (1961). This technique was performed on the isotope concentrations found using Montel et al.'s (1996) model. The present author generalized Nicolaysen's method slightly (Fig. 41) in that the concentration of the parent isotope (i.e. ^{238}U, ^{235}U, ^{232}Th) was plotted on the x-axis and the concentration of the daughter isotope (i.e. ^{206}Pb, ^{207}Pb, ^{208}Pb) was plotted on the y-axis, as opposed to plotting the normalized radiogenic/stable isotope ratios (i.e. $^{87}Rb/^{86}Sr$ and $^{87}Sr/^{86}Sr$) on these axes, respectively. The utility of this scatter plot (Fig. 41) is that points that are related to each other by being the same age will fall along a linear array, called an isochron. The relationship between an isochron line and age is illustrated by the following equation, where τ = age, α = the angle of the isochron relative to the abscissa, and λ = the decay constant of the parent isotope: $\tau = ln(1 + tan(\alpha))/\lambda$ (Nicolaysen, 1961). Isoplot's "robust regression" lines (Ludwig, 2009) were fit through each scatterplot and were used to determine α for each isochron. Isoplot's method of robust regression is based on Rock and Duffy's (1986) technique for fitting a line to a scatter plot which makes no assumptions regarding the distribution of the residuals of the population being measured. As the distribution of the data reported here is unknown, the author felt a robust regression was more appropriate to use than a regression using the method of least squares, which requires that the residuals of the data are normally distributed (Ludwig, 2009).

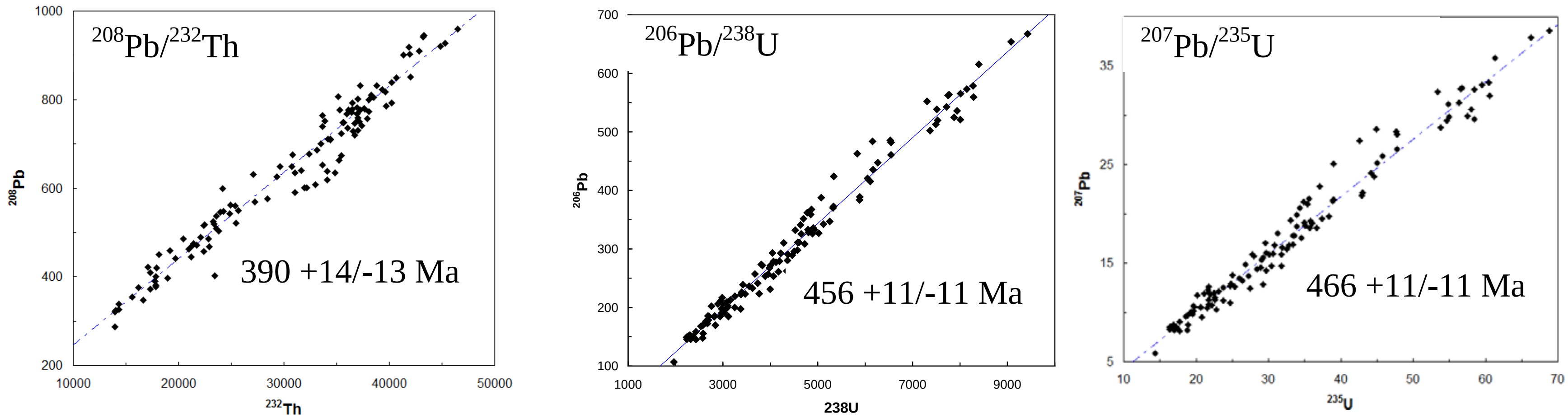

Figure 41 - Isochrons determined from calculated Pb isotope concentrations in sample KJR-093.

U-Pb ID-TIMS

Rørstad Granite (Sample LEA-10-1)

Sample LEA-10-1 was collected from an unfoliated exposure of the Rørstad granite southeast of the village of Tårnvika (Fig. 37, Table 3). Zircon and monazite were separated from the sample and analyzed.

Zircon

The dominant population of zircons in sample LEA-10-1 consists of prismatic light-brown, uranium-enriched (Speer, 1980; Corfu et al., 2003) metamict overgrowths mantling clear cores (see Appendix 3). Crystals generally appear inclusion free using a binocular microscope, but back-scattered electron (BSE) images document monazite inclusions concentrated in concentric growth bands (Fig. 42). Such inclusions, enriched in rare earth elements, may be useful for future geochemical characterization.

Core/overgrowth boundaries are uneven and rounded. Cores are rounded and have a frosted appearance when viewed under a binocular microscope (Fig. 43), evidence of a detrital origin. Detrital zircon cores have a distinctly different color than the overgrowth as a result of different concentrations of uranium. Squeezing the zircon crystal with tweezers often causes the core to cleanly separate from the overgrowth along the relatively weak interface between the two.

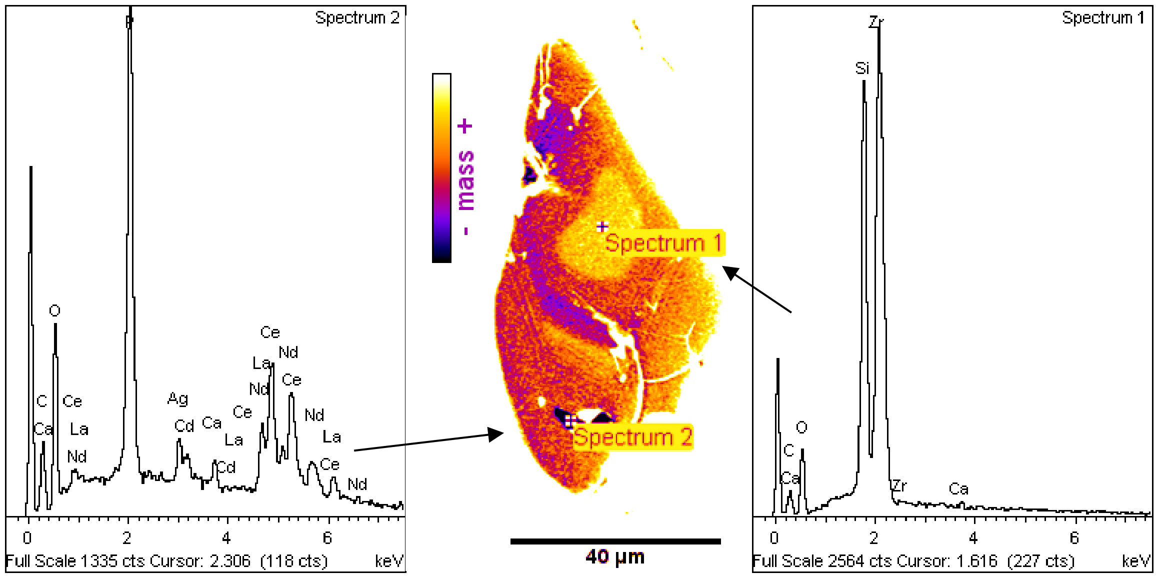

Figure 42 - Backscatter electron image of a zircon grain interpreted to have a detrital core and rounded contact with concentrically zoned igneous overgrowth. Spectrum 1 is a spot analysis of the detrital zircon core. Spectrum 2 is a monazite inclusion within the igneous zircon overgrowth.

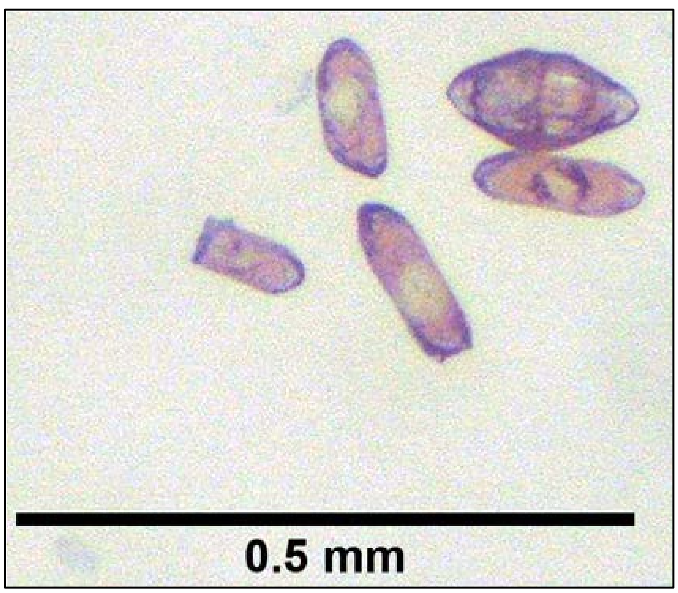

Figure 43 - Zircon crystals characteristic of sample LEA-10-1. Note frosty, transparent (low uranium) detrital cores mantled by dark brown metamic (high uranium) igneous overgrowths.

Most zircons from sample LEA-10-1 have an elongation ratio (length:width) between 2 and 3. The population has well-developed (110) prisms nearly always capped by well-developed (011) and (121) pyramids. Some crystals are bipyramidal with a (121) pyramid capping the (011) pyramid. This style of growth is considered an “S5” zircon in Pupin’s classification system, a morphotype characteristic of calc-alkaline to alkalic granites (Pupin, 1980; Speer, 1980).

Three zircons with conspicuous overgrowths on detrital cores were selected for analysis using ID-TIMS. The overgrowths were separated from the cores by gently squeezing the original grains using tweezers. The overgrowths were then mechanically abraded (see Appendix 5). The overgrowths ranged from 1.5% to 2.8% discordant and had common-lead concentrations from below the detection limit to 86 ppm. Uranium concentration ranged from 773 to 969 ppm (See Appendix 3). The $^{207}Pb/^{206}Pb$ age determined for sample LEA-10-1 was 950.6 + 5.2/-5.3 Ma (95% confidence, average of 3 analyses, weighted by 2σ absolute error), a Neoproterozoic (Tonian) age, with some discordance between the $^{206}Pb/^{238}U$ and $^{207}Pb/^{235}Pb$ ages as a result of Pb loss.

The Pb loss evident in the analyses of zircons from sample LEA-10-1 warrants further examination since Pb loss events recorded in the U-Pb system are often geologically significant (Wetherill, 1956, 1963). When plotted on a Concordia diagram (Fig. 44), the analyses form a tight grouping just below the line of concordia. It is difficult to determine a meaningful discordia through this grouping as the data fall around a point, not on a line. The absence of a discordia clearly precludes the determination of the upper and lower concordia/discordia intercepts, which are taken to represent the crystallization age and the age of the Pb-loss event, respectively (Dickin, 2005). In the absence of a discordia defined by U/Pb data, a forced-discordia was constrained to intersect the measured grouping and ages of known times when a Pb-loss event could have occurred for the sample. Possible Pb-loss events were chosen based on geochronological evidence collected in this study, as well as those that are reported in the literature; U/Pb* ages determined from other zircons and monazites; an ^{40}Ar-^{39}Ar muscovite cooling age; and monazite chemical ages (sample KJR-093). Present-day Pb-loss was also considered. The Pb-loss model results are reported in Table 4 and discussed below.

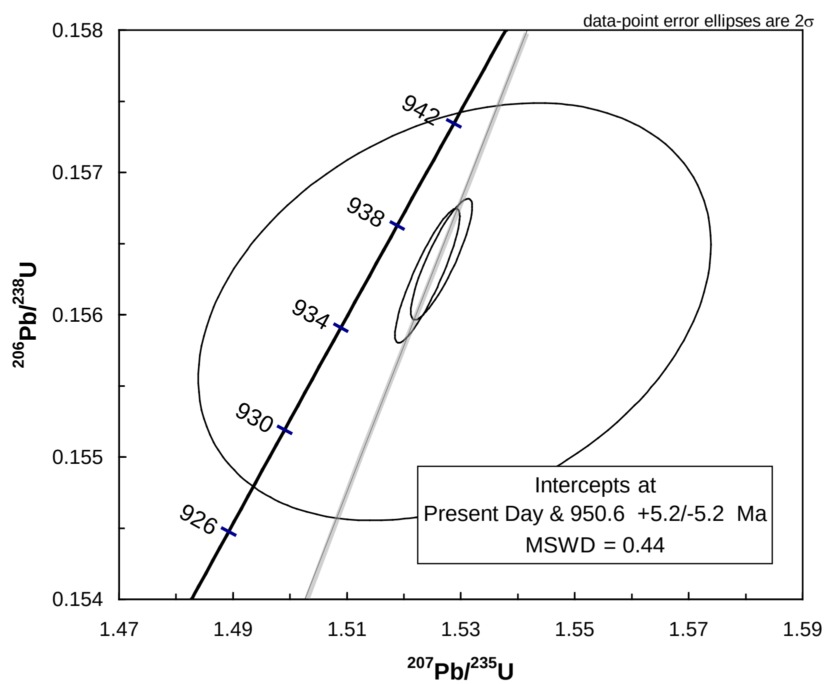

Figure 44 - U/Pb* Concordia diagram anchored at 0 Ma, from 3 zircons analyzed from sample LEA-10-1.

Table 4 - Results of different forced-discordia models applied to LEA-10-1 zircons.

Model	Age of Pb-loss		Basis for modeled Pb-loss	Derived Closure Temperature Age			$^{207}Pb/^{206}Pb$ Discrepacy	MSWD
"Grampian"	470	± 15	KJR-093 monazite chemical age	961.5	±3.7		~11 Ma	0.35
Scandian	431.49	± 0.86	KJR-243 $^{207}Pb/^{206}Pb$ ID-TIMS	959.9	±3.4		~10 Ma	0.36
Devonian Decompression	392.0	±1.4	KJR-093 $^{40}Ar/^{39}Ar$	958.4	±8.3		~7 Ma	0.37
Present-date Pb-loss	0		Pb loss occurring at the present time.	950.6	±5.2		0	0.44

The model that yielded the best results was that the only significant Pb-loss event that sample LEA-10-1 has undergone can be attributed to present-day weathering. The mean square weighted deviation (MSWD) for this model is closest to 1 of all of the models and suggests that the data represent an isochron as per Wendt and Carl (1991), as opposed to an errorchron.

The lack of whole rock chemistry data for the LEA-10-1 host rock or for the zircon crystals themselves makes it difficult to assign specific geological significance to the determined age, but some inferences can be made in this regard. As previously noted, zircon crystal morphology implies that the Rørstad magma was calcalkaline to alkaline. The presence of abundant oligoclase (optically determined to be An_{15}-An_{30}) suggests that the melt was more alkaline than calcalkaline. Watson (1979) demonstrated that zircon crystallization from alkaline melt varies significantly with the relative concentration of Al_2O_3, Na_2O, and K_2O. Zircon becomes saturated and crystallization begins at low concentrations (< 100 ppm) in peraluminous melts. Saturation levels in peralkaline melts can be much higher than in peraluminous melts, with dissolved Zr reaching as high as 39,000 ppm. However, the presence of dissolved Fe_2O_3 significantly reduces the solubility of zircon in peralkaline melts (Watson, 1979). The relative abundance of biotite in the Tårnvika pluton suggests that Fe_2O_3 may have been a significant component in the melt, and thus inhibited high concentrations of Zr. Any CaO in the melt would have similarly inhibited Zr saturation, but again, CaO does not seem to have been a significant component, as plagioclase appears to be relatively albitic and no other major calcium phases were identified. Zircon overgrowths would have begun forming shortly after intrusion of the melt simply because the presence of Fe_2O_3 would have inhibited high concentration of dissolved Zr were the melt peralkaline or in the event the melt was peraluminous, saturation levels would have been low regardless. Early formed zircon implies that the 950 Ma age reflects emplacement of the Rørstad granite.

Monazite

Sample LEA-10-1 also had abundant monazite, four of which were selected for analysis using ID-TIMS. The monazite crystals selected were all light yellow and subhedral to subrounded (e.g. Fig. 45). The long dimensions of monazite grains were 1/10 mm to 1/8 mm, with aspect ratios ranging from ~1 to ~2. The monazite grains ranged from -8.8% to 0.9% discordant and had common lead concentrations that ranged from 0.74 ppm to 14.60 ppm. Uranium concentration ranged from 4,528 ppm to 9,525 ppm (Appendix 3)

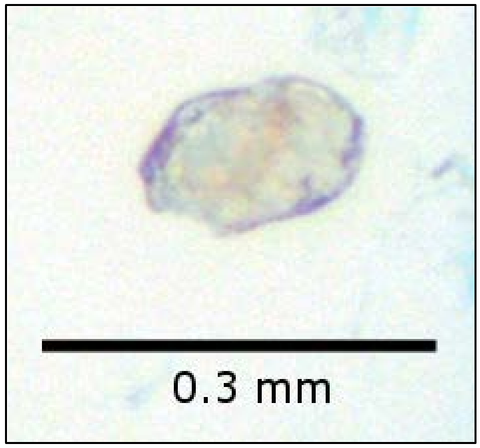

Figure 45 - Binocular photograph showing monazite crystal diagnostic of those found in sample LEA-10-1. Note yellow to brown color and subhedral morphology.

Two of the analyzed grains (307/22 and 307/28, Fig. 46), yielded similar $^{207}Pb/^{206}Pb$ ages of 929.1 ± 1.5 Ma and 935.3 ± 2.0 Ma, indicating a thermal event slightly younger than that recorded in the zircons from the same sample. The weighted mean of these two $^{207}Pb/^{206}Pb$ ages is 931 ± 38 Ma (Fig. 46), which agrees within error with the zircon age of 950.6 + 5.2/-5.3 obtained from this sample. The two remaining monazite analyses were from a rim and core (analyses 307/39 and 307/40, Figure 47) from a single crystal that broke during microscopic selection of minerals for analyses. This single crystal recorded ages that are older than all other ages determined in this study, with the core yielding a $^{207}Pb/^{206}Pb$ age of 987.7 ± 2.4 Ma and the rim yielding a $^{207}Pb/^{206}Pb$ age of 918.7 ± 2.5 Ma (see Appendix 3).

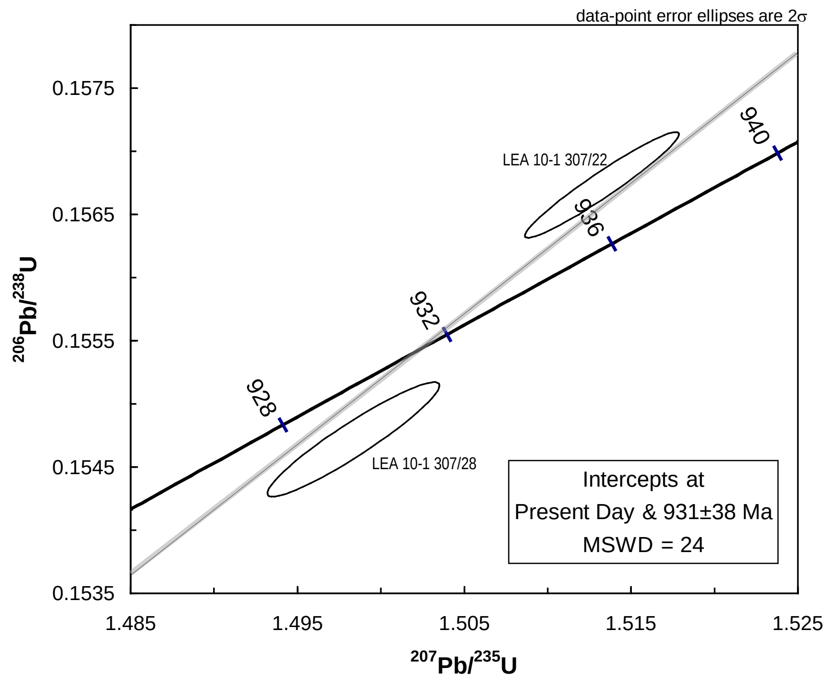

Figure 46 - U/Pb* Concordia diagram of monazite analyses 307/22 and 307/28 from rock sample LEA-10-1.

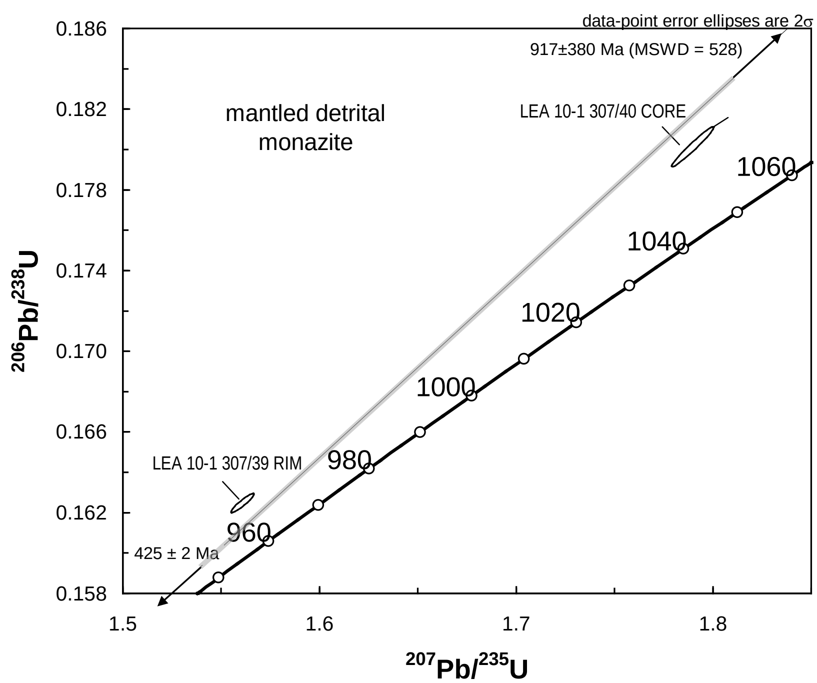

Figure 47 - U/Pb* Concordia diagram of monazite analyses 307/39 and 30/40 from sample LEA-10-1.

Interpreting monazite ages is often not straight forward, as individual grains may contain many compositional domains commonly interpreted to reflect episodic growth during distinct tectonothermal events (Williams, 2007). While the destructive nature of ID-TIMS precludes documenting compositional variation in the grains analyzed, the high-precision characterization of both the ^{238}U-^{206}Pb and ^{235}U-^{207}Pb decay series allows indirect examination of the complexity of the grain analyzed (Parrish, 1990). A large degree of discordance indicates the measurement of U and Pb from an admixture of compositional domains. The integrity of individual age determinations from LEA-10-1 monazites, therefore, suggest a more complicated thermal history than the zircon ages alone would suggest. The combined monazite and zircon ages for sample LEA-10-1 point to a series of thermal events at times not previously documented in rocks of northern Norway.

Fjærehesten Granite (Sample LEA-10-2)

Sample LEA-10-2 was collected from the Fjærhesten granite exposed at Durmålsvatnet (Fig. 37, Table 3) and contains zircon, rutile, and monazite, phases with potentially useful U-Pb* retention. A second population of small zircon inclusions within muscovite, called skating crystals (Frondel, 1990), was also measured, albeit in a non-traditional manner which is described in Appendix I. The variety of U-Pb phases makes sample LEA-10-2 especially important for understanding the temperature/time history of the Fjærehesten granite.

<u>*Zircon*</u>

The population of zircons analyzed from sample LEA-10-2 was characterized by clear, euhedral prismatic crystals with elongation ratios from 3 to 6. The crystals were all difficult to work with, breaking easily during mineral picking. As a result, grains in this population tended to be fragments, with complete crystals being comparatively rare. Zircons in the population are bipyramidal with well-developed {121} faces and subordinate {011} faces. All crystals are dominated by a strongly developed {010} prism. The zircons are most similar to the "S2" morphotype in Pupin's (1980) scheme, indicative of an aluminous monzogranite. Low uranium content (120-253 ppm) resulted in a lack of microscopically obvious radiation damage, despite relatively high discordance (from 3.6% to 11.2%). Common lead was low, ranging from 0.5 to 1.7 picograms. Analyzing the two most concordant zircons (307/9 and 311/18) (Fig. 48A) along with the zircon-in-muscovite inclusions (311/21 & 311/113) (Fig. 48B) yielded a concordia age 428.4 ± 1.2 Ma with a MSWD of 6.0 (Fig. 48B).

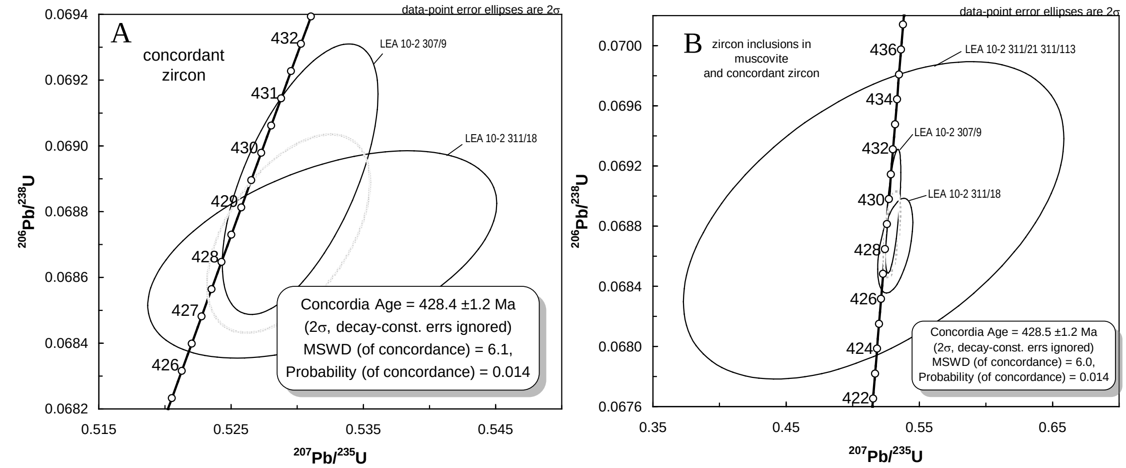

Figure 48 - U/Pb* Concordia diagrams for analyses from sample LEA-10-2:

A) Most concordant zircon grains from sample LEA-10-2 (307/9 and 311/18), records emplacement age of the Fjærehesten Granite at 428.4 ± 1.2 Ma.

B) All concordant zircons, including zircon skating crystal inclusions in muscovite.

Monazite

Three monazite crystals from sample LEA-10-2 were analyzed using ID-TIMS. The monazite crystals selected were all light yellow and subhedral to subrounded. The long dimensions of the grains were 1/10 mm to 1/8 mm, with aspect ratios ranging from ~1 to ~2, morphologically similar to the crystals found in sample LEA-10-1. Isotopic analysis of monazite grains in LEA-10-2 ranged from -0.1% to 4.3% discordant and had common lead concentrations that ranged from 0.63 ppm to 0.83 ppm. Uranium concentration ranged from 629 ppm to 997 ppm (Appendix 3). The three analyzed grains (311/103, 311/107, and 307/85), together yield a concordia age of 428.49 +/- 0.96 Ma

(MSWD = 0.22) (Fig. 49). The small uncertainty of this set of monazite crystal analyses is in agreement with the zircon grains analyzed from this sample.

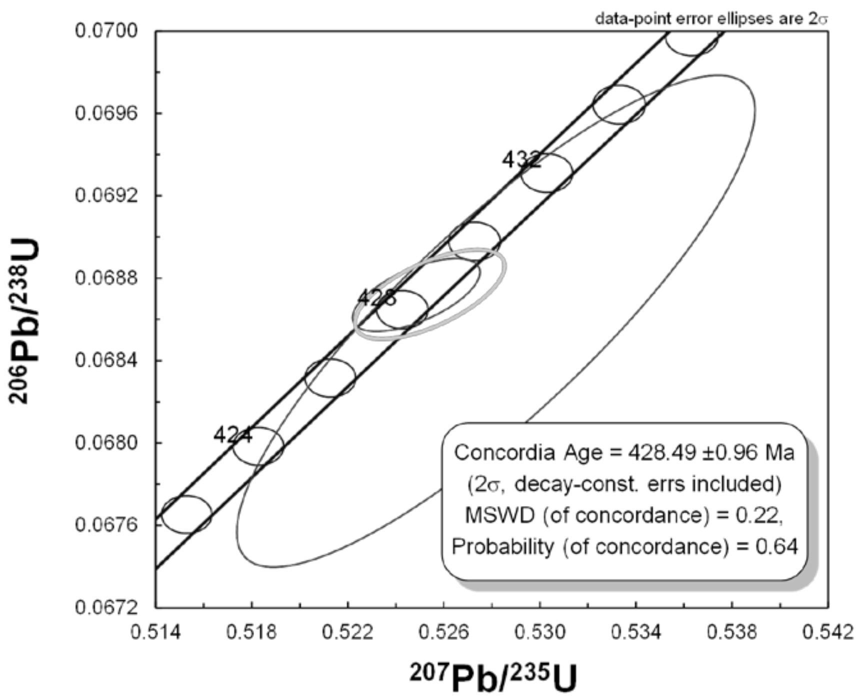

Figure 49 – ID-TIMS analysis of monazite grains from LEA-10-2 (311/103, 311/107, and 307/85), yielding a Concordia age of 428.49 ± 0.96 Ma.

Rutile

Three rutile crystals were selected from LEA-10-2, all of which were morphologically similar euhedral to subhedral crystals with a dark brown to gray color. Uranium concentration was low, from 6 to 35 ppm. Radiogenic Pb ranged from 1-5 ppm, with total common Pb measured ranging from 2.8 to 5.5 pg. There was a significant range in the ages determined from the measurements. The $^{238}U/^{206}Pb$ ages determined for the three crystals were all precise with uncertainties < 5.3 Ma, but they do not define a single age population that agree within uncertainty.

The ages reported, 469.8 ± 5.3, 458.4 ± 2.9 Ma, and 434.6 ± 3.8 (Fig. 50) all correspond with ages for tectonothermal events that are known or are suspected to have affected the rocks in the region (Barnes et al., 2007). The ~470 Ma age is broadly similar to a monazite chemical age described below, as is the ~458 Ma rutile age determined from sample LEA-10-2. The lack of agreement between the two older rutile ages makes confidently interpreting this age difficult. The younger ~434 Ma rutile age likely represents a rutile that grew during Scandian metamorphism. The ~470 age may record Grampian/Taconic metamorphism that has been documented in the rocks of the Helgeland Nappe Complex and ~458 Ma age may record a period of magmatism that is also recorded in the Helgeland Nappe Complex (Barnes et al., 2007).

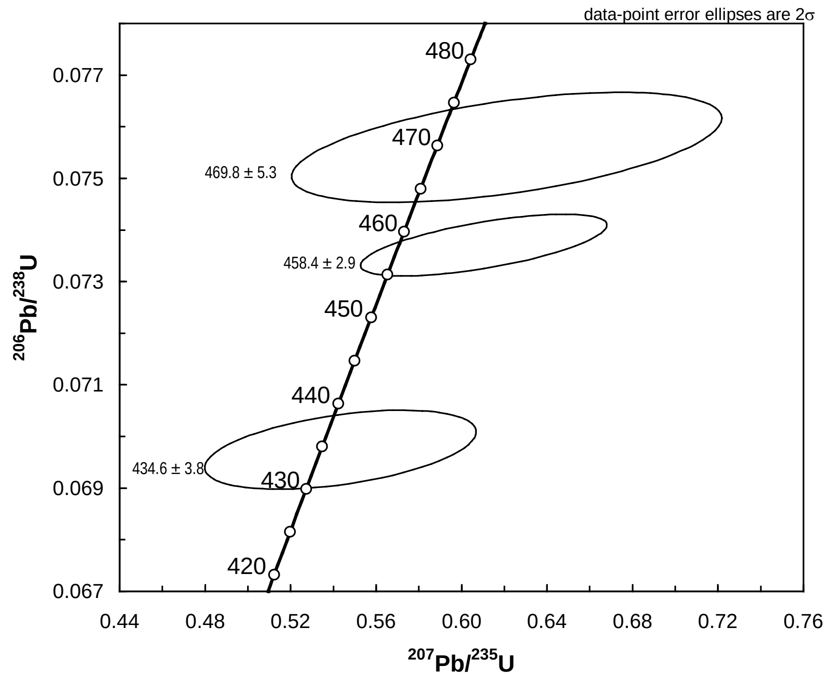

Figure 50 – $^{206}Pb/^{238}U$ vs. $^{207}Pb/^{235}U$ plot of three rutile crystals from sample LEA-10-2. Crystals do not represent a single family and are interpreted as representing distinct events.

Zircon 'Skating Crystals' in Muscovite

A conspicuous component present in the heavy mineral separates was a family of translucent muscovite with abundant euhedral zircon inclusions, referred to as skating crystals (Frondel, 1940), with elongation ratios < 6:1. Several muscovite crystals containing zircon skating crystals and also several pure muscovite crystals were dissolved, as if they were zircon. The pure muscovite and zircon-bearing muscovite crystals were similar in form and size apart from the zircon inclusions. Common Pb was measured in the pure muscovite portion and used to correct the Pb measured in the zircon-bearing portion. Any excess common Pb measured in the inclusion-bearing portion was assumed to be a result of the zircon inclusions. The skating crystals yielded an age of 429.4 ± 4.6 Ma (Fig. 51). This age places a maximum age constraint on the initiation of muscovite crystallization in the sample.

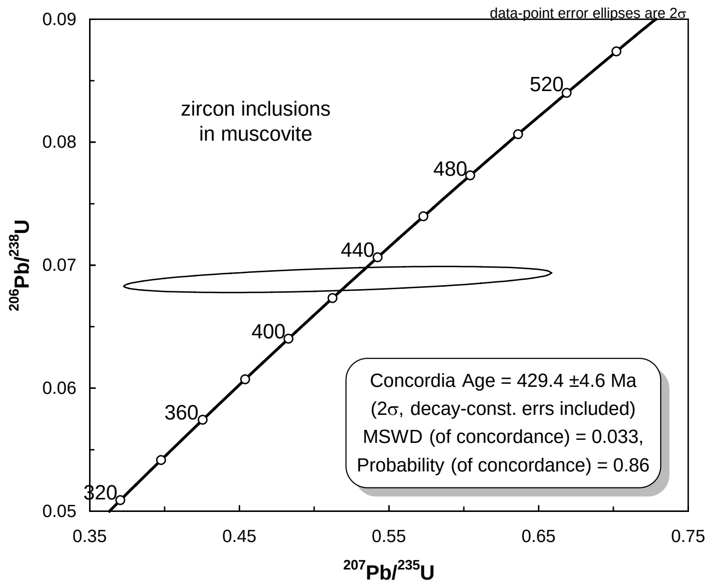

Figure 51 - U-Pb age concordia diagrams obtained for Scandian "skating crystals", zircon inclusions in muscovite, from the Durmålsvatnet Pluton. Sample LEA-10-2 (311/21 & 311/113).

Kjerringøy Paragneiss (Sample KJR-243)

Sample KJR-243 was collected from a pavement outcrop of migmatitic biotite gneiss 2 km west of the ferry at Misten (Fig. 37, Table 3). Zircons from the sample were easily separated into two families based on morphology, referred to as groups A and B (Fig. 52). Group A consisted of clear, euhedral to subhedral prismatic crystals with elongation ratios ranging from 2 to 8 and sporadic inclusions visible when viewed under a binocular microscope. Detrital cores are visible in SEM images (Fig. 53). Uranium content ranged from 88 to 1,800 ppm. Zircons in group A tend to be highly discordant, ranging from 9.8% to 17.3% discordant. Group A zircons belonged to the “S2” morphotype, indicating growth in an aluminous monzogranite (Pupin, 1980).

Although group A zircons are morphologically similar, they do not yield consistent ages. The $^{207}Pb/^{206}Pb$ ages determined range from 482.7 ± 4.0 Ma to 768.5 ± 11.9 Ma (Fig. 54). It is difficult to envision these as detrital grains inherited from the sedimentary protolith, as they show no sign of weathering, maintaining their euhedral form. It is probable that this group is complexly zoned in a way that was not readily identifiable under a binocular microscope. SEM backscattered electron images (e.g. Fig. 53) of zircon from this group do show complex zoning. The concordia diagrams for these samples and the spread of ages all suggest that the Group A zircons record more than one metamorphic event.

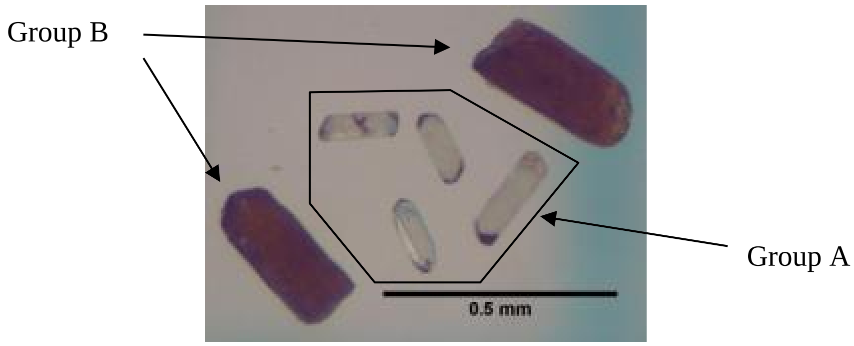

Figure 52 – Zircon crystals characterizing the two populations in sample KJR-243. Group A contains clear crystals and Group B contains large brown crystals.

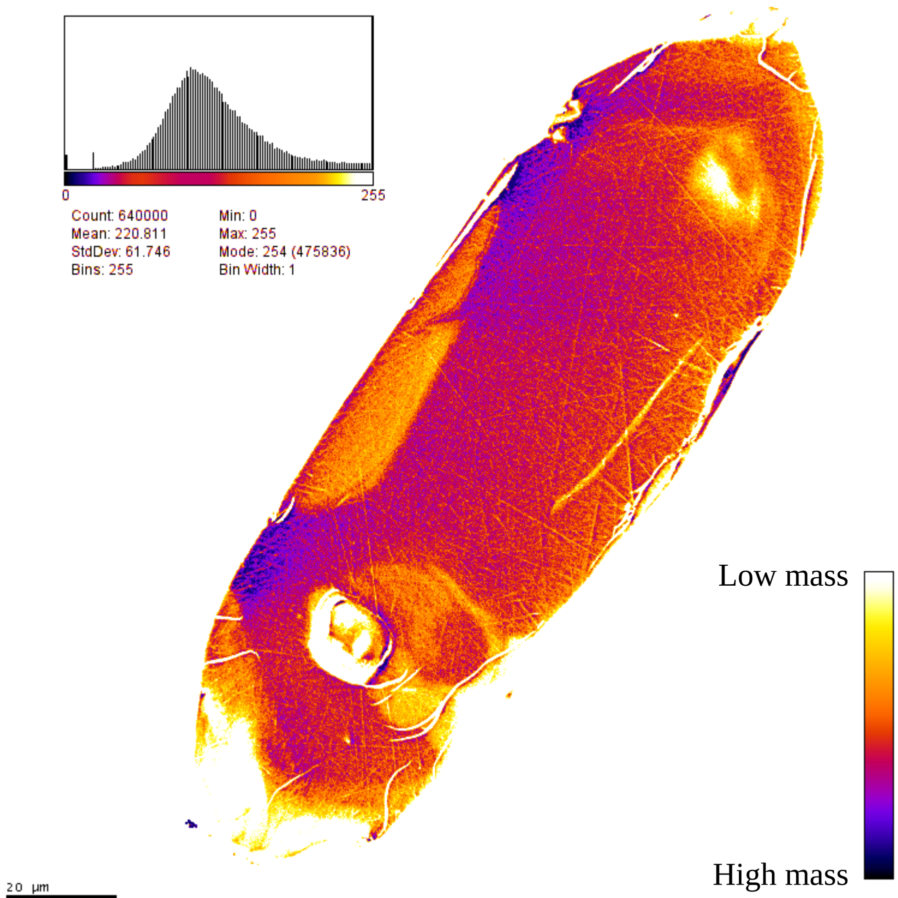

Figure 53 - SEM backscattered electron image of KJR-243 Group A zircon with high-uranium detrital cores mantled by igneous (anatectic) overgrowths. Histogram shows the mass distrubution in this zircon.

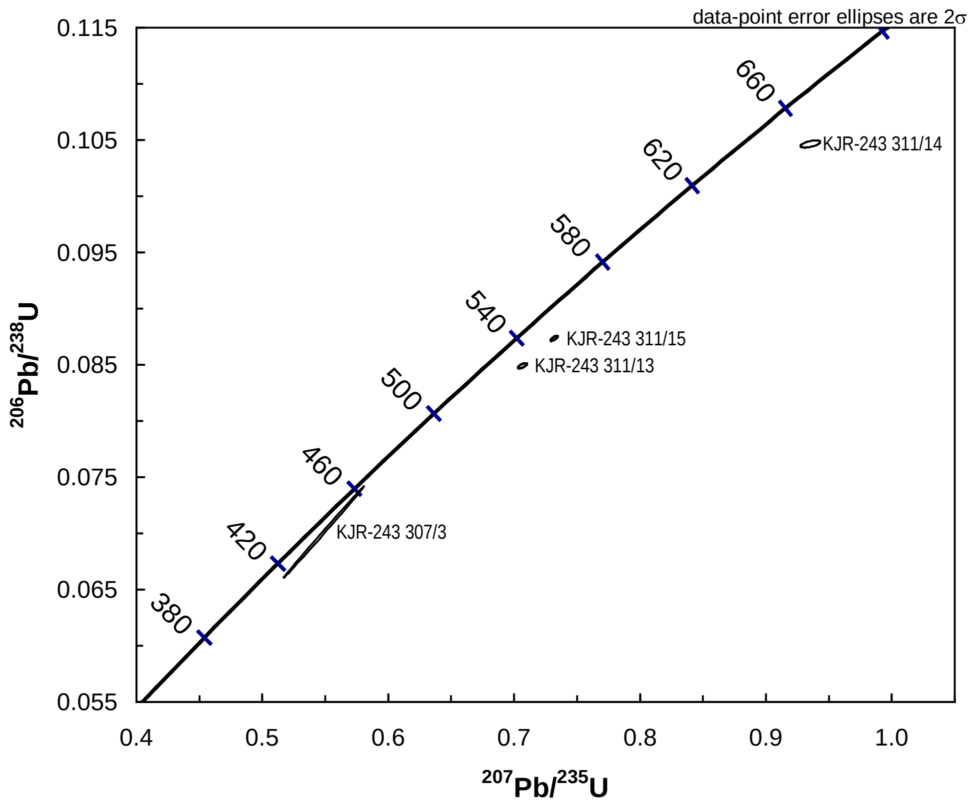

Figure 54 – U-Pb ages determined for Group A zircons from sample KJR-243. Group A zircons are discordant and do not define an isochron.

Corfu (2004) reported a similarly broad range of ages from a population of self-similar zircon and rutile from the Leknes Group that he suggested might represent a Sveconorwegian phase of metamorphism at ~1,000 Ma followed by two separate Palaeozoic phases at ~470 and ~460. Corfu (2004) stated that this thermal history is most simply explained by invoking the existence of an exotic Lofoten terrane juxtaposed via a Caledonian fault against the Baltican rocks of the Hinnøy-West Troms domain. Now that similar ages relations are documented for rocks in the current study area, perhaps future studies will document that these are geologically significant thermal events, and possibly that the Leknes Group correlate to the Uppermost Allochthon.

Group B zircons are clearly igneous in origin, belonging to Pupin's "S5" morphotype (1980). These zircons lack distinguishable cores (Fig. 55) and the generally euhedral grains have elongation ratios of 2-4, although complete crystals are comparatively rare. Group B zircons are uranium rich, with concentrations ranging from 2,722 to 20,268 ppm. While Group B zircons are highly concordant, with from 1.5% to 1.7% discordance, they do show anomalously low lead for the amount of uranium measured (Fig. 56). This may indicate protactinium partitioning during decay (Parrish and Noble, 2003) or simply lead loss due to damage to the crystal lattice. As such, a weighted average of $^{207}Pb/^{206}Pb$ ages of 431.49 ± 0.86 Ma is used as the most reliable age for this group (Fig. 57), as it is unaffected by disturbance of the U/Pb system.

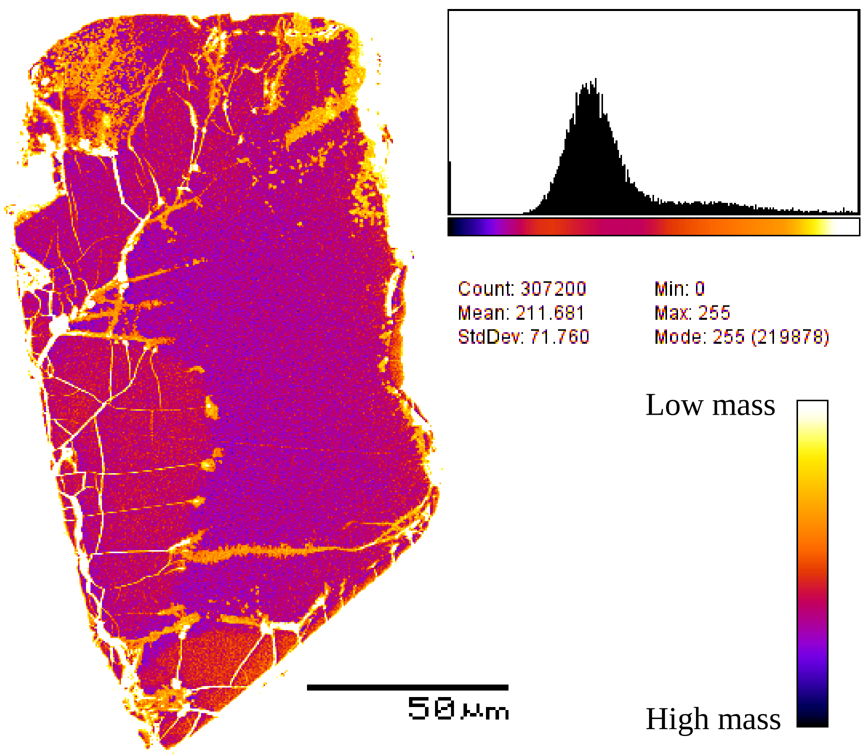

Figure 55 - SEM backscattered electron image of KJR-243 Group B zircon showing uniform growth and a lack of zoning. Lower mass is detected along fractures, presumably as a result of Pb having been leached along fracture surfaces. Histogram shows the mass distrubution in this zircon.

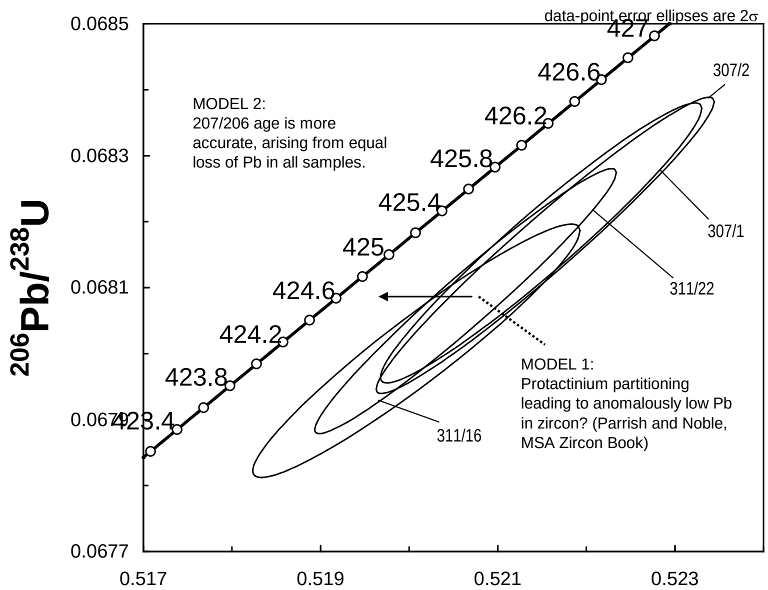

Figure 56 – U-Pb age concordia diagram for Group B zircons (307/1, 307/2, 311/16, 311/22) from sample KJR-243. Unusual discordance may indicate protactinium partitioning during decay (Parrish and Noble, 2003) or simple lead loss.

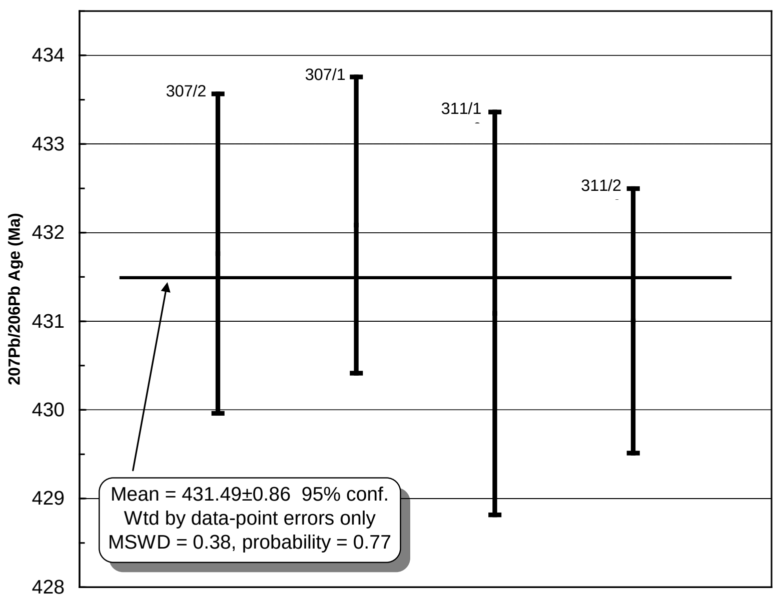

Figure 57 - Weighted average of 431.49 ± 0.86 Ma for $^{207}Pb/^{206}Pb$ ages obtained for Group B zircons (307/1, 307/2, 311/16, 311/22) from sample KJR-243.

$^{40}Ar/^{39}Ar$ Muscovite Dating

A single muscovite grain from garnet-muscovite-kyanite schist from the Kjerringøy paragneiss (sample KJR-093) was analyzed at the Auburn Noble Isotope Mass Analysis Laboratory using methods described by Steltenpohl et al. (2011). The crystal formed during D_3 mylonitization, belonging to a population of muscovite that share well-developed faces with garnet rims. $^{40}Ar/^{39}Ar$ incremental heating ages were determined for this single crystal. Results are shown in Appendix 4. The data define a scattered, disturbed spectrum with a plateau (Fig. 58). There is no obvious architecture to the spectrum, though most adjacent steps with overlapping ages fall between 390 and 387 Ma; i.e., the data do not define a curve, convex or concave. The sample has a weighted mean age of 392.0 ± 1.9 Ma (MSWD = 22, n = 27 steps).

For comparison, Steltenpohl et al. (2009) reported three $^{40}Ar/^{39}Ar$ muscovite cooling ages from the footwall of the Steigtinden shear zone in the Vatnvatnet area (Fig. 1), within the Heggmo Nappe. These ages ranged from ~410 Ma to ~385 Ma and were interpreted by Steltenpohl et al. (2009) to indicate the timing of extensional movement along the Steigtinden shear zone. While the source of the scatter in the data reported herein is not understood, the roughly weighted mean age of 390 Ma is interpreted to record broadly coherent cooling of rocks through the 350 °C isotherm (Hames and Bowring, 1994), which is comparable to regional trends following the Scandian event (Coker et al., 1995).

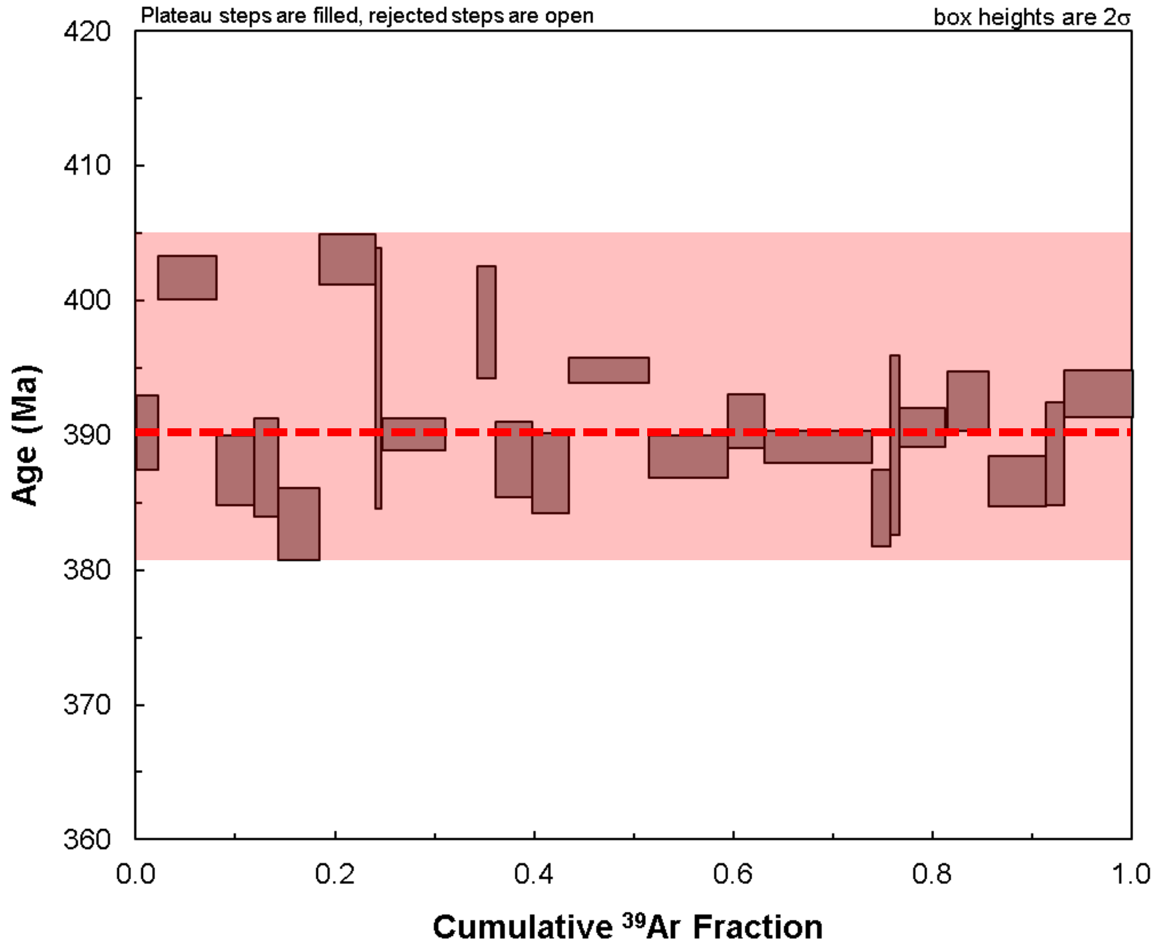

Figure 58 – Plateau at ~390 Ma (red dashed line) from muscovite separated from sample KJR-093. Minimum age of ~380 Ma and maximum age of ~405 Ma (shaded red area).

DISCUSSION

Heggmo Nappe

Agyei-Dwarko (2010) argued that the Rørstad granite and Kjerringoy paragneiss (Table 1, Plate 1) exposed at Bratten (Fig. 1) are overturned and are in thrust contact structurally above the Bodø Nappe. This study does not support the presence of a thrust fault in this position. Gustavson (1991) places the mica schist/calcsilicate contact several hundred meters to the east, where the present author believes the true boundary between the Heggmo and Bodø Nappes can be found. The current author interprets that Agyei-Dwarko's "Bodø Group" is in fact Kjerringøy paragneiss and that the contact with the "cover sequence" is actually an intrusive contact between the Rørstad granite and the Kjerringøy paragneiss that has been mylonitized. Similar tectonized intrusive contacts are abundant along the margins of the Tårnvika pluton.

It is also difficult to reconcile the Kjerringøy paragneiss and Rørstad granite being thrust above the Bodø Nappe as the Bodø Nappe appears to have been emplaced by the FOSZ, an extensional structure that otherwise shows no evidence of contractional strains. If the mylonite exposed at Bratten is a late thrust, then why is there no other evidence of this late compression? If the Heggmo Nappe/Bodø Nappe boundary is east of Bratten, as the present author contends, then the pressure/temperature conditions of 8.1 kbar and 750 °C as estimated by Agyei-Dwarko (2010) would in actuality be estimates for the Kjerringøy paragneiss. Agyei-Dwarko's geothermobarometric analyses yielded a lower pressure (8.1 kbar < 9.5 kbar) and higher temperature (750 °C > 672 °C) than the estimates derived by the present author (Fig. 36). This may reflect thermal imprint at lower pressures related to the intrusion of the Rørstad granite near where Agyei-Dwarko's sample was collected.

The present author interprets the Bratten gneisses to be part of the sheared and appressed limb shared between the Heggmovatn antiform and the Landegodefjorden synform (Plate 1, Plate 2). The following interpretation provides a simpler explanation for the observations made in the field area and is in keeping with the deformational history observed in the rocks.

Tectonic Provenance of the Heggmo Nappe

Early Neoproterozoic (Tonian) intrusions within the Heggmo Nappe make it distinct from all other allochthons in the Caledonides of Norway. The Landegode, Bratten, and Tårnvika megacrystic granites all have broadly similar ages of 946 ± 5 Ma (Augland et al., 2013), 924.8 ± 7.4 Ma (Agyei-Dwarko, 2010) , and 950.6 ± 5.3 Ma (this study), respectively. The Tonian ages reported in this study are similar to those reported throughout the North Atlantic region and held to represent a single event, the Valhalla orogeny (Cawood et al., 2010). This North Atlantic record of tectonothermal activity is commonly associated with a later phase of Ordovician-Silurian plutonism or metamorphism. Strachan et al. (1995) report U/Pb SHRIMP ages for what they consider to be a Grenvillian metamorphic event occurring at 955 ± 13 Ma recorded in northeast Greenland. Strachen et al. (1995) also report later metamorphic growth of zircon at 445 ±

10 Ma. Watt et al. (2000) report a U/Pb SHRIMP determination on the emplacement age of 938 ± 13 Ma for an undeformed granite in the Stauning Alper and Nathorst Land regions in northeast Greenland. Anatexis at 420 ± 8 Ma was found in rocks of the same area. Kalsbeek et al. (2000) have documented high-grade metamorphism at 950-920 Ma in rocks in Andréeland, East Greenland, intruded by plutons ranging from 436 to 430 Ma. Tonian\Ordovician-Silurian fingerprints are also reported in Svalbard's Northwestern Terrane, where ~958 Ma orthogneisses are cut by an undeformed granite with an age of 420.2 ± 3.4 Ma (Pettersson et al., 2009). Metamorphism at 938-925 Ma also affected rocks of the Shetland Islands, which are overprinted by Caledonian metamorphosm (Cutts et al., 2009).

All of the metasediments intruded by the North Atlantic Tonian intrusives belong to the Krummedal Group of northeast Greenland, or its equivalents (Strachen et al., 1995; Kalsbeek et al., 2000; Watt et al., 2000; Cutts et al., 2009; Pettersson et al., 2009; Agyei-Dwarko, 2010). A thorough discussion of the similarities between the rocks found in the Heggmo Nappe and the Krummedal Group is reported by Agyei-Dwarko (2010). The 956-945 Ma age for the Rørstad granite (Fig. 44), the 428.5 ± 1.2 Ma emplacement age for the Durmålsvatnet pluton (Fig. 48A), and the Krummedal Group-equivalent host-lithology reported in this study firmly associates the rocks of the study area with those reported throughout the conjugate hinterland regions of the North Atlantic Caledonides.

It is important to note that the two nearest exposures of undeniably Baltic basement have a very different thermochronological history than that of the Heggmo Nappe. The central Nordland basement windows, ~70 km to the southwest (Figure 1 inset and Fig. 4), were determined by Skår (2002) to have emplacement ages ranging from

1800 to 1795 Ma, which is diagnostic for Sveccofennian basement that fingerprints much of Baltica. The Sommerset window, only 22 km due east from Tårnvika (Fig. 4), exposes a heterogeneous and coarse-grained granite with an age of ~1720 Ma (Romer et al., 1991). Neither of these exposures contain Caledonian intrusions, which is a typical signal of the Baltic basement. The longstanding interpretation of the Heggmo Nappe granites and orthogneisses as representing Baltic basement (Rutland and Nicholson, 1965; Nicholson and Rutland; 1969; Bennet, 1970; Wilson and Nicholson, 1973; Cooper and Bradshaw, 1980; Thelander et al., 1980; Cooper, 1985; Gustavson and Blystad, 1995; Gustavson, 1996) is untenable in light of the new geochronology that documents vastly contrasting intrusive histories.

It is also now well-established that some rocks in the Uppermost Allochton have a significant pre-Scandian history of deformation and plutonism that overlaps in time with the Taconic event in eastern North America (Roberts, 2002; Barnes et al., 2007). This study reports U/Pb rutile ages that range from 475 to 456 Ma for the Durmålsvatnet pluton (Fig. 50) and a monazite chemical age of 469.2 ± 2.3 Ma for the Kjerringøy paragneiss, in agreement with Augland et al.'s (2013) report of migmatization in the rocks of Landegode/Bratten (Fig. 1) at ~459 Ma. Farther south, Barnes et al. (2007) report migmitization of the Horta nappe in Helgeland (Fig. 1) after ~478 Ma, followed by periodic magmatic activity lasting into the Silurian. These pre-Scandian relics are taken as evidence for Grampian/Taconian activity traditionally associated with the northern Appalachians, Scotland, and the Caledonides of northeast Greenland (Roberts et al., 2007, Leslie et al., 2008). The current author interprets the Heggmo Nappe to have been migmatized during the Grampian orogeny on the Laurentian margin of Iapetus.

Model A: Scandian Emplacement of the Heggmo Nappe

The discovery of Grampian/Taconian deformation in the rocks of the Heggmo Nappe begs the question as to how exactly it was emplaced structurally below the Rödingsfjället Nappe in the established tectonostratigraphy for the area (Cooper, 1978; Zeltner, 2001; Agyei-Dwarko, 2010). The traditional "Scandian nappe stacking" model (Roberts and Gee, 1985) does not adequately explain the relationship between these two nappes because it requires eastward emplacement of allochthons onto Baltica along tops-up-to-east, west-dipping thrust faults. Evidence for such structures has not been observed in the study area. Indeed, the earliest-formed structures observed in the study area are generally overturned to the west, at odds with traditional Scandian thrust-and-fold vergence. The Vågfjellet and Løding faults to the south of the study area have previously been interpreted as tops-up-to-east, west-dipping thrust faults (Gustavson and Blystad, 1995; Zeltner, 2001) on which the Rödingsfjället Nappe was emplaced onto the Scandian nappe stack. Despite this interpretation, the current author was unable to find reports in the literature or evidence in the field to support these faults as being thrust faults.

Analysis of the Vågfjellet and Løding faults via three-point problem determination of the orientation along the fault (Fig. 21) shows that the planes of both faults dip to the east, not to the west. Earlier interpretations of these faults as west-dipping and tops-up-to-the-east thrust faults was heavily influenced by the traditional model of Roberts and Gee (1985) that requires the existence of such faults on which the Scandian allocthons were emplaced onto Baltica. There is no doubt that such allochthon-emplacing faults exist in the region, but they are not found in the study area and must, therefore, surface farther to the east. In short, the observed east-dipping, west-vergent geometry of structures in the study area is difficult to reconcile with their being the result of solely east-vergent Scandian nappe tectonics.

Model B: A Taconian Nappe Stack Emplaced as a Single Unit Onto Baltica in the Scandian Event

Given the pre-Scandian tectonothermal and intrusive history and the structural geometry that has been shown to exist in the rocks of the Heggmo Nappe, it stands to reason that at least some, if not at all, of the structures observed in the field area are pre-Scandian in origin. Precedent for such pre-Scandian structures in the Uppermost Allochthon was set by Barnes et al. (2007), who documented east-dipping, tops-to-west faults and pre-Scandian metamorphism and magmatism in the Helgeland Nappe Complex to the south of the study area. Presuming that the structural style documented in the Helgeland area (see inset on Figure 1) extends north into the study area, a simpler explanation for the observed topographic traces of the Vågfjellet and Løding faults (Fig. 21) is that they are in fact tops-up-to-west, east-dipping imbricated thrust faults above which the the Heggmo Nappe was emplaced from the east. Presumably this was the result of an event equivalent to the accretion of the Taconic Arc during the Grampian orogeny in east Greenland (Leslie et al., 2008). This exotic-to-Baltica terrane was then deformed as a single unit when it was emplaced onto the rocks of the Upper Allochthon in the Scandian orogeny.

The current author interprets the Heggmo Nappe to have been migmatized during the Taconic/Grampian event on the Laurentian margin of Iapetus, and later thrust-emplaced eastwards onto Baltica during the Scandian orogeny. Subsequent east-west compression caused it to be folded into the F_2 Heggmovatn antiform and Steigtinden synform. The composite allochthon later was orphaned onto Baltica when the North Atlantic basin began to form in the Eocene.

Fjær-Osvika Shear Zone

Structures recording late- to post-Scandian orogenic collapse have been identified throughout the Norwegian Caledonides (Fossen, 1992, 2010; Fossen and Rykkelid, 1993), with studies generally focused on specific areas: Loften and northern Norway (Steltenpohl and Bartley, 1993; Coker et al., 1995; Northrup, 1996; Klein et al., 1999; Zeltner, 2001; Steltenpohl et al., 2004, 2009, 2011; Mager, 2005), central Norway (Braathen et al., 2002; Osmundsen et al., 2003), and southern Norway (Andersen and Jamtveit, 1990; Walsh et al., 2007). Prior work has shown broad agreement in the timing of extension (Devonian), but a wide range in the structural setting in which the extensional detachments occurred. In southwestern Norway, eclogite facies Baltic basement rocks in the footwall are juxtaposed against unmetamorphosed Devonian sediments in the hanging wall (Andersen and Jamtveit, 1990). The northernmost detachment faults in the Lofoten region involve amphibolite-facies rocks in both the hanging wall and the footwall and no Devonian sediments are preserved (Steltenpohl et al., 2011). The shear zones between the upper and lower plates also are much thinner in north Norway (hundreds of meters) than in southern Norway (thousands of meters) (Osmundsen et al., 2003; Steltenpohl et al., 2011; this study)

North of the study area Steltenpohl et al. (2011) have described the Eidsfjord shear zone, a low-angle, mylonitic, tops-west normal detachment fault that places migmatitic gneiss and anorthosite in the hanging wall against mangerite in the foot wall. $^{40}Ar/^{39}Ar$ age determinations show it was deforming/recrystallizing at 403.6 ± 1.1 Ma. The authors interpret this to be Norway's northernmost expression of the Early Devonian detachment system.

The Fjær/Osvika shear zone is geometrically similar to the Eidsfjord shear zone (Steltenpohl et al., 2011). Both the FOSZ and the Eidsfjord detachment are corrugated, or scoop-shaped faults that dip toward the Caledonian hinterland and exhibit normal tops-down-to-the-northwest movement. Both shear zones have mylonitic boundaries a few hundred meters thick and are cut by brittle, high-angle Mesozoic to Tertiary normal faults.

There are some significant differences between the Eidsfjord detachment and the FOSZ, however. The Eidsfjord detachment fault is closer to the boundary between continental and oceanic crust than any of the other Devonian normal faults in Norway (Steltenpohl, 2011), occurring roughly 60 km to the east of the boundary found offshore. The FOSZ is at least 200 km from this boundary, separated from it by the highly extended Vestfjord basin and the Lofoten terrane (Steltenpohl et al., 2004). The Eidsfjord detachment contains an abundance of consipicuous pseudotachylite veins, which are not seen in the FOSZ.

Regional correlations of the Bodø Nappe imply that the FOSZ detachment system in this part of Norway is signicantly larger than previously thought. Workers have suggested the rocks of the Bodø Nappe (Rutland and Nicholson, 1965; Cooper, 1978) are correlative with those of the Govdistind unit, which Tørudbakken and Brattli (1985) refer to as the Kovstind unit while others call it the Vegdal Group (Hollingworth et al., 1960; Rutland and Nicholson, 1965; Cooper, 1978). Tørudbakken and Brattli (1985) describe the Govdistind unit as a large synformal body with a high-strain zone as its lower boundary and that it cuts discordantly downward through the underlying units from south to north. Gustavson and Gjelle (1991) placed the Kovstind at the top of the Beiarn Nappe.

Relations mapped in the field and extended using aerial photographs (e.g., Fig. 59) and satellite imagery suggest that the Caledonian Fjærhesten granite in the area forms large sills that mimic the shape of the Steigtinden-Kjerringøy synform (Plate 2). The granite may have functioned as a competent buttress unit providing a slip horizon for the observed extensional motion. It is noted that nowhere is the Fjærhesten granite observed to cut the Fjær-Osvika/Steigtinden shear zone, but it is commonly juxtaposed against it.

The observed hinterland plunging synformal hanging wall of the FOSZ, the mylonitic boundary, the late timing of deformation as determined through $^{40}Ar/^{39}Ar$ geochronology, and the similarity to well-studied structures in the area suggest that the Fjær/Osvika shear zone is a late-Scandian low-angle normal fault.

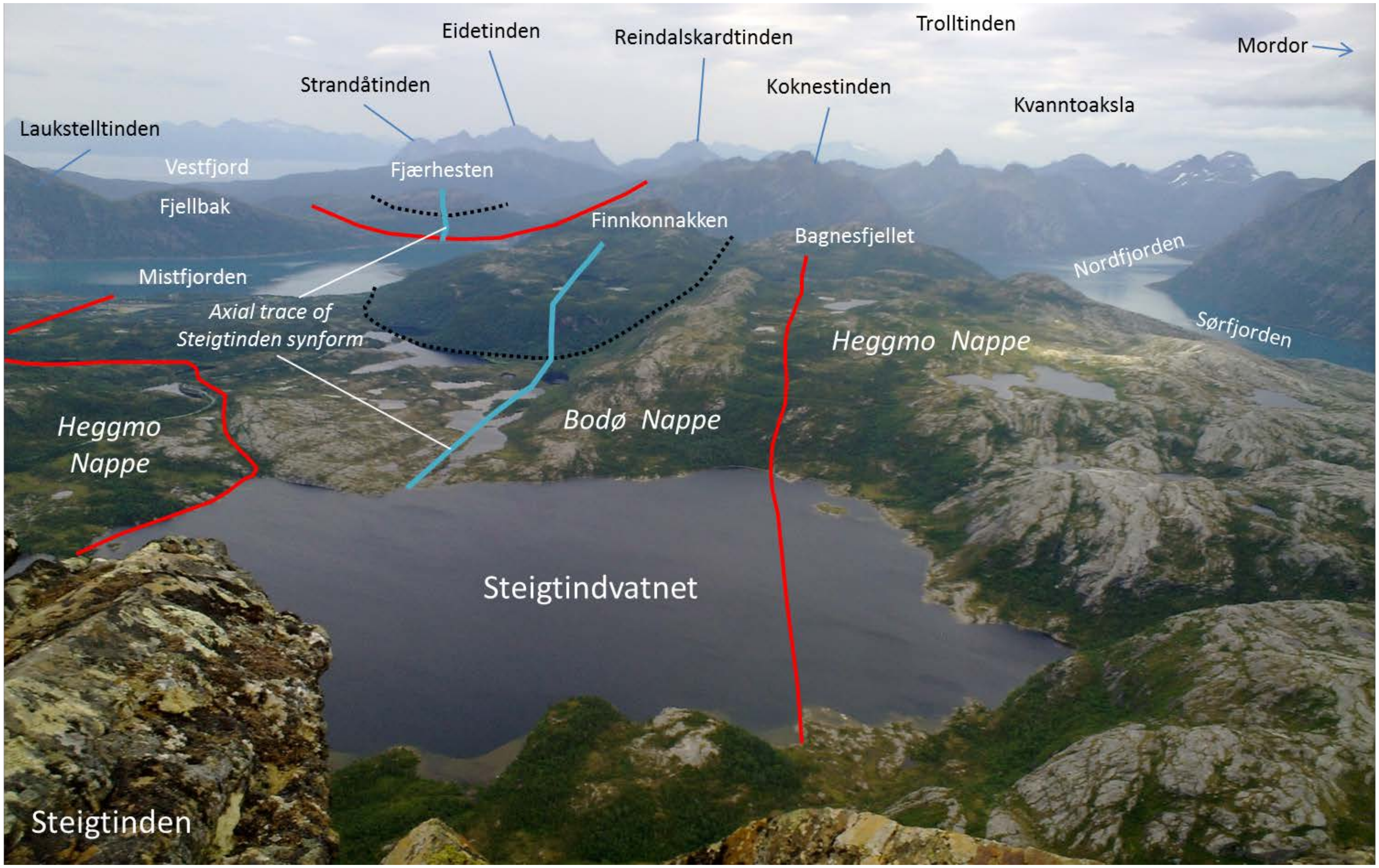

Figure 59 - Annotated photograph taken from the summit of Steigtinden, looking north towards Kjerringøy. Italicized labels refer to geological features in the photo. For scale, Steigtindvatnet is roughly 1.6 km wide at the widest point in the photograph. Photo courtesy of John Pedersen, www.turbading.com.

CONCLUSIONS

The oldest rock unit in the Heggmo Nappe is the Kjerringøy paragneiss, the protolith of which was likely deposited in the Mesoproterozoic Asgård Sea along the extended passive margin of northeastern Laurentia (Fig. 60A). The depositional setting in this basin varied spatially through time, with the accumulation of limestones, sandstones, mudrocks, and volcanics. This basin received abundant detrital material from the Grenville orogen to the south and a minor amount of Archaean material from the Laurentian shield to the west. Maximum and minimum ages of detrital zircons deposited in the basin and the cross-cutting Rørstad granite indicate that deposition was active in the period from ~1050 Ma to ~950 Ma (Fig. 60B).

The Kjerringøy paragneiss was intruded by the Rørstad granite at 950-930 Ma contemporaneous with F_{0V} isoclinal folding (Fig. 60B). This magmatism and deformation appears to have been the result of a change in the rotation of Baltica relative to the Laurentian shield during the breakup of Rodinia, known as the Valhalla orogeny. The Valhalla orogeny was accompanied by late intrusion of dioritic dikes and felsic aplites and appears to have happened in pulses, with a phase of metamorphism occurring around 920 Ma.

Following the Valhalla orogeny, the Laurentian and Baltican cratons began to separate, creating a series of extensional basins that paralleled the Valhallan orogenic welt. Subsidence in the rocks of the study area had begun by 900 Ma, by which time

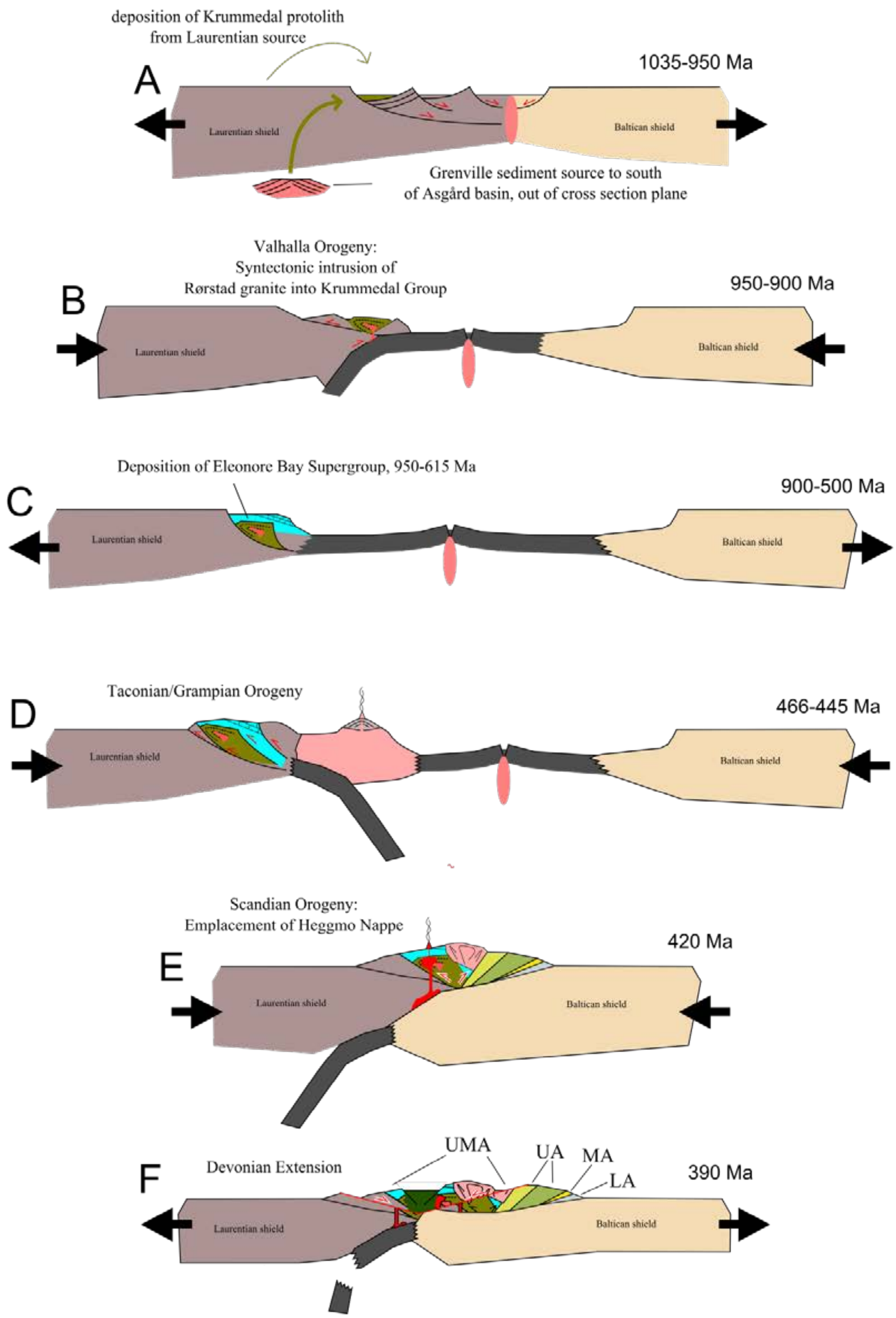

Figure 60 - Schematic diagrams showing the evolution of the Heggmo Nappe from the Neoproterozoic to the Devonian. UMA = Uppermost Allochthon, UA = Upper Allochthon, MA = Middle Allochthon, LA = Lower Allochton.

deposition of the Eleonore Bay Supergroup had begun, directly on the rocks of the Krummedal sequence (Fig. 60C) (Sønderholm et al., 2008).

The Heggmo Nappe was metamorphosed around 470 Ma during the Taconian/Grampian orogeny, reaching kyanite-grade conditions of amphibolite facies metamorphism (Fig. 60D). Some structural levels in the Kjerringøy paragneiss were migmitized at this time. This event may have involved the collision with Laurentia of a volcanic arc formed above a subduction zone dipping away from Laurentia. The prominent S_1 gneissosity and schistosity found throughout the study area developed at this time, along with tight-to-isoclinal F_1 folds. The Rödingsfjället Nappe was emplaced via the Vågfjellet fault at this time. Late Taconian/Grampian deformation produced S_1 S-planes.

The Kjerringøy paragneiss and orthogneiss were part of the overriding Laurentian plate during the Scandian orogeny (Fig. 60E) and were intruded by the ~430 Ma Fjærhesten granite. There does not appear to have been a great deal of mineral growth associated with this event beyond that associated with crystallization of the Fjærhesten granite and the recrystallization of muscovite, which resulted in L_2 length-preferred muscovite lineation and the S_2 foliation. Deformation associated with this event is most strongly expressed as regional, open-cylindrical F_2 folds that plunge to the southwest in the study area, particularly the Steigtinden and Tårnvikfjellet synforms. Outcrop scale F_2 folds are commonly overturned to the west, likely as a result of their formation on the Laurentian side of the Scandian orogeny.

It is unclear exactly when in the Devonian that extensional collapse of the orogenic welt began in the rocks of study area (Fig. 60F). Extension along the FOSZ continued, however, some 30-40 Ma after intrusion of the Fjærhesten granite. It is likely that the Fjærhesten granite acted as a competent buttress unit provding a slip horizon for the tops-down-to-the-west normal movement. This unfoliated intrusion mimics the trend of the S_3 mylonitic shear zone in places which is folded into the F_3 Kjerringøy synform. A $^{40}Ar/^{39}Ar$ M_2 muscovite cooling age shows that the FOSZ likely had been active prior to ~390 Ma. D_3 deformation is characterized by F_3 sheath folding, plastic flow folding, and mylonitization. Outcrop scale D_3 deformation is almost exclusively found within the Bodø Nappe, with the Heggmo Nappe showing D_3-effects only proximal to the FOSZ.

The youngest structures seen in the study area are part of a regional set of Mesozoic to Tertiary F_4 brittle normal faults associated with the breakup and dispersal of Pangaea and the opening of the North Atlantic. This D_4 deformation is expressed as low displacement (< 100 m) southwest/northeast-trending subvertical faults, commonly with veining and hydrothermal alteration along the fault planes. D_4 deformation cuts all older structures and is found in both the Heggmo and Bodo Nappes. The precise age of this deformation in the study area is unknown.

REFERENCES CITED

Agyei-Dwarko, N.Y., 2010, Basement – cover relationships in the Bodø area, The "basement" rocks in the Heggmovatn and Bodø areas: a Fennoscandian, Laurentian or suspect terrane? [M. Sc. thesis]: University of Oslo, 155 p.

Andersen, T.B., and Jamtveit, B., 1990, Uplift of deep crust during orogenic extensional collapse: A model based on field studies in the Sogn-Sunnfjord Region of western Norway: Tectonics, v. 9, p. 1097-1111.

Andersen, T.B., Jamtveit, B., Dewey, J.F., and Swensson, E., 1991, Subduction and eduction of continental crust: major mechanisms during continent-continent collision and orogenic extensional collapse, a model based on the south Norwegian Caledonides: Terra Nova, v. 3, p. 303-310.

Andresen, A., Augland, L.E., and Agyei-Dwarko, N., 2011, The Landegode-Heggmovatn "basement terranes"- fragments of the Laurentian Grenville Orogen in the Scandinavian Caledonides?: Geophysical Research Abstracts, v. 13, EGU2011.

Andresen, A., and Tull, J.F., 1983, The age of the Lødingen granite and its possible regional significance: Norsk Geologisk Tidsskrift, v. 63, p. 269-276.

Asklund, B., 1955, Norges geologi och fjällkedjeproblemen: Stockholm. Geol. För. Förh. v. 77 p. 185-203.

Augland, L.E., Andresen, A., Corfu, F., Agyei-Dwarko, N.W., Larionov, A.N., 2013, The Bratten-Landegode gneiss complex: a fragment of Laurentian continental crust in the Uppermost Allochthon of the Scandinavian Caledonides, in Corfu, F., Gasser, D., and Chew, D.M., eds., New Perspectives on the Caledonides of Scandinavia and Related Areas, Geological Society, London, Special Publication 390, p. unknown.

Barnes, C.G., Frost, C.D., Yoshinobu, A.S., McArthur, K., Barnes, M.A., Allen, C.M., Nordgulen, Ø., and Prestvik, T., 2007, Timing of sedimentation, metamorphism, and plutonism in the Helgeland Nappe Complex, north-central Norwegian Caledonides: Geosphere, v. 3, p. 683-703.

Bennet, J.D., 1970, The structural geology of the Saura region, Nordland: Norges Geologiske Undersøkelse, n. 264, p. 1-86.

Bingen, B., Nordgulen, Ø., and Viola, G., 2008, A four-phase model for the Sveconorwegian orogeny, SW Scandinavia: Norwegian Journal of Geology, v. 88, p. 43-72.

Bogdanova, S.V., Bingen, B., Gorbatschev, R., Kheraskova, T.N., Kozlov, V.I., Puchkov, V.N., and Volozh, Y.A, 2008, The East European Craton (Baltica) before and during the assembly of Rodinia: Precambrian Research, v. 160, p. 23-45.

Bohlen, S.R., Wall, V.J., Boettcher, A.L., 1983, Experimental investigations and geological applications of equilibria in the system FeO-TiO_2-Al_2O_3-SiO_2-H_2O: American Mineralogist, v. 68, p. 1049-1058.

Braathen, A., Osmundsen, P.T., Nordgulen, O., Roberts, D., and Meyer, G. B., 2002, Orogen-parallel extension of the Caledonides in northern Central Norway: an overview: Norsk Geologisk Tidsskrift, v. 82, n. 4, p. 225-242.

Carter, B.T., 2000, Geological investigations in Steigen-Engeløya, north-central Norway (68° N) and their significance for tectionic evolution [M.Sc. thesis]: Auburn University, 135 p.

Cawood, P.A., Nemchin, A.A., Smith, M., and Loewy, S., 2003, Source of the Dalradian Supergroup constrained by U-Pb dating of detrital zircon and complications for the East Laurentian margin: Geological Society [London] Journal, v. 160, p. 231–246.

Cawood, P.A., Nemchin, A.A., Strachan, R., Prave, T., and Krabbendam, M., 2007, Sedimentary basin and detrital zircon record along East Laurentia and Baltica during assembly and breakup of Rodinia: Journal of the Geological Society, London, v. 164, p. 257-275.

Cawood, P.A., Strachan, R., Cutts, K., Kinny, P.D., Hand, M., and Pisarevsky, S., 2010, Neoproterozoic orogeny along the margin of Rodinia: Valhalla orogen, North Atlantic: Geology, v. 38, p. 99-102.

Claesson, S., 1980, Pre-Silurian orogenic deformation in the north-central Scandinavian Caledonides: Geologiska Föreningens I Stockholm Förhandlingar, v. 101 [for 1979], p. 353-356.

Coker, J.E., Steltenpohl, M.G., Andresen, A., and Kunk, M.J., 1995, An $^{40}Ar/^{39}Ar$ thermochronology of the Ofoten-Troms region: Implications for terrane amalgamation and extensional collapse of the northern Scandinavian Caledonides: Tectonics, v. 14, p. 435-447.

Cooper, M.A., 1978, The geology and geochemistry of the Sørfold area, N. Norway [Ph.D. thesis]: Bristol, University of Bristol, 331 p.

Cooper, M.A., 1980, Geological Map of Kjerringöy: Norges Geologiske Undersøkelse, scale 1:50 000, 1 sheet.

Cooper, M.A, 1985, Deformation patterns and their evolution in the Caledonides of the Sørfolda area, north Norway, *in* Gee, D.G., and Sturt, B.A., eds., The Caledonide Orogen – Scandinavia and Related Areas: John Wiley & Sons, p. 543-551.

Cooper, M.A., and Bradshaw, R., 1980, The significance of basement gneiss domes in the tectonic evolution of the Salta Region, Norway: Journal of the Geological Society, London, v. 137, p. 231-240.

Corfu, F., 2004, U-Pb Age, Setting and Tectonic Significance of the Anorthosite-Mangerite-Charnockite-Granite Suite, Lofoten-Vesterålen, Norway: Journal of Petrology, v. 45, p. 1799-1819.

Corfu, F., Hanchar, J.M., Hoskin, P.W.O., Kinny, P., 2003, Atlas of zircon textures, *in* Hanchar, J.M. and Hoskin, P.W.O., eds., Reviews in Mineralogy and Geochemistry, Volume 53, Zircon: Washington, D.C., Mineralogical Society of America, p. 468-500.

Cutts, K.A., Hand, M., Kelsey, D.E., Wade, B., Strachan, R.A., Clark, C., and Netting, A., 2009, Evidence for 930 Ma metamorphism in the Shetland Islands, Scottish Caledonides: implications for Neoproterozoic tectonics in the Laurentia-Baltica sector of Rodinia: Journal of the Geological Society, London, v. 166, p, 1033-1047.

Davis, D.W., Blackburn, C.E., and Krogh, T.E., 1982, Zircon U-Pb ages from the Wabigoon-Manitou Lakes region, Wabigoon Subprovince, northwest Ontario: Canadian Journal of Earth Sciences, v. 19, p. 254-266.

de Ferranti, J., 2013, Viewfinder Panoramas – Digital Elevation Data: http://www.viewfinderpanoramas.org/dem3.html (accessed November 2, 2012).

Deer, W.A., Howie, R.A., and Zussman, J., 1996, An Introduction to the Rock-Forming Minerals (2nd Edition): Essex, Pearson Education Limited, 696 p.

Dewey, J.F., Strachan, R.A., 2003, Changing-Silurian-Devonian relative plate motion in the Caledonides: sinistral transpression to sinistral transtension: Journal of the Geological Society, London, v. 160, p. 219-229.

Dickin, A.P., 2005, Radiogenic Isotope Geology: Cambridge, Cambridge University Press, 492 p.

Dodson, M.H., 1973, Closure temperature in cooling geochronological and petrological systems: Contributions to Mineralogy and Petrology, v. 40, p. 259-274.

Eig, K., and Bergh, S.G., 2010, Late Cretaceous–Cenozoic fracturing *in* Lofoten, North Norway: Tectonic significance, fracture mechanisms and controlling factors: Tectonophysics, v. 499, p. 190-205.

Essene, E.J., 1989, The current status of thermobarometry in metamorphic rocks, in Daly, J.S., Cliff, R.A. and Yardley, B.W.D., eds., Evolution of Metamorphic Belts: Geological Society Special Publication, No. 43, p. 1-44.

Ewing, R.C., Meldrum, A., Wang, L., Weber, W.J., and Corrales, L.R., 2003, Radiation Effects in Zircon, *in* Hanchar, J.M. and Hoskin, P.W.O., eds., Reviews in Mineralogy & Geochemistry, Volume 53, Zircon: Washington, D.C., Mineralogical Society of America, p. 387-425.

Ferry, J.M., Spear, F.S., 1978, Experimental calibration of the partitioning of Fe and Mg between biotite and garnet: Contributions to Mineralogy and Petrology, v. 66, p. 113-117.

Fossen, H., 1992, The role of extensional tectonics in the Caledonides of south Norway: Journal of Structural Geology, v. 14, n. 8/9, p. 1033-1046.

Fossen, H., 2010, Extensional tectonics in the North Atlantic Caledonides: a regional view, *in* Law, R.D., Butler R.W.H., Holdsworth, R.E., Krabbendam, M., and Strachan, R.A., eds., Continental Tectonics and Mountain Building: The Legacy of Peach and Horne: Geological Society, London, Special Publication 335, p. 767-793.

Frondel, C., 1940, Oriented inclusions of staurolite, zircon and garnet in muscovite. Skating crystals and their significance: American Mineralogist, v. 25, p. 69-87.

Gaál, G., and Gorbatschev, R., 1987, An outline of the Precambrian evolution of the Baltic Shield: Precambrian Research, v. 35, p. 15-52.

Gee, D.G., 1975, A tectonic model for the central part of the Scandinavian Caledonides: American Journal of Science, v. 275-A, p. 468-515.

Gee, D.G., 2005, Scandinavian Caledonides (with Greenland), *in* Selley, R.C., Cocks, L.R.M. and Plimer, I.R., eds., Encyclopedia of Geology, Elsevier, Amsterdam, p. 64 -74.

Gee, D.G., Kumpulainen, R., Roberts, D., Stephens, M.B., Thon, A., and Zachrisson, E., 1985, Scandinavian Caledonides Tectonostratigraphic Map, *in* Gee, D.G., and Sturt, B.A., eds., The Caledonide Orogen – Scandinavia and Related Areas: John Wiley & Sons, scale 1:2 000 000, 1 sheet.

Gerstenberger, H., and Haase, G., 1997, Technical Note: A highly effective emitter substance for mass spectrometric Pb isotope ratio determinations: Chemical Geology, v. 136, p. 309-312.

Gorbatschev, R., 1985, Precambrian basement of the Scandinavian Caledonides, *in* Gee, D.G., and Sturt, B.A., eds., The Caledonide Orogen – Scandinavia and Related Areas: John Wiley & Sons, p. 197-212.

Graversen, O., Marker, M., Søvegjarto, U., 1981, Precambrian and Caledonian nappe tectonics in the Central Scandinavian Caledonides, Nordland, Norway: Terra Cognita, v. 1, n. 48 (abstract).

Gustavson, M., 1991, Geologisk kart over Norge, berggrunnskart BODØ 2029 IV: Norges geologiske undersøkelse, scale 1:50 000, 1 sheet.

Gustavson, M., 1996, Geologisk kart over Norge, berggrunnskart SULITJELMA: Norges geologiske undersøkelse, scale 1:250 000, 1 sheet.

Gustavson, M., and Blystad, P., 1995, Geologisk kart over Norge, berggrunnskart BODØ: Norges geologiske undersøkelse, scale 1:250 000, 1 sheet.

Gustavson, M., and Gjelle, S.T., 1991, Geologisk kart over Norge, berggrunnskart MO I RANA: Norges geologiske undersøkelse, scale 1:250 000, 1 sheet.

Hames, W.E. and Andresen, A., 1996, Timing of Paleozoic orogeny and extension in the continental shelf of north-central Norway as indicated by laser $^{40}Ar/^{39}Ar$ muscovite dating: Geology, v. 24, no. 11, p. 1005-1008.

Hames, W.E., and Bowring, S.A., 1994, An empirical study of the argon diffusion geometry in muscovite: Earth and Planetary Science Letters, v. 124, p. 161-169.

Hames, W.E., Renne, P.R., and Ruppel, C., 2000, New evidence for geologically instantaneous emplacement of earliest Jurassic Central Atlantic magmatic province basalts on the North American Margin: Geology, v. 28, p. 859-862.

Henriksen, N., and Higgins, A.K., 2008, Geological research and mapping in the Caledonian orogen of East Greenland, 82° N - 70° N: Geological Society of America Memoir 202, p. 1-27.

Hodges, K.V., 1982a, Tectonic Stratigraphy and Structural Evolution of the Efjord-Sitasjaure Area, Northern Scandinavian Caledonides [Ph.D. thesis]: Cambridge, Massachusetts Institute of Technology, 58 p.

Hodges, K.V., 1982b, The use of discordant apparent mineral ages in determining closure temperatures and cooling rates in geological environments [Ph.D. thesis]: Cambridge, Massachusetts Institute of Technology, 58 p.

Hodges, K.V., Bartley, J.M., and Burchfiel, B.C., 1982, Structural evolution of an A-type subduction zone, Lofoten-Rombak area, northern Scandinavian Caledonides: Tectonics, v. 1, n. 441, p. 441-462.

Hollingworth, S.E., Wells, M.K., and Bradshaw, R., 1960, Geology and structure of the Glomfjord Region, northern Norway: International Geological Congress, v. 21, p. 33-42.

Hoskin, P.W.O. and Schaltegger, U., 2003, The Composition of Zircon and Igneous and Metamorphic Petrogenesis, *in* Hanchar, J.M. and Hoskin, P.W.O., eds., Reviews in Mineralogy & Geochemistry, Volume 53, Zircon: Washington, D.C., Mineralogical Society of America, p. 468-500.

Jaffey, A.H., Flynn, K.F., Glendenin, L.E., Bentley, W.C., and Essling, A.M., 1971, Precision measurement of halflives and specific activities of ^{235}U and ^{238}U: Physical Reviews, Section C, Nuclear Physics, v. 4, p. 1889-1906.

Kalsbeek, F., Thrane, K., Higgins, A.K., Jepsen, H.F., Leslie, A.G., Nutman, A.P., and Frei, R., 2008, Polyorogenic history of the East Greenland Caledonides: Geological Society of America Memoir 202, p. 55-72.

Kalsbeek F., Thrane, K., Nutman, A.P., and Jepsen, H.F., 2000, Late Mesoproterozoic to early Neoproterozoic history of the East Greenland Caledonides: evidence for Grenvillian orogenesis?: Journal of the Geological Society, London, v. 157, p. 1215-1225.

Kautsky, G., 1953, Der geologische Bau des Sulitjelma-Salojauregegietes in den nordskandinavischen Kaledoniden: Sveriges geologiska undersökning Serie C, v. 528, p. 1-228.

Keppler, H., and Wyllie, P.J., 1990, Role of fluids in transport and fractionation of uranium and thorium in magmatic processes: Nature, v. 348, p. 531-533.

Klein, A., Steltenpohl, M.G., Hames, W.E., Andresen, A., 1999, Ductile and brittle extension in the southern Lofoten archipelago, north Norway: implications for differences in tectonic style along an ancient collisional margin: American Journal of Science, v. 299, p. 69-89.

Korja, A., Lahtinen, A., and Nironen, M., 2006, The Svecofennian orogen: a collage of microcontinents and island arcs: Geological Society, London, Memoirs, v. 32, p. 561-578.

Krogh, T.E., 1973, A low-contamination method for hydrothermal decomposition of zircon and extraction of U and Pb for isotopic age determinations: Geochimica et Cosmochimica Acta, v. 37, p. 485-494.

Krogh, T.E., 1982a, Improved accuracy of U-Pb zircon dating by selection of more concordant fractions using a high gradient magnetic separation technique: Geochimica et Cosmochimica Acta, v. 46, p. 631-635.

Krogh, T.E., 1982b, Improved accuracy of U-Pb zircon ages by the creation of more concordant systems using an air abrasion technique: Geochimica et Cosmochimica Acta, v. 46, p. 637-649.

Leslie, A.G., and Higgins, A.K., 2008, Foreland-propagating Caledonian thrust systems in East Greenland: Geological Society of America Memoir 202, p. 169-199.

Leslie, A.G., and Nutman, A.P., 2003, Evidence for Neoproterozoic orogenesis and early high temperature Scandian deformation events in the southern East Greenland Caledonides: Geological Magazine, v. 140, p. 309–333.

Leslie, A.G., Smith, M., and Soper, N.J., 2008, Laurentian margin evolution and the Caledonian orogeny - A template for Scotland and East Greenland: Geological Society of America Memoir 202, p. 307-343.

Lindh, A., and Persson, P.-O, 1990, Proterozoic Granitoid Rocks of the Baltic Shield – Trends of Development, *in* Gower, C.F., Rivers, T., and Ryan, A.B., eds., Mid-Proterozoic Laurentia-Baltica: Geological Association of Canada, Special Paper 38, p. 23-40.

Ludwig, K.R., 2009, Isoplot/Ex Version 3.71.09.05.23nx. A Geochronological Toolkit for Microsoft *Excel*: Berkley Geochronology Center Special Publication, n. 4.

Mager, S.M., 2005, The late- to post-Caledonian extensional history of northwest Hinnøy, north Norway [M. Sc. thesis]: Auburn University, 88 p.

Mattinson, J.M., 2005, Zircon U-Pb chemical abrasion ("CA-TIMS") method: Combined annealing and multi-step partial dissolution analysis for improved precision and accuracy of zircon ages: Chemical Geology, v. 220, p. 47-66.

Montel, J.M., Foret, S., Veschambre, M., Nicollet, C., and Provost, A., 1996, Electron microprobe dating of monazite: Chemical Geology, v. 131, p. 37-53.

Neuendorf, K.K.E, Mehl, Jr., J.P., and Jackson, J.A., editors, 2005, Glossary of Geology: Alexandria, Virginia, American Geological Institute, 779 p.

Nicholson, R., 1970, The tectonic pattern of the Bodø-Sulitjelma area, a review. *in* Proceedings, The caledonian geology of Northern Norway, January 10th-12th 1970: Cardiff, University College, v. 269, p. 74-76.

Nicholson, R., and Rutland, R.W.R., 1969, A Section across the Norwegian Caledonides; Bodø to Sulitjelma: Norges Geologiske Undersøkelse, n. 260, p. 1-86.

Nicolaysen, L.O., 1961, Graphic interpretation of discordant age measurements on metamorphic rocks: Annals New York Academy of Science, v. 91, p. 198-206.

Northrup, C.J., 1996, Structural expressions and tectonic implications of general noncoaxial flow in the midcrust of a collisional orogen: The northern Scandinavian Caledonides: Tectonics, v. 15, n. 2, p. 490-505.

Osmundsen, P.T., Braathen, A., Nordgulen, Ø., Roberts, D., Meyer, G.B., and Eide, E., 2003, The Devonian Nesna shear zone and adjacent gneiss-cored culminations, North–Central Norwegian Caledonides: Journal of the Geological Society, London, v. 150, p. 137-150.

Parrish, R.R, 1990, U-Pb dating of monazite and its application to geological problems: Canadian Journal of Earth Sciences, v. 27, p. 1431-1450.

Parrish, R.R. and Noble, S.R., 2003, Zircon U-Th-Pb Geochronology by Isotope Dilution – Thermal Ionization Mass Spectrometry (ID-TIMS) , *in* Hanchar, J.M. and Hoskin, P.W.O., eds., Reviews in Mineralogy & Geochemistry, Volume 53, Zircon: Washington, D.C., Mineralogical Society of America, p. 183-213.

Passchier, C.W., and Trouw, R.A.J., 2005, Microtectonics, Berlin, Springer, 366 p.

Pettersson, C.H., Tebenkov, A.M., Larionov, A.N., Andresen, A., and Pease, V., 2009, Timing of migmitization and granite genesis in the Northwestern Terrane of Svalbard, Norway: implications for regional correlations in the Arctic Caledonides: Journal of the Geological Society, London, v. 166, p. 147-158.

Pupin, J.P., 1980, Zircon and Granite Petrology: Contributions to Mineralogy and Petrology, v. 73, p. 207-220.

Ramberg, H., 1980, Diapirism and gravity collapse in the Scandinavian Caledonides: Journal of the Geological Society, London, v. 137, p. 261-270.

Renne, P.R., Swisher, C.C., Deino, A.L., 1998, Intercalibration of standards, absolute ages and uncertainties in $^{40}Ar/^{39}Ar$ dating: Chemical Geology (Isotope Geoscience Section), v. 145, p. 117-152.

Roberts, D., 1988, Timing of Silurian to middle Devonian deformation in the Caledonides of Scandinavia, Svalbard and E Greenland, *in* Harris, A.L., Fettes, D.J., eds., The Caledonian-Appalachian Orogen: Geological Society Special Publication No. 38, p. 429-435.

Roberts, D., 2003, The Scandinavian Caledonides: event chronology, palaeogeographic settings and likely modern analogues: Tectonophysics, v. 365, p. 283-299.

Roberts, D., and Gee, D.G., 1985, An introduction to the structure of the Scandinavian Caledonides, *in* Gee, D.G., and Sturt, B.A., eds., The Caledonide orogen - Scandinavia and related areas: Chichester, England, Wiley & Sons, p. 553-569.

Roberts, D., Nordgulen, Ø., and Melezhik, V., 2007, The Uppermost Allochthon in the Scandinavian Caledonides: From a Laurentian ancestry through Taconian orogeny to Scandian crustal growth on Baltica, *in* Hatcher, R.D. Jr., Carlson, M.P., McBride, J.H., and Martínez Catalán, J.R., eds., 4-D Framework of Continental Crust: Geological Society of America Memoir 200, p. 357–377.

Rock, N.M.S., and Duffy, T.R., 1986, REGRES: A FORTRAN-77 program to calculate nonparametric and “structural” parametric solutions to bivariate regression equations: Computers and Geoscience, v. 12, n. 6, p. 807-818.

Romer, R.L., Kjøsnes, B., Korneliussen, A., Lindahl, I., Skyseth, T., Stendal, M., and Sundvoll, B., 1992, The Archaean-Proterozoic boundary beneath the Caledonides of northern Norway and Sweden: U-Pb, Rb-Sr, and εNd data from the Rombak-Tysfjord area: Norges geologiske undersøkelse, Rapport 91.225, 67 pp.

Rutland, R.W.R., and Nicholson, R., 1965, Tectonics of the Caledonides of part of Nordland, Norway: Quarterly Journal of the Geological Society London, v. 121, p. 73-109.

Rykkelid, E., and Fossen, H., 1992, Composite fabrics in mid-crustal gneisses: observations from the Øygarden Complex, West Norway Caledonides: Journal of Structural Geology, v. 14, n. 1, p. 1-9.

Siivola, J., and Schmid, R., 2007, A systematic nomenclature for metamorphic rocks: 12. List of mineral abbreviations. Recommendations by the IUGS Subcommission on the Systematics of Metamorphic Rocks. Recommendations, web version of 01.02.2007.

Silvennoinen, A., Gustavson, M., Perttunen, V., Siedlecka, A., Sjöstrand, T., Stephens, M.B., and Zachrisson, E., 1987, Geologic Map, Northern Fennoscandia: Geological Surveys of Finland, Norway, and Sweden, scale 1:1 000 000, 1 sheet.

Skår, Ø., 2002, U-Pb geochronology and geochemistry of early Proterozoic rocks of the tectonic basement windows in central Nordland, Caledonides of north-central Norway: Precambrian Research, v. 116, p. 265-283.

Solli, A., and Nordgulen, Ø., 2008, Bedrock map of Norway and the Caledonides in Sweden and Finland: Geological Survey of Norway, scale 1:2,000,000, 1 sheet.

Spear, F.S., 1993, Metamorphic Phase Equilibria and Pressure-Temperature-Time Paths, 799 p., Mineralogical Society of America, Washington, D. C.

Speer, J.A., 1980, Zircon, *in* Ribbe, P.H., ed., Reviews in Mineralogy, Volume 5, Orthosilicates: Washington, D.C., Mineralogical Society of America, p. 67-112.

Stacey, J.S., and Kramers, J.D., 1975, Approximation of terrestrial lead isotope evolution by a two-stage model: Earth and Planetary Science Letters, v. 34, p. 207-226.

Steffen, K., Selverstone, J., and Brearley, A., 2001, Episodic weakening and strengthening during synmetamorphic deformation in a deep crustal shear zone in the Alps, *in* Holdsworth, R.E., Strachan, R.A., MagLoughlin, J.F., Knipe, R.J., eds., The Nature and Tectonic Significance of Fault Zone Weakening: Geological Society Special Publication, n. 186, p. 141-156.

Steiger, R.H., and Jäger, E., 1977, Subcommision on geochronology: Convention on the use of decay constants in geo- and cosmochronology: Earth and Planetary Science Letters, v. 36, p. 359-362.

Steltenpohl, M.G., and Bartley, J.M., Postcollisional extension of the Caledonide orogen in Scandinavia: Structural expressions and tectonic significance: Comment and Reply: Geology, v. 12, p. 123-140.

Steltenpohl, M.G., Ball, J.B., Moecher, D.P., and Andresen, A., 2010, The Eidsfjord Detachment: an Early Devonian, Paleoseismogenic Low-angle Normal Detachment Fault Exposed in Lofoten-Vesterålen, North Norway. In: Norges Geologisk Forening (Geological Society of Norway), Nordic Geologic Winter Meeting, Abstracts and Proceedings, v. 1, p. 186-189.

Steltenpohl, M.G., Carter, B.T., Andresen, A., and Zeltner, D.L., 2009, $^{40}Ar/^{39}Ar$ Thermochronology of Late- and Postorogenic Extension in the Caledonides of North-Central Norway: The Journal of Geology, v. 117, p.399-414.

Steltenpohl, M.G., Hames, W.E., and Andresen, A., 2004, The Silurian to Permian history of a metamorphic core complex in Lofoten, northern Scandinavian Caledonides: Tectonics, v. 23, 1-23.

Steltenpohl, M.G., Hames, W., Andresen, A., and Markl, G., 2003, New Caledonian eclogite province in Norway and potential Laurentian (Taconic) and Baltic links: Geology, v. 31, p. 985-988.

Steltenpohl, M.G., Moecher, D., Andresen, A., Ball, J., Mager, S., and Hames, W.E., 2011, The Eidsfjord shear zone, Lofoten-Vesterålen, north Norway: An Early Devonian, paleoseismogenic low-angle normal fault: Journal of Structural Geology, v. 33, n. 5, p. 1023-1043.

Stephens, M.B., and Gee, D.G., 1985: A tectonic model for the evolution of the eugeoclinal terranes in the central Scandinavian Caledonides, *in* Gee, D.G., and Sturt, B.A., eds., The Caledonide Orogen – Scandinavia and Related Areas: John Wiley & Sons, p. 953-978.

Stephens, M.B., Gustavson, M., Ramberg, I.B., and Zachrisson, 1985, The Caledonides of central-north Scandinavia – a tectonostratigraphic overview, *in* Gee, D.G., and Sturt, B.A., eds., The Caledonide Orogen – Scandinavia and Related Areas: John Wiley & Sons, p. 135-162.

Stephens, M.B., Kullerud, K., Claesson, S., 1993, Early Caledonian tectonothermal evolution in outboard terranes, central Scandinavian Caledonides: new constraints from U-Pb zircon dates: Journal of the Geological Society, London, v. 150, p. 51-56.

Strachan, R.A., Nutman, A.P., and Friderichsen, J.D., 1995, SHRIMP U-Pb geochronology and metamorphic history of the Smallefjord sequence, NE Greenland Caledonides: Journal of the Geological Society, London, v. 152, p. 779-784.

Styles, M.T., 1974, The Structure, Metamorphism, and Igneous Petrology of the Beiarn Area, Nordland, Northern Norway [Ph.D. thesis]: Manchester, University of Manchester, 131 p.

Sønderholm, M., Frederiksen, K.S., Smith, M.P., and Tirsgaard, H., 2008, Neoproterozoic sedimentary basins with glacigenic deposits of the East Greenland Caledonides: Geological Society of America Memoir 202, p. 99-136.

Thelander, T., Bakker, E., and Nicholson, R., 1980, Basement-cover relationships in the Nasafjället Window, central Swedish Caledonides: Geologiska Föreningens I Stockholm Förhandlingar, v. 102, p. 569-580.

Tørudbakken, B.O, and Brattli, B., 1985, Ages of metamorphic and deformational events in the Beiarn Nappe Complex, Nordland, Norway: Norges Geologiske Undersøkelse Bulletin, v. 399, p. 27-39.

Walsh, E.O., Hacker, B.R., Gans, P.B., Grove, M., and Gehrels, G., Protolith ages and exhumation histories of (ultra)high-pressure rocks across the Western Gneiss

Region, Norway. Geological Society of America Bulletin, v. 110, n. 3-4, p. 289-301.

Waters, D.J., 2004, Practical Aspects of Mineral Thermobarometry: http://www.earth.ox.ac.uk/~davewa/pt/pt04.html, accessed 4 March, 2011.

Watson, E.B., 1979, Zircon saturation in felsic liquids: Experimental results and applications to trace element geochemistry: Contributions to Mineralogy and Petrology, v. 70, p. 407-419.

Watt, G.R., Kinny, P.D., and Friderichsen, J.D., 2000, U-Pb geochronology of Neoproterozoic and Caledonian tectonothermal events in the East Greenland Caledonides: Journal of the Geological Society, London, v. 157, p. 1030-1048.

Wendt, I., and Carl, C., 1991, The statistical distribution of the mean squared weighted deviation: Chemical Geology (Isotope Geoscience Section), v. 86, p. 275-285.

Wetherill, G.W., 1956, Discordant Uranium Ages, I: Transactions, American Geophysical Union, v. 37, n. 3, p. 320-326.

Wetherill, G.W., 1963, Discordant Uranium-Lead Ages: 2. Discordant ages resulting from diffusion of Lead and Uranium: Journal of Geophysical Research, v. 68, n. 10, p. 2957-2965.

Williams, M.L., Jercinovic, M.J., and Hetherington, C.J., 2007, Microprobe Monazite Geochronology: Understanding Geologic Processes by Integrating Composition and Chronology: Annual Reviews of Earth and Planetary Sciences, v. 35, p. 137-175.

Williams, M.L., Jercinovic, M.J., and Terry, M.P., 1999, Age mapping and dating of monazite on the electron microprobe: Deconvoluting multistage tectonic histories: Geology, v. 27, n. 11, p. 1023-1026.

Wilson, M.R., 1981, Geochronological results from Sulitjelma, Norway: Terra Cognita, v. 1, n. 160 (abstract).

Wilson, M.R., and Nicholson, R., 1973, The structural setting and geochronology of basal granitic gneisses in the gneisses in the Caledonides of part of Nordland, Norway: Journal of the Geological Society, London, v. 129, p. 365-386.

Zeltner, D.L., 2001, Geological investigations in east Bodø, north-central Norway [M.Sc. thesis]: Auburn University, 101 p.

Zheng, Y.F., 1989, Influences of the nature of the initial Rb-Sr system on isochron validity: Chemical Geology, v. 80, p. 1-16.

APPENDIX 1 – Station Locations

Table printed in OCR font so that data can easily be scanned and processed with optical character recognition software. Coordinates provided are UTM 33N WGS84 (EPSG 32633).

Station	Easting (X)	Northing (Y)
LEA-10-1	505849	7493461
LEA-10-2	491908	7483866
LND-000	467941	7474429
LND-001	467941	7474429
LND-002	468167	7474404
LND-003	468381	7474539
LND-004	468362	7474728
LND-005	468431	7474804
LND-006	468544	7474897
LND-007	468511	7474820
LND-008	468499	7474767
LND-009	468384	7474449
LND-010	467922	7473606
LND-011	467879	7473472
LND-012	468374	7473841
LND-013	468865	7474007
LND-014	468657	7473933
LND-015	468938	7474017
LND-016	469392	7474283
LND-017	469662	7474539
LND-018	470678	7474856
LND-019	471833	7474878
LND-020	472599	7475195
LND-021	473065	7475397
KJR-001	487928	7487656
KJR-002	488150	7487707
KJR-003	488197	7487640
KJR-004	488587	7487676
KJR-005	488768	7487688
KJR-006	489074	7487523
KJR-007	489352	7487273
KJR-008	489947	7486751
KJR-009	490201	7486682
KJR-010	490419	7486711
KJR-011	490924	7487145
KJR-012	490883	7487289
KJR-013	490282	7487319
KJR-014	490248	7487321
KJR-015	490240	7487352
KJR-016	490198	7487380
KJR-017	490026	7487558
KJR-018	489947	7487784
KJR-019	490009	7488163
KJR-020	487819	7487219
KJR-021	487692	7487065
KJR-022	487529	7486874
KJR-023	487476	7486839
KJR-024	487353	7486752
KJR-025	487331	7486733
KJR-026	487287	7486709
KJR-027	487219	7486560
KJR-028	487212	7486541
KJR-029	487111	7486372
KJR-030	487033	7486351
KJR-031	486914	7486270
KJR-032	486762	7486279
KJR-033	486648	7486229
KJR-034	486534	7486182
KJR-035	486471	7485984
KJR-036	486443	7485926
KJR-037	486508	7485905
KJR-038	486619	7485749
KJR-039	486675	7485699
KJR-040	487055	7485568
KJR-041	487269	7485627
KJR-042	487392	7485457
KJR-043	487498	7486068
KJR-044	487485	7486188
KJR-045	487425	7486415
KJR-046	487631	7486989
KJR-047	488047	7487487
KJR-048	486831	7486118
KJR-049	486383	7485879
KJR-050	486347	7485880
KJR-051	486273	7485810
KJR-052	486187	7485786
KJR-053	486136	7485777
KJR-054	486086	7485730
KJR-055	486017	7485661
KJR-056	485983	7485600
KJR-057	485933	7485534
KJR-058	485916	7485471
KJR-059	485910	7485392
KJR-060	485837	7485337
KJR-061	485729	7485248
KJR-062	485667	7485126
KJR-063	485592	7485065
KJR-064	485511	7485008
KJR-065	485470	7484995

Station	Easting (X)	Northing (Y)
KJR-066	485422	7484935
KJR-067	485377	7484871
KJR-068	485373	7484820
KJR-069	485266	7484788
KJR-070	485166	7484713
KJR-071	485031	7484579
KJR-072	487044	7486685
KJR-073	486916	7486671
KJR-074	486846	7486759
KJR-075	486568	7486723
KJR-076	486512	7486770
KJR-077	487035	7486891
KJR-078	487078	7487007
KJR-079	483981	7477342
KJR-080	484049	7477392
KJR-081	484202	7477568
KJR-082	484219	7477604
KJR-083	484256	7478122
KJR-084	484159	7478262
KJR-085	484116	7478359
KJR-086	484252	7478349
KJR-087	484314	7478409
KJR-088	484352	7478499
KJR-089	484373	7478633
KJR-090	484402	7478778
KJR-091	484445	7479046
KJR-092	484414	7479231
KJR-093	484326	7479327
KJR-094	484289	7479505
KJR-095	484330	7479660
KJR-096	484246	7479634
KJR-097	484287	7479731
KJR-098	484365	7479872
KJR-099	484314	7479969
KJR-100	484351	7480044
KJR-101	484706	7474907
KJR-102	484772	7474975
KJR-103	484832	7474978
KJR-104	484947	7474985
KJR-105	485015	7475135
KJR-106	485017	7475222
KJR-107	485192	7475355
KJR-108	485357	7475421
KJR-109	485474	7475465
KJR-110	485454	7475594
KJR-111	485545	7475723
KJR-112	485644	7475774
KJR-113	485700	7476010
KJR-114	485799	7476089
KJR-115	485775	7476096
KJR-116	485672	7476162
KJR-117	485685	7476295
KJR-118	485653	7476458
KJR-119	485547	7476541
KJR-120	485421	7476592

Station	Easting (X)	Northing (Y)
KJR-121	483720	7473919
KJR-122	484356	7475070
KJR-123	484400	7475110
KJR-124	484530	7475154
KJR-125	484635	7475297
KJR-126	484768	7475406
KJR-127	485090	7475719
KJR-128	485204	7475798
KJR-129	484645	7476145
KJR-130	484606	7476222
KJR-131	484335	7476681
KJR-132	484325	7476759
KJR-133	484294	7476828
KJR-134	484327	7476879
KJR-135	484394	7476908
KJR-136	484440	7476862
KJR-137	484565	7477033
KJR-138	484546	7477174
KJR-139	484613	7477191
KJR-140	484643	7477225
KJR-141	485194	7484455
KJR-142	485266	7484423
KJR-143	485384	7484335
KJR-144	485531	7484443
KJR-145	485640	7484270
KJR-146	485765	7484220
KJR-147	485825	7484136
KJR-148	485856	7484076
KJR-149	485963	7483940
KJR-150	486103	7483865
KJR-151	486314	7483525
KJR-152	486461	7483365
KJR-153	486496	7483221
KJR-154	486545	7483203
KJR-155	486589	7483147
KJR-156	486625	7483312
KJR-157	486670	7483007
KJR-158	486941	7482809
KJR-159	486939	7482787
KJR-160	487020	7482704
KJR-161	487083	7482667
KJR-162	487162	7482636
KJR-163	489687	7480249
KJR-164	489582	7480181
KJR-165	489679	7480084
KJR-166	489727	7479982
KJR-167	489892	7479968
KJR-168	490127	7478971
KJR-169	490101	7478881
KJR-170	490088	7478794
KJR-171	490063	7478829
KJR-172	489953	7478671
KJR-173	489919	7478539
KJR-174	489642	7478446
KJR-175	489565	7478414

Station	Easting (X)	Northing (Y)
KJR-176	489184	7478418
KJR-177	488963	7478379
KJR-178	488872	7478391
KJR-179	488855	7478312
KJR-180	488830	7477936
KJR-181	488959	7477935
KJR-182	488407	7477537
KJR-183	488168	7477575
KJR-184	487938	7477486
KJR-185	487554	7477230
KJR-186	487384	7477220
KJR-187	486869	7476859
KJR-188	486356	7476526
KJR-189	487303	7486997
KJR-190	487407	7487147
KJR-191	487429	7487455
KJR-192	487404	7487532
KJR-193	487742	7487518
KJR-194	487879	7487526
KJR-195	488156	7487791
KJR-196	488167	7487821
KJR-197	488212	7487883
KJR-198	488229	7487901
KJR-199	488282	7487947
KJR-200	488404	7488037
KJR-201	488520	7488107
KJR-202	488700	7488132
KJR-203	488958	7488368
KJR-204	489054	7488368
KJR-205	489146	7488331
KJR-206	489234	7488381
KJR-207	488075	7482621
KJR-208	488965	7485456
KJR-209	489245	7485015
KJR-210	489447	7484637
KJR-211	489640	7484208
KJR-212	490190	7483778
KJR-213	491625	7483829
KJR-214	491727	7483816
KJR-215	491835	7483856
KJR-216	491919	7484121
KJR-217	491950	7484232
KJR-218	492084	7484332
KJR-219	492636	7484705
KJR-220	493434	7484747
KJR-221	493392	7484942
KJR-222	494959	7493453
KJR-223	494882	7493445
KJR-224	494705	7493326
KJR-225	494569	7493064
KJR-226	494340	7492747
KJR-227	494084	7492929
KJR-228	493936	7492910
KJR-229	493546	7492761
KJR-230	493541	7492576
KJR-231	493327	7492323
KJR-232	493172	7492143
KJR-233	492987	7492015
KJR-234	493098	7491872
KJR-235	493129	7491717
KJR-236	493686	7491700
KJR-237	493323	7491499
KJR-238	492996	7491595
KJR-239	492805	7491633
KJR-240	492722	7491633
KJR-241	492482	7491531
KJR-242	488808	7477884
KJR-243	487057	7482762
KJR-244	491245	7490000
KJR-245	491265	7489859
KJR-246	491877	7488951
KJR-247	491844	7488738
KJR-248	491848	7488542
KJR-249	491904	7488080
KJR-250	491743	7487765
KJR-251	491773	7487465
KJR-252	491993	7487173
KJR-253	492123	7487104
KJR-254	492295	7486964
KJR-255	492334	7486883
KJR-256	492441	7486800
KJR-257	492527	7486785
KJR-258	492765	7486801
KJR-259	493059	7486807
KJR-260	493773	7486681
KJR-261	494018	7486565
KJR-262	494367	7486527
KJR-263	494578	7486492
KJR-264	494615	7486497
KJR-265	494936	7486442
KJR-266	495141	7486396
KJR-267	496749	7486278
KJR-268	497283	7486382
KJR-269	489345	7488470
KJR-270	489436	7488714
KJR-271	489544	7488785
KJR-272	489279	7488828
KJR-273	489657	7488934
KJR-274	489669	7489083
KJR-275	489611	7489292
KJR-276	489863	7489328
KJR-277	490006	7489565
KJR-278	490104	7489656
KJR-279	490185	7489733
KJR-280	490323	7489770
KJR-281	490529	7489921
KJR-282	490797	7490026
KJR-283	491041	7490174
KJR-284	491724	7490388
KJR-285	491583	7490649

Station	Easting (X)	Northing (Y)
KJR-286	491707	7490796
KJR-287	491910	7490917
KJR-288	492458	7491077
KJR-289	493149	7476270
KJR-290	493115	7476435
KJR-291	492987	7476562
KJR-292	492812	7476719
KJR-293	492648	7476743
KJR-294	492545	7476972
KJR-295	492383	7477045
KJR-296	492213	7477114
KJR-297	492036	7477056
KJR-298	491902	7476976
KJR-299	491694	7476979
KJR-300	491535	7477091
KJR-301	491312	7477136
KJR-302	490098	7477087
TVK-01	505019	7494030
TVK-02	505063	7494047
TVK-04	505175	7494074
TVK-05	505358	7494043
TVK-06	505357	7494072
TVK-07	505348	7494748
TVK-08	505443	7494780
TVK-09	505418	7494512
TVK-10	505538	7494503
TVK-11	505618	7494411
TVK-12	505759	7494434
TVK-13	505801	7494398
TVK-14	506031	7494268
TVK-15	506154	7494404
TVK-16	506268	7494444
TVK-17	506354	7494400
TVK-18	506413	7494240
TVK-19	506421	7494117
TVK-20	506416	7493972
TVK-21	506411	7493954
TVK-22	506429	7493916
TVK-23	506381	7493820
TVK-24	506238	7493712
TVK-25	506005	7493662
TVK-26	505987	7493651
TVK-27	505893	7493595
TVK-28	505773	7493623
TVK-29	505647	7493576
TVK-30	505574	7493623
TVK-31	505561	7493681
TVK-32	505500	7493759
TVK-33	505473	7493850
TVK-34	505463	7493909
TVK-35	505421	7494082
TVK-36	505364	7494207
TVK-37	504986	7495009
TVK-38	504993	7494839
TVK-39	505069	7494721

Station	Easting (X)	Northing (Y)
TVK-40	505199	7494782
TVK-41	506310	7493843
TVK-42	506326	7493615
TVK-43	506353	7493506
TVK-44	506350	7493483
TVK-45	506357	7493444
TVK-46	506376	7493390
TVK-47	506373	7493342
TVK-48	506343	7493155
TVK-49	506313	7493111
TVK-50	506353	7492953
TVK-51	506148	7494180
TVK-52	506226	7492958
TVK-53	506212	7492816
TVK-54	506138	7492720
TVK-55	506431	7492773
TVK-56	506240	7492583
TVK-57	505972	7492537
TVK-58	505724	7492152
TVK-59	505595	7492078
TVK-60	505439	7492164
TVK-61	505231	7492038
TVK-62	505127	7492011
TVK-63	505037	7491956
TVK-64	504773	7491888
TVK-65	504449	7491875
TVK-66	504357	7491910
TVK-67	504213	7491871
TVK-68	503928	7491988
TVK-69	503929	7491991
TVK-70	503988	7492190
TVK-71	503995	7492208
TVK-72	504042	7492325
TVK-73	504085	7492519
TVK-74	504136	7492742
TVK-75	504169	7492893
TVK-76	504193	7493012
TVK-77	504320	7493470
TVK-78	504194	7493409
TVK-79	504169	7493237
TVK-80	504111	7493199
TVK-81	504020	7493118
TVK-82	503994	7492985
TVK-83	503938	7492928
TVK-84	504016	7492813
TVK-85	504272	7492749
TVK-86	504258	7492818
TVK-87	504327	7492902
TVK-88	504336	7493112
TVK-89	504430	7493195
TVK-90	504384	7493229
TVK-91	504359	7493351
TVK-92	504773	7493988
TVK-93	503919	7496871
TVK-94	505765	7493505

Station	Easting (X)	Northing (Y)
TVK-95	505064	7495339
TVK-96	505108	7495459
TVK-97	505090	7495658
TVK-98	505045	7495800
TVK-99	504845	7496035
TVK-100	504781	7496120
TVK-101	504768	7496158
TVK-102	504720	7496222
TVK-103	504668	7496337
TVK-113	503644	7497054
TVK-114	503616	7497046
TVK-115	503489	7497138
TVK-116	503418	7497181
TVK-118	503270	7497284
TVK-119	503178	7497355
TVK-121	502931	7497468
TVK-122	502882	7497486
TVK-123	502784	7497511
TVK-124	502605	7497516
TVK-125	502567	7497503
TVK-126	502175	7497386
TVK-127	502049	7497301
TVK-128	501780	7497324
TVK-129	501688	7497318
TVK-130	501448	7497258
TVK-131	501389	7497237
TVK-132A	501292	7497196
TVK-132B	501005	7497095
TVK-133	500952	7497038
TVK-134	500827	7496953
TVK-135	500750	7496928
TVK-136	500616	7496893
TVK-137	500456	7496850
TVK-138	500359	7496818
TVK-140	499216	7496282
TVK-142	501228	7496964
TVK-143	501279	7496924
TVK-144	501346	7496823
TVK-145	501257	7496672
TVK-145A	500897	7496959
TVK-146	503119	7497376
TVK-147	499015	7496185
TVK-148	498798	7496064
TVK-150	498618	7495965
TVK-151	498381	7495846
TVK-152	498051	7495767
TVK-153	497922	7495749
TVK-154	497665	7495631
TVK-155	497347	7495487
TVK-156	497092	7495353
TVK-157	496813	7495212
TVK-158	496697	7494941
TVK-159	496574	7494928
TVK-160	496485	7494751
TVK-161	495482	7494180

Station	Easting (X)	Northing (Y)
TVK-162	495553	7494320
TVK-163	495637	7494512
TVK-164	495781	7494520
TVK-165	495954	7494664
TVK-166	496133	7494778
TVK-167	496345	7494903

APPENDIX 2 – Microprobe Data

Obtained using a CAMECA SX50 electron microprobe (EMP) at the Electron Beam Laboratories in the Geosciences Department at Virginia Tech.

Analysis timestamp: Mon Feb14 13:45:372011
notes: miscellaneous based on 12 Oxygens

Hames1-AGrtTrav1

	SiO_2	TiO_2	Al_2O_3	MgO	CaO	MnO	FeO	Na_2O	K_2O	Total	x	y
#1	36.883	2.562	18.776	10.92	0	0	18.476	0.294	8.598	96.509	-12926	7214
#2	36.658	2.503	18.596	10.924	0	0.006	18.296	0.301	8.589	95.873	-12919	7212
#3	36.817	2.549	18.593	10.801	0.01	0.031	18.413	0.291	8.635	96.14	-12912	7210
#4	36.515	2.551	17.971	10.355	0.015	0	18.089	0.281	8.404	94.181	-12906	7208
#5	37.589	2.521	19.419	11.366	0	0.002	17.967	0.296	8.495	97.655	-12899	7206
#6	35.55	2.428	17.543	10.124	0.007	0	17.798	0.289	8.475	92.214	-12892	7205
#7	36.491	2.398	18.466	10.659	0	0	18.005	0.308	8.547	94.874	-12885	7203
#8	36.645	2.494	18.781	10.825	0	0	18.363	0.286	8.552	95.946	-12879	7201
#9	36.587	2.431	18.777	10.906	0	0	18.01	0.295	8.68	95.686	-12872	7199
#10	36.729	2.06	19.093	11.051	0	0	17.764	0.267	8.446	95.41	-12865	7197
#11	36.893	1.79	19.108	11.021	0	0.015	17.48	0.291	8.506	95.104	-12858	7195
#12	37.023	1.952	19.1	11.062	0	0.044	17.71	0.287	8.54	95.718	-12852	7193
#13	36.739	1.923	19.372	11.038	0.007	0	17.862	0.297	8.466	95.704	-12845	7191
#14	36.479	1.6	21.402	14.062	0	0	149.905	0.396	7.908	231.752	-12838	7190
#15	36.972	1.819	19.098	11.063	0	0.037	17.951	0.326	8.54	95.806	-12831	7188
#16	37.056	1.843	19.055	11.066	0	0	17.654	0.315	8.602	95.591	-12825	7186

	SiO_2	TiO_2	Al_2O_3	MgO	CaO	MnO	FeO	Na_2O	K_2O	Total	x	y
#17	37.081	1.854	19.14	11.225	0	0.04	17.771	0.306	8.614	96.031	-12818	7184
#18	37.142	1.88	19.245	11.076	0	0	17.76	0.288	8.645	96.036	-12811	7182
#19	36.804	1.992	19.009	11.243	0	0	17.756	0.31	8.604	95.718	-12804	7180
#20	36.898	2.018	19.004	11.023	0	0.015	17.648	0.281	8.488	95.375	-12798	7178
#21	36.923	1.958	19.034	11.207	0	0	17.656	0.263	8.605	95.646	-12791	7176
#22	37.298	1.861	18.914	11.098	0	0	17.451	0.277	8.572	95.471	-12784	7175
#23	36.799	2.019	19.266	11.086	0	0	17.783	0.264	8.569	95.786	-12777	7173
#24	36.932	2.012	19.077	11.138	0	0.006	17.691	0.32	8.77	95.946	-12771	7171
#25	36.982	1.883	18.912	11.217	0	0	17.69	0.277	8.573	95.534	-12764	7169
#26	36.872	2.044	18.977	11.165	0	0.033	17.612	0.308	8.647	95.658	-12757	7167
#27	36.84	2.054	19.011	11.137	0	0.019	18.001	0.298	8.343	95.703	-12750	7165
#28	36.879	2.022	18.846	11.15	0	0	17.677	0.291	8.511	95.376	-12744	7163
#29	36.676	2.06	18.967	11.216	0	0.006	17.807	0.324	8.49	95.546	-12737	7161
#30	36.064	1.945	18.518	11.032	0	0.002	17.612	0.299	8.353	93.825	-12730	7160
#31	36.891	1.962	18.878	11.189	0	0.029	17.849	0.266	8.57	95.634	-12723	7158
#32	36.941	2.044	18.831	11.009	0.004	0.004	17.868	0.28	8.556	95.537	-12717	7156
#33	35.912	1.971	18.143	10.56	0	0	18.092	0.277	8.494	93.449	-12710	7154
#34	36.702	1.875	19.014	11.314	0.01	0.037	17.621	0.268	8.45	95.291	-12703	7152
#35	36.883	1.986	18.935	11.229	0	0	17.67	0.281	8.533	95.517	-12696	7150
#36	35.929	1.926	18.466	10.845	0.039	0	17.571	0.294	8.333	93.403	-12690	7148
#37	37.005	1.928	18.634	11.039	0	0.027	17.448	0.304	8.546	94.931	-12683	7146
#38	36.691	1.877	19.023	11.177	0	0	17.78	0.286	8.442	95.276	-12676	7145
#39	36.724	1.929	18.977	11.354	0.015	0.004	17.504	0.311	8.495	95.313	-12669	7143
#40	36.793	1.826	19.121	11.302	0	0.033	17.845	0.273	8.437	95.63	-12663	7141
#41	37.3	1.85	19.331	11.324	0	0.006	17.616	0.295	8.429	96.151	-12656	7139
#42	36.799	1.918	19.243	11.406	0	0	17.617	0.3	8.505	95.788	-12649	7137
#43	37.203	1.885	19.204	11.16	0.009	0.035	18.008	0.268	8.409	96.181	-12642	7135
#44	36.279	1.739	18.055	10.292	0.01	0.069	17.736	0.257	8.337	92.774	-12636	7133
#45	23.919	0.031	14.545	1.245	1.521	0.832	27.84	0	0.057	69.99	-12629	7131
#46	37.648	0	21.493	3.207	1.845	0.588	36.433	0.021	0.008	101.243	-12622	7129
#47	37.664	0.003	21.749	3.546	1.784	0.836	36.597	0.013	0.006	102.198	-12615	7128

	SiO_2	TiO_2	Al_2O_3	MgO	CaO	MnO	FeO	Na_2O	K_2O	Total	x	y
#48	37.613	0.001	21.845	3.762	1.798	0.73	36.018	0	0	101.767	-12609	7126
#49	37.66	0.018	21.712	3.997	1.77	0.69	36.273	0.02	0	102.14	-12602	7124
#50	37.48	0.004	21.649	4.079	1.837	0.651	36.106	0.004	0	101.81	-12595	7122
#51	37.768	0.035	21.844	4.139	1.836	0.59	35.26	0.009	0	101.481	-12588	7120
#52	37.87	0.009	21.954	4.288	1.843	0.658	35.416	0.017	0	102.055	-12582	7118
#53	37.989	0	21.9	4.292	1.911	0.651	35.358	0	0	102.101	-12575	7116
#54	37.751	0	21.989	4.37	1.916	0.509	35.552	0	0	102.087	-12568	7114
#55	38.109	0.023	21.796	4.443	1.846	0.59	35.79	0.004	0.004	102.605	-12561	7113
#56	37.68	0.031	21.954	4.444	1.904	0.6	35.314	0.002	0	101.929	-12555	7111
#57	37.852	0.005	21.915	4.529	1.767	0.509	35.381	0.013	0	101.971	-12548	7109
#58	37.813	0	22.124	4.455	1.796	0.491	34.606	0.016	0	101.301	-12541	7107
#59	37.735	0.012	21.972	4.485	1.841	0.61	35.226	0.002	0	101.883	-12534	7105
#60	37.824	0	22.019	4.517	1.762	0.653	34.661	0.018	0	101.454	-12527	7103
#61	37.958	0	21.933	4.552	1.961	0.647	34.843	0.03	0.004	101.928	-12521	7101
#62	37.605	0	22.003	4.539	1.847	0.637	34.684	0.027	0.003	101.345	-12514	7099
#63	37.769	0.007	22.074	4.653	1.948	0.546	34.834	0.005	0	101.836	-12507	7098
#64	37.817	0.021	21.866	4.626	1.948	0.706	34.828	0.032	0	101.844	-12500	7096
#65	37.99	0.001	22.039	4.632	1.85	0.629	34.73	0.004	0	101.875	-12494	7094
#66	37.884	0	22.168	4.604	1.913	0.635	34.306	0	0.006	101.516	-12487	7092
#67	37.952	0.012	22.011	4.63	1.866	0.706	34.456	0.026	0	101.659	-12480	7090
#68	37.987	0.015	22.248	4.513	1.959	0.662	34.021	0.016	0.007	101.428	-12473	7088
#69	37.515	0.041	22.046	4.708	1.83	0.657	34.716	0.007	0	101.52	-12467	7086
#70	37.861	0.052	22.07	4.72	1.863	0.866	34.222	0.023	0	101.677	-12460	7084
#71	37.954	0	22.198	4.753	1.906	0.743	34.336	0.02	0	101.91	-12453	7083
#72	37.895	0.003	22.269	4.702	1.955	0.82	33.955	0.013	0	101.612	-12446	7081
#73	38.014	0	22.241	4.693	1.884	0.737	34.155	0.021	0	101.745	-12440	7079
#74	37.739	0.039	22.148	4.716	1.749	0.86	34.215	0.007	0.002	101.475	-12433	7077
#75	37.606	0	22.15	4.785	1.816	0.864	34.221	0.007	0	101.449	-12426	7075
#76	37.605	0	22.056	4.82	1.697	0.801	34.489	0	0	101.468	-12419	7073
#77	37.671	0.005	22.296	4.881	1.702	0.805	34.221	0	0	101.581	-12413	7071
#78	37.836	0	22.183	4.796	1.713	0.869	33.771	0.027	0	101.195	-12406	7069

	SiO_2	TiO_2	Al_2O_3	MgO	CaO	MnO	FeO	Na_2O	K_2O	Total	x	y
#79	37.95	0.026	22.162	4.831	1.745	0.82	34.182	0	0	101.716	-12399	7068
#80	37.794	0.009	22.183	4.808	1.726	0.918	34.361	0	0.002	101.801	-12392	7066
#81	38.296	0	22.057	4.68	1.916	0.868	34.39	0.002	0	102.209	-12386	7064
#82	38.276	0	22.061	4.726	1.877	0.935	33.991	0.005	0	101.871	-12379	7062
#83	37.918	0	22.205	4.781	1.867	0.886	34.513	0.011	0.002	102.183	-12372	7060
#84	38.407	0.011	22.089	4.802	1.88	0.946	33.994	0.005	0	102.134	-12365	7058
#85	37.925	0.014	22.178	4.703	1.856	0.866	34.323	0	0	101.865	-12359	7056
#86	38.082	0.005	22.148	4.727	1.816	0.901	33.767	0.001	0	101.447	-12352	7054
#87	38.148	0	22.106	4.725	1.81	0.992	34.042	0	0.002	101.825	-12345	7052
#88	38.055	0.019	22.043	4.81	1.785	0.976	33.983	0	0	101.671	-12338	7051
#89	38.216	0	22.152	4.943	1.753	1.08	34.361	0	0	102.505	-12332	7049
#90	37.973	0.032	22.143	4.846	1.701	0.979	34.093	0.008	0.001	101.776	-12325	7047
#91	37.628	0.031	22.255	4.792	1.686	0.931	33.8	0.016	0.007	101.146	-12318	7045
#92	38.085	0.007	22.286	4.868	1.659	0.948	33.708	0.037	0	101.598	-12311	7043
#93	38.17	0.002	22.089	4.794	1.65	1.007	34.353	0	0	102.065	-12305	7041
#94	37.948	0.02	22.214	4.81	1.686	1.119	33.987	0	0	101.784	-12298	7039
#95	37.976	0	22.295	4.893	1.661	1.178	34.083	0.015	0	102.101	-12291	7037
#96	37.961	0.016	22.132	4.831	1.678	1.089	33.996	0	0	101.703	-12284	7036
#97	38.399	0	22.319	4.793	1.655	1.094	33.778	0.016	0.026	102.08	-12278	7034
#98	38.064	0.001	22.154	4.816	1.684	0.978	33.944	0.01	0	101.651	-12271	7032
#99	38.066	0	22.088	4.767	1.802	1.111	33.981	0.026	0.025	101.866	-12264	7030
#100	37.998	0	22.08	4.805	1.766	1.081	33.949	0.016	0.005	101.7	-12257	7028
#101	37.89	0.016	22.192	4.798	1.703	1.251	33.751	0.002	0	101.603	-12251	7026
#102	38.391	0.002	22.221	4.878	1.689	1.187	33.889	0.012	0.009	102.278	-12244	7024
#103	38.19	0	22.198	4.85	1.718	1.121	34.146	0	0	102.223	-12237	7022
#104	38.236	0.006	22.216	4.784	1.745	1.126	33.936	0.021	0.002	102.072	-12230	7021
#105	38.069	0	22.254	4.724	1.75	1.146	33.955	0.041	0.001	101.94	-12224	7019
#106	38.172	0	22.057	4.791	1.714	1.257	33.549	0.004	0.014	101.558	-12217	7017
#107	38.047	0.004	22.444	4.817	1.764	1.142	33.53	0.002	0	101.75	-12210	7015
#108	38.295	0	22.729	4.894	1.785	1.088	33.905	0.019	0	102.715	-12203	7013
#109	38.196	0.013	22.192	4.743	1.742	1.102	33.682	0.02	0	101.69	-12197	7011

	SiO_2	TiO_2	Al_2O_3	MgO	CaO	MnO	FeO	Na_2O	K_2O	Total	x	y
#110	38.172	0	22.153	4.763	1.864	1.146	33.57	0.017	0.016	101.701	-12190	7009
#111	38.335	0.038	22.234	4.713	1.875	1.269	34.113	0	0	102.577	-12183	7007
#112	40.061	0.026	23.001	4.944	1.885	1.259	34.011	0	0.005	105.192	-12176	7006
#113	33.923	0	20.347	4.105	1.948	1.195	33.855	0.003	0.011	95.387	-12170	7004
#114	38.33	0	22.22	4.782	1.915	1.185	33.445	0.008	0.016	101.901	-12163	7002
#115	38.291	0.006	22.175	4.754	1.946	1.298	33.751	0.013	0	102.234	-12156	7000
#116	39.313	0	23.13	5.122	1.987	1.327	33.415	0	0	104.294	-12149	6998
#117	35.167	0.019	21.908	4.691	1.882	1.252	33.837	0.009	0.01	98.775	-12142	6996
#118	33.713	0	21.715	4.566	1.97	1.298	33.498	0	0.002	96.762	-12136	6994
#119	34.279	0	21.673	4.667	1.899	1.175	33.457	0.006	0	97.156	-12129	6992
#120	37.488	0.016	21.836	4.654	1.925	1.253	33.387	0.008	0	100.567	-12122	6990
#121	37.312	0.003	22.516	4.75	2.054	1.258	33.075	0.007	0	100.975	-12115	6989
#122	35.846	0	21.14	4.41	1.951	1.192	32.568	0.013	0	97.12	-12109	6987
#123	35.297	0	21.718	4.482	1.936	1.205	31.892	0.016	0.015	96.561	-12102	6985
#124	25.359	0	18.27	3.529	1.822	1.035	24.755	0.084	0.031	74.885	-12095	6983
#125	0.622	0.032	0.066	0	48.646	0.017	0.539	0.066	0.011	49.999	-12088	6981
#126	0.05	0	0.002	0	51.964	0.024	0.403	0.067	0	52.51	-12082	6979
#127	0.037	0.001	0	0	51.89	0.049	0.397	0.074	0	52.448	-12075	6977
#128	0.05	0	0	0	52.076	0.028	0.377	0.058	0	52.589	-12068	6975
#129	0.114	0	0.023	0	51.89	0.079	0.476	0.039	0	52.621	-12061	6974
#130	0.063	0.005	0.009	0	51.555	0.006	0.454	0.073	0	52.165	-12055	6972
#131	0.147	0.003	0.039	0	52.162	0.051	0.629	0.051	0	53.082	-12048	6970
#132	32.613	0.027	20.492	4.451	1.719	1.049	32.861	0.034	0.002	93.248	-12041	6968
#133	33.721	0.066	21.061	4.321	1.835	1.201	33.023	0.038	0.01	95.276	-12034	6966
#134	37.861	0.049	22.074	4.562	2.055	1.381	33.465	0.002	0	101.449	-12028	6964
#135	37.936	0.111	21.958	4.625	1.956	1.424	33.336	0.027	0.013	101.386	-12021	6962
#136	37.772	0.15	22.056	4.497	2.021	1.303	32.951	0	0.002	100.752	-12014	6960
#137	38.145	0.164	21.954	4.328	1.993	1.395	33.443	0.02	0	101.442	-12007	6959
#138	37.87	0.053	21.949	4.723	1.911	1.429	33.651	0.022	0.006	101.614	-12001	6957
#139	38.068	0.024	22.021	4.77	1.931	1.314	33.812	0.019	0	101.959	-11994	6955
#140	38.117	0.012	22.035	4.676	1.958	1.311	33.443	0.022	0	101.574	-11987	6953

	SiO_2	TiO_2	Al_2O_3	MgO	CaO	MnO	FeO	Na_2O	K_2O	Total	x	y
#141	38.13	0.003	22.039	4.678	1.924	1.387	33.748	0.009	0.016	101.934	-11980	6951
#142	38.37	0	22.109	4.653	1.991	1.388	33.549	0.016	0.006	102.082	-11974	6949
#143	38.462	0.006	21.804	4.636	1.982	1.359	33.403	0.006	0.016	101.674	-11967	6947
#144	37.818	0.011	21.857	4.603	1.901	1.32	33.526	0.005	0	101.041	-11960	6945
#145	38.175	0.016	21.984	4.724	2.018	1.387	33.83	0	0.005	102.139	-11953	6944
#146	38.098	0	21.948	4.767	1.956	1.323	33.445	0.019	0.002	101.558	-11947	6942
#147	38.309	0	21.975	4.592	1.932	0	33.887	0	0.002	100.697	-11940	6940
#148	38.521	0	21.967	4.673	1.932	1.408	33.563	0.002	0.005	102.071	-11933	6938
#149	84.081	0.023	7.337	0.956	0.467	0.277	6.643	0	0.011	99.795	-11926	6936
#150	98.486	0	0.022	0.007	0.017	0.061	0.755	0	0	99.348	-11920	6934
#151	99.402	0	0.038	0	0.003	0.011	0.664	0.009	0	100.127	-11913	6932
#152	99.347	0	0.014	0.005	0.021	0	0.688	0.021	0	100.096	-11906	6930
#153	99.422	0	0.013	0	0	0.033	0.61	0	0	100.078	-11899	6929
#154	99.567	0	0.014	0.001	0	0.067	0.614	0.003	0	100.266	-11893	6927
#155	99.499	0	0.029	0	0.016	0.02	0.63	0.001	0.01	100.205	-11886	6925
#156	99.504	0.003	0.008	0.001	0.014	0.041	0.635	0.012	0	100.218	-11879	6923
#157	99.481	0	0.021	0	0.01	0.035	0.649	0	0	100.196	-11872	6921
#158	99.472	0	0	0	0.018	0	0.693	0.007	0.001	100.191	-11866	6919
#159	99.823	0	0.016	0.004	0	0	0.759	0	0	100.602	-11859	6917
#160	84.252	0	3.81	0.726	0.488	0.302	7.69	0.01	0.003	97.281	-11852	6915
#161	39.528	0.018	23.474	5.175	1.931	1.447	33.475	0.02	0.016	105.084	-11845	6913
#162	34.802	0.003	21	4.419	2.012	1.404	33.366	0	0.005	97.011	-11839	6912
#163	35.045	0	21.449	4.567	2.003	1.412	33.801	0	0	98.277	-11832	6910
#164	36.756	0.012	21.232	4.549	1.968	1.502	33.556	0	0	99.575	-11825	6908
#165	37.987	0.014	21.605	4.57	1.912	1.451	33.717	0.005	0.005	101.266	-11818	6906
#166	37.89	0.022	21.735	4.518	1.901	1.384	33.829	0	0.003	101.282	-11812	6904
#167	38.052	0	21.851	4.59	1.967	1.43	33.381	0	0	101.271	-11805	6902
#168	37.918	0.021	22.009	4.691	1.987	1.377	33.683	0.027	0.008	101.721	-11798	6900
#169	38.144	0.004	21.933	4.71	1.9	1.309	34.259	0	0	102.259	-11791	6898
#170	37.762	0	22.171	4.655	1.917	1.399	33.609	0	0	101.513	-11785	6897
#171	99.228	0.023	0.028	0	0.005	0	0.769	0	0.011	100.064	-11778	6895

	SiO_2	TiO_2	Al_2O_3	MgO	CaO	MnO	FeO	Na_2O	K_2O	Total	x	y
#172	99.14	0.013	0.031	0.009	0.002	0.017	0.647	0	0.008	99.867	-11771	6893
#173	99.094	0.016	0.006	0.023	0.006	0.03	0.519	0	0	99.694	-11764	6891
#174	99.194	0	0.001	0.002	0.015	0.017	0.467	0	0	99.696	-11757	6889
#175	98.773	0	0	0	0	0.022	0.371	0	0	99.166	-11751	6887
#176	99.48	0	0.147	0	0.001	0.02	0.448	0.06	0.011	100.167	-11744	6885
#177	99.449	0.004	0.016	0.009	0.007	0	0.436	0	0	99.921	-11737	6883
#178	99.008	0.001	0	0	0	0.02	0.427	0.003	0	99.459	-11730	6882
#179	98.956	0	0.014	0	0	0.024	0.514	0.002	0.015	99.525	-11724	6880
#180	99.195	0	0.018	0.007	0	0.004	0.56	0	0.003	99.787	-11717	6878
#181	76.817	0	6.937	1.479	0.736	0.472	12.779	0.009	0.002	99.231	-11710	6876
#182	38.287	0	21.924	4.721	2.008	1.344	33.289	0.025	0.004	101.602	-11703	6874
#183	38.51	0.026	22.031	4.6	1.868	1.424	33.804	0	0.008	102.271	-11697	6872
#184	38.216	0.023	21.993	4.687	1.907	1.439	33.305	0	0.005	101.575	-11690	6870
#185	38.254	0	22.057	4.668	1.963	1.436	33.582	0.011	0.002	101.973	-11683	6868
#186	38.093	0.021	22.071	4.67	1.943	1.434	33.462	0.023	0.015	101.732	-11676	6867
#187	37.886	0.037	21.886	4.598	1.935	1.452	33.562	0.016	0.012	101.384	-11670	6865
#188	38.144	0.016	21.958	4.7	1.867	1.325	33.508	0.029	0.004	101.551	-11663	6863
#189	38.314	0	21.925	4.637	1.972	1.42	33.396	0.013	0.004	101.681	-11656	6861
#190	59.714	0	14.492	3.094	1.297	0.939	23.502	0.004	0	103.042	-11649	6859
#191	98.784	0	0.031	0.013	0	0.059	0.815	0	0.002	99.704	-11643	6857
#192	99.236	0.018	0.004	0	0.013	0.067	0.767	0.006	0	100.111	-11636	6855
#193	97.425	0.009	0.016	0	0.005	0.059	0.633	0	0.01	98.157	-11629	6853
#194	99.023	0.002	0.01	0	0.013	0	0.693	0	0.001	99.742	-11622	6852
#195	98.781	0	0.019	0	0.001	0.039	0.66	0	0	99.5	-11616	6850
#196	99.419	0.002	0	0	0.005	0.035	0.626	0	0.008	100.095	-11609	6848
#197	99.537	0.03	0.008	0.009	0.004	0.007	0.825	0	0.006	100.426	-11602	6846
#198	97.078	0	0.359	0.049	0.028	0.056	1.127	0.005	0.011	98.713	-11595	6844
#199	38.129	0	21.942	4.594	1.968	1.394	33.205	0.022	0.002	101.256	-11589	6842
#200	38.133	0.002	22.07	4.697	1.948	1.583	33.748	0.008	0	102.189	-11582	6840
#201	38.1	0.031	21.971	4.648	1.948	1.527	33.363	0.008	0	101.596	-11575	6838
#202	38.132	0.007	22.042	4.669	2.001	1.371	33.835	0.01	0.003	102.07	-11568	6836

	SiO_2	TiO_2	Al_2O_3	MgO	CaO	MnO	FeO	Na_2O	K_2O	Total	x	y
#203	38.166	0.028	22.03	4.698	1.964	1.414	33.57	0.026	0.008	101.904	-11562	6835
#204	38.206	0.024	21.977	4.662	1.989	1.38	33.111	0	0.004	101.353	-11555	6833
#205	38.35	0.01	21.996	4.579	1.869	1.379	32.594	0	0	100.777	-11548	6831
#206	90.948	0	3.493	0.751	0.396	0.266	7.094	0	0	102.948	-11541	6829
#207	55.456	0.01	17.063	3.574	1.477	1.08	26.215	0	0	104.875	-11535	6827
#208	38.248	0	22.147	4.679	1.955	1.443	33.431	0.014	0	101.917	-11528	6825
#209	37.969	0.015	21.811	4.688	1.924	1.415	33.073	0	0	100.895	-11521	6823
#210	38.354	0.033	22.009	4.673	1.973	1.378	33.417	0.008	0	101.845	-11514	6821
#211	38.426	0.016	21.856	4.77	2.039	1.5	33.319	0.011	0	101.937	-11508	6820
#212	38.211	0	21.957	4.751	1.915	1.357	33.774	0.012	0.011	101.988	-11501	6818
#213	38.36	0	22.141	4.566	1.969	1.494	33.296	0.024	0	101.85	-11494	6816
#214	99.47	0.031	0.068	0	0.009	0.05	0.72	0	0.013	100.361	-11487	6814
#215	99.132	0	0.018	0.004	0.001	0.052	0.562	0	0.001	99.77	-11481	6812
#216	99.732	0.001	0.018	0.008	0.018	0.037	0.589	0.012	0.001	100.416	-11474	6810
#217	99.633	0.012	0.015	0.003	0.016	0.015	0.674	0	0.013	100.381	-11467	6808
#218	38.274	0	22.185	4.675	1.934	1.392	33.771	0	0.002	102.233	-11460	6806
#219	38.791	0	22.039	4.663	1.907	1.483	33.528	0	0	102.411	-11454	6805
#220	38.237	0.008	22.02	4.613	1.947	1.515	33.744	0.016	0.007	102.107	-11447	6803
#221	38.138	0.004	22.074	4.626	1.99	1.494	33.902	0	0.002	102.23	-11440	6801
#222	38.06	0.031	22.18	4.706	1.962	1.575	33.793	0.008	0	102.315	-11433	6799
#223	38.371	0.026	22.217	4.732	1.912	1.386	33.646	0.027	0.011	102.328	-11427	6797
#224	38.248	0	22.089	4.653	1.962	1.42	33.844	0.017	0.003	102.236	-11420	6795
#225	38.069	0.004	22.097	4.713	1.969	1.428	33.442	0.021	0	101.743	-11413	6793
#226	39.156	0.015	21.78	4.646	1.926	1.388	33.451	0.022	0.016	102.4	-11406	6791
#227	98.387	0.006	0.561	0.107	0.065	0.026	1.134	0.018	0	100.304	-11400	6790
#228	98.655	0	0.038	0	0.039	0	0.672	0.032	0.017	99.453	-11393	6788
#229	95.548	0.012	0.047	0.062	0.342	0.007	0.581	0.092	0.03	96.721	-11386	6786
#230	94.325	0	0.042	0.105	0.513	0	0.485	0.295	0.133	95.898	-11379	6784
#231	97.545	0	0.024	0.026	0.143	0	0.487	0.155	0.105	98.485	-11372	6782
#232	98.636	0	0.014	0.013	0.021	0.022	0.398	0.057	0.013	99.174	-11366	6780
#233	98.862	0.021	0.009	0.002	0.03	0.033	0.365	0.032	0.02	99.374	-11359	6778

	SiO_2	TiO_2	Al_2O_3	MgO	CaO	MnO	FeO	Na_2O	K_2O	Total	x	y
#234	99.039	0	0.007	0.002	0.022	0.017	0.309	0.018	0.015	99.429	-11352	6776
#235	98.024	0.009	0.011	0.007	0.014	0.013	0.326	0.03	0.029	98.463	-11345	6775
#236	97.617	0.004	0.011	0.013	0.065	0.017	0.353	0.089	0.037	98.206	-11339	6773
#237	96.837	0	0.585	0.108	0.096	0.076	0.707	0.07	0.044	98.523	-11332	6771
#238	97.695	0	0.178	0.034	0.047	0.03	0.556	0.122	0.071	98.733	-11325	6769
#239	99.308	0	0.016	0.012	0.045	0	0.413	0.054	0.031	99.879	-11318	6767
#240	97.994	0.013	0	0	0.015	0.046	0.388	0.049	0.02	98.525	-11312	6765
#241	98.516	0	0.016	0.01	0.035	0.015	0.398	0.023	0.017	99.03	-11305	6763
#242	99.027	0.014	0.02	0.004	0.026	0.059	0.421	0.04	0.009	99.62	-11298	6761
#243	99.153	0	0.003	0.003	0.028	0.017	0.374	0.017	0.021	99.616	-11291	6759
#244	99.136	0.005	0.003	0.01	0.034	0.026	0.423	0.058	0.038	99.733	-11285	6758
#245	98.494	0.004	0.004	0.015	0.041	0.03	0.467	0.067	0.023	99.145	-11278	6756
#246	98.777	0.008	0.014	0.01	0.063	0	0.637	0.041	0.022	99.572	-11271	6754
#247	88.657	0.005	4.24	0.874	0.55	0.334	5.299	0.034	0.009	100.002	-11264	6752
#248	38.377	0.022	21.94	4.679	1.996	1.422	33.483	0.045	0.013	101.977	-11258	6750
#249	38.074	0	22.003	4.611	1.977	1.406	33.423	0.03	0.012	101.536	-11251	6748
#250	38.083	0	21.486	4.581	2.07	1.336	32.806	0.157	0.033	100.552	-11244	6746
#251	37.01	0.004	21.527	4.51	2.181	1.321	31.758	0.208	0.056	98.575	-11237	6744
#252	37.296	0.022	21.581	4.619	2.102	1.391	32.13	0.122	0.025	99.288	-11231	6743
#253	38.538	0	22.063	4.691	2.012	1.406	33.822	0.007	0	102.539	-11224	6741
#254	38.332	0.025	22.013	4.646	2.002	1.388	33.492	0.003	0	101.901	-11217	6739
#255	38.257	0	22.118	4.729	1.996	1.483	33.321	0.005	0	101.909	-11210	6737
#256	38.186	0	21.893	4.638	2.034	1.499	33.352	0.016	0.008	101.626	-11204	6735
#257	38.426	0.001	21.987	4.669	1.955	1.527	33.953	0.016	0.006	102.54	-11197	6733
#258	38.445	0	22.106	4.693	1.984	1.47	34.211	0	0	102.909	-11190	6731
#259	38.382	0.023	22.055	4.674	2.022	1.472	33.823	0	0.002	102.453	-11183	6729
#260	38.257	0.051	22.165	4.675	2.007	1.472	33.93	0	0.002	102.559	-11177	6728
#261	38.494	0	22.076	4.635	2.063	1.417	33.364	0	0.003	102.052	-11170	6726
#262	38.54	0	22.057	4.73	1.936	1.37	33.351	0.01	0	101.994	-11163	6724
#263	38.047	0	22.055	4.637	2.006	1.437	34.304	0.016	0	102.502	-11156	6722
#264	38.124	0	22.179	4.741	2.004	1.515	34.483	0.031	0.008	103.085	-11150	6720

	SiO_2	TiO_2	Al_2O_3	MgO	CaO	MnO	FeO	Na_2O	K_2O	Total	x	y
#265	38.137	0	22.114	4.663	1.947	1.418	33.545	0.028	0.006	101.858	-11143	6718
#266	38.045	0	21.91	4.68	1.984	1.462	33.779	0	0.001	101.861	-11136	6716
#267	37.765	0.166	21.423	4.545	1.939	1.353	33.125	0.031	0.009	100.356	-11129	6714
#268	64.264	0	8.54	2.141	1.03	0.717	19.791	0.103	0.04	96.626	-11123	6713
#269	38.084	0	21.477	4.368	1.968	1.464	33.348	0	0	100.709	-11116	6711
#270	37.735	0	22.605	4.718	1.947	1.378	33.471	0.03	0.016	101.9	-11109	6709
#271	38.232	0.003	22.012	4.564	1.906	1.298	33.851	0	0.01	101.876	-11102	6707
#272	38.219	0.011	22.16	4.684	1.959	1.405	33.974	0	0	102.412	-11096	6705
#273	38.554	0.012	22.036	4.708	1.952	1.419	34.353	0.004	0.012	103.05	-11089	6703
#274	37.687	0.007	22.951	4.913	1.85	1.483	33.438	0.016	0.019	102.364	-11082	6701
#275	34.83	0	20.874	4.316	1.985	1.366	33.023	0.015	0	96.409	-11075	6699
#276	38.563	0	22.02	4.416	1.977	1.554	34.345	0	0.006	102.881	-11069	6697
#277	38.144	0.001	21.844	4.244	2.044	1.542	34.255	0.009	0.004	102.087	-11062	6696
#278	38.284	0.016	22.072	4.051	1.991	1.381	34.77	0	0.006	102.571	-11055	6694
#279	39.426	0.015	21.502	3.922	1.959	1.514	33.35	0.027	0.03	101.745	-11048	6692
#280	92.557	0	0.715	0.117	0.09	0.037	2.408	0.002	0	95.926	-11042	6690
#281	99.435	0.013	0.014	0.012	0.006	0	0.573	0	0	100.053	-11035	6688
#282	99.809	0.015	0.014	0.005	0.003	0	0.587	0.001	0	100.434	-11028	6686
#283	99.625	0.002	0.009	0	0.035	0	0.521	0.006	0.004	100.202	-11021	6684
#284	99.817	0.021	0	0	0.024	0.072	0.44	0	0	100.374	-11014	6682
#285	99.773	0	0.005	0	0	0.037	0.444	0	0.018	100.277	-11008	6681
#286	100.094	0	0	0.007	0.001	0.022	0.467	0	0	100.591	-11001	6679
#287	100.163	0.074	0.013	0	0	0.024	0.425	0	0	100.699	-10994	6677
#288	99.636	0.013	0.01	0	0	0.015	0.519	0.004	0.004	100.201	-10987	6675
#289	99.701	0.02	0.043	0	0.011	0	0.488	0.01	0.004	100.277	-10981	6673
#290	99.337	0.005	0.429	0.014	0	0.046	0.711	0.012	0.068	100.622	-10974	6671
#291	36.962	0	21.353	3.193	1.995	1.517	34.871	0.012	0	99.903	-10967	6669
#292	38.194	0.013	22.072	3.928	2.04	1.563	34.571	0.008	0.008	102.397	-10960	6667
#293	38.3	0	22.242	4.175	2.008	1.529	34.692	0.003	0.015	102.964	-10954	6666
#294	38.364	0.005	21.864	4.234	1.973	1.372	34.164	0	0.015	101.991	-10947	6664
#295	38.444	0.011	22.002	4.322	2.044	1.391	34.027	0	0	102.241	-10940	6662

	SiO_2	TiO_2	Al_2O_3	MgO	CaO	MnO	FeO	Na_2O	K_2O	Total	x	y
#296	38.248	0.015	22.003	4.329	2.078	1.427	34.085	0	0	102.185	-10933	6660
#297	38.336	0.003	22.04	4.514	2.04	1.364	34.238	0.016	0.011	102.562	-10927	6658
#298	38.362	0.025	21.912	4.519	2.004	1.468	34.004	0.019	0.001	102.314	-10920	6656
#299	37.525	0	22.273	4.511	1.978	1.494	33.596	0.014	0.012	101.403	-10913	6654
#300	36.96	0	20.874	4.2	1.971	1.441	33.137	0.007	0	98.59	-10906	6652
#301	38.196	0.027	22.053	4.312	2.021	1.512	33.904	0.002	0.004	102.031	-10900	6651
#302	38.395	0.014	21.999	4.384	2.044	1.437	34.31	0	0	102.583	-10893	6649
#303	38.087	0.036	21.788	4.313	2.093	1.467	34.147	0.031	0	101.962	-10886	6647
#304	38.66	0.046	21.876	4.211	2.018	1.449	34.67	0	0	102.93	-10879	6645
#305	38.181	0.031	22.057	4.31	2.059	1.467	34.479	0.002	0	102.586	-10873	6643
#306	38.257	0.086	22.014	4.212	2.029	1.423	34.296	0	0.003	102.32	-10866	6641
#307	38.443	0.168	22.049	4.182	2.054	1.507	34.54	0	0	102.943	-10859	6639
#308	38.412	0.316	21.743	4.074	2.032	1.32	33.982	0.016	0	101.895	-10852	6637
#309	38.4	0.438	21.467	4.001	1.997	1.421	34.051	0.011	0	101.786	-10846	6636
#310	100.329	0.138	0.265	0.041	0.044	0.061	0.461	0	0.002	101.341	-10839	6634
#311	100.183	0.092	0.044	0.001	0	0.009	0.347	0	0.006	100.682	-10832	6632
#312	99.989	0.085	0.01	0	0.011	0.026	0.322	0.008	0	100.451	-10825	6630
#313	99.819	0.063	0.021	0	0	0.044	0.353	0.008	0.002	100.31	-10819	6628
#314	98.27	0.049	0.109	0.029	0	0.024	0.452	0	0.01	98.943	-10812	6626
#315	44.655	0.051	21.364	4.349	1.728	1.189	28.873	0	0	102.209	-10805	6624
#316	19.949	0.052	11.823	2.161	1.115	0.579	35.003	0.167	0.149	70.998	-10798	6622
#317	11.931	0.046	10.23	1.905	1.522	0.872	20.399	0.133	0.127	47.165	-10792	6620
#318	38.147	0.023	22.049	4.462	1.958	1.375	34.057	0.019	0.008	102.098	-10785	6619
#319	38.869	0	22.146	4.648	2.001	1.524	33.617	0	0	102.805	-10778	6617
#320	94.062	0	2.6	0.534	0.292	0.17	4.289	0.004	0.01	101.961	-10771	6615
#321	100.011	0.018	0.015	0	0.01	0.035	0.801	0	0.007	100.897	-10765	6613
#322	99.764	0	0.087	0.009	0.009	0.091	0.916	0.004	0.021	100.901	-10758	6611
#323	38.614	0	22.055	4.595	2.082	1.412	33.755	0.016	0	102.529	-10751	6609
#324	38.374	0	21.872	4.759	2.017	1.458	33.923	0.017	0	102.42	-10744	6607
#325	38.34	0.01	22.117	4.685	2.016	1.363	33.86	0	0	102.391	-10738	6605
#326	38.43	0	22.087	4.716	2.093	1.383	34.175	0.005	0	102.889	-10731	6604

	SiO_2	TiO_2	Al_2O_3	MgO	CaO	MnO	FeO	Na_2O	K_2O	Total	x	y
#327	38.68	0.006	22.051	4.656	2.155	1.297	33.715	0.015	0.006	102.581	-10724	6602
#328	38.4	0.006	22.145	4.715	2.094	1.475	33.902	0.013	0.01	102.76	-10717	6600
#329	41.671	0.027	20.536	4.373	1.882	1.408	32.551	0	0.01	102.458	-10711	6598
#330	38.426	0.007	22.262	4.732	2.086	1.361	34.186	0.023	0	103.083	-10704	6596
#331	38.585	0.004	22.102	4.721	2.138	1.389	34.063	0.001	0	103.003	-10697	6594
#332	38.35	0	22.01	4.692	2.155	1.356	34.314	0.036	0.002	102.915	-10690	6592
#333	38.504	0.035	22.077	4.694	2.08	1.308	34.196	0	0	102.894	-10684	6590
#334	38.395	0	21.96	4.779	2.065	1.284	34.096	0	0	102.579	-10677	6589
#335	38.048	0.012	21.776	4.696	2.093	1.301	34.266	0	0.016	102.208	-10670	6587
#336	38.447	0.016	21.917	4.691	2.102	1.357	33.843	0	0	102.373	-10663	6585
#337	38.643	0	21.936	4.786	2.085	1.471	34.035	0.024	0.004	102.984	-10657	6583
#338	38.228	0	22.167	4.833	1.998	1.281	34.537	0	0.012	103.056	-10650	6581
#339	98.235	0.004	0.69	0.123	0.064	0.039	1.461	0.01	0.005	100.631	-10643	6579
#340	100.046	0	0.026	0	0.026	0.085	0.97	0	0	101.153	-10636	6577
#341	91.627	0.011	2.003	0.386	0.253	0.224	4.296	0.001	0.007	98.808	-10629	6575
#342	39.266	0.032	22.655	4.785	2.028	1.315	34.185	0.009	0.008	104.283	-10623	6574
#343	31.431	0.057	13.787	0.565	0.439	0.239	3.423	0.14	0.085	50.166	-10616	6572
#344	40.226	0.021	1.545	0.086	0.468	0.009	1.459	0.039	0.114	43.967	-10609	6570
#345	99.784	0.006	0.027	0.012	0.015	0.004	0.531	0	0.005	100.384	-10602	6568
#346	100.021	0.002	0.017	0	0	0	0.492	0	0	100.532	-10596	6566
#347	100.064	0	0.015	0.009	0.011	0	0.411	0	0.003	100.513	-10589	6564
#348	100.265	0.027	0.026	0	0	0.011	0.432	0	0.001	100.762	-10582	6562
#349	99.631	0	0.009	0	0.018	0.007	0.392	0.018	0	100.075	-10575	6560
#350	100.103	0.016	0.023	0	0.011	0.057	0.461	0	0	100.671	-10569	6559
#351	100.449	0	0.009	0	0.012	0	0.49	0	0	100.96	-10562	6557
#352	99.254	0.012	0.001	0	0.003	0.03	0.5	0.001	0	99.801	-10555	6555
#353	100.301	0.006	0.032	0	0.013	0.022	0.606	0	0.001	100.981	-10548	6553
#354	38.835	0.006	22.099	4.652	2.088	1.355	33.991	0.009	0	103.035	-10542	6551
#355	38.554	0	21.918	4.677	2.159	1.411	34.442	0.008	0	103.169	-10535	6549
#356	38.472	0	22.061	4.671	2.168	1.386	34.59	0.002	0.006	103.356	-10528	6547
#357	38.661	0	22.027	4.643	2.128	1.428	33.813	0.015	0	102.715	-10521	6545

	SiO_2	TiO_2	Al_2O_3	MgO	CaO	MnO	FeO	Na_2O	K_2O	Total	x	y
#358	38.875	0.026	22.111	4.79	2.094	1.185	34.154	0.008	0	103.243	-10515	6543
#359	38.374	0.032	22.326	4.75	2.072	1.32	34.454	0	0.014	103.342	-10508	6542
#360	38.344	0.054	22.267	4.646	2.097	1.406	33.942	0.005	0	102.761	-10501	6540
#361	38.522	0.036	22.059	4.706	2.198	1.396	34.102	0	0.006	103.025	-10494	6538
#362	38.313	0.072	22.13	4.57	2.145	1.294	34.205	0	0	102.729	-10488	6536
#363	38.303	0.232	22.011	4.245	2.122	1.42	34.91	0.03	0	103.273	-10481	6534
#364	38.091	0.58	22.146	3.41	2.123	1.553	35.672	0	0.002	103.577	-10474	6532
#365	0.071	51.468	0	0.142	0.009	0.293	48.303	0.004	0.01	100.3	-10467	6530
#366	0.093	50.993	0.073	0.126	0.037	0.291	48.343	0	0.002	99.958	-10461	6528
#367	38.056	0.753	21.812	3.35	2.143	1.539	35.566	0	0	103.219	-10454	6527
#368	38.363	0.295	22.104	4.259	2.284	1.303	34.994	0	0.009	103.611	-10447	6525
#369	38.765	0.121	22.033	4.59	2.356	1.279	33.979	0.006	0.001	103.13	-10440	6523
#370	38.306	0.089	22.048	4.64	2.328	1.266	34.457	0.009	0.006	103.149	-10434	6521
#371	38.497	0.029	21.958	4.633	2.337	1.299	34.162	0.022	0.003	102.94	-10427	6519
#372	38.465	0.012	21.988	4.668	2.293	1.239	34.496	0.027	0.011	103.199	-10420	6517
#373	38.432	0.007	22.195	4.707	2.372	1.319	33.975	0.033	0	103.04	-10413	6515
#374	38.673	0.01	22.111	4.584	2.322	1.265	34.001	0.013	0	102.979	-10407	6513
#375	38.344	0.041	22.153	4.682	2.535	1.248	33.938	0.03	0.005	102.976	-10400	6512
#376	38.737	0.036	22.082	4.577	2.419	1.297	34.126	0.016	0.01	103.3	-10393	6510
#377	38.466	0.028	22.069	4.622	2.475	1.301	34.105	0	0	103.066	-10386	6508
#378	38.729	0	22.139	4.685	2.315	1.264	34.553	0.025	0	103.71	-10380	6506
#379	38.701	0	22.33	4.623	2.26	1.214	34.048	0.016	0	103.192	-10373	6504
#380	22.337	0.002	24.2	5.912	0.053	0.218	34.714	0.023	0.024	87.483	-10366	6502
#381	53.962	0.015	0.401	2.581	0.716	1.472	24.257	0.005	0	83.409	-10359	6500
#382	92.344	0.009	1.648	0.291	0.205	0.141	3.341	0	0.015	97.994	-10353	6498
#383	38.545	0.02	22.158	4.657	2.34	1.252	33.986	0	0	102.958	-10346	6497
#384	38.475	0.002	22.067	4.616	2.369	1.392	34.79	0.005	0	103.716	-10339	6495
#385	38.738	0.013	22.149	4.657	2.276	1.279	34.05	0.009	0.005	103.176	-10332	6493
#386	38.692	0.022	21.906	4.471	2.349	1.298	34.39	0	0	103.128	-10326	6491
#387	38.704	0.017	21.981	4.635	2.257	1.327	34.193	0.018	0.007	103.139	-10319	6489
#388	38.816	0	21.747	4.634	2.28	1.213	34.265	0	0	102.955	-10312	6487

	SiO_2	TiO_2	Al_2O_3	MgO	CaO	MnO	FeO	Na_2O	K_2O	Total	x	y
#389	38.598	0.034	21.988	4.662	2.361	1.358	33.897	0.03	0	102.928	-10305	6485
#390	38.589	0.023	22.07	4.563	2.389	1.239	34.389	0	0.001	103.263	-10299	6483
#391	38.632	0.01	21.835	4.671	2.402	1.27	34.328	0	0	103.148	-10292	6482
#392	38.41	0.025	21.924	4.594	2.413	1.334	34.403	0.007	0.006	103.116	-10285	6480
#393	38.543	0	21.885	4.516	2.386	1.226	33.738	0.009	0.011	102.314	-10278	6478
#394	38.674	0.017	22.032	4.718	2.387	1.191	34.352	0.035	0.003	103.409	-10272	6476
#395	38.241	0.023	22.025	4.633	2.341	1.231	34.263	0.009	0.013	102.779	-10265	6474
#396	38.513	0.027	21.983	4.636	2.297	1.274	34.033	0.012	0.003	102.778	-10258	6472
#397	38.367	0.025	21.994	4.636	2.283	1.265	34.623	0.02	0.002	103.215	-10251	6470
#398	38.425	0.017	21.949	4.596	2.276	1.14	34.201	0	0.01	102.614	-10244	6468
#399	38.797	0	21.997	4.583	0.127	1.231	34.648	0.02	0.008	101.411	-10238	6466
#400	38.636	0.006	21.935	4.594	2.318	1.303	34.074	0	0	102.866	-10231	6465
#401	38.724	0.017	21.828	4.638	2.383	1.27	34.224	0.036	0	103.12	-10224	6463
#402	38.256	0.026	21.953	4.663	2.281	1.201	34.391	0.025	0.004	102.8	-10217	6461
#403	38.635	0.005	21.848	4.604	2.395	1.239	34.458	0	0	103.184	-10211	6459
#404	38.804	0.001	22.024	4.656	2.324	1.146	34.647	0	0	103.602	-10204	6457
#405	38.882	0	22.013	4.538	2.361	1.27	34.09	0	0	103.154	-10197	6455
#406	38.558	0	21.909	4.699	2.364	1.14	34.233	0.007	0	102.91	-10190	6453
#407	38.634	0.007	21.923	4.578	2.345	1.235	34.297	0	0	103.019	-10184	6451
#408	38.597	0.016	21.88	4.629	2.286	1.255	34.636	0	0	103.299	-10177	6450
#409	38.552	0.027	22	4.558	2.464	1.201	34.117	0	0	102.919	-10170	6448
#410	38.548	0.004	22	4.602	2.395	1.298	34.173	0	0	103.02	-10163	6446
#411	38.681	0.026	22.131	4.565	2.498	1.188	34.011	0.007	0.011	103.118	-10157	6444
#412	38.654	0.022	22.101	4.565	2.489	1.252	34.466	0.001	0	103.55	-10150	6442
#413	38.605	0.004	22.053	4.452	2.598	1.131	34.008	0	0	102.851	-10143	6440
#414	38.692	0.02	22.032	4.436	2.463	1.155	34.124	0.02	0.011	102.953	-10136	6438
#415	32.413	0.009	1.243	0.267	0.289	0.225	6.778	0	0.065	41.289	-10130	6436
#416	38.526	0	21.936	4.498	2.469	1.237	34.481	0.016	0.003	103.166	-10123	6435
#417	38.45	0.001	21.897	4.609	2.473	1.233	34.343	0.006	0	103.012	-10116	6433
#418	38.468	0.02	22.089	4.566	2.497	1.203	34.393	0.023	0.008	103.267	-10109	6431
#419	38.769	0.009	22.114	4.535	2.437	1.063	34.485	0.002	0.035	103.449	-10103	6429

	SiO_2	TiO_2	Al_2O_3	MgO	CaO	MnO	FeO	Na_2O	K_2O	Total	x	y
#420	38.285	0.009	22.003	4.57	2.492	1.17	34.543	0.007	0.013	103.092	-10096	6427
#421	38.718	0.041	22.145	4.547	2.483	1.133	33.711	0.001	0	102.779	-10089	6425
#422	38.549	0	21.989	4.724	2.356	1.102	34.479	0	0	103.199	-10082	6423
#423	38.51	0.027	22.189	4.572	2.373	1.163	34.254	0	0	103.088	-10076	6421
#424	38.806	0.027	22.122	4.56	2.457	1.068	34.382	0	0	103.422	-10069	6420
#425	38.645	0.032	21.946	4.641	2.316	1.275	33.991	0.019	0.003	102.868	-10062	6418
#426	38.472	0.009	22.235	4.664	2.307	1.23	34.068	0.003	0.007	102.995	-10055	6416
#427	38.502	0.032	21.966	4.549	2.351	1.213	34.054	0.012	0	102.679	-10049	6414
#428	38.669	0.001	22.011	4.679	2.416	1.205	34.313	0.013	0.003	103.31	-10042	6412
#429	38.218	0.031	22.008	4.585	2.437	1.152	34.278	0	0	102.709	-10035	6410
#430	38.65	0.013	22.077	4.661	2.296	1.098	34.25	0.019	0.003	103.067	-10028	6408
#431	38.464	0.032	22.053	4.615	2.249	1.117	34.755	0.009	0	103.294	-10022	6406
#432	38.399	0.017	22.061	4.604	2.39	1.222	34.159	0	0	102.852	-10015	6404
#433	38.492	0.007	21.876	4.436	2.353	1.174	34.626	0	0.014	102.978	-10008	6403
#434	38.523	0.004	22.084	4.243	2.237	1.171	35.194	0.002	0.019	103.477	-10001	6401
#435	38.298	0.015	22.066	4.4	2.319	1.054	34.915	0.006	0	103.073	-9995	6399
#436	34.281	0.008	20.003	3.94	3.184	0.983	26.611	0.034	0.017	89.061	-9988	6397
#437	38.711	0.017	22.163	4.656	2.275	1.139	33.989	0.003	0	102.953	-9981	6395
#438	38.496	0.003	22.117	4.549	2.237	1.051	34.673	0.003	0.003	103.132	-9974	6393
#439	38.524	0.016	22.102	4.602	2.138	1.099	34.779	0.005	0.014	103.279	-9968	6391
#440	38.372	0.013	22.181	4.637	2.031	1.152	34.544	0	0	102.93	-9961	6389
#441	38.723	0.038	22.048	4.676	1.987	1.194	34.865	0.013	0	103.544	-9954	6388
#442	38.467	0	22.059	4.741	2.067	1.171	35.127	0.011	0.015	103.658	-9947	6386
#443	38.009	0.008	21.605	4.491	2.142	1.065	33.98	0.027	0	101.327	-9941	6384
#444	38.4	0.022	22.144	4.686	2.015	1.076	35.141	0.018	0.007	103.509	-9934	6382
#445	38.635	0.008	22.01	4.688	2.146	1.079	34.686	0.016	0	103.268	-9927	6380
#446	38.505	0.009	22.089	4.607	2.017	1.01	34.509	0.005	0	102.751	-9920	6378
#447	38.373	0.007	22.002	4.65	1.889	1.178	34.705	0.007	0	102.811	-9914	6376
#448	38.61	0.017	22.198	4.809	1.974	1.16	34.632	0.009	0.007	103.416	-9907	6374
#449	38.488	0	22.001	4.677	1.94	0.99	34.619	0.015	0.012	102.742	-9900	6373
#450	38.857	0.007	22.223	4.68	1.951	1.057	34.548	0.011	0	103.334	-9893	6371

	SiO_2	TiO_2	Al_2O_3	MgO	CaO	MnO	FeO	Na_2O	K_2O	Total	x	y
#451	38.351	0.016	21.996	4.58	2.041	1.004	34.446	0.009	0	102.443	-9887	6369
#452	38.55	0.009	22.023	4.636	2.037	1.01	34.775	0	0	103.04	-9880	6367
#453	38.719	0.003	22.081	4.668	1.952	1.025	34.252	0	0	102.7	-9873	6365
#454	38.295	0.002	22.032	4.708	1.912	1.022	34.877	0	0	102.848	-9866	6363
#455	38.285	0	22.011	4.655	1.947	1.012	34.944	0.009	0.018	102.881	-9859	6361
#456	38.394	0	22.212	4.698	1.838	1.05	34.84	0.005	0	103.037	-9853	6359
#457	38.391	0.03	22.115	4.687	1.846	1.042	34.698	0.005	0	102.814	-9846	6358
#458	38.212	0.033	22.281	4.628	1.745	1.048	34.973	0	0.021	102.941	-9839	6356
#459	38.19	0.009	22.148	4.642	1.728	0.934	35.159	0.013	0.002	102.825	-9832	6354
#460	38.287	0	22.099	4.627	1.692	0.991	34.904	0.013	0	102.613	-9826	6352
#461	38.431	0	22.072	4.669	1.701	0.904	35.328	0	0.012	103.117	-9819	6350
#462	38.321	0	22.164	4.712	1.744	0.947	34.809	0	0.003	102.7	-9812	6348
#463	38.578	0	22.03	4.662	1.671	0.958	35.417	0.039	0	103.355	-9805	6346
#464	38.602	0	21.999	4.583	1.757	0.847	35.541	0.023	0	103.352	-9799	6344
#465	38.662	0	22.222	4.598	1.736	0.827	35.533	0.012	0	103.59	-9792	6343
#466	38.414	0.025	22.129	4.5	1.806	0.847	35.191	0	0	102.912	-9785	6341
#467	38.829	0.018	22.115	4.329	1.797	0.843	35.85	0	0	103.781	-9778	6339
#468	38.571	0.032	22.255	4.375	1.874	0.815	35.647	0.024	0	103.593	-9772	6337
#469	38.542	0.014	22.049	4.22	1.817	0.746	35.923	0.014	0.009	103.334	-9765	6335
#470	38.343	0.019	22.125	3.981	1.948	0.828	36.255	0.012	0.017	103.528	-9758	6333
#471	38.359	0.019	22.296	3.81	1.862	0.84	36.676	0	0	103.862	-9751	6331
#472	38.715	0	22.077	3.822	1.815	0.842	36.486	0.003	0.004	103.764	-9745	6329
#473	38.966	0	21.844	3.596	1.767	0.822	35.674	0.038	0.004	102.711	-9738	6327
#474	32.187	0	19.89	3.254	1.771	0.874	36.901	0	0	94.877	-9731	6326
#475	38.223	0	21.895	3.566	1.83	0.806	36.977	0	0	103.297	-9724	6324
#476	38.821	0.001	22.984	3.939	1.71	0.71	31.413	0.204	0.052	99.834	-9718	6322
#477	21.548	0.006	14.127	1.793	1.652	0.526	23.002	0.382	0.254	63.29	-9711	6320
#478	37.954	0.027	21.952	3.53	1.843	0.722	36.497	0.006	0	102.531	-9704	6318
#479	38.075	0.013	22.111	3.435	1.891	0.788	36.911	0.003	0.001	103.228	-9697	6316
#480	38.266	0.029	21.868	3.304	1.819	0.746	37.163	0	0.002	103.197	-9691	6314
#481	36.272	0.032	19.901	2.668	1.719	0.712	35.687	0.002	0	96.993	-9684	6312

	SiO_2	TiO_2	Al_2O_3	MgO	CaO	MnO	FeO	Na_2O	K_2O	Total	x	y
#482	2.017	0.041	1.72	0.403	0.483	0.089	5.961	0.016	0.039	10.769	-9677	6311
#483	37.931	0.012	21.968	2.866	1.798	0.926	37.4	0	0.014	102.915	-9670	6309
#484	37.477	0	22.073	2.388	1.766	1.12	37.867	0.006	0.023	102.72	-9664	6307
#485	27.422	0.531	12.32	5.102	0.497	0.235	21.148	0.103	3.868	71.226	-9657	6305
#486	36.06	0.025	59.095	0.149	0.007	0	1.915	0.015	0.074	97.34	-9650	6303
#487	38.135	0.005	62.541	0.01	0	0	0.954	0.008	0.006	101.659	-9643	6301
#488	38.057	0.013	62.491	0.001	0	0.039	0.817	0	0	101.418	-9637	6299
#489	38.114	0	62.603	0.015	0.034	0	0.884	0.005	0	101.655	-9630	6297
#490	38.376	0.002	63.168	0.004	0	0	0.864	0.004	0.003	102.421	-9623	6296
#491	38.165	0	63.023	0.019	0	0.004	0.913	0	0.001	102.125	-9616	6294
#492	38.243	0	63.092	0.013	0	0	0.841	0.003	0	102.192	-9610	6292
#493	38.357	0	63.246	0.009	0.012	0	0.794	0	0.006	102.424	-9603	6290
#494	38.537	0.009	63.339	0.002	0.027	0	0.747	0	0	102.661	-9596	6288
#495	38.803	0.021	63.483	0.01	0	0	0.806	0	0.016	103.139	-9589	6286
#496	46.369	0.026	38.259	0.47	0.022	0.009	1.784	0.475	3.164	90.578	-9583	6284
#497	47.133	0.027	38.801	0.253	0.009	0	0.729	0.378	2.77	90.1	-9576	6282
#498	46.941	0.016	36.778	0.532	0	0.037	1.604	0.872	5.954	92.734	-9569	6281
#499	91.25	0.009	2.863	0.154	0.01	0	1.067	0.1	0.823	96.276	-9562	6279
#500	99.707	0.008	0.038	0	0.013	0.004	0.123	0.001	0.008	99.902	-9556	6277
#501	99.89	0.009	0	0.006	0	0.013	0.104	0	0.014	100.036	-9549	6275
#502	99.662	0	0.015	0.009	0	0.037	0.01	0.004	0.003	99.74	-9542	6273
#503	99.887	0.012	0.011	0.009	0	0.046	0	0.012	0	99.977	-9535	6271
#504	100.088	0	0.006	0.002	0.014	0.002	0.046	0	0.003	100.161	-9529	6269
#505	99.842	0.007	0.021	0	0.004	0	0.023	0.006	0.018	99.921	-9522	6267
#506	100.28	0.019	0	0.006	0.005	0	0.025	0	0.005	100.34	-9515	6266
#507	100.177	0	0.006	0	0	0	0.012	0	0	100.195	-9508	6264
#508	99.831	0.014	0.004	0	0.006	0	0	0.003	0.003	99.861	-9502	6262
#509	98.173	0.018	0	0	0	0.017	0	0.001	0.004	98.213	-9495	6260
#510	100.133	0	0.004	0	0	0.017	0.073	0.015	0	100.242	-9488	6258

Hames1GrtTrav2

	SiO_2	TiO_2	Al_2O_3	MgO	CaO	MnO	FeO	Na_2O	K_2O	Total	x	y
#1	38.679	0	22.06	4.673	1.658	0.76	35.98	0	0.018	103.828	-10964	4971
#2	38.688	0	21.981	4.62	1.761	0.791	35.215	0	0.002	103.058	-10959	4969
#3	38.727	0.008	21.973	4.586	1.846	0.78	35.671	0	0	103.591	-10954	4967
#4	38.653	0.001	22.027	4.613	1.761	0.79	35.644	0.002	0	103.491	-10949	4965
#5	38.682	0.003	22.102	4.617	1.826	0.855	35.738	0.005	0	103.828	-10944	4963
#6	38.631	0.009	21.689	4.514	1.766	0.794	35.413	0.004	0.006	102.826	-10939	4961
#7	38.437	0.008	21.882	4.547	1.836	0.794	35.849	0	0	103.353	-10935	4959
#8	38.779	0	22.035	4.528	1.766	0.697	36.028	0.017	0	103.85	-10930	4957
#9	38.682	0.04	22.074	4.629	1.791	0.801	35.355	0.011	0	103.383	-10925	4955
#10	38.831	0.007	22.016	4.538	1.801	0.815	35.432	0.011	0	103.451	-10920	4953
#11	38.732	0.019	22.092	4.628	1.762	0.732	35.785	0.011	0.011	103.772	-10915	4951
#12	38.408	0.014	21.993	4.606	1.815	0.772	35.913	0.003	0	103.524	-10910	4949
#13	38.655	0	21.774	4.599	1.813	0.697	35.768	0.012	0	103.318	-10905	4947
#14	38.625	0.035	22.058	4.598	1.904	0.669	35.795	0.003	0	103.687	-10900	4945
#15	38.602	0.033	22.024	4.653	1.936	0.787	35.276	0.025	0.001	103.337	-10895	4943
#16	38.806	0	22.183	4.552	1.85	0.712	35.932	0.022	0.011	104.068	-10890	4941
#17	38.802	0.006	22.128	4.603	1.825	0.752	35.876	0.007	0.019	104.018	-10885	4939
#18	38.899	0	22.274	4.667	1.885	0.621	35.796	0	0	104.142	-10881	4937
#19	38.923	0.01	22.17	4.674	1.946	0.758	35.943	0.004	0	104.428	-10876	4935
#20	39.029	0.024	22	4.616	1.931	0.703	36.145	0.011	0.004	104.463	-10871	4933
#21	38.858	0.003	22.159	4.516	1.926	0.712	35.675	0.017	0.002	103.868	-10866	4931
#22	38.614	2.071	22.103	4.377	1.872	0.664	35.898	0.008	0.002	105.609	-10861	4929
#23	38.652	0	22.134	4.135	1.949	0.622	36.501	0.002	0.005	104	-10856	4927
#24	38.775	0.033	22.045	3.837	1.942	0.705	36.669	0.031	0.004	104.041	-10851	4924
#25	38.496	0.005	22.127	3.283	1.907	0.774	37.307	0.019	0	103.918	-10846	4922
#26	15.008	0.089	9.147	2.719	0.436	0.367	12.378	0.027	0.335	40.506	-10841	4920
#27	29.447	0.748	21.551	14.575	0.012	0	21.351	0.072	2.872	90.628	-10836	4918

	SiO_2	TiO_2	Al_2O_3	MgO	CaO	MnO	FeO	Na_2O	K_2O	Total	x	y
#28	33.917	1.191	20.303	12.884	0.008	0.054	20.062	0.17	5.964	94.553	-10831	4916
#29	27.823	0.385	22.589	15.268	0.029	0.078	23.187	0.041	1.557	90.957	-10827	4914
#30	26.137	0.093	23.803	16.344	0.001	0.043	23.892	0.007	0.13	90.45	-10822	4912
#31	28.058	0.403	22.794	15.609	0.014	0.006	22.613	0.046	1.534	91.077	-10817	4910
#32	31.179	0.898	21.336	14.179	0	0	21.408	0.125	4.097	93.222	-10812	4908
#33	26.472	0.151	23.53	16.264	0.01	0.037	23.087	0.022	0.419	89.992	-10807	4906
#34	29.28	0.559	21.952	15.178	0.011	0.049	22.086	0.093	2.603	91.811	-10802	4904
#35	26.958	0.082	23.614	17.273	0.016	0.002	23.266	0	0.026	91.237	-10797	4902
#36	27.018	0.332	21.57	15.046	0.017	0.037	22.464	0.045	1.186	87.715	-10792	4900
#37	25.879	0.113	23.126	16	0	0.053	23.961	0.025	0.149	89.306	-10787	4898
#38	28.4	0.507	22.218	15.243	0.012	0.033	22.431	0.061	2.01	90.915	-10782	4896
#39	30.261	0.688	21.445	14.336	0.012	0.004	21.978	0.091	3.261	92.076	-10777	4894
#40	31.559	0.873	21.115	13.946	0	0.089	21.243	0.146	4.225	93.196	-10773	4892
#41	30.547	0.758	21.547	14.378	0	0.052	21.963	0.121	3.451	92.817	-10768	4890
#42	35.217	1.472	19.653	12.454	0	0	19.562	0.268	6.949	95.575	-10763	4888
#43	34.05	1.261	20.085	13.018	0	0	20.013	0.161	5.977	94.565	-10758	4886
#44	35.038	1.363	19.91	12.538	0	0.006	19.78	0.214	6.92	95.769	-10753	4884
#45	35.258	1.378	19.925	12.684	0	0.037	19.414	0.231	6.741	95.668	-10748	4882
#46	34.254	1.269	20.109	12.967	0	0.023	20.032	0.199	6.258	95.111	-10743	4880
#47	33.278	1.152	20.573	13.333	0	0.031	19.862	0.163	5.647	94.039	-10738	4878
#48	36.103	1.513	19.428	12.095	0	0	19.355	0.246	7.484	96.224	-10733	4876
#49	36.927	1.625	18.901	11.377	0	0.015	18.755	0.268	8.562	96.43	-10728	4874
#50	37.312	1.655	19.336	11.335	0	0.037	17.805	0.268	8.274	96.022	-10723	4872
#51	36.822	1.689	19.59	11.507	0	0	18.631	0.306	8.262	96.807	-10718	4870
#52	37.08	1.687	19.6	11.559	0	0.025	19.039	0.266	8.522	97.778	-10714	4868
#53	37.233	1.627	19.4	11.525	0	0.004	18.518	0.25	8.265	96.822	-10709	4866
#54	36.229	1.702	18.707	11.142	0	0	19.424	0.256	8.374	95.834	-10704	4864
#55	37.529	1.607	19.444	11.529	0	0.008	18.815	0.28	8.493	97.705	-10699	4862
#56	37.449	1.511	19.637	11.552	0	0.002	19.276	0.314	8.579	98.32	-10694	4860
#57	37.257	1.706	18.925	11.061	0	0.017	19.276	0.207	7.018	95.467	-10689	4858
#58	22.328	0.898	11.398	6.419	0.089	0.021	13.279	0.153	4.838	59.423	-10684	4856

	SiO_2	TiO_2	Al_2O_3	MgO	CaO	MnO	FeO	Na_2O	K_2O	Total	x	y
#59	35.914	1.154	18.967	11.662	0	0	19.392	0.153	6.324	93.566	-10679	4854
#60	61.014	0.593	10.277	6.193	0.018	0	11.208	0.104	3.757	93.164	-10674	4852
#61	36.891	1.286	19.41	11.441	0	0	18.028	0.281	8.525	95.862	-10669	4850
#62	36.115	1.207	19.803	11.275	0.002	0.008	19.116	0.269	8.336	96.131	-10664	4848
#63	36.228	1.316	19.316	11.207	0	0.002	19.339	0.262	8.592	96.262	-10660	4846
#64	34.531	1.145	19.395	11.409	0	0.039	20.588	0.221	7.096	94.424	-10655	4844
#65	36.862	1.322	19.121	11.215	0	0	18.803	0.278	8.308	95.909	-10650	4842
#66	36.947	1.323	18.801	11.679	0	0	19.023	0.232	8.643	96.648	-10645	4840
#67	36.913	1.326	18.819	11.513	0	0.004	19.195	0.209	8.558	96.537	-10640	4838
#68	37.034	1.341	18.64	11.271	0	0.019	19.299	0.217	8.756	96.577	-10635	4835
#69	37.001	1.342	18.69	11.528	0	0	19.421	0.247	8.305	96.534	-10630	4833
#70	37.169	1.302	18.85	11.587	0	0.021	19.511	0.255	8.098	96.793	-10625	4831
#71	36.849	1.363	19.202	11.492	0	0.004	19.05	0.261	8.32	96.541	-10620	4829
#72	36.897	1.308	19.018	11.521	0	0.002	19.278	0.271	8.561	96.856	-10615	4827
#73	36.263	1.421	19.021	11.769	0	0.004	20.209	0.202	7.777	96.666	-10610	4825
#74	36.183	1.413	18.843	11.475	0	0.019	20.568	0.247	7.903	96.651	-10606	4823
#75	37.227	1.416	18.831	11.084	0	0.012	19.676	0.255	8.174	96.675	-10601	4821
#76	35.279	1.326	18.831	11.444	0	0.021	20.301	0.185	7.374	94.761	-10596	4819
#77	37.037	1.424	19.086	11.585	0	0	19.318	0.274	8.174	96.898	-10591	4817
#78	37.112	1.475	19.029	11.512	0	0.019	19.304	0.258	8.79	97.499	-10586	4815
#79	36.893	1.397	19.032	11.558	0	0.01	19.219	0.238	8.615	96.962	-10581	4813
#80	37.083	1.463	19.054	11.579	0	0.012	19.318	0.249	8.492	97.25	-10576	4811
#81	34.572	1.361	19.482	12.47	0.004	0.021	20.311	0.204	6.461	94.886	-10571	4809
#82	33.414	1.194	20.255	13.105	0	0.017	20.882	0.14	5.309	94.316	-10566	4807
#83	35.288	1.393	18.643	11.382	0.002	0.05	19.371	0.202	7.229	93.56	-10561	4805
#84	36.08	1.495	18.964	11.334	0	0.027	20.22	0.217	7.796	96.133	-10556	4803
#85	37.232	1.52	19.013	11.451	0	0.025	19.564	0.273	8.225	97.303	-10552	4801
#86	39.736	1.57	18.441	9.39	0	0.013	16.243	0.218	7.677	93.288	-10547	4799
#87	37.552	1.547	19.609	11.533	0	0.031	17.765	0.29	8.961	97.288	-10542	4797
#88	37.37	1.382	19.668	11.463	0	0.04	17.548	0.269	8.487	96.227	-10537	4795
#89	37.533	1.504	19.746	11.642	0	0.052	17.851	0.268	8.679	97.275	-10532	4793

	SiO_2	TiO_2	Al_2O_3	MgO	CaO	MnO	FeO	Na_2O	K_2O	Total	x	y
#90	37.657	1.477	19.446	11.573	0	0	17.969	0.29	8.485	96.897	-10527	4791

Hames1GrtTrav4

	SiO_2	TiO_2	Al_2O_3	MgO	CaO	MnO	FeO	Na_2O	K_2O	Total	X	Y
#1	47.421	0.829	35.741	0.824	0	0	1.306	1.17	9.114	96.405	-11987	8310
#2	46.997	0.96	36	0.847	0	0	1.351	1.139	8.751	96.045	-11987	8302
#3	46.899	1.027	35.548	0.89	0.006	0.026	1.515	1.047	8.56	95.518	-11986	8294
#4	45.894	1.039	33.352	0.935	0	0.017	1.66	0.985	8.74	92.622	-11986	8286
#5	46.807	0.972	35.63	0.878	0	0.011	1.457	1.043	9.069	95.867	-11985	8277
#6	47.047	1.074	35.37	0.961	0	0.002	1.801	1.02	9.027	96.302	-11985	8269
#7	42.941	1.037	33.291	0.791	0.001	0	1.492	1.01	8.13	88.693	-11984	8261
#8	47.602	1.042	35.964	0.829	0.01	0	1.411	1.117	8.516	96.491	-11984	8253
#9	47.49	1.027	35.761	0.759	0.005	0	1.354	1.184	8.648	96.228	-11983	8245
#10	46.987	0.928	36.066	0.712	0	0.043	1.272	1.194	8.717	95.919	-11983	8237
#11	47.42	0.99	35.641	0.859	0	0.015	1.431	1.081	8.846	96.283	-11982	8228
#12	47.559	0.996	35.884	0.897	0	0	1.48	1.123	9.118	97.057	-11982	8220
#13	47.384	1.183	35.081	0.953	0	0.013	1.507	1.021	8.931	96.073	-11981	8212
#14	46.955	0.908	35.808	0.808	0	0.004	1.46	1.111	8.902	95.956	-11981	8204
#15	47.097	1.03	35.433	0.832	0	0.002	1.466	1.066	8.916	95.842	-11980	8196
#16	47.68	1.183	35.515	0.852	0	0.019	1.333	1.064	8.792	96.438	-11980	8188
#17	46.771	1.282	34.778	1.008	0	0.013	1.719	0.933	8.947	95.451	-11979	8180
#18	47.288	1.25	34.81	0.999	0.008	0.024	1.842	0.933	8.886	96.04	-11979	8171
#19	46.915	1.31	34.52	0.996	0	0	1.842	1.002	8.918	95.503	-11978	8163
#20	47.062	1.239	34.798	0.948	0	0.011	1.646	1	8.64	95.344	-11978	8155
#21	47.202	1.221	34.875	0.961	0	0.015	1.764	0.972	8.922	95.932	-11977	8147
#22	47.079	1.339	35.108	0.969	0	0	1.723	0.997	8.964	96.179	-11977	8139
#23	46.902	1.202	35.003	0.926	0	0.071	1.517	0.986	8.951	95.558	-11976	8131
#24	46.843	1.121	34.953	0.914	0	0.011	1.635	1.015	8.918	95.41	-11976	8122
#25	47.038	1.251	34.967	1.036	0	0	1.835	0.971	8.931	96.029	-11975	8114
#26	47.05	1.178	35.389	0.888	0	0.049	1.535	1.011	8.962	96.062	-11975	8106

	SiO_2	TiO_2	Al_2O_3	MgO	CaO	MnO	FeO	Na_2O	K_2O	Total	X	Y
#27	47.116	1.274	35.162	0.974	0	0	1.515	0.967	8.987	95.995	-11974	8098
#28	47.205	1.242	35.027	0.97	0	0	1.721	0.978	9.028	96.171	-11974	8090
#29	46.968	1.258	34.788	0.936	0.008	0.024	1.547	0.937	8.971	95.437	-11973	8082
#30	47.725	1.282	34.798	0.941	0	0.019	1.717	0.96	9.114	96.556	-11973	8074
#31	46.695	1.252	34.821	0.968	0	0	1.713	0.957	9.046	95.452	-11972	8065
#32	47.407	1.347	34.956	1.001	0	0	1.609	0.917	8.92	96.157	-11972	8057
#33	46.648	1.231	34.82	0.993	0.008	0	1.854	0.957	8.93	95.441	-11971	8049
#34	47.155	1.293	34.963	0.988	0	0	1.596	0.939	8.992	95.926	-11971	8041
#35	46.907	1.282	34.842	0.997	0	0	1.795	0.941	9.013	95.777	-11970	8033
#36	46.789	1.194	34.412	0.995	0	0	1.791	0.958	8.84	94.979	-11970	8025
#37	46.697	1.251	34.731	0.973	0	0	1.603	0.995	8.901	95.151	-11969	8017
#38	46.998	1.264	34.846	0.98	0	0.004	1.721	0.976	8.998	95.787	-11969	8008
#39	46.539	1.244	34.999	0.961	0	0	1.774	1.006	8.989	95.512	-11968	8000
#40	46.005	1.219	35.627	0.932	0.006	0	1.815	1.033	8.809	95.446	-11968	7992
#41	47.042	1.197	34.976	0.949	0	0.075	1.796	0.994	9.038	96.067	-11967	7984
#42	46.317	1.222	35.221	0.964	0.002	0.006	1.741	0.979	8.971	95.423	-11967	7976
#43	46.858	1.149	34.333	0.92	0	0	1.787	0.915	8.935	94.897	-11966	7968
#44	46.895	1.213	35.02	0.95	0	0	1.729	1.035	8.741	95.583	-11966	7959
#45	46.571	1.22	35.123	0.934	0	0	1.766	0.992	8.835	95.441	-11965	7951
#46	46.88	1.172	34.982	0.857	0	0	1.613	0.992	8.784	95.28	-11965	7943
#47	46.826	1.178	35.33	0.844	0	0.034	1.717	1.011	8.808	95.748	-11964	7935
#48	46.817	1.101	35.204	0.936	0	0	1.79	1.041	8.998	95.887	-11964	7927
#49	46.881	1.015	35.35	0.931	0	0	1.772	0.998	8.643	95.59	-11963	7919
#50	47.049	0.902	35.277	0.851	0	0.011	1.715	0.94	8.884	95.629	-11963	7911
#51	97.282	0.012	2.368	0.047	0	0	0.22	0.056	0.484	100.469	-11962	7902
#52	47.052	0.679	35.397	0.91	0	0	1.811	1.058	9.01	95.917	-11962	7894
#53	47.756	0.64	35.109	0.921	0	0	1.844	1.015	8.953	96.238	-11961	7886
#54	46.355	0.634	35.261	0.912	0.024	0	2.246	1.022	8.757	95.211	-11961	7878
#55	35.444	0.428	26	0.63	0	0.006	1.285	0.719	6.374	70.886	-11960	7870
#56	47.241	0.552	35.91	0.916	0	0.052	1.879	1.1	8.966	96.616	-11960	7862
#57	47.231	0.492	35.648	0.885	0.006	0.009	1.746	1.099	8.841	95.957	-11959	7853

	SiO_2	TiO_2	Al_2O_3	MgO	CaO	MnO	FeO	Na_2O	K_2O	Total	X	Y
#58	47.044	0.487	35.941	0.837	0	0	1.869	1.178	8.667	96.023	-11959	7845
#59	47.063	0.516	36.232	0.815	0.015	0.032	1.724	1.173	8.834	96.404	-11958	7837
#60	46.032	0.391	34.633	0.864	0	0.054	1.859	1.071	8.284	93.188	-11958	7829

Hames1RutTrav2

	SiO_2	TiO_2	Al_2O_3	MgO	CaO	MnO	FeO	Na_2O	K_2O	Total	X	Y
#1	0.094	51.522	0	0.191	0.004	0.288	48.362	0	0.017	100.478	-11821	15004
#2	0.05	51.451	0.001	0.185	0	0.152	48.823	0.002	0.018	100.682	-11816	15005
#3	0.056	51.302	0	0.205	0.002	0.196	48.355	0	0.023	100.139	-11812	15006
#4	0.021	51.566	0.013	0.194	0.005	0.263	48.306	0	0.015	100.383	-11807	15007
#5	0.031	83.202	0.014	0.052	0.001	0.057	13.061	0	0.008	96.426	-11802	15009
#6	0.026	96.885	0.051	0	0.005	0.017	1.087	0.026	0	98.097	-11797	15010
#7	0.042	95.727	0.042	0	0	0.029	0.921	0.016	0.001	96.778	-11793	15011
#8	0.024	97.137	0.021	0	0.002	0.002	0.814	0	0	98	-11788	15012
#9	0.015	97.646	0.026	0	0.004	0.017	0.826	0.007	0	98.541	-11783	15013
#10	0	97.092	0.034	0.006	0	0	0.877	0.017	0.007	98.033	-11778	15014
#11	0.003	97.256	0.027	0.005	0	0.014	0.871	0.021	0	98.197	-11774	15015
#12	0.018	97.597	0.076	0.003	0.018	0.027	0.799	0.005	0	98.543	-11769	15017
#13	0.018	96.616	0.023	0.011	0.001	0	0.863	0.03	0	97.562	-11764	15018
#14	0.006	95.35	0.022	0.01	0	0	0.974	0.002	0.011	96.375	-11760	15019
#15	0.019	96.168	0.048	0	0.012	0	0.853	0	0	97.1	-11755	15020
#16	0.009	96.265	0.005	0	0.01	0.043	0.9	0.017	0.01	97.259	-11750	15021
#17	0.041	96.152	0.024	0	0.008	0	0.91	0	0.001	97.136	-11745	15022
#18	0.042	96.871	0.045	0.005	0.021	0	0.871	0.009	0	97.864	-11741	15023
#19	0.009	97.225	0.037	0	0.014	0	0.898	0.001	0.004	98.188	-11736	15024
#20	0.03	97.173	0.059	0	0.016	0	0.885	0	0.002	98.165	-11731	15026
#21	0.054	97.214	0.038	0	0.002	0.017	0.744	0.006	0.01	98.085	-11727	15027
#22	0.071	96.84	0.025	0	0.01	0.014	0.921	0	0.013	97.894	-11722	15028
#23	0.033	96.164	0.027	0	0.017	0	1.083	0	0.003	97.327	-11717	15029
#24	0.024	89.686	0.067	0.01	0.01	0	4.861	0.003	0	94.661	-11712	15030

	SiO_2	TiO_2	Al_2O_3	MgO	CaO	MnO	FeO	Na_2O	K_2O	Total	X	Y
#25	0	52.047	0	0.21	0	0.214	48.042	0.016	0.003	100.532	-11708	15031
#26	0.041	52.216	0	0.19	0	0.216	47.87	0.009	0.023	100.565	-11703	15032
#27	0.038	51.683	0.019	0.211	0.024	0.202	47.796	0	0.015	99.988	-11698	15034
#28	0.012	51.889	0	0.202	0.005	0.196	48.213	0.013	0.02	100.55	-11693	15035
#29	0.065	51.672	0	0.194	0	0.177	48.063	0	0.012	100.183	-11689	15036
#30	0.167	51.043	0.014	0.186	0	0.189	47.435	0.011	0.06	99.105	-11684	15037

Monazite Traverse 1

Anal #	Th	U	Pb	Y	X	Y
Trav 1-1	36059	4492	1057	8923	-18779	22851
Trav 1-2	32997	3400	841	13596	-18780	22848
Trav 1-3	39729	2338	958	10681	-18780	22844
Trav 1-4	39338	2282	1001	10383	-18781	22841
Trav 1-5	34422	2835	926	12522	-18782	22838
Trav 1-6	24153	5376	1080	17386	-18782	22835
Trav 1-7	22882	5057	844	16513	-18783	22831
Trav 1-8	33689	3271	881	9445	-18784	22828
Trav 1-9	32129	3137	807	6646	-18785	22825
Trav 1-10	37042	2450	946	11036	-18785	22822
Trav 1-11	36532	2335	904	10961	-18786	22818
Trav 1-12	35697	2251	926	10758	-18787	22815
Trav 1-13	35455	2258	897	10698	-18787	22812
Trav 1-14	35193	2449	836	11070	-18788	22808
Trav 1-15	35483	2600	858	11258	-18789	22805
Trav 1-16	35582	2660	955	11629	-18789	22802
Trav 1-17	35112	2776	1042	12182	-18790	22799
Trav 1-18	16674	5927	790	18020	-18791	22795
Trav 1-19	22418	8457	1205	21523	-18791	22792
Trav 1-20	22864	8346	1117	22608	-18792	22789
Trav 1-21	22393	8067	1048	22123	-18793	22785
Trav 1-22	23318	7565	1130	20235	-18793	22782
Trav 1-23	29616	8336	1295	18723	-18794	22779
Trav 1-24	23774	7997	1105	19338	-18795	22776
Trav 1-25	14027	4669	714	16607	-18796	22772
Trav 1-26	24843	6093	1019	17935	-18796	22769
Trav 1-27	35267	2996	1020	12233	-18797	22766
Trav 1-28	37180	2995	973	12240	-18798	22763
Trav 1-29	31061	4379	888	11561	-18798	22759

Monazite Traverse 2

Anal #	Th	U	Pb	Y	X	Y
Trav 2-1	30726	4008	959	15101	-18864	22772
Trav 2-2	29295	4031	939	14854	-18861	22773
Trav 2-3	25483	3921	815	14538	-18858	22773
Trav 2-4	24923	3832	877	14502	-18855	22774
Trav 2-5	17805	2981	648	13150	-18852	22775
Trav 2-6	15561	3005	608	13815	-18849	22776
Trav 2-7	17300	4903	827	16152	-18846	22776
Trav 2-8	18927	4926	769	15506	-18843	22777
Trav 2-9	17896	4734	819	14966	-18840	22778
Trav 2-10	17766	4683	762	15094	-18837	22779
Trav 2-11	17315	4939	755	15265	-18834	22779

Anal #	Th	U	Pb	Y	X	Y
Trav 2-12	17808	4963	758	15504	-18831	22780
Trav 2-13	19188	5111	898	15864	-18828	22781
Trav 2-14	16202	4884	785	16203	-18825	22781
Trav 2-15	13965	4761	643	16668	-18822	22782
Trav 2-16	13923	4558	701	16541	-18819	22783
Trav 2-17	14312	4310	683	16208	-18816	22784
Trav 2-18	18128	5877	976	19989	-18813	22784
Trav 2-19	21724	7580	1062	23314	-18810	22785
Trav 2-20	21442	6208	969	18545	-18806	22786
Trav 2-21	22430	6590	1062	19055	-18803	22787
Trav 2-22	19732	6311	949	18729	-18800	22787
Trav 2-23	17842	6150	854	18918	-18797	22788
Trav 2-24	20481	7356	1108	21509	-18794	22789
Trav 2-25	24258	9143	1281	23130	-18791	22790
Trav 2-26	23395	9494	1266	22197	-18788	22790
Trav 2-27	20940	8200	1106	20642	-18785	22791
Trav 2-28	21220	7934	1036	20431	-18782	22792
Trav 2-29	22102	8068	1125	20824	-18779	22792
Trav 2-30	23949	7803	1177	20467	-18776	22793
Trav 2-31	25687	7422	1117	20176	-18773	22794
Trav 2-32	25389	6594	1082	19218	-18770	22795
Trav 2-33	31076	3984	970	35521	-18767	22795
Trav 2-34	32370	3422	943	14902	-18764	22796
Trav 2-35	33152	3404	947	14794	-18761	22797
Trav 2-36	36933	3276	1039	14011	-18758	22798
Trav 2-37	34842	4027	898	10413	-18755	22798

Monazite Traverse 3

Anal #	Th	U	Pb	Y	X	Y
Trav 3-1	36452	3183	1018	12615	-18828	22822
Trav 3-2	36527	3107	1023	12452	-18825	22820
Trav 3-3	37038	3021	1042	12619	-18823	22818
Trav 3-4	37364	3051	966	12708	-18820	22817
Trav 3-5	36743	3111	980	12583	-18818	22815
Trav 3-6	36997	2962	948	12536	-18815	22813
Trav 3-7	37267	2915	1071	12291	-18813	22811
Trav 3-8	36143	2724	992	11148	-18810	22809
Trav 3-9	36519	2701	1010	11563	-18808	22808
Trav 3-10	31937	2862	802	12695	-18805	22806
Trav 3-11	34149	2631	916	12351	-18803	22804
Trav 3-12	37211	2320	958	11345	-18800	22802
Trav 3-13	37928	2389	936	11467	-18797	22800
Trav 3-14	36935	2556	966	11715	-18795	22799
Trav 3-15	28445	3493	837	14281	-18792	22797
Trav 3-16	14295	4813	753	16866	-18790	22795
Trav 3-17	17114	6197	967	18760	-18787	22793
Trav 3-18	21198	7774	1079	20782	-18785	22792
Trav 3-19	23566	7823	1171	21332	-18782	22790
Trav 3-20	23617	7543	1088	20933	-18780	22788
Trav 3-21	27077	6575	1180	19613	-18777	22786
Trav 3-22	33844	3862	1066	14638	-18775	22784
Trav 3-23	38063	2692	977	11842	-18772	22783
Trav 3-24	37716	3120	1014	12090	-18770	22781

Monazite Traverse 2-1

Anal #	Th	U	Pb	Y	X	Y
Trav 2-1-1	23416	1980	517	1682	-3671	13931
Trav 2-1-2	36834	3759	1020	8312	-3668	13931
Trav 2-1-3	37586	5288	1180	18430	-3665	13931
Trav 2-1-4	38066	5155	1193	17697	-3662	13931
Trav 2-1-5	35984	4609	1126	16334	-3658	13931
Trav 2-1-6	33693	4076	1102	14991	-3655	13931
Trav 2-1-7	38505	4220	1126	14242	-3652	13931
Trav 2-1-8	38306	4150	1129	14207	-3649	13931
Trav 2-1-9	40223	4201	1094	14281	-3646	13931
Trav 2-1-10	40698	4405	1183	14658	-3643	13931
Trav 2-1-11	41313	4829	1281	15806	-3640	13931
Trav 2-1-12	41884	5371	1344	17139	-3637	13931
Trav 2-1-13	44832	5923	1359	18664	-3633	13931
Trav 2-1-14	43293	5358	1368	17622	-3630	13931
Trav 2-1-15	33474	3579	976	14615	-3627	13931

Monazite Traverse 2-2

Anal #	Th	U	Pb	Y	X	Y
Trav 2-2-1	41961	4094	1226	15899	-3648	13959
Trav 2-2-2	42872	4639	1270	17395	-3648	13956
Trav 2-2-3	38783	4841	1210	17441	-3648	13953
Trav 2-2-4	31644	3646	913	14992	-3648	13949
Trav 2-2-5	36706	4093	1015	15026	-3648	13946
Trav 2-2-6	45323	4603	1270	15139	-3648	13943
Trav 2-2-7	46460	4536	1298	14711	-3648	13940
Trav 2-2-8	43215	4250	1276	14419	-3648	13937
Trav 2-2-9	33634	3703	1036	13946	-3648	13933
Trav 2-2-10	42040	4391	1173	14691	-3648	13930
Trav 2-2-11	34095	3791	899	13774	-3648	13927
Trav 2-2-12	30793	3444	953	13630	-3648	13924
Trav 2-2-13	27218	2996	802	13232	-3648	13921
Trav 2-2-14	34124	2591	798	12572	-3648	13918
Trav 2-2-15	40260	2708	1049	12070	-3648	13914
Trav 2-2-16	39632	2846	1034	11771	-3648	13911
Trav 2-2-17	34437	2592	906	9022	-3648	13908

Full thin-section x-ray intensity maps. Color bar applies to all images:

Low concentration  High Concentration

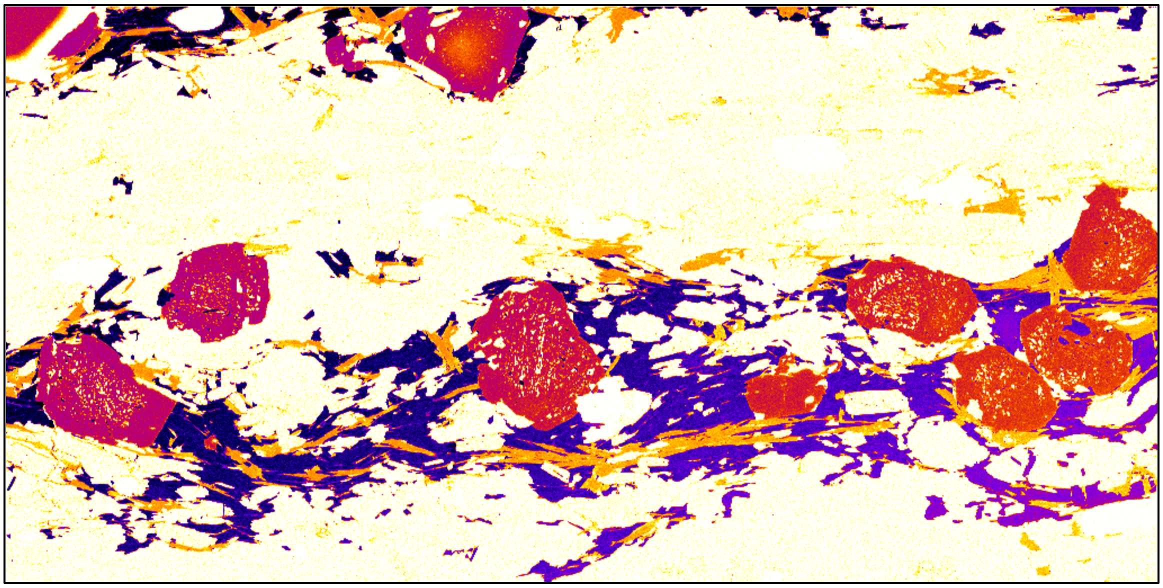

Mg

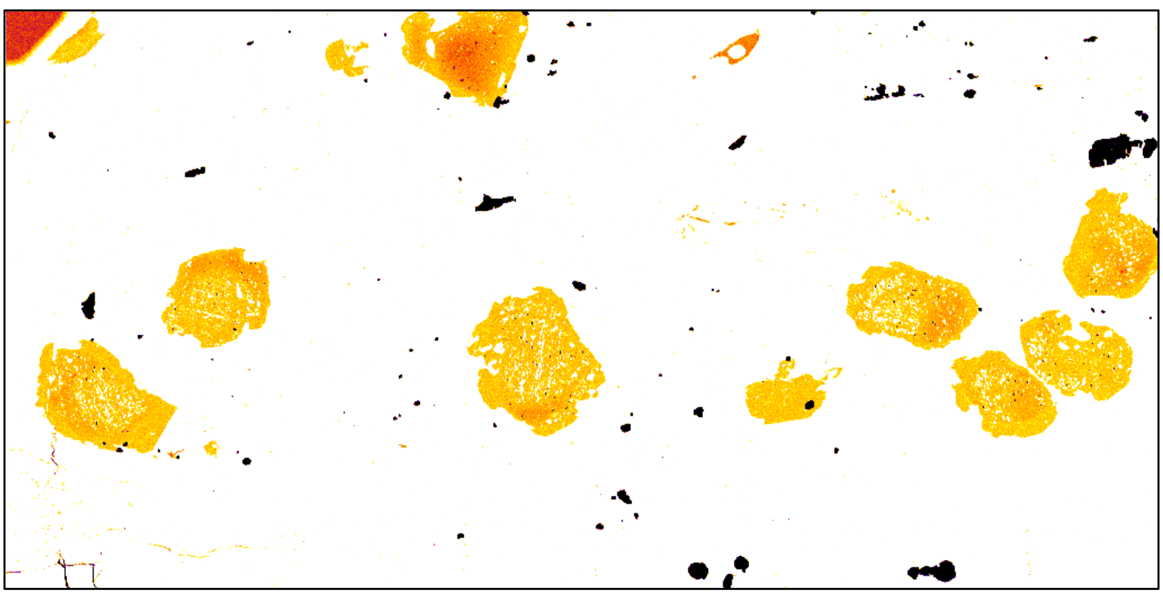

Ca

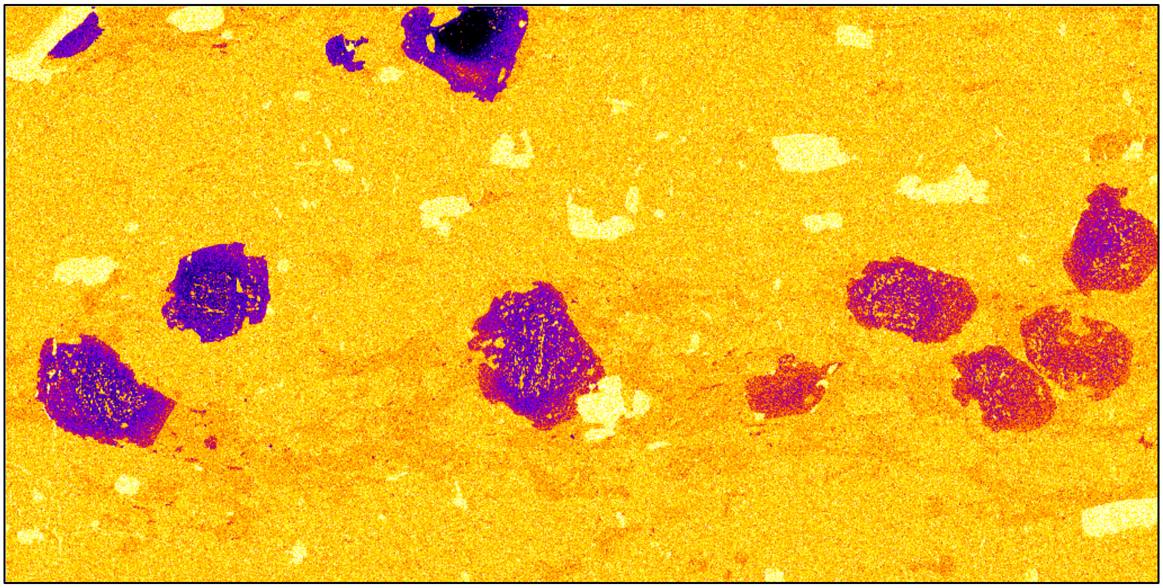
Mn

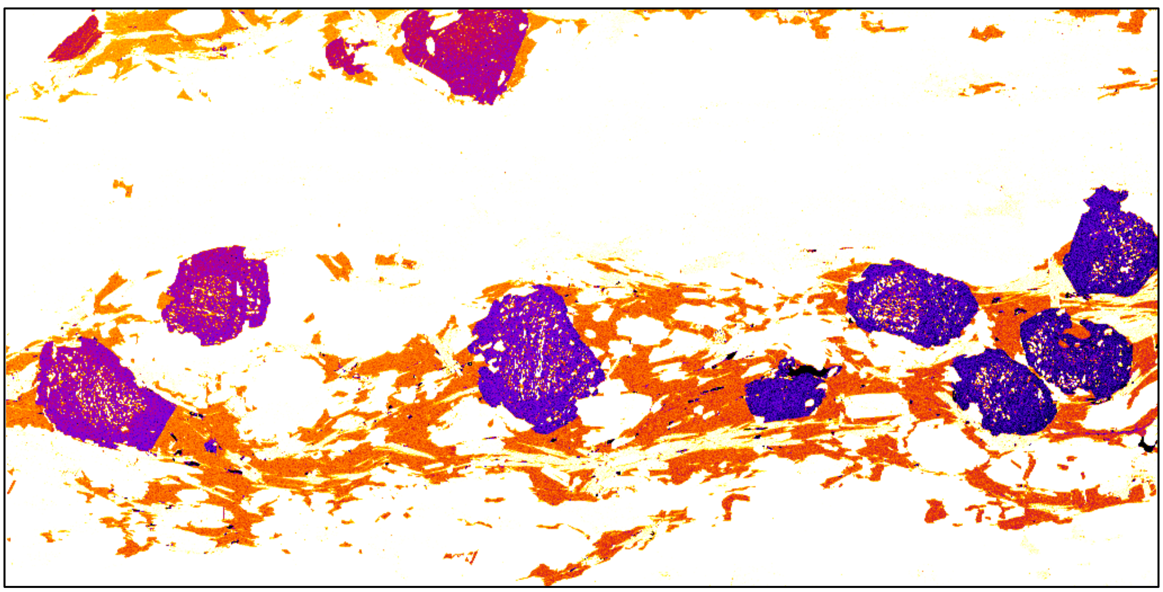
Fe

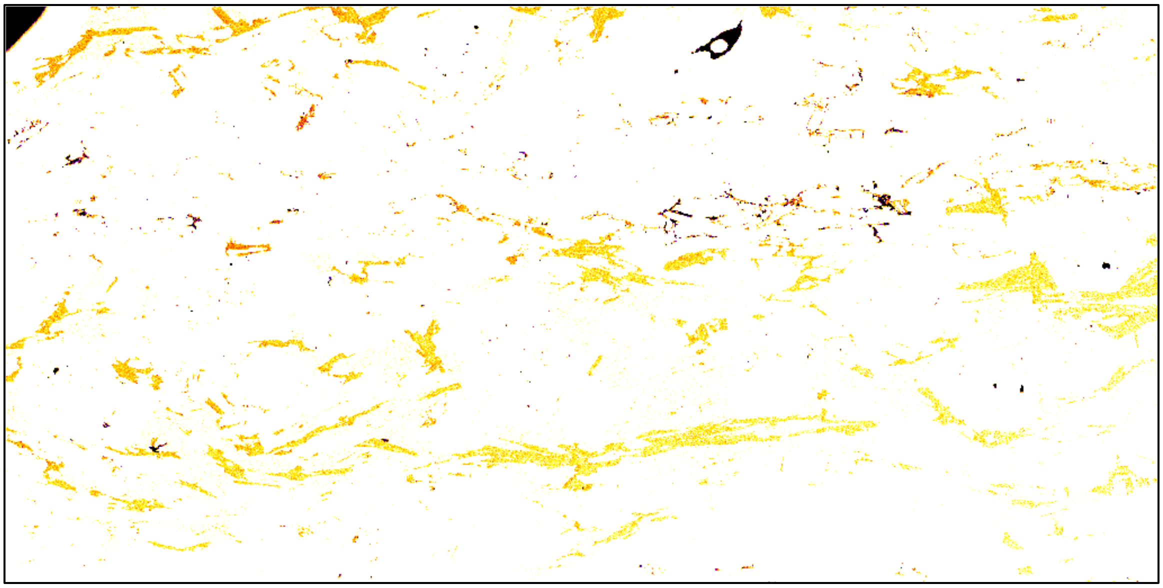

Na

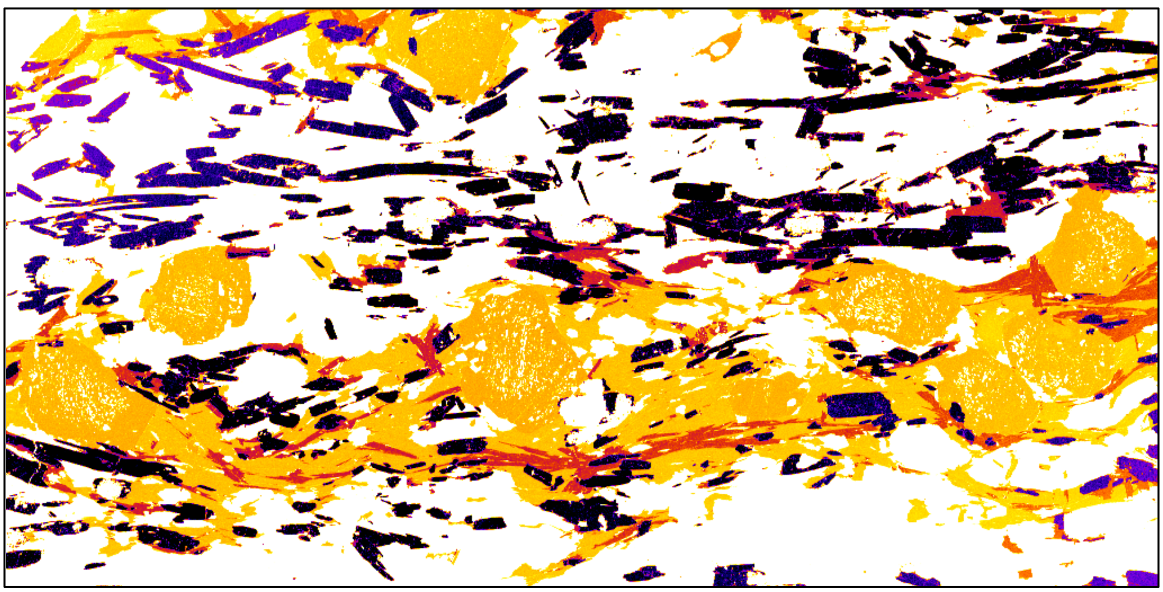

Al

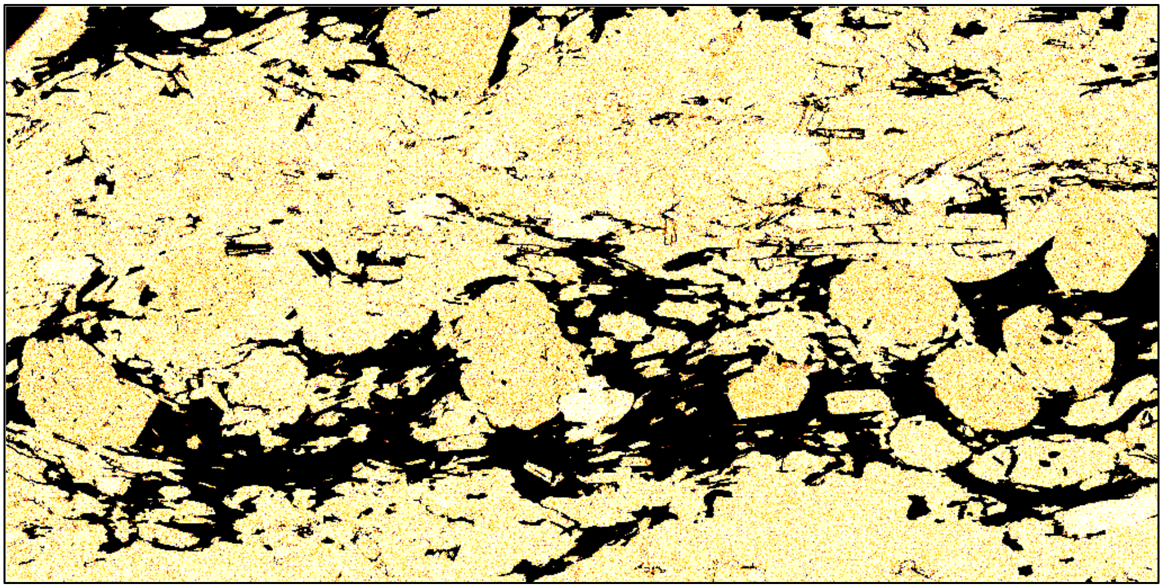

K

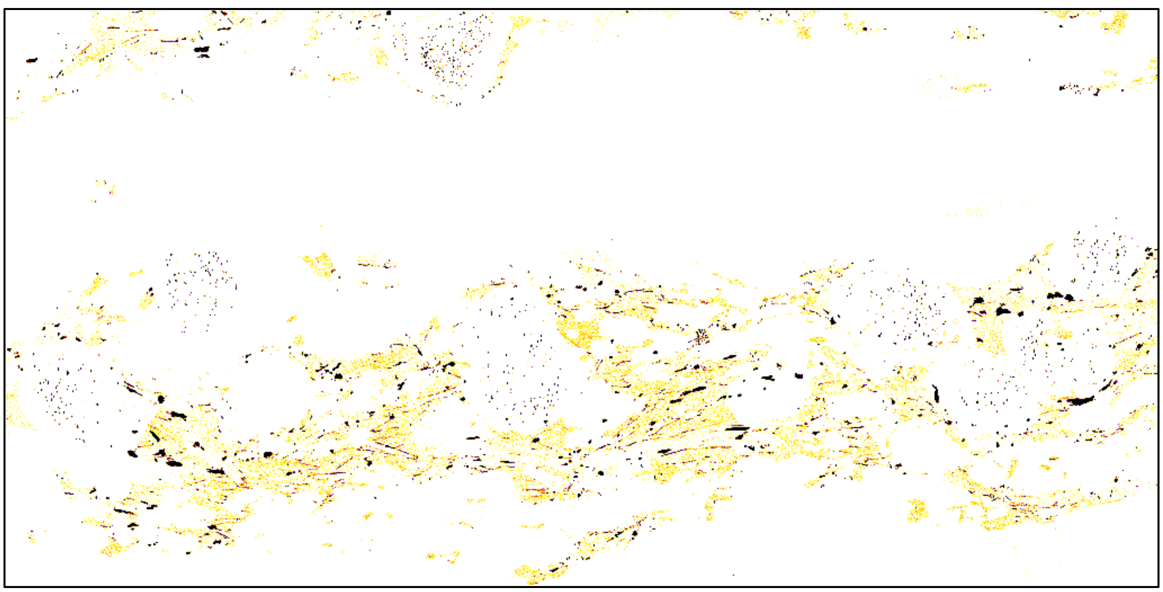

Ti

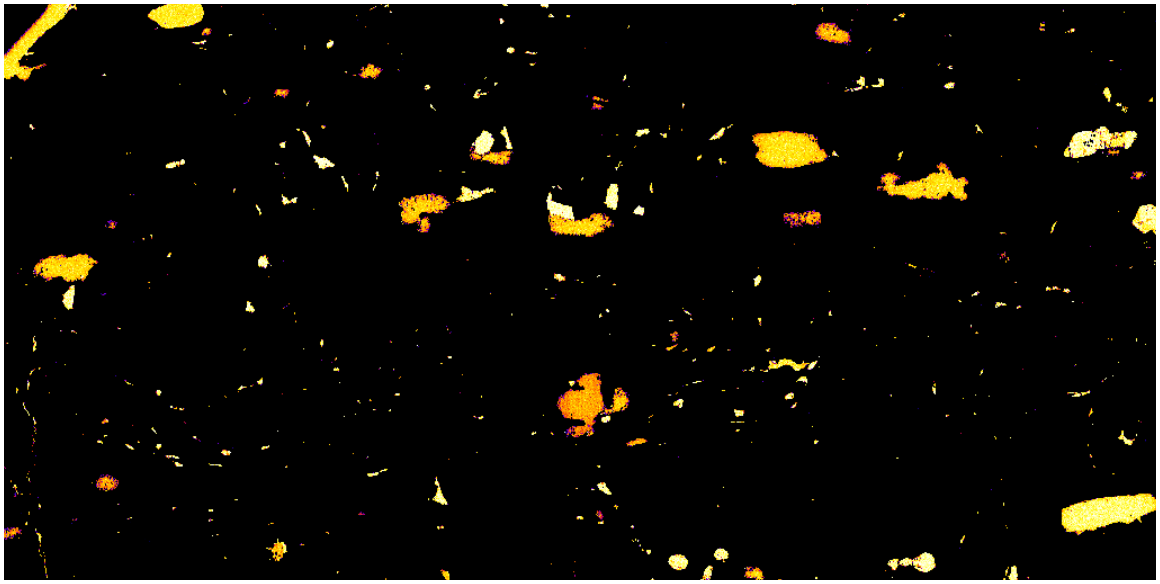

Si

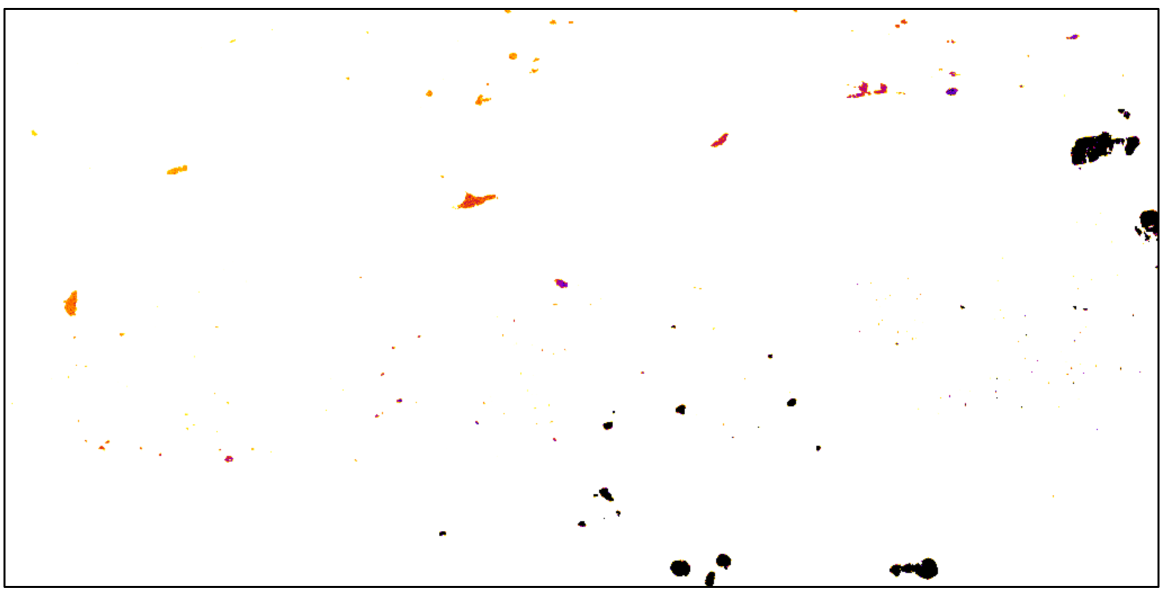

P

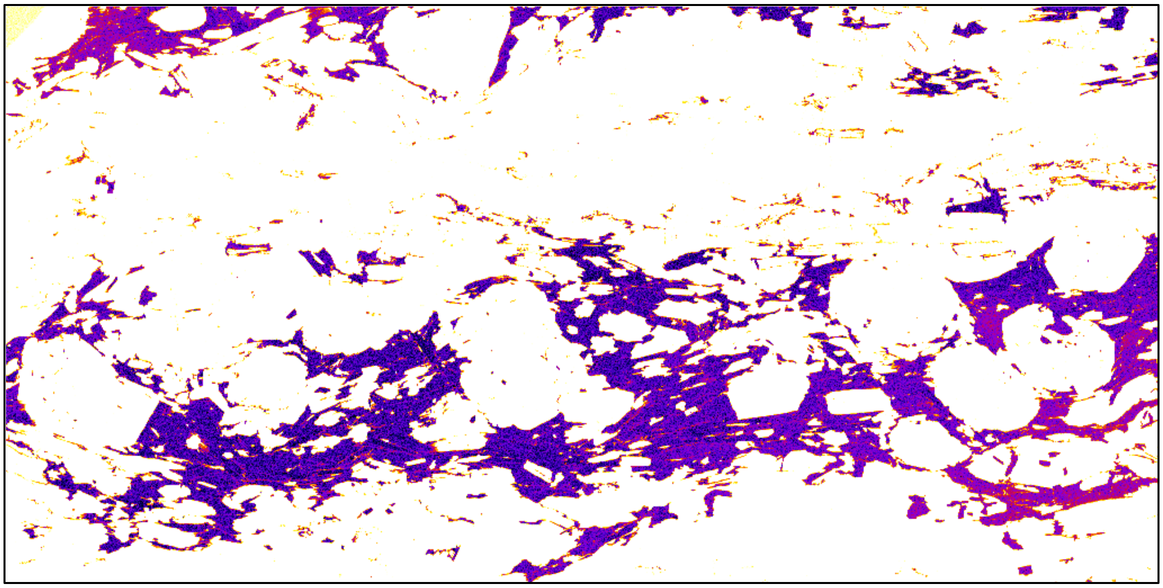
K

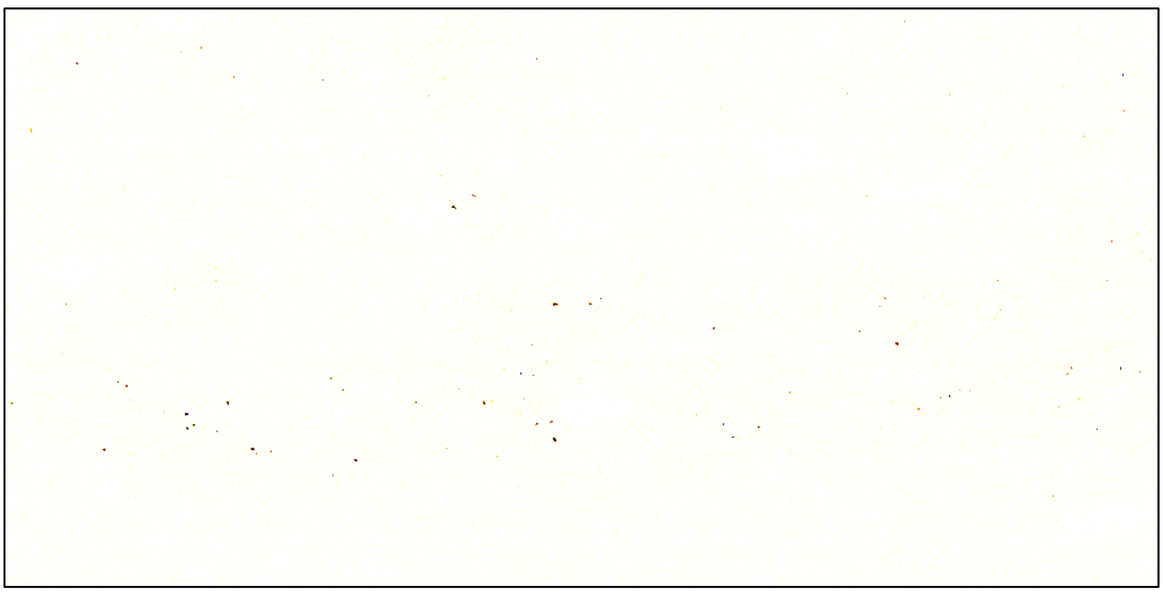
Ce

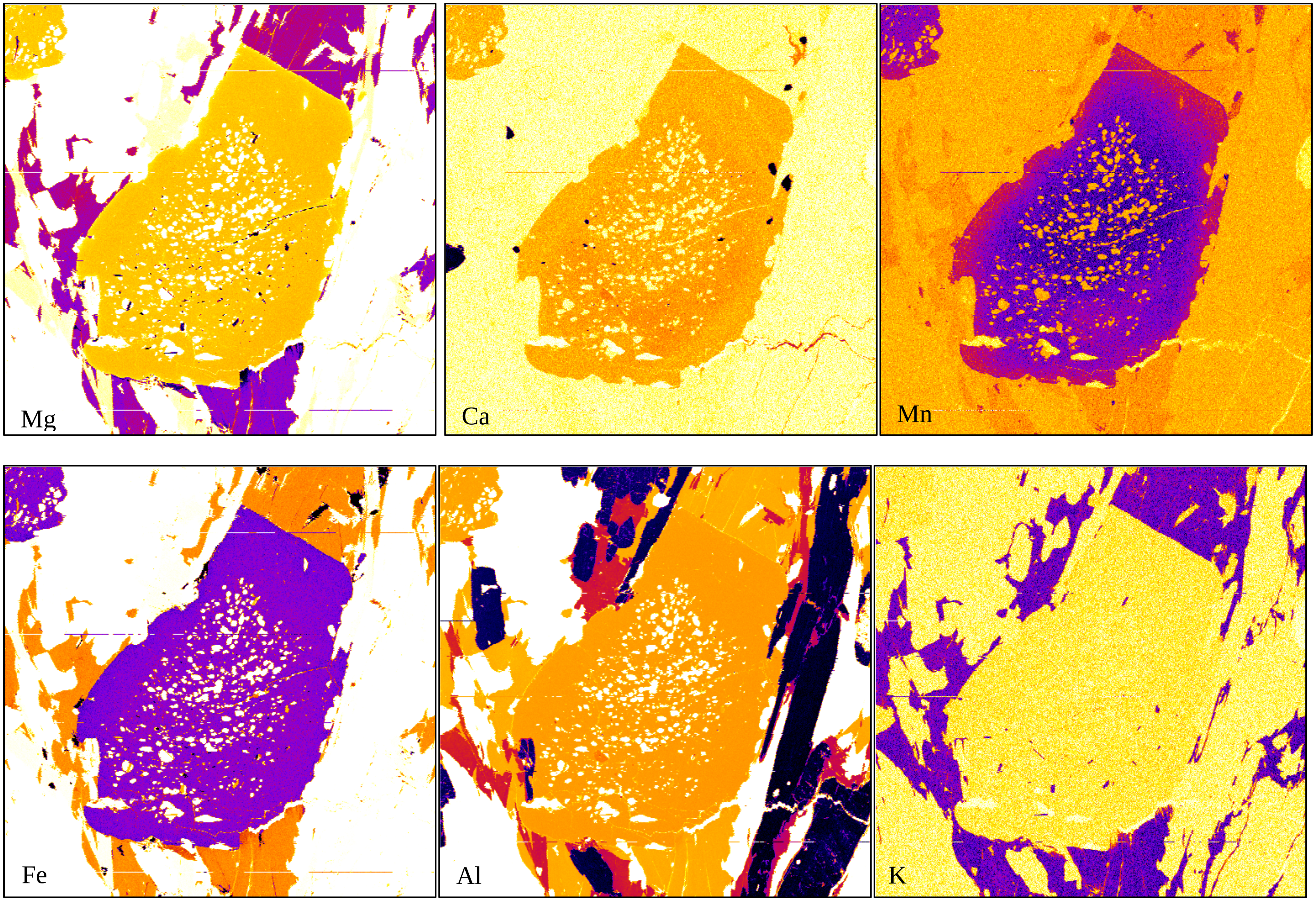
Mg
Ca
Mn
Fe
Al
K

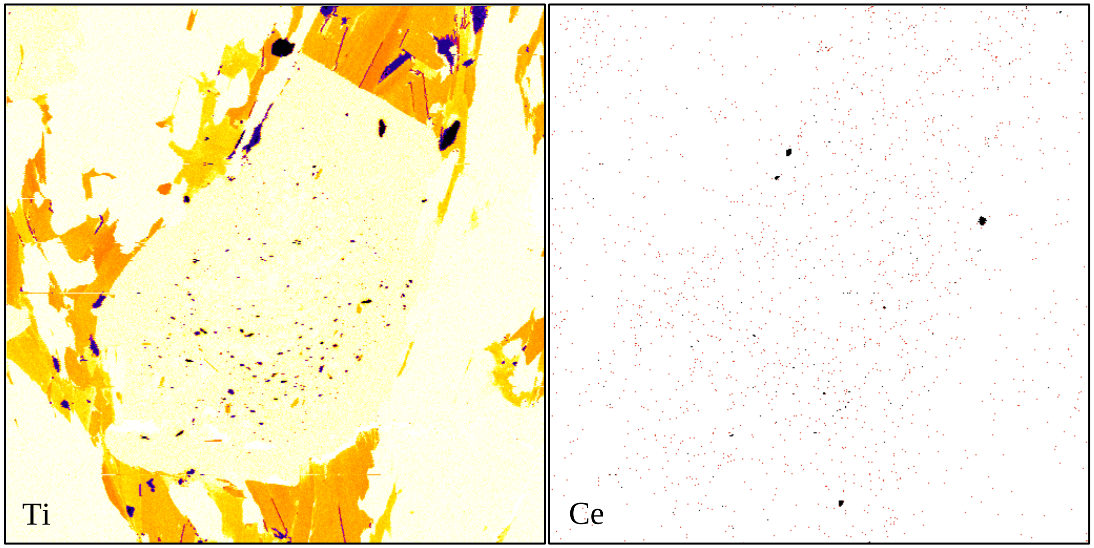
Ti
Ce

APPENDIX 3 – ID – TIMS data

Fraction Analysed	Properties	Weight	Pbt	U	Th/U	Th	Pbc	Pbcom	206/204	207/235	2σ	206/238	2σ	rho	207/206	2σ	206/238	2σ	207/235	2σ	207/206	2σ	Discordance
		[μg]	[ppm]	[ppm]		[ppm]	[ppm]	[pg]			[abs]		[abs]			[abs]		[abs]		[abs]		[abs]	[%]
KJR-243 307/2	Z B [1]	1	688	11118	0.01	57	0.00	1.4	34184	0.5215	0.0015	0.06817	0.00017	0.96	0.05548	0.00005	425.1	1.0	426.1	1.0	431.8	1.8	1.6
KJR-243 307/1	Z B [1]	4	1249	20186	0.00	63	0.00	2.0	172687	0.5215	0.0016	0.06816	0.00018	0.97	0.05549	0.00004	425.1	1.1	426.2	1.0	432.1	1.7	1.7
KJR-243 311/16	Z B P [1]	12	168	2722	0.01	19	0.10	3.2	43264	0.5201	0.0015	0.06800	0.00016	0.95	0.05547	0.00006	424.1	0.9	425.2	1.0	431.1	2.3	1.7
KJR-243 311/22	Z B P [1]	2	1254	20268	0.00	85	1.14	4.3	40261	0.5206	0.0014	0.06808	0.00016	0.97	0.05546	0.00004	424.6	1.0	425.6	0.9	431.0	1.5	1.5
KJR-243 307/3	Z P [1]	1	117	1823	0.04	64	0.00	0.7	10800	0.5489	0.0260	0.07012	0.00331	1.00	0.05677	0.00010	436.9	19.9	444.3	16.9	482.7	4.0	9.8
KJR-243 311/15	Z P [1]	1	78	939	0.17	156	0.00	1.1	4868	0.7317	0.0022	0.08734	0.00019	0.79	0.06076	0.00012	539.8	1.1	557.5	1.3	630.7	4.1	15.0
KJR-243 311/14	Z P [1]	2	9	88	0.16	14	0.00	1.2	1017	0.9353	0.0063	0.10465	0.00026	0.58	0.06482	0.00037	641.6	1.5	670.4	3.3	768.5	11.9	17.3
KJR-243 311/13	Z P [1]	1	74	921	0.14	125	0.22	2.2	2214	0.7066	0.0028	0.08491	0.00019	0.68	0.06035	0.00018	525.4	1.1	542.7	1.7	616.3	6.4	15.4
LEA 10-1 307/4	Z AA TIP [1]	1	229	969	0.07	70	86.86	88.7	125	1.5289	0.0368	0.15602	0.00120	0.32	0.07107	0.00162	934.6	6.7	942.1	14.7	959.5	45.9	2.8
LEA 10-1 307/7	Z TIP [1]	1	143	990	0.02	17	0.00	0.9	10686	1.5241	0.0046	0.15627	0.00039	0.88	0.07073	0.00010	936.0	2.1	940.1	1.9	949.7	2.9	1.5
LEA 10-1 311/23	Z AA TIP [1]	1	112	773	0.03	27	0.00	1.6	4871	1.5266	0.0044	0.15639	0.00035	0.86	0.07080	0.00010	936.7	1.9	941.1	1.8	951.5	3.0	1.7
LEA 10-1 307/22	MO [1]	1	2170	7138	3.75	26735	1.81	3.9	18120	1.5133	0.0038	0.15673	0.00034	0.96	0.07002	0.00005	938.6	1.9	935.8	1.5	929.1	1.5	-1.1
LEA 10-1 307/28	MO [1]	1	1071	4528	2.25	10192	1.37	3.4	13007	1.4983	0.0042	0.15472	0.00037	0.94	0.07024	0.00007	927.4	2.1	929.7	1.7	935.3	2.0	0.9
LEA 10-1 307/40	MO CORE [1]	1	1794	4695	4.44	20861	0.74	2.8	19134	1.7899	0.0088	0.18014	0.00081	0.97	0.07206	0.00008	1067.7	4.4	1041.8	3.2	987.7	2.4	-8.8
LEA 10-1 307/39	MO TIP [1]	1	2924	9525	3.54	33733	14.60	17.0	5721	1.5608	0.0048	0.16248	0.00039	0.93	0.06967	0.00008	970.5	2.2	954.8	1.9	918.7	2.5	-6.1
LEA 10-2 307/8	R P [1]	1	3	35	0.25	9	0.75	2.8	78	0.6104	0.0471	0.07371	0.00049	0.65	0.06006	0.00438	458.4	2.9	483.8	29.3	605.8	150.4	25.2
LEA 10-2 311/20	R [3]	1	5	21	4.68	100	1.70	3.7	45	0.6211	0.0822	0.07560	0.00087	0.53	0.05958	0.00755	469.8	5.3	490.5	50.3	588.5	253.4	20.9
LEA 10-2 311/19	R IN [4]	8	1	6	6.05	34	0.43	5.5	54	0.5433	0.0519	0.06974	0.00062	0.45	0.05650	0.00519	434.6	3.8	440.6	33.6	472.0	191.2	8.2
LEA 10-2 311/103	MO [1]	1	235	629	16.93	10646	0.63	2.6	1042	0.5282	0.0088	0.06859	0.00098	0.86	0.05585	0.00048	427.7	5.9	430.6	5.8	446.3	18.9	4.3
LEA 10-2 311/107	MO [1]	1	316	997	13.24	13206	0.55	2.6	1696	0.5248	0.0022	0.06872	0.00014	0.63	0.05539	0.00018	428.4	0.9	428.4	1.4	428.1	7.2	-0.1
LEA 10-2 307/85	MO [1]	1	314	859	15.51	13324	0.83	2.8	1334	0.5320	0.0031	0.06951	0.00024	0.70	0.05552	0.00023	433.2	1.4	433.2	2.0	433.0	9.2	0.0
LEA 10-2 307/9	Z P [1]	1	19	253	0.65	165	0.00	0.7	1677	0.5302	0.0048	0.06890	0.00034	0.63	0.05581	0.00040	429.5	2.0	432.0	3.2	445.0	15.7	3.6
LEA 10-2 311/18	Z P "SUSPECT" [1]	1	11	150	0.56	85	0.00	1.7	395	0.5319	0.0108	0.06867	0.00026	0.49	0.05618	0.00105	428.1	1.6	433.1	7.1	459.4	41.0	7.0
LEA 10-2 311/17	Z TIP [1]	3	8	120	0.11	14	0.00	0.5	3039	0.5787	0.0024	0.07303	0.00018	0.74	0.05747	0.00016	454.4	1.1	463.7	1.6	509.8	6.3	11.2
LEA 10-2 311/21 311/113	MU IN:Z [7]	116	4	4	0.16	1	4.07	469.9	23	0.5157	0.1168	0.06884	0.00086	0.51	0.05433	0.01197	429.2	5.2	422.3	75.4	384.9	431.0	-11.9
LEA 10-2 311/110 311/115	MU [9]	78	4	0	2.58	0	4.12	323.6	18	2.6033	12.5056	0.23217	0.20129	-4.46	0.08133	0.63501	1345.9	993.0	1301.6	1522.8	1229.3	1000.0	-10.5

APPENDIX 4 – $^{40}Ar/^{39}Ar$

Sample: KJR-093 (referred to as JZP-001 by Auburn Noble Isotope Mass Analysis Laboratory)

Date of Analysis: 7/5/2011

J value: 0.016135 ± 0.000082

P	t	40 V			39 V			38 V			37 V			36 V			Moles 40Ar*	%Rad	R		Age (Ma)		%-sd
1.6	10	0.07622	+	0.00055	0.00332	+	0.00006	0.00013	+	0.00003	0.00081	+	0.00030	0.000204	+	0.000021	5.34E-16	20.81%	4.7756	132.785	+	54.931	41.37%
1.6	10	2.95394	+	0.00266	0.19239	+	0.00037	0.00237	+	0.00006	-0.00018	+	0.00013	0.000165	+	0.000027	2.07E-14	98.35%	15.1013	390.290	+	1.368	0.35%
1.6	10	8.34148	+	0.00422	0.53207	+	0.00061	0.00651	+	0.00008	-0.00007	+	0.00016	0.000146	+	0.000043	5.84E-14	99.48%	15.5965	401.763	+	0.792	0.20%
1.6	10	5.14720	+	0.00292	0.33989	+	0.00073	0.00411	+	0.00005	0.00027	+	0.00015	0.000185	+	0.000042	3.60E-14	98.94%	14.9829	387.538	+	1.285	0.33%
1.6	10	3.28431	+	0.00366	0.21554	+	0.00047	0.00263	+	0.00006	-0.00009	+	0.00013	0.000180	+	0.000044	2.30E-14	98.38%	14.9905	387.714	+	1.824	0.47%
1.6	10	5.52541	+	0.00339	0.36869	+	0.00090	0.00459	+	0.00007	-0.00016	+	0.00017	0.000221	+	0.000042	3.87E-14	98.82%	14.8095	383.498	+	1.312	0.34%
1.6	10	0.00098	+	0.00017	0.00000	+	0.00009	-0.00001	+	0.00004	-0.00011	+	0.00019	0.000064	+	0.000041	6.83E-18	-1831.63%	4031.6706	7544.205	+	######	2098.68%
1.6	10	8.25830	+	0.00528	0.51686	+	0.00100	0.00623	+	0.00007	-0.00009	+	0.00019	0.000562	+	0.000023	5.78E-14	97.99%	15.6565	403.149	+	0.908	0.23%
1.6	10	0.00112	+	0.00026	0.00142	+	0.00007	-0.00003	+	0.00004	-0.00026	+	0.00008	0.000041	+	0.000033	7.82E-18	-988.25%	-7.7736	-239.513	+	-211.852	88.45%
1.6	10	0.79298	+	0.00160	0.05089	+	0.00031	0.00066	+	0.00004	-0.00007	+	0.00012	0.000053	+	0.000027	5.55E-15	98.04%	15.2760	394.348	+	4.836	1.23%
1.6	10	0.00081	+	0.00024	0.00060	+	0.00007	-0.00005	+	0.00004	0.00010	+	0.00017	0.000007	+	0.000019	5.68E-18	-159.14%	-2.1355	-62.693	+	-267.709	427.02%
1.6	10	8.81889	+	0.00498	0.58194	+	0.00065	0.00718	+	0.00008	-0.00002	+	0.00020	0.000113	+	0.000025	6.18E-14	99.62%	15.0970	390.191	+	0.594	0.15%
1.6	10	0.04131	+	0.00033	0.05747	+	0.00033	0.00065	+	0.00004	-0.00031	+	0.00008	-0.000009	+	0.000019	2.89E-16	106.73%	0.7182	20.605	+	2.830	13.74%
1.6	10	0.30408	+	0.00043	0.01837	+	0.00013	0.00020	+	0.00004	-0.00009	+	0.00022	0.000021	+	0.000041	2.13E-15	97.94%	16.2138	415.962	+	16.987	4.08%
1.6	10	0.22512	+	0.00045	0.21828	+	0.00087	0.00266	+	0.00007	0.00060	+	0.00016	0.000162	+	0.000018	1.58E-15	78.79%	0.8126	23.296	+	0.704	3.02%
0	0	2.50153	+	0.00226	0.15836	+	0.00063	0.00192	+	0.00005	0.00006	+	0.00015	0.000182	+	0.000025	1.75E-14	97.85%	15.4564	398.526	+	2.071	0.52%
1.6	10	5.02383	+	0.00888	0.33176	+	0.00094	0.00416	+	0.00005	0.00020	+	0.00011	0.000141	+	0.000020	3.52E-14	99.17%	15.0173	388.338	+	1.388	0.36%
1.6	10	5.02397	+	0.00888	0.33180	+	0.00094	0.00409	+	0.00004	0.00021	+	0.00011	0.000191	+	0.000030	3.52E-14	98.88%	14.9719	387.282	+	1.478	0.38%
1.6	10	11.39151	+	0.00656	0.72854	+	0.00044	0.00904	+	0.00014	0.00103	+	0.00016	0.000826	+	0.000031	7.98E-14	97.86%	15.3010	394.927	+	0.466	0.12%
1.6	10	11.04448	+	0.00606	0.72590	+	0.00132	0.00939	+	0.00019	0.00196	+	0.00012	0.000467	+	0.000028	7.73E-14	98.75%	15.0251	388.519	+	0.803	0.21%
1.6	10	4.83533	+	0.00411	0.31878	+	0.00065	0.00396	+	0.00007	0.00010	+	0.00014	0.000034	+	0.000020	3.39E-14	99.79%	15.1364	391.106	+	0.993	0.25%
1.6	10	14.83854	+	0.00556	0.98086	+	0.00128	0.01216	+	0.00007	0.00175	+	0.00016	0.000239	+	0.000030	1.04E-13	99.52%	15.0562	389.244	+	0.581	0.15%
1.6	10	2.54828	+	0.00204	0.16787	+	0.00046	0.00210	+	0.00005	-0.00010	+	0.00013	0.000180	+	0.000019	1.78E-14	97.91%	14.8621	384.725	+	1.410	0.37%
1.6	10	0.00224	+	0.00021	0.00058	+	0.00005	0.00003	+	0.00004	0.00013	+	0.00017	0.000033	+	0.000024	1.57E-17	-338.65%	-13.1212	-424.927	+	-405.505	95.43%
1.6	10	1.22256	+	0.00179	0.08117	+	0.00049	0.00096	+	0.00006	0.00015	+	0.00018	-0.000001	+	0.000025	8.56E-15	100.02%	15.0612	389.360	+	3.351	0.86%
1.6	10	0.00051	+	0.00020	0.00054	+	0.00006	-0.00002	+	0.00002	-0.00026	+	0.00012	0.000020	+	0.000018	3.55E-18	-1043.17%	-9.7838	-306.995	+	-305.188	99.41%
1.6	10	6.34078	+	0.00299	0.41678	+	0.00056	0.00502	+	0.00005	0.00005	+	0.00020	0.000134	+	0.000025	4.44E-14	99.38%	15.1192	390.708	+	0.727	0.19%
1.6	10	0.01463	+	0.00028	0.02046	+	0.00012	0.00025	+	0.00004	0.00002	+	0.00021	0.000017	+	0.000020	1.02E-16	65.56%	0.4688	13.476	+	8.466	62.82%
1.6	10	5.77176	+	0.00485	0.37848	+	0.00091	0.00453	+	0.00006	-0.00032	+	0.00014	0.000062	+	0.000024	4.04E-14	99.68%	15.2013	392.615	+	1.118	0.28%
1.6	10	7.74523	+	0.00257	0.51684	+	0.00112	0.00620	+	0.00005	0.00001	+	0.00012	0.000069	+	0.000024	5.42E-14	99.74%	14.9463	386.685	+	0.917	0.24%
1.6	10	2.56543	+	0.00138	0.16504	+	0.00057	0.00204	+	0.00005	0.00009	+	0.00015	0.000284	+	0.000027	1.80E-14	96.72%	15.0352	388.755	+	1.895	0.49%
1.6	10	9.50246	+	0.00408	0.62131	+	0.00124	0.00776	+	0.00010	0.00048	+	0.00017	0.000145	+	0.000025	6.65E-14	99.55%	15.2253	393.172	+	0.862	0.22%

APPENDIX 5 – Analytical Methods

Isotope Dilution – Thermal Ionization Mass Spectrometry (ID-TIMS)

Sample Preparation

Throughout the entire analysis process (collection, preparation, and measurement) an emphasis was placed on avoiding any contamination by foreign mineral grains. To mitigate contamination that could have occurred during collection and transport, samples as collected in the field were first scrubbed using dish detergent and a stiff-bristled brush and then rinsed under a faucet, removing superficial debris and weathered fragments of the sample itself. Samples larger than fist-sized (≥ 300 cm^3) were cut into smaller pieces. Each sample was placed in an ultrasonic bath for 10 minutes to remove more tenacious superficial debris and biological material. The sample was then given one more rinse under a faucet and then rinsed in alcohol to quickly remove excess water. The cleaned sample was then dried in a clean oven on low heat (< 40 °C) for 45 minutes. Low heat and long duration were used in order to avoid potential alteration of minerals in the event future $^{40}Ar/^{39}Ar$ geochronology is attempted on muscovite separated from the sample. The dried sample was then sealed inside a new plastic bag to prevent contamination in the event further sample preparation was delayed.

Before a jaw crusher was used for gross disaggregation, all work surfaces that were to come into contact with a given sampler were first thoroughly cleaned to avoid contamination by mineral grains embedded in the crusher itself. All surfaces were first ground using a rotary wire-brush attached to an electric drill, followed by more precise hand-grinding using a finer brush, focusing on areas the rotary brush could not reach. Where possible, parts were first removed from the jaw crusher to facilitate cleaning. The resultant polished surfaces were finally cleaned using alcohol. Ear-, eye-, and skin-protection were used throughout this process, as well as a dust/debris-collection system.

Upon post-cleaning reassembly of the jaw crusher in preparation for sample disaggregation, a new sample bag was placed between the crusher plates and the jaw crusher proper (the plate fasteners penetrated the bag itself), in order to minimize the risk of grains contaminating the jaw crusher with respect to future samples. In the event that the sample-collection bag was damaged in the process of collecting the disaggregated sample, a second bag was placed around the primary bag from beneath. These bags were both then placed on a support in order to reduce the stress placed on the bags, particularly the primary bag fastened to the jaw crusher. The jaw-crusher was then activated and the sample fed in. The disaggregated sample was then collected in the sample bag. Samples were then further crushed in a grain mill.

Crushed samples were further hydraulically-separated using a Wilfley table. The minerals that were heavy enough to survive the Wilfley table where then dried and magnetically separated. Gross separation was first conducted by letting the sample free-fall past a magnet. Free fall survivors were then separated further by immersion in a flask of methylene iodide. Minerals denser than the methylene iodide were then subjected to iterative separation in a Frantz magnetic separator. Separates were passed down a vibrating, inclined track and through an increasingly strong magnetic field. The end product of this chain of separations is a few thousand grains in which heavy minerals with relatively low magnetic susceptibility (e.g. rutile, sphene, monazite, and zircon) are concentrated.

Picking Minerals

The heaviest, least magnetic group of separates is likely to be the most concentrated in zircon. This group is placed in a plastic tray and submerged in alcohol. Manual mineral separation is then conducted using a binocular microscope and a pair of tweezers. Grains are first grouped by mineralogy and then sorted into morphologically defined subgroups within a given group of minerals. Examples of these subgroups might be clear prismatic zircons with no obvious cores separated into one subgroup while another subgroup might consist of grains with dark uranium-rich rims mantling clear uranium-poor detrital cores. The purpose of identifying subgroups is to ultimately partition the minerals found into groups defined by their petrogenesis. Subgroups are further sorted to find the most pristine representative samples for analysis.

Zircon Abrasion

As a rule, zircon crystals as found in nature are almost universally discordant, with discordance increasing with age. The atomic structure of zircon is regularly disrupted as a result of α-decay events occurring within the thorium and uranium decay chains, with individual α-decay events producing as many as 2000 permanent atomic displacements in the zircon crystal lattice (Ewing et al., 2003). The cumulative effect of this radiation damage are discontinuities through which elements with weak affinities to the zircon lattice, such as radiogenic lead, can be mobilized and ultimately leached from the zircon crystal. The effects of radiation damage are most profound away from the interior of the crystal, as the damage is more likely to intersect the crystal surface and cause cracking and pitting. The damaged and irregular zircon surface is much more susceptible to chemical alteration, with open-system behavior evidenced by marked reductions in density, elastic modulus, and hardness (Ewing et al., 2003).

To mitigate the precision-ruining effects of measuring the domain of discordant radiation-damaged outer portions of a zircon, it is common to physically (Krogh, 1982) or chemically (Mattinson, 2005) abrade zircons to remove the outermost layer so that the only material that is measured is zircon that has never behaved as an open-system, i.e. zircon that hasn't suffered from lead loss.

Chemical Abrasion

Chemical abrasion was used to selectively remove discordant domains from specific zircons prior to analysis. Chemical abrasion involves high-temperature annealing of individual zircon crystals, followed by partial dissolution of the crystal (Mattinson, 2005). Annealing consisted of heating the individual grains at 950 °C for 48 hours. Portions of the zircon crystal that have not received catastrophic radiation damage will see a decrease in solubility as a result of annealing (Mattinson, 2005). Metamict portions of the zircon will not anneal, despite the time spent in high temperature conditions. Subsequent partial dissolution in HF preferentially removed the highly soluble and discordant (i.e. metamict) domains while leaving annealed portions of the crystal untouched (Mattinson, 2005). Partial dissolution involved immersion in HF for <24 hours, at 300 °C.

Air Abrasion

Extremely metamict zircon crystals are unsuitable for chemical abrasion and must be physically abraded in an air abrasion chamber. Chemical abrasion is not helpful as pervasive radiation damage precludes successful annealing, making partial dissolution in HF untenable, as the crystal remains highly soluble and subject to premature total dissolution.

The metamict zircons were placed inside a small brass container, along with a few milligrams of powdered pyrite. A compressed air (< 50 psi) inlet in the center of the chamber causes the pyrite and zircon to continually tumble around in the chamber, gradually removing through mechanical means the concentrated metamict domains on the surface of the zircon crystals. Pressure does not build up in the chamber as there are numerous filtered outlets. The pyrite is present to aid in polishing the zircons and to serve as a cushion to reduce the chance of breaking the zircons into pieces too small to be easily manipulated during processing. After several hours of air abrasion in the chamber, the zircon/pyrite mixture is removed from the chamber and placed in a bath of weak HNO_3 where the pyrite is preferentially dissolved, leaving only zircon grains, ready for further preparation. This process is described in detail by Krogh (1982b) and also by Davis et al. (1982).

Zircon Dissolution / Isotope Dilution

To ensure the zircon grains were completely free of extraneous Pb, they were all thoroughly washed before being dissolved. First they were rinsed in a bath of HNO_3 for 20-30 minutes, after which the acid was removed using a pipette and the zircons were rinsed in deionized water. The water was removed and then the samples were rinsed in acetone. After a second acetone rinse, the samples were dried on a hotplate for 60 seconds. The cleaned zircon grains were then weighed, after which the samples were placed in Teflon bombs and then spiked with a known amount of tracer consisting of a mixture of ^{205}Pb and ^{235}U. After the samples were spiked, a drop of HF was added. The bombs were then sealed and placed in an oven for 3 days at 189 °C, in order to dissolve the zircon grains (Krogh, 1973).

After the Teflon bombs were removed from the oven and had cooled sufficiently, the samples were opened and placed on a hotplate for four hours to allow the remaining HF to evaporate. Ten drops of HCl were then added to the samples which were then recapped and put back on the hotplate for a few hours. After cooling, the samples (which now are more-or-less entirely dissolved in the 10 drops of HCl) were transferred from the bombs into ion-exchange columns. The samples were then rinsed several times within the ion exchange columns using dilute HCl. This process effectively removes chemical species other than U and Pb from the solution. The rinsing solution is collected in case additional analysis is desired. The remaining solution containing only U and Pb was rinsed out of the ion exchange columns using first a rinse of strong HCl (to remove the Pb) and then two rinses of de-ionized water (to remove the U). The Pb and U were collected separately and placed back in cleaned bombs along with a drop of ion emitter (primarily H_3PO_4) and placed on a hot plate. The water and HCl evaporated at this point, leaving the Pb and U dissolved in the drop of H_3PO_4. Sample loading and analysis was performed on a Finnigan MAT 263 mass spectrometer, the procedure used was as described by Gerstenberger and Haase (1997).